# CRITICAL ZONE (CZ) EXPORT TO STREAMS AS INDICATOR FOR CZ STRUCTURE AND FUNCTION

EDITED BY: Julia Perdrial, Ashlee Dere, Nicole West and Pamela L. Sullivan

PUBLISHED IN: Frontiers in Earth Science and Frontiers in Environmental Science

frontiers Research Topics

# frontiers



ISSN 1664-8714
ISBN 978-2-88963-623-5
DOI 10.3389/978-2-88963-623-5

## About Frontiers

Frontiers is more than just an open-access publisher of scholarly articles: it is a pioneering approach to the world of academia, radically improving the way scholarly research is managed. The grand vision of Frontiers is a world where all people have an equal opportunity to seek, share and generate knowledge. Frontiers provides immediate and permanent online open access to all its publications, but this alone is not enough to realize our grand goals.

## Frontiers Journal Series

The Frontiers Journal Series is a multi-tier and interdisciplinary set of open-access, online journals, promising a paradigm shift from the current review, selection and dissemination processes in academic publishing. All Frontiers journals are driven by researchers for researchers; therefore, they constitute a service to the scholarly community. At the same time, the Frontiers Journal Series operates on a revolutionary invention, the tiered publishing system, initially addressing specific communities of scholars, and gradually climbing up to broader public understanding, thus serving the interests of the lay society, too.

## Dedication to Quality

Each Frontiers article is a landmark of the highest quality, thanks to genuinely collaborative interactions between authors and review editors, who include some of the world's best academicians. Research must be certified by peers before entering a stream of knowledge that may eventually reach the public - and shape society; therefore, Frontiers only applies the most rigorous and unbiased reviews.
Frontiers revolutionizes research publishing by freely delivering the most outstanding research, evaluated with no bias from both the academic and social point of view. By applying the most advanced information technologies, Frontiers is catapulting scholarly publishing into a new generation.

## What are Frontiers Research Topics?

Frontiers Research Topics are very popular trademarks of the Frontiers Journals Series: they are collections of at least ten articles, all centered on a particular subject. With their unique mix of varied contributions from Original Research to Review Articles, Frontiers Research Topics unify the most influential researchers, the latest key findings and historical advances in a hot research area! Find out more on how to host your own Frontiers Research Topic or contribute to one as an author by contacting the Frontiers Editorial Office: researchtopics@frontiersin.org

# CRITICAL ZONE (CZ) EXPORT TO STREAMS AS INDICATOR FOR CZ STRUCTURE AND FUNCTION

Topic Editors:
**Julia Perdrial,** University of Vermont, United States
**Ashlee Dere,** University of Nebraska Omaha, United States
**Nicole West,** Central Michigan University, United States
**Pamela L. Sullivan,** University of Kansas, United States

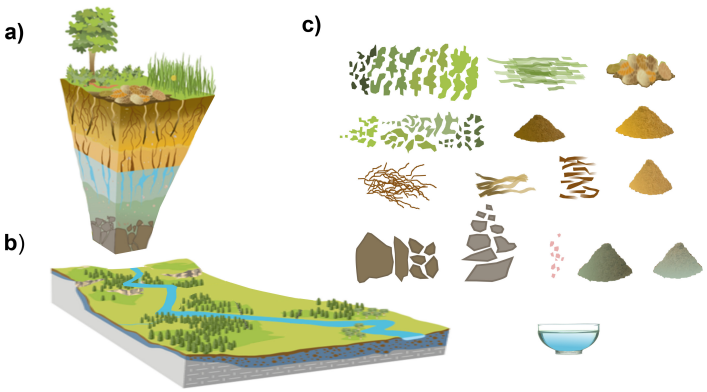


Credit: (*modified after Chorover et al. 2007, with permission*)

**Citation:** Perdrial, J., Dere, A., West, N., Sullivan, P. L., eds. (2020). Critical Zone (CZ) Export to Streams as Indicator for CZ Structure and Function. Lausanne: Frontiers Media SA. doi: 10.3389/978-2-88963-623-5

# Table of Contents

frontiers in Earth Science

EDITORIAL
published: 25 February 2020
doi: 10.3389/feart.2020.00037

# Editorial: Critical Zone (CZ) Export to Streams as Indicator for CZ Structure and Function

*Julia Perdrial*[1]*, *Pamela L. Sullivan*[2], *Ashlee Dere*[3] *and Nicole West*[4]

[1] Department of Geology, University of Vermont, Burlington, VT, United States, [2] College of Earth, Ocean, and Atmospheric Science, Oregon State University, Corvallis, OR, United States, [3] Department of Geography/Geology, University of Nebraska at Omaha, Omaha, NE, United States, [4] Department of Earth and Atmospheric Sciences, Central Michigan University, Mt. Pleasant, MI, United States

**Keywords: critical zone, stream, system, interdisciplinary, catchment**

## Editorial on the Research Topic

## Critical Zone (CZ) Export to Streams as Indicator for CZ Structure and Function

The critical zone (CZ) is commonly defined as the zone of life, spanning from the tops of the tree canopy down to the actively cycled ground water (Brantley et al., 2007; Chorover et al., 2007; Richter and Mobley, 2009). Considering the CZ as an open thermodynamic system, where energy and matter can exchange freely, precipitation is one of many important CZ inputs, while stream exports dissipate energy and matter (Chorover et al., 2011).

Traditionally, investigations of the Earth's surface are limited to separate parts of the CZ (e.g., the biosphere, lithosphere or hydrosphere) that are analyzed outside of their context. However, streams are integrators of the physical structure and connected nature of subsurface pore space in the CZ as well as the biogeochemical reactions that play out along the multitude of flow paths. In order to decipher such pathways and related CZ processes, we need to investigate CZ processes within the catchment context.

For example, we know that relief and soil thickness play a large role in determining hydrologic flowpaths, fluid residence time, and soil drainage class (Maher, 2011). These processes can result in changes in soil dynamics, including biogeochemistry, that cascade through the system and ultimately control stream water composition (Perdrial et al., 2015).

To probe stream water dynamics, high-frequency datasets are now increasingly generated and long-term datasets are used to identify changes in CZ processes (Crowther et al., 2016; Robinson et al., 2016; Hirmas et al., 2018). For example, many streams show long-term changes in fluxes of dissolved organic carbon (Raymond and Saiers, 2010; Perdrial et al., 2014; Zarnetske et al., 2018), weathering solutes (McIntosh et al., 2017), and nutrients (Björnerås et al., 2017; Jarvie et al., 2018), which have been related to changes in climate drivers, land use, and overall soil conditions. In particular, investigations of the relationships between solutes and their discharge regimes have shown strong potential to understand the impacts of extreme perturbations (Chorover et al., 2017; McIntosh et al., 2017) and the sensitivity of CZ processes to these changes (Abbott et al., 2018; Sullivan et al., 2018). The goal of this special topic issue is to highlight opportunities as well as limitations of streams as indicator of CZ structure and processes.

Several contributions highlight how relief, topography, and soil thickness affect CZ evolution and are reflected in stream composition. Cincotta et al. and Armfield et al. found that CZ



***Edited and reviewed by:***
*Alexandra V. Turchyn, University of Cambridge, United Kingdom*

***Correspondence:**
*Julia Perdrial*
*Julia.Perdrial@uvm.edu*

***Specialty section:***
*This article was submitted to Biogeoscience, a section of the journal Frontiers in Earth Science*

***Received:*** *03 December 2019*
***Accepted:*** *04 February 2020*
***Published:*** *25 February 2020*

***Citation:***
*Perdrial J, Sullivan PL, Dere A and West N (2020) Editorial: Critical Zone (CZ) Export to Streams as Indicator for CZ Structure and Function. Front. Earth Sci. 8:37. doi: 10.3389/feart.2020.00037*

composition varies drastically with landscape position in a northeastern United States forested headwater catchment, and that near stream environments disproportionally affect stream water response. Bailey et al. found that, along stream segments, the connectivity to shallow and deep upslope soils strongly impacted stream water geochemistry. Resulting elluvial soil processes were found to control stream chemistry in shallow soil environments while illuvial soil processes persisted in deep soils. Using a refined model and two contrasting forested sites, Billings et al. explored linkages between upland and depositional environments and the impact of soil organic carbon (SOC) erosion and burial on carbon budgets within watersheds on decadal to centennial time scales. They noted that the reactivity and distribution of SOC across watersheds is necessary to predict carbon storage across the landscape.

Several Critical Zone Observatory (CZO) studies reveal the importance of biotic processes and storm event magnitude in controlling elemental behavior. Olshansky et al. found that concentration-discharge patterns during snowmelt in the Jemez River Basin CZO in New Mexico indicate biologically mediated silicate weathering that propagates from the shallow CZ down through groundwater and strongly impacts stream water composition. A logical extension of this work is that processes impacting root/microbial respiration and biologically generated acids will alter both silicate weathering and stream water composition. Using sensor data from the Luquillo CZO in Puerto Rico, Wymore et al. found transport vs. supply limitation using concentration-discharge patterns of specific conductance and turbidity. The authors note that these relationships are especially influenced by the magnitude of events (including the category 5 Hurricane Maria) and CZ lithology.

Variations in bedrock lithology are also a theme in a cross site comparison of oxyanion dynamics at several CZOs (including Boulder Creek, Calhoun, Luquillo, and Southern Sierra). The study by Richardson et al. emphasizes the importance of deep bedrock and transport processes within the CZ as controls for stream water dynamics. The role of land use (agricultural and restored prairie) is investigated in the contribution by Dere et al., where solute fluxes through soils and to streams in Nebraska and Iowa are quantified. Their results indicate that changes in land use propagate to streams and drive weathering product export less than 50 years after land use change.

## AUTHOR CONTRIBUTIONS

All authors listed have made a substantial, direct and intellectual contribution to the work, and approved it for publication.

## FUNDING

This research was supported by the National Science Foundation, grant no. EAR-1724171.

## REFERENCES

Abbott, B. W., Moatar, F., Gauthier, O., Fovet, O., Antoine, V., and Ragueneau, O. (2018). Trends and seasonality of river nutrients in agricultural catchments: 18 years of weekly citizen science in France. *Sci. Total Environ.* 624, 845–858. doi: 10.1016/j.scitotenv.2017.12.176

Björnerås, C., Weyhenmeyer, G. A., Evans, C. D., Gessner, M. O., Grossart, H.-P., Kangur, K., et al. (2017). Widespread increases in iron concentration in European and North American freshwaters. *Glob. Biogeochem. Cycles* 31, 1488–1500. doi: 10.1002/2017GB005749

Brantley, S. L., Goldhaber, M. B., and Ragnarsdottir, K. V. (2007). Crossing disciplines and scales to understand the critical zone. *Elements* 3, 307–314. doi: 10.2113/gselements.3.5.307

Chorover, J., Derry, L. A., and McDowell, W. H. (2017). Concentration-discharge relations in the critical zone: implications for resolving critical zone structure, function, and evolution. *Water Resour. Res.* 53, 8654–8659. doi: 10.1002/2017WR021111

Chorover, J., Kretzschmar, R., Garcia-Pichel, F., and Sparks, D. L. (2007). Soil biogeochemical processes within the critical zone. *Elements* 3, 321–326. doi: 10.2113/gselements.3.5.321

Chorover, J., Troch, P., Rasmussen, C., Brooks, P. D., Pelletier, J. D., Breshears, D. D., et al. (2011). Probing how water, carbon, and energy drive landscape evolution and surface water dynamics: the Jemez River Basin – Santa Catalina Mountains Critical Zone Observatory. *Vadose Zone J.* 10, 884–899. doi: 10.2136/vzj2010.0132

Crowther, T. W., Todd-Brown, K. E. O., Rowe, C. W., Wieder, W. R., Carey, J. C., Machmuller, M. B., et al. (2016). Quantifying global soil carbon losses in response to warming. *Nature* 540, 104–108. doi: 10.1038/nature20150

Hirmas, D. R., Giménez, D., Nemes, A., Kerry, R., Brunsell, N. A., and Wilson, C. J. (2018). Climate-induced changes in continental-scale soil macroporosity may intensify water cycle. *Nature* 561, 100–103. doi: 10.1038/s41586-018-0463-x

Jarvie, H. P., Edwards, F. K., Bowes, M. J., Scarlett, P., Bachiller-Jareno, N., Smith, D. R., et al. (2018). Phosphorus and nitrogen limitation and impairment of headwater streams relative to rivers in Great Britain: a national perspective on eutrophication. *Sci. Total Environ.* 621, 849–862. doi: 10.1016/j.scitotenv.2017.11.128

Maher, K. (2011). The role of fluid residence time and topographic scales in determining chemical fluxes from landscapes. *Earth Planet. Sci. Lett.* 312, 48–58. doi: 10.1016/j.epsl.2011.09.040

McIntosh, J. C., Schaumberg, C., Perdrial, J., Harpold, A., Vázquez-Ortega, A., Rasmussen, C., et al. (2017). Geochemical evolution of the critical zone across variable time scales informs concentration-discharge relationships: Jemez River Basin Critical Zone Observatory. *Water Resour. Res.* 53, 4169–4196. doi: 10.1002/2016WR019712

Perdrial, J. N., McIntosh, J. C., Harpold, A., Brooks, P. D., Zapata-Rios, X., Ray, J., et al. (2014). Stream water carbon controls in seasonally snow-covered mountain catchments: impact of inter annual variability of water fluxes, catchment aspect and seasonal processes. *Biogeochemistry* 118, 273–290. doi: 10.1007/s10533-013-9929-y

Perdrial, J. N., Thompson, A. A., and Chorover, J. (2015). "Soil geochemistry in the critical zone: influence on atmosphere, surface- and groundwater composition," in *Principles and Dynamics of the Critical Zone,* eds J. R. Giardino and C. Houser (Elsevier), 173–201. doi: 10.1016/B978-0-444-63369-9.00006-9

Raymond, P. A., and Saiers, J. E. (2010). Event controlled DOC export from forested watersheds. *Biogeochemistry* 100, 197–209. doi: 10.1007/s10533-010-9416-7

Richter, D. d., and Mobley, M. L. (2009). Monitoring Earth's critical zone. *Science* 326, 1067–1068. doi: 10.1126/science.1179117

Robinson, D. A., Jones, S. B., Lebron, I., Reinsch, S., Domínguez, M. T., Smith, A. R., et al. (2016). Experimental evidence for drought induced

alternative stable states of soil moisture. *Sci. Rep.* 6:20018. doi: 10.1038/srep 20018

Sullivan, P. L., Stops, M. W., Macpherson, G. L., Li, L., Hirmas, D. R., and Dodds, W. K. (2018). How landscape heterogeneity governs stream water concentration-discharge behavior in carbonate terrains (Konza Prairie, KS: USA). *Chem. Geol.* 527:118989. doi: 10.1016/j.chemgeo.2018.12.002

Zarnetske, J. P., Bouda, M., Abbott, B. W., Saiers, J., and Raymond, P. A. (2018). Generality of hydrologic transport limitation of watershed organic carbon flux across ecoregions of the united states. *Geophys. Res. Lett.* 45, 11702–11711. doi: 10.1029/2018GL080005

**Conflict of Interest:** The authors declare that the research was conducted in the absence of any commercial or financial relationships that could be construed as a potential conflict of interest.

frontiers in Earth Science

ORIGINAL RESEARCH
published: 09 November 2018
doi: 10.3389/feart.2018.00181

# Subsurface Pore Water Contributions to Stream Concentration-Discharge Relations Across a Snowmelt Hydrograph

*Yaniv Olshansky[1], Alissa M. White[2], Bryan G. Moravec[1], Jennifer McIntosh[2] and Jon Chorover[1]**

[1] Department of Soil, Water and Environmental Science, The University of Arizona, Tucson, AZ, United States, [2] Department of Hydrology and Atmospheric Sciences, The University of Arizona, Tucson, AZ, United States

OPEN ACCESS

**Edited by:**
Pamela L. Sullivan,
The University of Kansas,
United States

**Reviewed by:**
Daniel Enrique Ibarra,
Stanford University, United States
Matthew Winnick,
University of Massachusetts Amherst,
United States
Elizabeth Herndon,
Kent State University, United States

***Correspondence:**
Jon Chorover
chorover@email.arizona.edu

**Specialty section:**
This article was submitted to Biogeoscience, a section of the journal Frontiers in Earth Science

**Received:** 02 June 2018
**Accepted:** 12 October 2018
**Published:** 09 November 2018

**Citation:**
Olshansky Y, White AM, Moravec BG, McIntosh J and Chorover J (2018) Subsurface Pore Water Contributions to Stream Concentration-Discharge Relations Across a Snowmelt Hydrograph. Front. Earth Sci. 6:181. doi: 10.3389/feart.2018.00181

This study investigated the concentration discharge (C-Q) patterns of selected elements transported to streams during spring snowmelt through an instrumented mixed-conifer forested catchment in rhyolitic terrain in the Jemez Mountains (NM, United States). High frequency, concurrent sampling of soil solution and gasses, groundwater, and surface water enabled identification and sourcing of five groups of solutes with distinct C-Q behavior. Non-hydrolyzing cations and strong acid anions, had mostly positive C-Q relations and a clockwise hysteresis pattern related to flushing of a limited reservoir of solutes accumulated in soils under snowpack. Rare earth elements (REEs) and dissolved organic carbon (DOC), demonstrated large positive C-Q relations and a clockwise hysteresis pattern, consistent with their co-transport as metal-ligand complexes, and signaling biologically induced weathering reactions in the soil. Silicon and dissolved inorganic carbon (DIC) exhibited chemostatic C-Q trends and an anti-clockwise hysteresis pattern consistent with sourcing from deep groundwater. Hydrolyzing metals (Mn, Al, Ti, and Zr) with high coefficients of variance (CV) for concentration relative to CV values for stream discharge and with no significant C-Q pattern, were found to be transported mainly as filterable colloids. Fe C-Q behavior was similar to this hydrolyzing metals group, but complexation with DOC was also important for Fe during the initial stage of the snowmelt hydrograph. Investigation of time-series of solutes and gasses provided evidence for biologically induced silicate weathering reactions that initiated in the soil subsurface and propagated down through groundwater to streams.

**Keywords: critical zone, mineral weathering, groundwater, cluster analysis, PCA**

## KEY POINTS

(1) Hydrologic and critical zone observatories provide opportunities for high frequency sensing and sampling to resolve coupled processes controlling catchment hydrochemical response.
(2) Cluster and principal components analysis of indices pertaining to concentration-discharge (C-Q) identified five groups of solutes with transport behavior governed by distinct hydrogeochemical processes.
(3) The results provide evidence of biologically influenced weathering reactions in soil and groundwater time-series that are propagated into stream C-Q relations.

## INTRODUCTION

Solute concentration-discharge (C-Q) relations in streams contain useful information on flow paths and biogeochemical processes that occur during water transport through the critical zone (Chorover et al., 2017). During transport, water interacts with multiple CZ compartments, including soil pores, groundwater, and hyporheic zones, accumulating and redistributing solutes and suspended matter. The chemical signature of the water changes as a function of contact times and composition in these compartments as a result of thermodynamic and kinetically limited reactions (e.g., ion exchange, mineral transformation, organic matter decomposition), and mixing of different sources. Streamwater C-Q relations integrate these multiple upgradient CZ processes (Evans and Davies, 1998; Pokrovsky et al., 2006; Godsey et al., 2009; Bouchez et al., 2017; Winnick et al., 2017).

Concentration-discharge relations are defined as *chemostatic* or *chemodynamic*, depending on whether variation in concentration is negligible or significant, respectively, relative to variation in discharge (Godsey et al., 2009; Herndon et al., 2015). Large solute reservoirs and high chemical reaction rates relative to advective velocity are hypothesized to generate chemostatic C-Q relations (Godsey et al., 2009; Thompson et al., 2011; Vaughan et al., 2017), whereas supply limited conditions (i.e., small mass stores and low reaction rates) result in solute dilution (Maher, 2011). Solute accretion (i.e., increased concentration with discharge) has been attributed to flushing of a concentrated source (e.g., soil pore water, hyporheic zones) during high flow events (Hoagland et al., 2017; Vaughan et al., 2017). Positive C-Q relations may also result from colloid mobilization during high through-flux events (Trostle et al., 2016).

Hysteresis in C-Q relations between rising and falling hydrograph limbs provides additional information on processes controlling solute export to the stream. Higher solute concentrations on the rising versus falling limb (i.e., clockwise hysteresis), suggests limited solute supply from a proximal source (Evans and Davies, 1998; Chanat et al., 2002; Bowes et al., 2009, 2015; Vaughan et al., 2017), whereas the opposite trend suggests longer transport time and a distal solute source, or a change in rate of groundwater relative to near surface water discharge to the stream. Alternatively, non-stationary transit time distributions of waters through the subsurface may also result in hysteresis in the C-Q relation (Benettin et al., 2015; Winnick et al., 2017).

Most studies on C-Q relations have focused solely on measurements of stream water itself and general catchment characteristics (i.e., size, relief, and geology). To improve mechanistic interpretations, it should be beneficial to concurrently assess time-dependent hydrochemical behavior of upgradient sources (i.e., soil pore water and groundwater). Few prior studies have simultaneously collected time-series data on the chemistry and hydrologic response of soil water, groundwater and streams (Kim et al., 2014, 2017; Herndon et al., 2015; Hoagland et al., 2017). Furthermore, while stream hydrochemistry can vary significantly over the course of individual hydrologic events, sampling across a wide range of discharge is frequently limited to grab samples taken at random discharge levels often separated in time by days to weeks (Evans and Davies, 1998; Godsey et al., 2009; McIntosh et al., 2017). Several recent studies have indicated the need for higher (sub-daily) sampling frequency to better resolve system response to hydrologic events (Bowes et al., 2009; Kirchner and Neal, 2013; McIntosh et al., 2017). Prior work at the Jemez Critical Zone Observatory (NM, United States) has indicated that most of the groundwater recharge and the largest variation in stream discharge occurs during the annual snowmelt period, which is characterized by a single large stream hydrograph that extends over several weeks (Zapata-Rios et al., 2016). In the present study, we collected time series data across a snowmelt hydrograph at daily minimum and maximum streamflow, to test the hypotheses that (i) event-based changes in soil and groundwater chemistry would be reflected in stream C-Q relations and (ii) this would enable us to better resolve mechanistic controls over stream hydrochemistry. Therefore, the aim of this study was to link stream C-Q relations to hydrochemical dynamics in up gradient sources, by simultaneously probing soil, groundwater and stream hydrologic and hydrochemical response.

## MATERIALS AND METHODS

### Site Description

The study site is part of the Jemez River Basin-Critical Zone Observatory (JRB-CZO) (Chorover et al., 2011), and the La Jara catchment studied here has been described in several prior publications (Perdrial et al., 2014, 2018; Vázquez-Ortega et al., 2015, 2016; Zapata-Rios et al., 2016; McIntosh et al., 2017). La Jara is a 3.3 $km^2$ catchment extending in elevation from 3432 to 2728 m, draining the south facing slope of Redondo dome under montane mixed conifer forest within the Valles Caldera National Preserve (VCNP) in the Jemez Mountains of northern New Mexico (**Figure 1**). The upper headwaters include a highly instrumented 0.15 $km^2$ zero order basin (ZOB). The La Jara catchment (LJ) and its nested ZOB are the focus of the current study. The site was impacted by the Thompson Ridge wildfire in May–June 2013 with medium to high severity burned areas distributed in a patch-wise fashion (Reale et al., 2015).

The instrumented ZOB and larger LJ catchment contain a mixture of the upper Tshirege member of Bandelier Tuff and caldera collapse breccias. While the LJ catchment is dominated by Bandelier Tuff, in the ZOB, these two geological substrates are bisected by a series of normal faults that lie parallel to the catchment axis. The Bandelier Tuff is rhyolitic welded to non-welded vitrophyre primarily made up of plagioclase, sanidine, quartz, pyroxene and biotite in a glass matrix intra-stratified by ash-fall deposits. Asymmetrical jointing in tuffs was observed from the surface to a depth of at least 50 m in drill cores excavated from the ZOB in June, 2016. Evidence of discontinuous hydrothermal alteration exists at

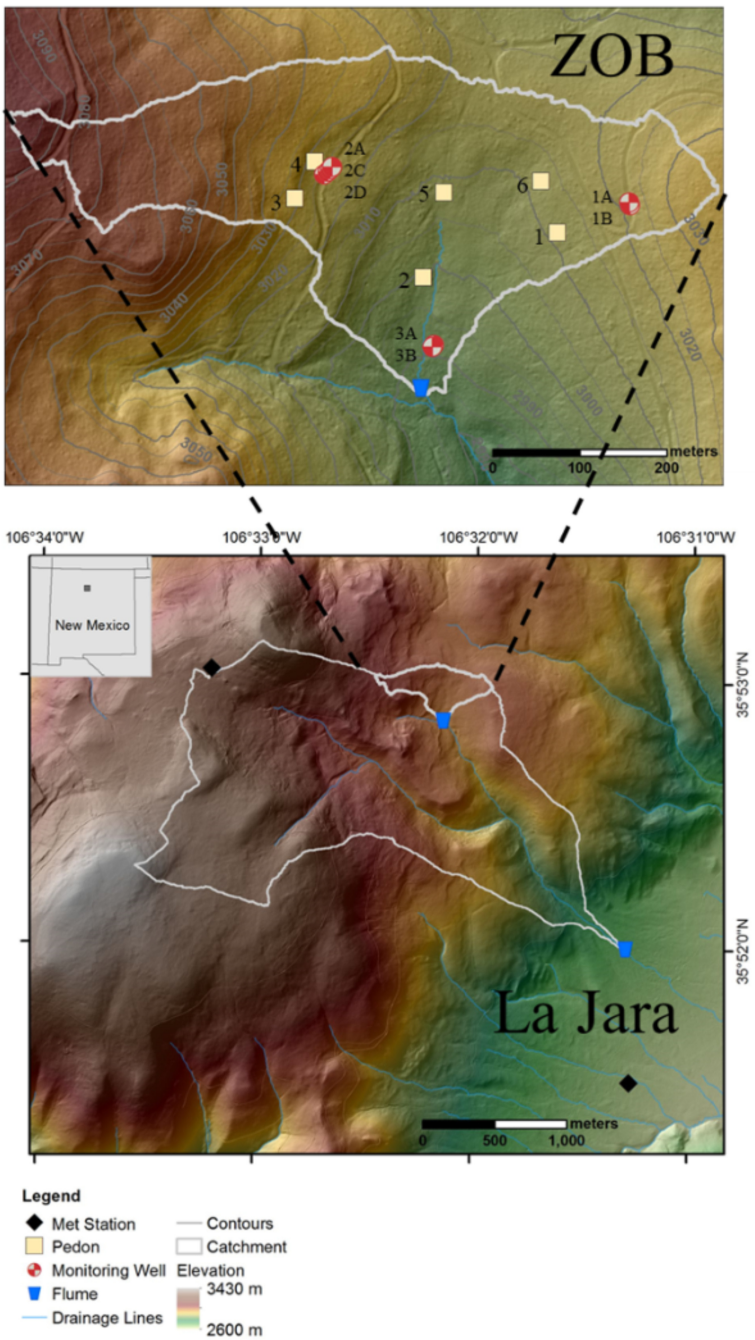


**FIGURE 1 |** Digital elevation model (DEM) of the La Jara catchment (LJ, outline in white) based on 2010 LiDAR flight data. LJ drains the southeastern slope of Redondo Peak within the Valles Caldera National Preserve. The mixed conifer zero order basin (ZOB, also outlined in white and shown in expanded form in upper inset), is an instrumented sub-catchment nested within the LJ catchment. Sampling locations of meteorological stations, flumes, instrumented pedons and groundwater monitoring wells are indicated.

the surface on some portions of the Bandelier Tuff, while upwelling of hydrothermal fluids has altered the volcaniclastics. Caldera collapse breccias consist primarily of reworked rhyolitic volcaniclastics and pre-caldera sedimentary rocks (Hulen and Nielson, 1986; Chipera et al., 2008).

## Field Data and Sample Collection

Water dynamics in the LJ catchment during spring 2017 were measured using two meteorological stations, six instrumented pedons and five monitoring wells located in the ZOB, and two flumes located at the outlet of the ZOB and at the base of LJ catchment (**Figure 1**).

Meteorological data (i.e., air temperature, precipitation and snow depth) were obtained from the Valles Caldera National Preserve Headquarters Redondo Climate Stations[1] (**Figure 1**). The *Redondo* station is located in the upper elevation of the LJ catchment close to the ZOB (hereafter upper LJ) whereas the *Headquarters* station is located closer to the LJ flume at the lower elevation of the catchment (hereafter lower LJ).

To probe the soil compartment of the CZ, six instrumented pedons were installed in the ZOB. Two pedons were located on the south-west facing slope, two were situated on the south-east facing slope, and two were placed in the convergent hollow (**Figure 1**). Soil volumetric water content (VWC) was measured continuously at three depths (10, 30, and 60 cm) in each of the six pedons, using 5TE sensors (Decagon, Pullman, WA, United States). Soil $P_{CO2}$, and temperature were measured continuously at depths of 2, 10, 30, and 60 cm, with GMP222 (Vaisala Inc., Houston, TX, United States). Biweekly soil water samples were collected from each pedon at four soil horizon depths (10–130 cm), using Prenart SuperQuartz soil-water samplers (2 μm pore size, Prenart Equipment ApS, Frederiksberg, Denmark). A vacuum pump applied constant suction of 40 kPa to collect the samples into acid-washed high density polyethylene (HDPE) bottles.

Groundwater was monitored with five wells located on the south-west (site 1) and south-east (site 2) facing slopes of the ZOB (**Figure 1**). Well depths were 43, 39, 47, 32, and 7 m below ground surface (mbgs, corresponding to elevations of 2989, 2992, 2983, 2990, and 3014 m above mean sea level) for Well 1A, Well 1B, Well 2A, Well 2C, and Well 2D, respectively. Well 2D probes a shallow perched aquifer on the south-east facing slope. The groundwater table was monitored using vibrating wire piezometers (Model 4500, Geokon Inc., Lebanon, NH, United States). Water samples were collected bimonthly from March to November 2017 from wells 1A, 1B, 2A, and 2C into acid-washed HDPE bottles using a vacuum pump (as described for the soil water samples above). Daily samples were collected from well 2D into acid-washed 1 L polypropylene bottles using an automatic water sampler (Teledyne ISCO, NE, United States). The outlets of the ZOB and LJ catchment were installed with Parshall flumes fitted with pressure transducers (InSitu Level TROLL 500 15 psig Model: 89010) that measured stage heights continuously at 15 min intervals over the study period. Discharge was estimated using standard stage-discharge relationships for 12 or 18 inch Parshall flumes. Water samples from these flumes, were collected in 1 L polypropylene bottles, during the highest and lowest daily discharge, using an automatic water sampler.

[1]https://wrcc.dri.edu/vallescaldera

## Aqueous Sample Processing Prior to Analysis

All water samples were packed on ice and sent overnight to UA to be filtered within 48 h of collection using 0.45 μm nylon filters. Sample aliquots for dissolved inorganic and organic carbon [dissolved inorganic carbon (DIC) and dissolved organic carbon (DOC), respectively] were filtered through combusted 0.7 μm glass-fiber filters. A subset of samples was used to evaluate colloidal contribution to element concentrations. These samples were cascade filtered through a 1.2 μm polycarbonate filter, and then through a 0.025 μm cellulose acetate/nitrate filter. Element concentrations in the "colloidal fraction" were calculated as the difference in concentrations measured for the 1.2 and 0.025 μm filtrates.

## Sample Analyses

Sample chemical analysis was performed at the University of Arizona Laboratory for Emerging Contaminants (ALEC). Sample aliquots for major and minor solutes ($Na^+$, $Mg^{2+}$, Al, Si, $K^+$, $Ca^{2+}$, Mn, Fe, $Sr^{2+}$, and Zr) as well as lanthanide series elements (rare earth elements, REEs, hereafter designated as light, medium and heavy, LREE: La to Nd, MREE: Sm to Tb, HREE: Dy to Lu) were preserved in acid-washed HDPE bottles by acidification to ca. pH 2 using trace metal grade nitric acid. All water samples were stored at 4°C prior to analysis by inductively coupled plasma mass spectrometry (ICP-MS, Perkin Elmer ELAN DRC II ICP- MS, Shelton, CT prior to 2013; and thereafter Agilent 7700x) equipped with either a dynamic reaction (Perkin Elmer) or collision (Agilent) cell to eliminate molecular isobaric interferences. Rhodium (Rh) was included as an internal standard for Fe, Al, Mn, and P, and indium (In) was used as an internal standard for REE based on similarities in first ionization potential. Calibration curves included at least five points, and correlation coefficients were $>0.995$. Creation of a satisfactory calibration curve was followed by the analysis of an initial calibration blank (ICB) and calibration verification (ICV) solution, with a concentration in the low to midrange of the calibration curve. A continuing calibration blank (CCB) and continuing calibration verification (CCV) solution were measured after every 20 samples and at the end of each batch. Each batch also included measurement of at least one quality control (QC) solution from a second source, such as the NIST 1643e. Acceptable QC responses were between 90 and 110% of the certified value. DIC and DOC were measured using a Shimadzu TOC-VCSH analyzer (Shimadzu Scientific Instruments, Columbia, MD, United States). Major anions ($Cl^-$, $NO_3^-$, $SO_4^{2-}$, and $PO_4$) were measured by ion chromatography (Dionex ICS-1000 equipped with an AS22 Analytical Column, Sunnyvale, CA, United States). Organic carbon molecular characterization was conducted by collecting UV-Vis absorbance spectra (190–655 nm) (Shimadzu Scientific Instruments UV-2501PC, Columbia, MD, United States), and fluorescence excitation–emission matrices (EEM) (FluoroMax-4

equipped with a 150 W Xe-arc lamp source, Horiba Jobin Yvon, Irvine, CA, United States). The EEMs were acquired by scanning excitation (Ex) from 200 to 450 nm and emission (Em) from 250 to 650 nm in 5 nm increments. Spectra were collected with Ex and Em slits at 5 and 2 nm band widths, respectively, with an integration time of 100 ms. Ultrapure water blank EEMs were subtracted and fluorescence intensities were normalized to the area under the water Raman peak, collected at an excitation of 350 nm. Inner-filter correction was performed based on the corresponding UV–Vis scans (Murphy et al., 2013). Details on the described methods, precision, and reproducibility for analysis performed in ALEC are reported elsewhere (Perdrial et al., 2014; Vázquez-Ortega et al., 2015; Trostle et al., 2016).

## Data Processing and Statistical Analysis

All data processing and statistical analyses were performed using *R* (R Core Team, 2017) and the following packages: CAR, lsmens, nlme, and ggplot2 (Wickham, 2009; Fox and Weisberg, 2011; Lenth, 2015; Pinheiro et al., 2017). C-Q relations for each limb of the hydrograph were fitted to a power law (Eq. 1) using non-linear least-squares estimates (Gauss–Newton).

$$C = a \times Q^{b} \tag{1}$$

Where $C$ is the solute concentration, $Q$ is the discharge, $b$ is the fitted power exponent and $a$ is a fitting parameter. The ratio of coefficients of variance for concentration and discharge ($CV_C/CV_Q$) was calculated as

$$\frac{CV_C}{CV_Q} = \frac{\mu_Q \sigma_C}{\mu_C \sigma_Q} \tag{2}$$

where μ and σ are the mean and standard deviation of the solute concentration ($C$) and discharge ($Q$), respectively. Solute export behavior was defined on the basis of the power law exponent, $b$ (Eq. 1), and the ratio $CV_C/CV_Q$ (Godsey et al., 2009; Thompson et al., 2011; Musolff et al., 2015). Chemostatic behavior was defined as $b = 0$ and $CV_C/CV_Q \leq 0.2$, whereas chemodynamic behavior is defined as $|b| \geq 0$ and/or $CV_C/CV_Q > 0.2$ (Hoagland et al., 2017).

The hysteresis index (HI), which quantifies the extent of offset between C-Q trends for each limb in the hydrograph was calculated following Vaughan et al. (2017). Normalized discharge ($Q_{i,norm}$) and concentration ($C_{i,norm}$) *values* were calculated as

$$Q_{i,\,norm} = \frac{Q_i - Q_{\min}}{Q_{\max} - Q_{\min}} \tag{3}$$

$$C_{i,\,norm} = \frac{C_i - C_{\min}}{C_{\max} - C_{\min}} \tag{4}$$

where $Q_i$ and $C_i$ are the discharge and concentration value at time $i$, and $Q_{\min}$, $C_{\min}$, $Q_{\max}$, and $C_{\max}$ are the minimum and maximum discharge and concentration values. The $C_{\text{norm}}$ values for each limb were interpolated at increments of 0.01 of $Q_{\text{norm}}$ by fitting local polynomial regression (LOESS function, stat package R Core Team, 2017). The hysteresis indices were then calculated by the difference between normalized solute concentration pairs at equivalent discharge. C-Q analysis were performed only for LJ stream and not for the ZOB stream due to low data resolution on volumetric discharge for the latter.

To further study the relations between solute *C-Q* behaviors, a hierarchical cluster analysis approach was applied. First, the fitted values of the power law exponents, $CV_C/CV_Q$ values, and mean HI indices for each solute and limb were combined into a single matrix. In cases of a poor fit to Eq. 1 (i.e., $p > 0.05$), $b$ was assigned a value of zero. Columns were standardized by subtracting the mean and dividing by the standard deviation of each column. The Euclidian distance matrix was calculated using the "dist" function in R. Hierarchical clustering was than calculated from the distance matrix using the "hclust" function with the "ward.D2" method. Principle component analysis (PCA) was performed on the standardized matrix, using the "prcomp" function to evaluate the different behaviors between clusters.

Differences between solute concentration means in water sources (i.e., soil, groundwater and streams) were assessed using linear mixed effect model for repeated measures (lme function, nlme package Pinheiro et al., 2017) one-way ANOVA and Tukey's honest significant difference (HSD) test (ANOVA and lsmean function car, and lsmeans packages, respectively, Fox and Weisberg, 2011; Pinheiro et al., 2017). Humification indices (HIX) were calculated as the ratio between the sum of fluorescence intensity in the 435–480 nm region to the region of 300–345 nm for a specific excitation wavelength of 255 nm (Ohno, 2002). Visual Minteq 3.1 was used for geochemical speciation modeling and saturation indices calculation. Carbonate speciation in streams and groundwater was calculated from pH and DIC data, whereas for soil pore water, carbonate speciation was calculated using $P_{CO2}$ and alkalinity (estimated by the diffrence between non-hydrolyzing cations and strong acid anions, Stumm and Morgan, 1981).

# RESULTS

## Water and Snow Dynamics

Snowpack accumulation began in late November 2016, as (daily mean) air temperature dropped to −4°C, below freezing, and it reached a maximum depth of *ca*. 1000 mm in upper LJ catchment in mid-January 2017 (data not shown). The onset of snowmelt was measured in the upper LJ climate station on March 1, 2017 as average air temperature increased above 0°C (**Figures 2A,B**). During the first 3 weeks (March-1 to March-22), snow depth in upper LJ decreased from 930 to 440 mm. A subsequent drop in air temperature decreased the rate of snowmelt and this was accompanied by further snow accumulation (ca. 200 mm) as a result of new precipitation events from March 22 to April 5. Air temperature increased again and snowmelt resumed until completion on April 21. Therefore, this snowmelt hydrograph can be considered as a large melting event superimposed by a sub-event with small snow accumulation and melting. It is important to note that air temperature measured in the lower LJ climate station, was higher by 2.5 ± 0.42 degree, and most of snowpack at this location had melted by mid-March.

Following snowmelt trends, mean VWC in the ZOB, averaged across the six instrumented pedons (**Figure 2C**), increased,

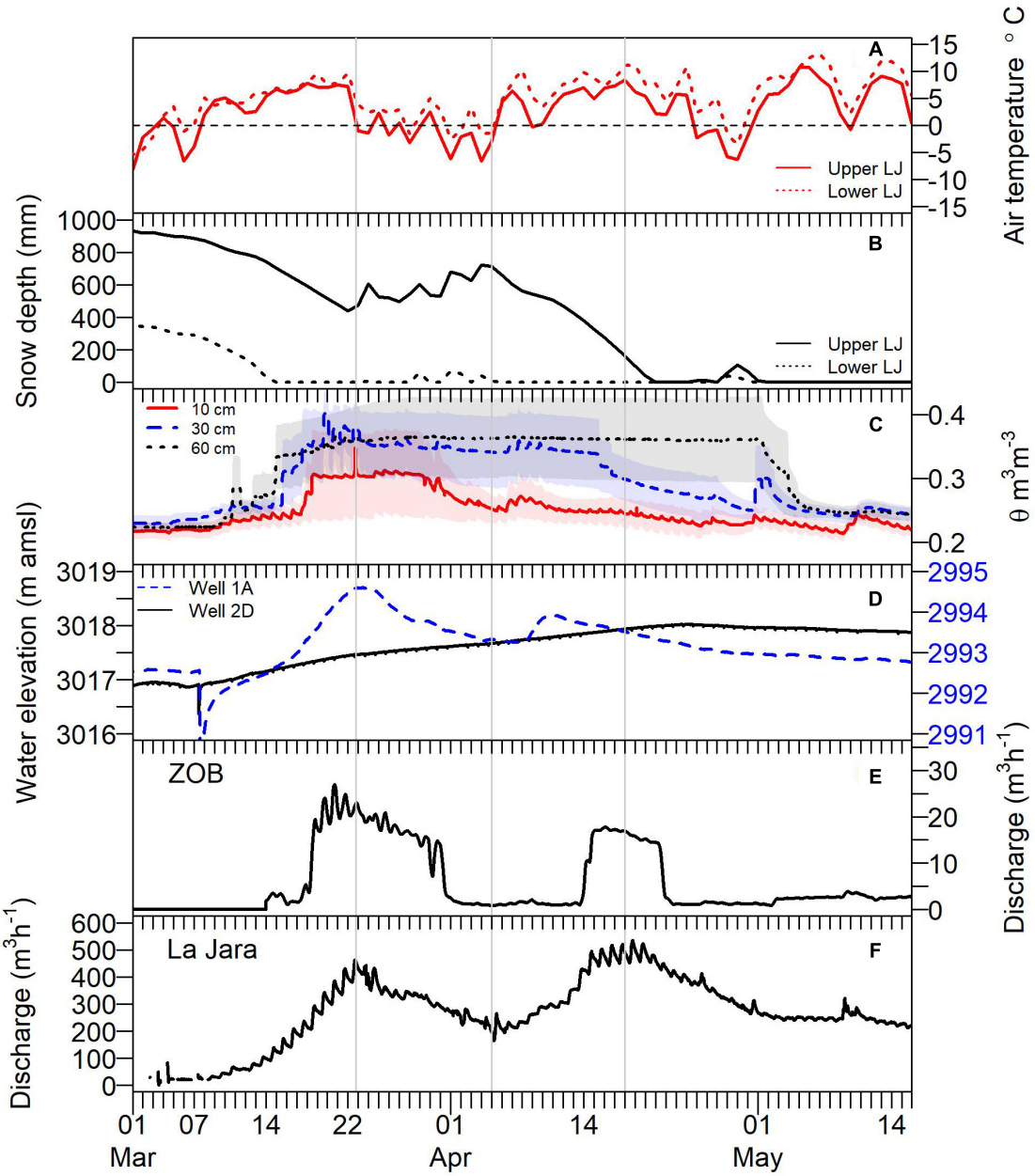


**FIGURE 2 |** Time series of hydrometeorological data: **(A)** air temperature and **(B)** snow depth at Redondo peak and Headquarters meteorological stations **(C)** mean (lines) and standard error (shaded) volumetric soil water content as a function of depth in ZOB, **(D)** groundwater elevation Well 1A (right axis) and Well 2D (left axis), respectively, and surface water discharge for **(E)** ZOB and **(F)** La Jara flumes.

signaling infiltration into the near surface soil layers. The duration of elevated VWC increased with soil depth, with surficial (10 cm depth) soils showing a relatively short-lived period of elevated water content between mid-March and early April, whereas the deeper horizons (60 cm depth) showed sustained saturation into early May, and the intermediate depth (30 cm) showed an intermediate behavior (**Figure 2C**). Previous work indicated minimal overland flow over still frozen ground (Liu et al., 2008; McIntosh et al., 2017).

The perched groundwater table elevation, represented here by Well 2D, showed a steady response to snowmelt (**Figure 2D**). Overall the perched water table increased by 1320 mm over the snowmelt period. Variation in the rate of groundwater elevation increase corresponded to the timing of snowmelt. During the initial melt period (March 1 – March 22) this rate was $1.6 \times 10^{-3} \pm 4 \times 10^{-6}$ m $h^{-1}$. During this period snow depth was negatively correlated with groundwater table elevation (slope = −1.25 m snow

m water table$^{-1}$, $R^2$ = 0.97). Then as the rate of snowpack ablation decreased with decreasing temperature (and new snow accumulated between March 22 and April 5), the groundwater table continued to rise, but at a greatly reduced rate of $6.5 \times 10^{-4} \pm 2 \times 10^{-6}$ m h$^{-1}$. For this period there was a positive correlation between snow depth and groundwater table elevation (slope = 0.61 m snow m water table$^{-1}$, $R^2$ = 0.59). The rate of the groundwater table rise increased again to $8 \times 10^{-4} \pm 1 \times 10^{-6}$ mh$^{-1}$ during the second period of snowmelt (April 5–24). Snow depth was negatively correlated with the groundwater table elevation (slope = −0.45 m snow m water table$^{-1}$, $R^2$ = 0.98). Maximum water table elevation was measured on April 24, 6 days after the second peak in the LJ hydrograph.

In contrast to the Well 2D, the deep groundwater table elevation measured in the south-west facing slope (Well 1A), exhibited two pronounced peaks. During the first peak (March 1–22) the groundwater table elevated by 2 m, corresponding to the initial period of snowmelt. Following the first peak, the water table decreased by 1.3 m. The minimum between the two water table peaks (April 8) was observed 3 days after the second snow accumulation peak. The second max in groundwater table occurred on April 10. This peak precedes the maximum water table elevation measured in Well 2D by 2 weeks, and coincides with the decrease in mean ZOB VWC at 10 and 30 m depth.

The hydrograph of the ZOB stream exhibited two pronounced peaks during spring snowmelt, March 20 to April 16, 2017 (**Figure 2E**). A similar pattern was observed in the hydrograph of the LJ stream (**Figure 2F**), however, maximum discharge consistently occurred 2 days later in LJ (March 22 and April 18), despite the fact that the ZOB is a higher elevation stream and subject to colder air temperatures (**Figure 2A**). During the first snowmelt period, ZOB and LJ stream discharge increased from ca. 0 to 30 m$^3$ h$^{-1}$ and 450 m$^3$ h$^{-1}$, these maximum values corresponding to specific discharges of $2 \times 10^{-4}$ and $1.36 \times 10^{-4}$ m h$^{-1}$, respectively (**Figures 2E,F**). The accumulation of the snowpack (March 22 to April 5) resulted in decreased discharge to 0 and 170 m$^3$ h$^{-1}$ in ZOB and LJ streams, respectively. As snowmelt resumed, a second hydrograph rise was observed (up to 20 and 170 m$^3$ h$^{-1}$, for ZOB and LJ streams, respectively). Both ZOB and LJ hydrographs contain daily peaks and troughs associated with diurnal fluctuations in temperature, and hence melt rates.

## Bulk and Time Series of Water Chemistry

Mean solute concentrations in soil solution, groundwater and streams (LJ and ZOB) are presented in **Table 1**. The pH in Well 2D groundwater was higher by 0.5 units than those of soil and stream waters. Soil solutions were significantly enriched in Zr, Al, DOC, and REEs. Mean concentrations of DIC, Si, Mn, $Na^+$, $SO_4^{2-}$, Mg, $Ca^{2+}$, and $Sr^{2+}$ were significantly higher in Well 2D than in the LJ stream. For example, DIC, Mn, $Ca^{2+}$, $SO_4^{2-}$ and $Sr^{2+}$ mean concentrations were 18, 16, 15, 7 and 7 times higher in Well 2D groundwater than in the LJ stream, respectively. Highest $NO_3^-$ concentrations, which were measured in the LJ stream, were 2–3 times higher than concentrations in the ZOB stream, ground water, and soil water. Deeper ground water at site 2 (Well 2C) showed similar chemistry to Well 2D, except that $Mg^{2+}$ was higher in Well 2C. Wells in site 1 (Well 1A, and Well 1B) had up to 10-fold lower $Ca^{2+}$, $SO_4^{2-}$, and DIC concentrations, whereas Mn was higher in this site compared to site 2 (**Supplementary Figure S2**). Groundwater was slightly oversaturated with respect to calcite (mean saturation index, SI = 0.22 ± 0.009) while streams and soil pore water showed consistent under-saturation (mean SI = −2.77 ± 0.08, −2.42 ± 0.08, and −3.26 ± 0.10 for LJ, ZOB streams, and soil pore water, respectively, **Supplementary Figure S1**). Since some degassing of $CO_{2(aq)}$ from water samples may have occurred before sample analysis, calculated SIs for calcite may overestimate the actual values in the streams and Well 2D waters. To address this issue calcite SI values were calculated for Well 2D water in equilibrium with three $P_{CO2}$ concentrations, 0.4, 4, and 40 mL L$^{-1}$. The calculated SIs were, 1.35 ± 0.01, 0.44 ± 0.01, and −0.55 ± 0.01. Therefore, even for high $P_{CO2}$ values, Well 2D water remained close to equilibrium with calcite. It is important to note that some calcite precipitation may have occurred between sample collection and analysis, and this may result in underestimation of calcite SI in Well 2D.

Time series of Si, DIC, $Ca^{2+}$, and $Na^+$ in soil water, groundwater and ZOB and LJ streams are shown in **Figure 3**. Si concentrations in both ZOB and LJ surface waters exhibited similar trends, and concentration ranges (ca. 200 to 1000 μM). Two pronounced peaks in surface water Si concentrations occurred during the first and second falling limbs of the snowmelt hydrographs. The first set of peaks in both surface water systems occurred March 24 to April 4 when Si concentration increased from ca. 370 μM to ca. 500 μM. The second set of peaks occurred May 8–18 and was substantially larger than the first; Si concentrations increased to 1030 μM. It is noteworthy that both surface water Si peaks follow the observation of elevated Si concentrations in groundwater (Well 2D). This is especially evident for the second peak in streamwater Si concentration that follows a rapid increase in Well 2D concentration that started April 26. The increased concentration of Si in groundwater occurred in two steps the first from ca. 500 to 800 μM (April 26) and then to ca. 1300 μM (May 5). This increase in Si concentration was also observed in the deeper groundwater wells located on both slopes of the ZOB (wells 1A and 2C, **Supplementary Figure S2**). Groundwater Si concentration decreased to 720 μM by June 28 (**Supplementary Figure S2**), however, due to a gap in data between May 17 and June 28, it is unclear precisely when the Si concentrations declined in Well 2D. Interestingly, the peaks in Si concentration in groundwater coincided with increases in concentrations of DIC, $Na^+$ and (to a lesser extent) $Ca^{2+}$ in the groundwater (**Figure 3**). Furthermore, these increases in groundwater solute concentrations preceded by a few days the increases in surface water Si concentrations.

The ZOB stream showed a decrease in DIC during the first hydrograph rise followed by an increase during the second descending limb of the hydrograph (**Figure 3**). In contrast to the ZOB stream, DIC concentrations in LJ stream exhibited smaller

**TABLE 1 |** Summary of pH and solute chemistry for various water types sampled in La Jara catchment.

| | LJ stream | | ZOB stream | | Well 2D groundwater | | Soil water | |
|---|---|---|---|---|---|---|---|---|
| **Element** | ***n*** | **Mean**† | ***n*** | **Mean** | ***n*** | **Mean** | ***n*** | **Mean** |
| pH | 141 | 7.05 (0.06) a | 127 | 6.99 (0.07) a | 65 | 7.56 (0.08) b | 86 | 7.02 (0.09) a |
| Si | 143 | 361 (20) b | 134 | 380 (20) b | 67 | 673 (67) c | 102 | 226 (32) a |
| DIC | 144 | 3.26 (0.06) a | 135 | 5.75 (0.25) b | 67 | 59 (1.2) c | 112 | 5.03 (2.14) ab |
| Zr | 143 | 2.33 (0.42) b | 134 | 3.78 (0.43) c | 67 | 0.54 (0.11) a | 102 | 8.21 (1.29) d |
| Ti | 143 | 11.6 (2.31) a | 134 | 21.6 (2.2) b | 67 | 33 (5.1) c | 102 | 37.5 (7.2) c |
| Mn | 143 | 28.9 (25.5) a | 134 | 37.5 (11.9) a | 67 | 480 (87) c | 102 | 160 (76) b |
| Al | 143 | 1.32 (0.12) b | 134 | 2.08 (0.16) c | 67 | 0.55 (0.13) a | 102 | 2.86 (0.46) d |
| $Na^+$ | 143 | 110 (2.16) c | 134 | 84.2 (2.23) b | 67 | 304 (19) d | 102 | 54.8 (12.8) a |
| $K^+$ | 143 | 34.3 (0.8) a | 134 | 45.8 (2.31) a | 67 | 41.2 (0.9) a | 102 | 117 (62) b |
| $SO_4^{2-}$ | 144 | 68.0 (1.6) a | 135 | 100 (2) b | 65 | 482 (4) c | 103 | 71.0 (24.0) a |
| $Mg^{2+}$ | 143 | 35.6 (0.8) a | 134 | 46.4 (1.8) b | 67 | 142 (3) c | 102 | 33.5 (7.0) a |
| $Sr^{2+}$ | 143 | 0.42 (0.01) a | 134 | 0.6 (0.02) b | 67 | 2.88 (0.14) c | 102 | 0.41 (0.08) a |
| $Ca^{2+}$ | 143 | 175 (5) a | 134 | 279 (8) b | 67 | 2650 (50) c | 102 | 193 (32) a |
| $Cl^-$ | 144 | 33.0 (1.1) a | 135 | 25.1 (1.4) a | 65 | 33 (1.2) a | 101 | 44.9 (24.9) a |
| $NO_3^-$ | 144 | 111 (3) c | 131 | 39.8 (4.5) a | 65 | 51.2 (3.2) ab | 92 | 61.8 (26.2) b |
| Fe | 142 | 0.58 (0.24) b | 134 | 0.88 (0.16) b | 67 | 0.15 (0.044) a | 102 | 0.91 (0.14) b |
| DOC | 143 | 3.85 (0.42) a | 134 | 9.22 (0.37) b | 67 | 2.86 (0.15) a | 112 | 12.8 (1.7) c |
| HREE | 143 | 0.28 (0.02) a | 134 | 1.1 (0.04) b | 67 | 0.07 (0.02) a | 102 | 2.34 (0.36) c |
| MREE | 143 | 0.25 (0.02) a | 134 | 1.04 (0.04) b | 67 | 0.07 (0.02) a | 102 | 2.36 (0.37) c |
| LREE | 143 | 1.52 (0.19) b | 134 | 4.98 (0.29) c | 67 | 0.23 (0.04) a | 66 | 6.72 (0.83) d |

*Mean values in μM except for Zr, Mn, and REE, which are reported in nM. The 95% confidence intervals are shown in parentheses.* †*Letters display differences between means examined using Tukey's-HSD.*

variability. Notably, the humification index (HIX) measured for dissolved organic matter (DOM) collected from the ZOB stream, was correlated with DIC ($R^2 = 0.53$, **Supplementary Figure S3**). In addition, DIC concentrations in the ZOB stream were correlated in time with $P_{CO2}$ measured in the ZOB instrumented pedons (**Supplementary Figure S4**). Linear correlation with soil $P_{CO2}$ explained up to 76% of the variance in ZOB stream DIC concentrations (**Supplementary Figures S5**, **S6**). It is important to note that stream water and soil gas $P_{CO2}$ values were similar for LJ and ZOB streams, and for soil gas ($1.28 \pm 0.33$, $2.18 \pm 0.33$, and $2.48 \pm 36$, mL $L^{-1}$, respectively).

## C-Q Relations

To increase the information obtained from the collected data, each limb (Rise 1, Descent 1, Rise 2, and Descent 2 are denoted as R1, D1, R2, D2, respectively) of the snowmelt hydrograph was analyzed separately (**Figure 4**). This approach allowed us to elucidate sequential trends in snowmelt hydrochemical response that would otherwise be missed in bulk analysis of *C-Q* data. *C-Q* trends differed among solutes and hydrograph sections (**Figure 4** and **Table 2**). For both R1 and R2, Si, DIC, and Na exhibited chemostatic or slight dilution trends ($b \leq 0$, Eq. 1) with relatively low $CV_C/CV_Q$ (<0.2). Besides $Na^+$, non-hydrolyzing cations and strong acid anions ($K^+$, $Ca^{2+}$, $Mg^{2+}$, $Sr^{2+}$, $SO_4^{2-}$, $Cl^-$, and $NO_3^-$) exhibited slight positive *C-Q* relations ($0.05 < b < 0.2$) with low $CV_C/CV_Q$ (<0.2) during R1. D1 showed lower positive or chemostatic trends for the anions ($SO_4^{2-}$, $NO_3$, and $Cl^-$). Other cations showed similar positive trends in R1 and D1 ($Mg^{2+}$, $Ca^{2+}$, $Sr^{2+}$, $K^+$). During R2, a shift from positive or chemostatic to dilution ($b < -0.1$) was observed for all non-hydrolyzing cations and strong acid anions except $K^+$, which retained a positive *C-Q* trend. During D2, all ions except $Na^+$ showed a positive power law slope ($b > 0.2$). The largest $b$ values were calculated for DOC and REEs in all of the four hydrograph limbs (**Table 2**). REEs exhibited higher positive *C-Q* trends during R2 and D2 ($b > 0.7$), while DOC showed highest $b$ values on the two descending limbs (0.49 and 0.65 for D1 and D2, respectively). The metals Mn, Al, Zr, and Ti exhibited scattered chemodynamic behavior (i.e., low $b$ values and poor fit to power law function and high $CV_C/CV_Q$). The power law slopes for Fe were similar to those for these other metals for the last three hydrograph limbs, but in the first rising limb, Fe concentrations were much higher than the subsequent hydrograph limbs and showed a tighter positive correlation with discharge (**Figure 4** and **Table 2**). All of these polyvalent metals (Mn, Al, Zr, Ti, and Fe) also exhibited a large colloidal fraction in both ZOB and LJ streams (**Figure 5**), whereas other elements did not show a significant colloidal contribution.

## C-Q Hysteresis

The La Jara stream snowmelt hydrograph exhibited different hysteresis patterns for the tested solutes. Since the snowmelt hydrograph in this work can best be described as one large snowmelt event superimposed with a smaller sub-event of snow accumulation and melting, hysteresis indices were calculated for the R1-D2 limbs as well as each of the sequential sub limbs (i.e., R1-D1, D1-R2, and R2-D2). Hysteresis indices (HIs) calculated as described in Section "Data Processing and Statistical

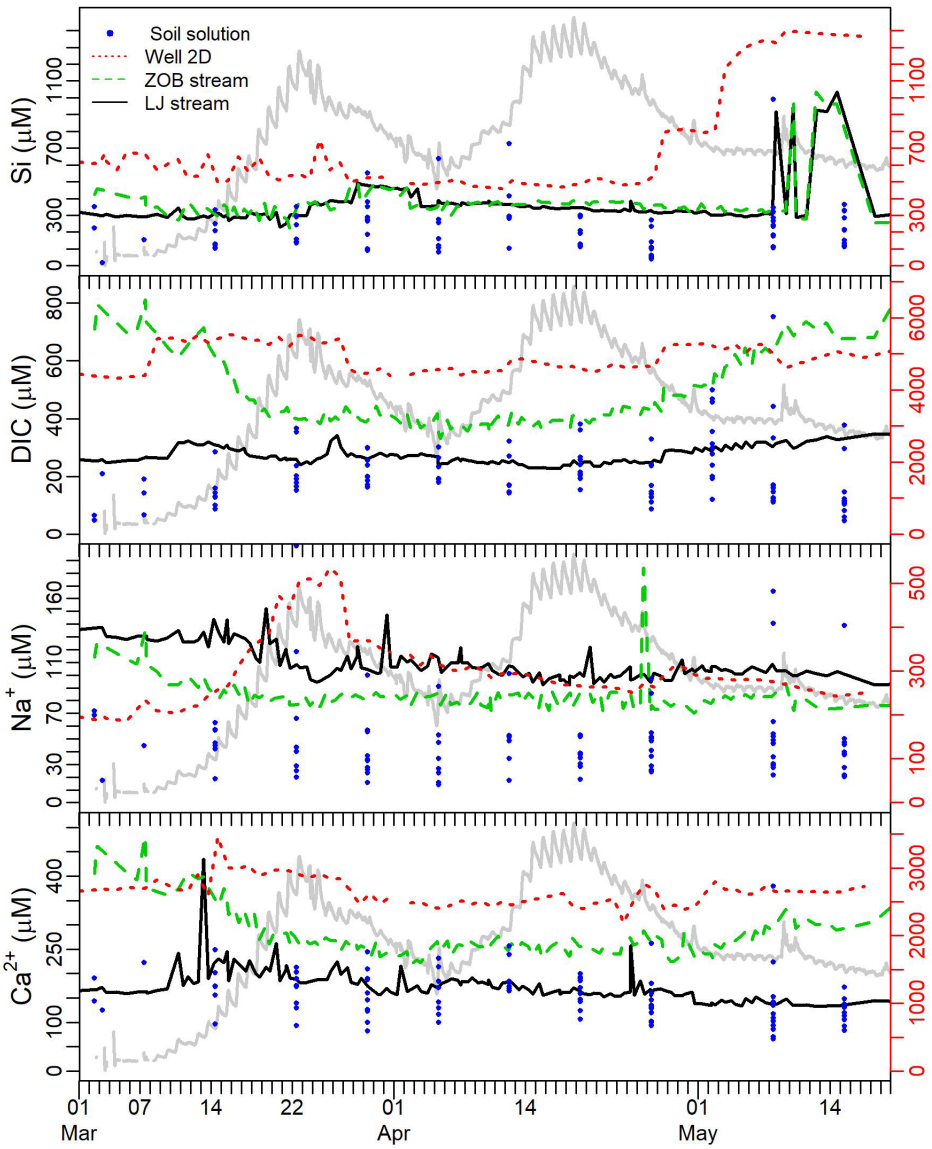


**FIGURE 3 |** Time series of Si, DIC, Na and Ca in soil solution (filled blue circles), groundwater monitoring Well 2D (dotted red line), ZOB flume (dashed green line) and LJ flume (solid black line). The LJ hydrograph trace (from **Figure 2F**) is shown in light gray in the background (no axis scale) for temporal reference.

Analysis," are presented in **Table 3** and **Supplementary Figure S7**. Pronounced anticlockwise hysteresis was observed between the R1 and D2 for Si, DIC, Zr, and Al. In contrast, major ions, DOC, and REEs exhibited overall clockwise hysteresis between R1 and D2. Strong clockwise hysteresis was observed for Fe for the first hydrograph peak (R1-D1) with no hysteresis for the second peak (R2-D2). The elements $Na^+$, $K^+$, Fe, DOC, and REEs, exhibited larger hysteresis on the first hydrograph peak. $Mg^{2+}$, $Ca^{2+}$, $Sr^{2+}$, DIC, and $Cl^-$ had similar hysteresis values for both hydrograph peaks, whereas $NO_3^-$, and $SO_4^{2-}$ had larger hysteresis on the second hydrograph peak. Si showed anticlockwise hysteresis for the first hydrograph peak.

## Cluster and Principle Component Analyses

Cluster analysis and PCA reduction methods were applied to separate solutes into groups with similar *C-Q* behaviors. As described in Section "Data Processing and Statistical Analysis," values of the power law exponent (*b* in equation 1), coefficients of variance ratio ($CV_C/CV_Q$), and mean HIs, were combined into a single matrix. Results of the cluster analysis and PCA performed on this matrix are presented in **Figure 6**. The solutes clustered into five groups: (1) Si and DIC, (2) non-hydrolyzing cations and strong acid anions ($Na^+$, $K^+$, $Ca^{2+}$, $Mg^{2+}$, $Sr^{2+}$, $SO_4^{2-}$, $Cl^-$, and $NO_3^-$), (3) DOC and REEs (4) Al, Mn, Zr and Ti, and, (5) Fe. The first three principle components (PC) explained 78% of

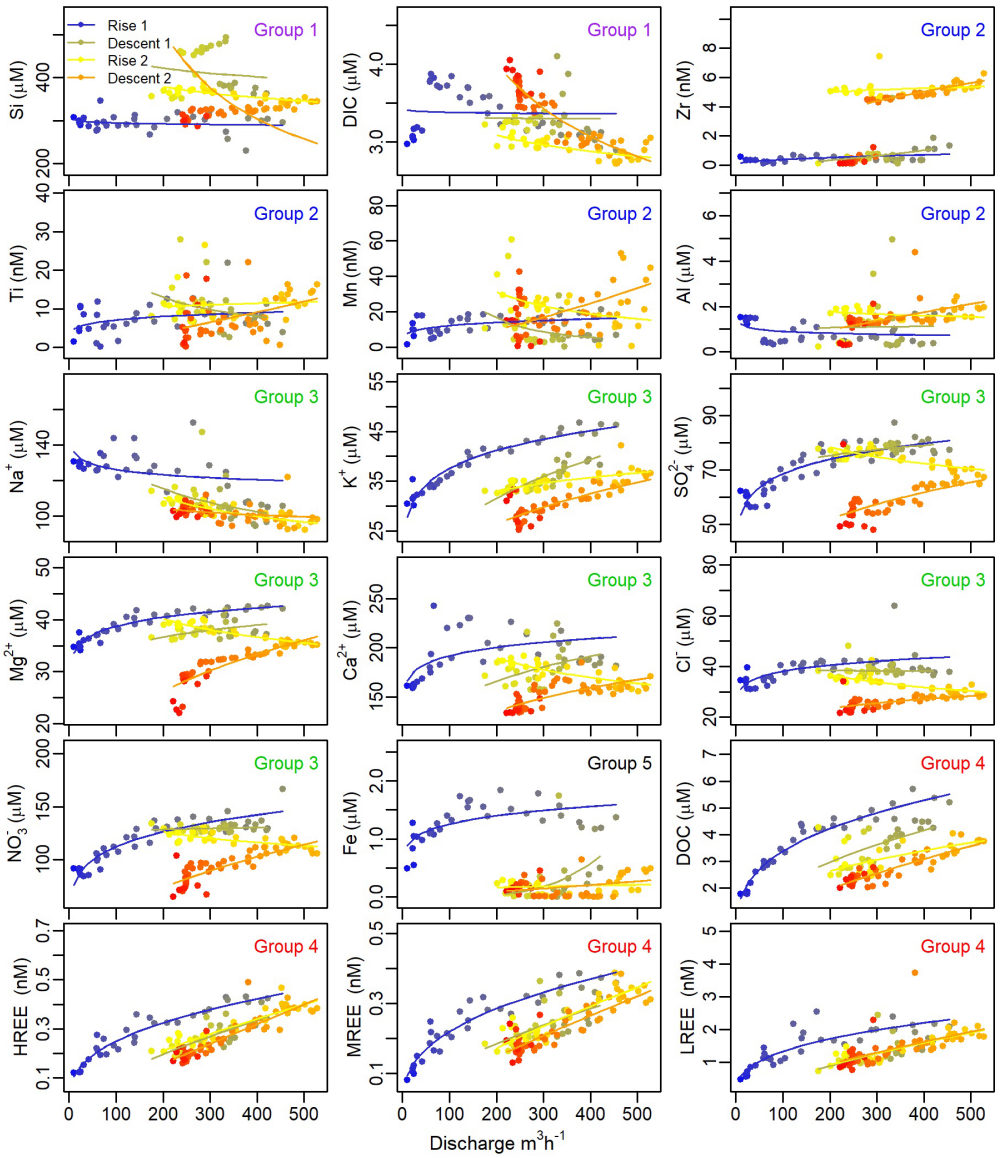


**FIGURE 4 |** La Jara flume *C-Q* relations for selected elements. Solids lines are best fits to power law (Eq. 1) for each of the four hydrographs limbs: first rising (blue), first falling (green), second rising (yellow), and second falling (orange). See **Table 2** for extracted parameters and associated statistics. Group numbers in each plot are linked to **Figure 6**.

the data variability, and the eigenvectors of these first three PCs are presented in **Supplementary Table S1**. Biplots of the first and second PCs (**Figure 6**), demonstrate that the hydrolyzing metals (groups 4 and 5) that exhibited higher $CV_C/CV_Q$, were separated based on the higher value of $CV_C/CV_Q$ loadings in PC1 and PC2. DOC and REEs (group 3) were separated by the high power law exponent value (negative correlation with $b$ values was dominant in PC2). Scores of group 1 plotted in the opposite direction of the power law exponent and HI loadings. $K^+$ and $Na^+$ were situated on the extremes of the major ions ellipsoid; $K^+$ scores plotted closer to group 3 (DOC and REEs) whereas $Na^+$ scores plotted closer to group 1 (Si and DIC). There was no strong separation observed between groups 3 and 4 in the biplot of PC1 and PC3, whereas Fe was strongly separated from the other elements based on its high hysteresis in the first hydrograph peak. Strong correlations were observed between DOC and REEs ($R^2 > 0.5$, $p < 0.001$) for all hydrograph limbs except D1.

## DISCUSSION

The aim of this study was to link hydrogeochemical processes in the critical zone pore waters to their manifestation in stream *C-Q* relations on the time scale of the snowmelt hydrograph. Spring snowmelt 2017 in the LJ Jara catchment, characterized

**TABLE 2 |** Summary of power law fit (Eq. 1) and coefficient of variance (Eq. 2) for *C-Q* relations in the LJ stream.

| | Rising limb 1 | | | Descending limb 1 | | |
|---|---|---|---|---|---|---|
| **Solute** | ***b*** | $R^{2\dagger}$ | $CV_C/CV_Q$ | ***b*** | $R^2$ | $CV_C/CV_Q$ |
| Si | *−0.01 (0.02)*‡ | *0.01* | 0.09 | *−0.07 (0.25)* | *0.03* | 0.65 |
| DIC | *0 (0.031)* | *−0.03* | *0.11* | *0 (0.14)* | *−0.04* | *0.36* |
| Zr | 0.44 (0.25) | 0.29** | 0.77 | *1.65 (1.58)* | *0.02* | *6.84* |
| Ti | *0.17 (0.21)* | *0.06* | *0.71* | *−0.68 (0.95)* | *0.05* | *2.63* |
| Mn | 0.19 (0.07) | 0.19* | 0.51 | *−1.54 (0.87)* | *0.08* | *5.51* |
| Al | *−0.14 (0.17)* | *0.03* | *0.63* | *0.09 (1.88)* | *−0.04* | *4.76* |
| $Na^+$ | −0.03 (0.03) | 0.14* | 0.11 | *−0.17 (0.17)* | *0.11* | *0.48* |
| $K^+$ | 0.13 (0.01) | 0.93*** | 0.17 | 0.32 (0.09) | 0.65*** | 0.4 |
| $SO_4^{2-}$ | 0.11 (0.02) | 0.74*** | 0.16 | 0.07 (0.04) | 0.36*** | 0.12 |
| $Mg^{2+}$ | 0.06 (0.01) | 0.87*** | 0.08 | 0.09 (0.07) | 0.16* | 0.21 |
| $Sr^{2+}$ | 0.06 (0.04) | 0.26** | 0.15 | 0.21 (0.18) | 0.14* | 0.51 |
| $Ca^{2+}$ | 0.06 (0.01) | 0.78*** | 0.09 | 0.11 (0.08) | 0.21* | 0.22 |
| $Cl^-$ | 0.09 (0.04) | 0.34*** | 0.19 | *−0.01 (0.12)* | *−0.04* | *0.3* |
| $NO_3^-$ | 0.17 (0.03) | 0.83*** | 0.23 | *0.02 (0.05)* | *−0.01* | *0.13* |
| Fe | 0.16 (0.07) | 0.43*** | 0.3 | 4.12 (1.98) | 0.19* | 8.82 |
| DOC | 0.32 (0.03) | 0.94*** | 0.4 | 0.49 (0.29) | 0.31** | 0.82 |
| HREE | 0.38 (0.05) | 0.92*** | 0.46 | 0.77 (0.29) | 0.55*** | 1.02 |
| MREE | 0.38 (0.05) | 0.91*** | 0.47 | 0.63 (0.37) | 0.32** | 1.08 |
| LREE | 0.36 (0.08) | 0.77*** | 0.5 | 0.85 (0.49) | 0.35** | 1.41 |
| | **Rising limb 2** | | | **Descending limb 2** | | |
| Si | −0.1 (0.03) | 0.68*** | 0.12 | −0.75 (0.61) | 0.09* | 1.8 |
| DIC | −0.1 (0.04) | 0.47*** | 0.15 | −0.39 (0.06) | 0.82*** | 0.4 |
| Zr | *0.07 (0.13)* | *0.01* | *0.35* | 0.49 (0.11) | 0.79*** | 0.55 |
| Ti | *0.11 (0.47)* | *−0.03* | *1.22* | 1.17 (0.82) | 0.14 ** | 2.82 |
| Mn | −0.73 (0.35) | 0.11* | 1.84 | 1.33 (0.33) | 0.22* | 2.49 |
| Al | *−0.15 (0.18)* | *0.06* | *0.48* | 0.86 (0.40) | 0.28*** | 1.62 |
| $Na^+$ | −0.14 (0.04) | 0.67*** | 0.18 | *−0.05 (0.05)* | *0.05* | *0.17* |
| $K^+$ | 0.12 (0.06) | 0.37*** | 0.19 | 0.3 (0.07) | 0.59*** | 0.37 |
| $SO_4^{2-}$ | −0.12 (0.03) | 0.62*** | 0.15 | 0.26 (0.10) | 0.37*** | 0.39 |
| $Mg^{2+}$ | −0.13 (0.03) | 0.79*** | 0.15 | 0.35 (0.06) | 0.73*** | 0.4 |
| $Sr^{2+}$ | −0.16 (0.05) | 0.65*** | 0.2 | 0.23 (0.07) | 0.52*** | 0.31 |
| $Ca^{2+}$ | −0.11 (0.03) | 0.72*** | 0.13 | 0.24 (0.04) | 0.79*** | 0.26 |
| $Cl^-$ | −0.21 (0.08) | 0.52*** | 0.3 | 0.2 (0.09) | 0.31*** | 0.34 |
| $NO_3^-$ | −0.12 (0.05) | 0.42*** | 0.18 | 0.48 (0.10) | 0.66*** | 0.58 |
| Fe | *0.27 (0.95)* | *−0.03* | *2.45* | 1.22 (1.10) | 0.05* | 3.74 |
| DOC | 0.37 (0.2) | 0.41** | 0.53 | 0.65 (0.10) | 0.8*** | 0.71 |
| HREE | 0.7 (0.13) | 0.81*** | 0.78 | 1.0 (0.16) | 0.78*** | 1.15 |
| MREE | 0.76 (0.15) | 0.79*** | 0.85 | 0.85 (0.15) | 0.73*** | 0.98 |
| LREE | 0.8 (0.17) | 0.77*** | 0.89 | 0.77 (0.32) | 0.33*** | 1.32 |

†*Asterisks represent level of significance with *$p < 0.05$, **$p < 0.01$, ***$p < 0.001$.* ‡*Poor fit to Eq. 1 ($p > 0.05$) are marked in italics. Power exponents (b) are presented with 95% confidence interval in parentheses.*

by two distinct hydrograph peaks resulting from snow melt and accumulation periods, provided a unique opportunity to test the hypothesis that stream hydrochemical response can be resolved in terms of soil solution and groundwater contributions. Results presented in Section "Water and Snow Dynamics," suggest that soil solution, groundwater and surface waters all responded rapidly to snow melt with a short lag between the upper ZOB stream and the LJ catchment outlet. Variation in groundwater table rise correlates with snow melt and stream discharge trends (**Figure 2**), consistent with connectivity between soil water, groundwater and streamwater on the hydrograph time scale. The following sections discuss the hydrogeochemical processes observed in the La Jara catchment during spring snowmelt of 2017. The first section interprets relationships among time series of the different CZ compartments, and associated analysis performed on the bulk data. The second section discusses the analysis of *C-Q* and its link to short term CZ processes.

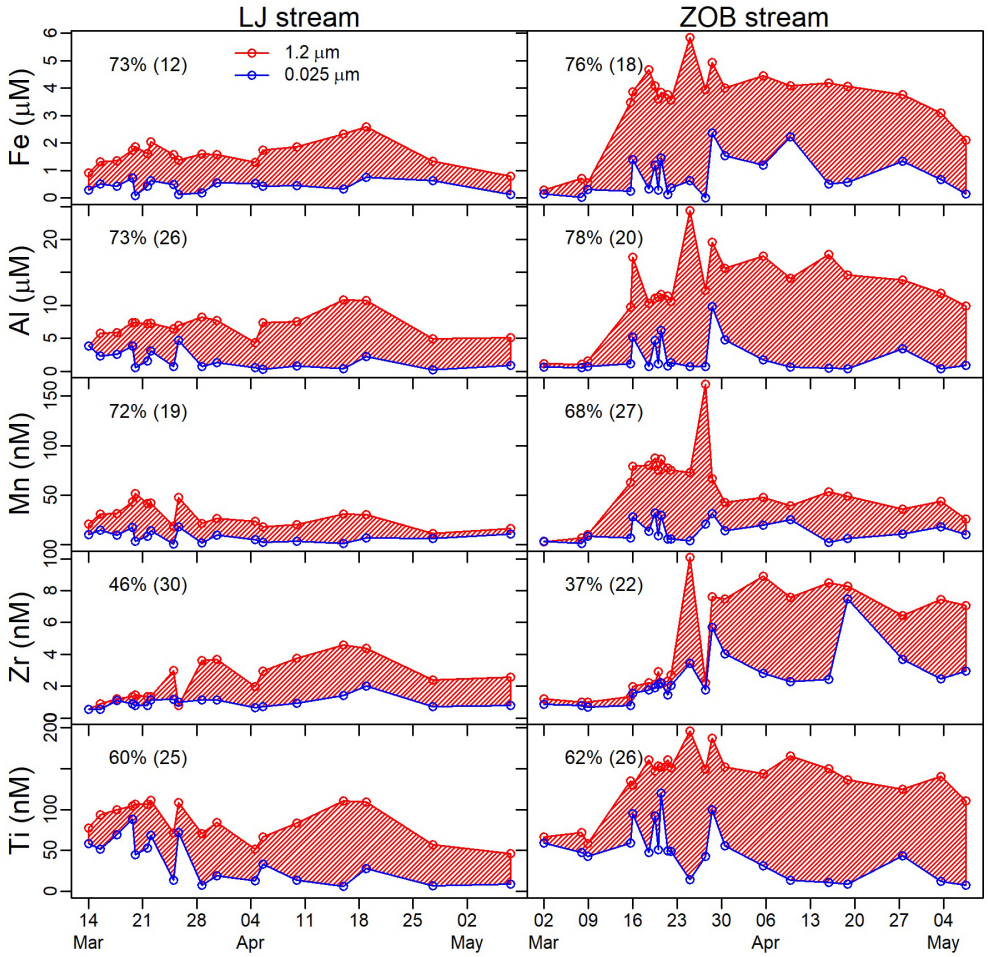


**FIGURE 5 |** Time series results for the cascade filtration data pertaining to Fe, Al, Mn, Zr, and Ti. Concentrations are shown for elements in filtrates following filtration at 1.2 μm (red) and 0.025 μm (blue). Area marked in red diagonal lines represents the elemental mass contribution of colloids (0.025–1.2 μm). Numbers inset in each plot are the mean and standard deviation of the colloidal fraction over the course of the experiment.

## Time Series Data

Elevated Si concentrations in groundwater have been postulated as the source for contributing the bulk of Si to LJ surface waters (McIntosh et al., 2017). Data on Si concentrations in soils, groundwater and surface waters (**Table 1** and **Figure 3**) support this hypothesis. During D1, Si values in LJ and ZOB streams reached similar values as found in groundwater (Well 2D), suggesting that at this period streamflow was associated with a progressively decreasing contribution of laterally transmitted soil water that diluted groundwater-derived Si during the high flow periods (R1 and R2). This suggests that pressure wave propagation from snow melt through the soil profile and into groundwater exhibits a lag where stream waters are heavily influenced by discharging groundwater later in the hydrograph pulse, even after soils (**Figure 2C**) have largely transferred drainage waters to the saturated subsurface (**Figure 2D**).

In contrast to Si, concentrations of $Ca^{2+}$, $Na^{+}$, $Mg^{2+}$, Mn, and $SO_4^{2-}$ did not elevate in the streams during D1, even though their concentrations were larger (by factors of 7–16, **Table 1**) in Well 2D groundwater relative to surface water. This suggests that stream water Si may have an additional or even different source than that represented solely by Well 2D. Indeed, concentrations of $SO_4^{2-}$, $Ca^{2+}$, and DIC in Wells 1A and 1B were lower than observed in Well 2D (**Figures 3** and **Supplementary Figure S2**), and are more consistent with concentrations measured in LJ and ZOB surface waters, which suggests that groundwater permeating the welded tuff on the eastern side of the ZOB is likely an important source to the ZOB and LJ streams. In any case, the relative magnitude of deeper groundwater contributions appears to increase during the descending limbs of the hydrograph, which helps to explain both *C-Q* and hysteresis behaviors, and the separation of solutes by source, as discussed further in Section "C-Q Analysis."

The increase in $Ca^{2+}$ and DIC concentrations in Well 2D during the first peak of the snowmelt hydrograph (**Figure 3**) is consistent with calcite dissolution. This is with agreement

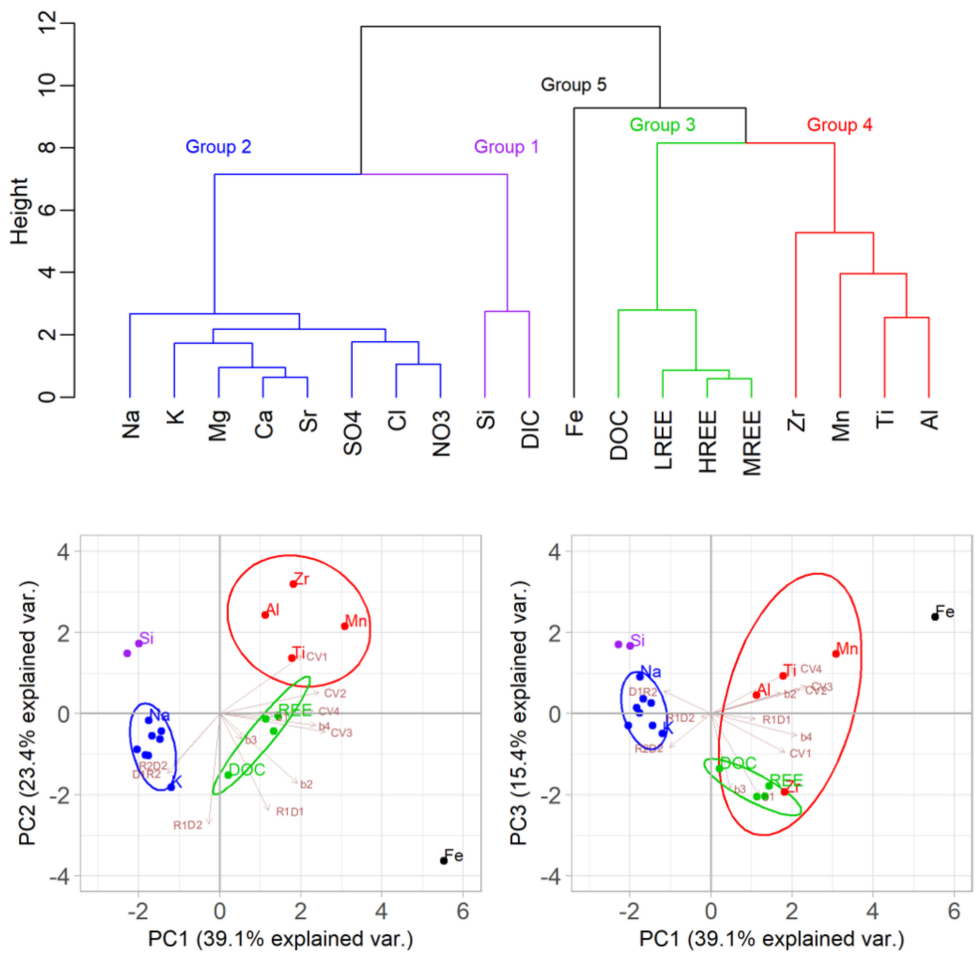


**FIGURE 6 |** Cluster dendogram **(top)** with colors representing the five distinct solute groups identified and where *Y*-axis Height is the value of the criterion associated with the clustering method. Moving along the clustering tree from bottom to top, each leaf (group) fuses into another. Fusion at larger height represents larger distance between the groups. Biplots of the principle component (PC) pairs **(bottom)** showing PCs 1 and 2 **(bottom left)** and PCs 1 and 3 **(bottom right)**. Loadings of the exponent a (equation 1), the coeficients of variance ($CV_C/CV_Q$), and the hysteresis indices between pairs of limbs (R for rise and D for falling limbs), are shown in brown arrows. Ellipsoid probability (95%) encapsulates the groups.

with saturation indices calculated from geochemical modeling; these indicate groundwater solutions are near equilibrium with calcite. Hence, the $Na^+$ peak in Well 2D during that same period may derive either from the weathering of primary silicate minerals, or from $Ca^{2+}$-induced displacement of $Na^+$ from clay surfaces. In the current study, $Ca^{2+}$ concentrations in Well 2D remained high (**Table 1** and **Figure 3**) regardless of changes in water table depth. This observation is different from the rapid decrease in $Ca^{2+}$ concentration in groundwater due to dilution with fresh rain water during the wet periods as reported for an argillite bedrock in the Eel River Critical Zone Observatory (Kim et al., 2014, 2017). This suggests that in the Jemez CZO study site, water percolating thorough the unsaturated zone to groundwater accumulates sufficient amounts of solutes (from relatively rapid mineral dissolution and cation exchange reactions) to maintain the high concentration in groundwater. A second silicate weathering pulse was observed as the water table in Well 2D began to recede. A similar Si pulse was captured at the same time in Wells 1A and 2C (**Supplementary Figure S2**). Moreover, in Well 1A this pulse was coincident with pulses of $Na^+$, Mn, $SO_4^{2-}$, $Cl^-$, DOC, and HIX. The increase in DOC and HIX, suggests that reactants (e.g., carbonic acid, DOM) giving rise to the weathering pulse propagate from the biologically active soil layers down through the vadose zone and into groundwater. The resulting fast Si pulse likely reflects dissolution of volcanic glass, which is prevalent in the ZOB subsurface. This rapid silicate dissolution during high water flow through the CZ is in agreement with previous observations for an argillite bedrock site (Kim et al., 2014, 2017). Furthermore this rapid pulse of Si in groundwater and streams offers an additional mechanism for rapid Si recharge of groundwater, contrasting with the slow silicate dissolution mechanism postulated previously for this study site (McIntosh et al., 2017), and is in agreement with the assumption of the dispersive mixing model.

**TABLE 3 |** Summary of mean hysteresis indices (HI) calculated for pairs of hydrograph limbs.

| Solute | R1-D2 | R1-D1 | D1-R2 | R2-D2 |
|---|---|---|---|---|
| Si | −0.11 (0.05) | −0.14 (0.01) | 0.05 (0.01) | −0.01 (0.04) |
| DIC | −0.11 (0.04) | −0.11 (0.05) | 0.26 (0.04) | −0.2 (0.04) |
| Zr | −0.22 (0.03) | 0.00 (0.01) | −0.32 (0.01) | 0.07 (0.03) |
| Ti | 0.08 (0.02) | 0.01 (0.03) | 0.07 (0.02) | 0.01 (0.03) |
| Mn | −0.01 (0.02) | 0.08 (0.03) | −0.20 (0.02) | −0.06 (0.06) |
| Al | −0.11 (0.02) | −0.04 (0.04) | −0.12 (0.03) | 0.00 (0.03) |
| $Na^+$ | 0.29 (0.03) | 0.22 (0.02) | 0.02 (0.01) | 0.02 (0.02) |
| $K^+$ | 0.62 (0.02) | 0.34 (0.02) | 0.06 (0.02) | 0.18 (0.02) |
| $SO_4^{2-}$ | 0.51 (0.02) | 0.03 (0.01) | 0.07 (0.02) | 0.32 (0.04) |
| $Mg^{2+}$ | 0.51 (0.03) | 0.16 (0.02) | 0.00 (0.03) | 0.25 (0.04) |
| $Sr^{2+}$ | 0.48 (0.02) | 0.19 (0.02) | 0.05 (0.03) | 0.18 (0.03) |
| $Ca^{2+}$ | 0.39 (0.04) | 0.2 (0.04) | 0.02 (0.04) | 0.15 (0.03) |
| $Cl^-$ | 0.4 (0.02) | 0.13 (0.01) | 0.12 (0.01) | 0.13 (0.02) |
| $NO_3^-$ | 0.42 (0.02) | 0.05 (0.01) | 0.1 (0.02) | 0.18 (0.03) |
| Fe | 0.71 (0.01) | 0.63 (0.04) | 0.06 (0.03) | −0.01 (0.02) |
| DOC | 0.55 (0.01) | 0.33 (0.03) | 0.14 (0.08) | 0.07 (0.06) |
| HREE | 0.25 (0.01) | 0.22 (0.02) | 0.00 (0.02) | 0.05 (0.02) |
| MREE | 0.19 (0.01) | 0.17 (0.02) | 0.02 (0.02) | 0.03 (0.02) |
| LREE | 0.16 (0.01) | 0.17 (0.03) | 0.04 (0.04) | −0.01 (0.02) |

*95% confidence intervals are presented in parentheses.*

On-going investigations into the mineralogy of cores extracted during the construction of wells 1 and 2 will help to elucidate the solid phases contributing to weathering pulses, and to explain the different trends in Na, Mn, $SO_4^{2-}$, $Cl^-$, and DOC concentrations between these wells on the eastern (Wells 1, Bandelier Tuff) and western (Wells 2, caldera breccia) slopes of the ZOB. For example, relative to the eastern slope, the western slope contains threefold higher mass concentration of Fe (oxy)hydroxide (*ca.* 30 g $kg^{-1}$ in the 1–15 m depth increment), predominantly as ferrihydrite, which we postulate acts as a reactive adsorbent for DOC (Gu et al., 1994; Eusterhues et al., 2005; Vazquez-Ortega et al., 2014). The western slope also contains calcite inclusions, not observed in the eastern slope boreholes, that likely contribute elevated $Ca^{2+}$ to Well 2D groundwater samples. Since calcium carbonate can contain significant amount of $SO_4^{2-}$ (ca. 10 mg $kg^{-1}$, Gill et al., 2008; Balan et al., 2014), the presence of calcite can explain the elevated $SO_4^{2-}$ concentrations in Well 2D water samples. In addition, we postulate that groundwater recharge on the eastern slope is dominated by fracture flow, whereas on the western slope it is dominated by matrix flow.

Analyzing multi-year time series on LJ surface water carbon dynamics, Perdrial et al. (2014) concluded that DOC with a terrestrial fluorescence signature and high humification index (HIX) originated from lateral water flow through near-surface soils, whereas DIC, as well as DOC with a stronger microbial fluorescence signature, were sourced from groundwater. Results of the present study indicate DIC dynamics in the ZOB stream are strongly influenced by soil biological activity. Specifically, DIC concentration and HIX (a reflection of partial microbial degradation of organic matter) in ZOB surface waters were highly correlated with each other (**Supplementary Figure S3**), as well as with $P_{CO2}$ in the soil profile (**Supplementary Figures S5**, **S6**) implying that soils serve as the dominant source of both DIC and DOC to groundwater and stream. Higher $P_{CO2}$ are known to accumulate under snowpack (Brooks et al., 1996), consistent with an active heterotrophic microbial community during the cold season whose respiratory products ($CO_2$ and DOC with high HIX values) are discharged to surface water during snowmelt, as demonstrated by the close similarity in $P_{CO2}$ between streams water and soil gas. Demonstrating important mechanism of $CO_2$ transport from soil to streams. It is important to note, however, that higher $P_{CO2}$ value occurs during the warm season (Brooks et al., 1996; Perdrial et al., 2014). This activity enables the processing of organic matter and accumulation of the degradation products in the soil profile. As water starts to move through the soil profile it transports this processed organic material, carbonic acid, and DOM to the subsurface and ZOB stream. Increased soil saturation during the snowmelt (**Figure 2C**), limits microbial activity (i.e., decrease in soil $P_{CO2}$), probably due to oxygen limitation. Thus, degradation of soil organic matter and transport of processed DOM to the stream decreases (i.e., lower HIX). As soils begin to drain, microbial and plant root activity increases (indicated by increased $P_{CO2}$ and HIX values). Hence, the soil hydrologic response from snow melt affects heterotrophic microbial activity. This, in turn, drives carbonic acid and complexing ligand (DOC with high HIX) production. These reactants propagate downward into the deeper subsurface to affect the second weathering pulse observed in the wells on both sides of the ZOB. These results provide support for the analytical model proposed by Calabrese et al. (2017), which suggests that transport of carbonic acid from bioactive soil exerts a principal control over subsurface bedrock chemical weathering rates. Results of the current study suggest that organic ligand production also controls these weathering reactions and needs to be included in future models.

## C-Q Analysis

Principle component analysis is commonly used to develop mixing models (Nils Christophersen, 1992; Hooper, 2003; Liu et al., 2008). Wymore et al. (2017) used PCA, to reduce dimensionality of catchment variables, enabled them to compare *C-Q* parameters between multiple sites. In the current study, cluster analysis and PCA enabled us to sort the large set of quantified major and trace solutes into five distinct groups on the basis of their hydrochemical behavior (Section "Cluster and Principle Component Analyses," **Figure 6**). These groups represent different coupled processes that occur in the CZ during spring snowmelt, which in this system represents the largest through-flux of fresh water. The first group, Si and DIC, represents mobile products of silicate weathering reaction. Elements of this group demonstrated chemostatic or dilution *C-Q* trends and anti-clockwise hysteresis patterns. Their higher concentrations in groundwater (**Table 1**), and the Si concentration peak during the first hydrograph recession (**Figure 3**), suggest that Si and DIC derive from a relatively large groundwater reservoir that is displaced by new meteoric

waters entering through surficial soils. Such an assessment is also consistent with the observed groundwater table rise (**Figure 2D**) that coincides with high downward fluxes through saturated soils (**Figure 2C**). Groundwater Si is, therefore, potentially recharged by pulsed upgradient weathering events, as observed in this study.

Non-hydrolyzing cations and strong acid anions formed the second group. With the exception of $Na^+$, ions in this group exhibited slightly positive power law exponents in the R1, D1, and D2 hydrograph limbs (**Table 2** and **Figure 4**). Most ions of this group exhibited dilution trends during the second hydrograph rise (R2), indicating lower generation rates of these ions during the second part of the snowmelt hydrograph, consistent with flushing and removal during the first hydrograph peak. The high frequency sampling method provide increased resolution for these trends and shifts in *C-Q* trend, compare to previous study that demonstrated chemostatic behavior of these elements (McIntosh et al., 2017). Potassium was unique in retaining a positive trend during the second rise of the hydrograph. All solutes in this group also showed clockwise hysteresis for both peaks in the hydrograph (**Table 3** and **Supplementary Figure S7**). These trends are consistent with a flush of a limited pool of nutrient ions ($Ca^{2+}$, $Mg^{2+}$, $K^+$, $NO_3^-$, $SO_4^{2-}$) that accumulate under snowpack as a result of both wet deposition followed by downward ion migration through the snowpack during freeze-thaw cycles as well as organic matter decomposition under the snowpack (Brooks et al., 1996; Schmidt and Lipson, 2004). Trend of positive or chemostatic *C-Q* relations for these elements also been observed in the Susquehanna Shale Hills CZO, and explain by the large contribution of soil later flow and mobilization accumulated elements to stream (Bao et al., 2017; Li et al., 2017a). $Na^+$, which is not a nutrient cation, diverged from the rest of the group in its display of slight dilution to chemostatic behavior. Likewise, on the PC biplots (**Figure 6**), $Na^+$ scored closest to the Si/DIC group. This difference is likely the result of lower biocycling of $Na^+$ (and hence less accumulation in decomposing organic matter of surface soils) relative to the other ions in this group. Moreover, groundwater obtained from wells on both sides of the ZOB was more enriched in $Na^+$ than was soil or stream water. Therefore, $Na^+$ discharge may be dominated by release from the deeper groundwater weathering zone (similar to the case for Si and DIC), as has been suggested in previous work from this site (Zapata-Rios et al., 2015). The other borderline member of this group was $K^+$, which did not change the power exponent sign from positive to negative during the second hydrograph rise, R2 (**Table 2**). Interestingly, on the PC biplot $K^+$ scored closer to group 3 solutes (DOC and REEs). Since soil is the primary source of DOC to streams, our analysis suggests that $K^+$ discharge is dominated by this source as well, and indeed it is also known to be mobilized readily by leaching of biomass (Tripler et al., 2006).

Prior observations of correlations between REE and DOC concentrations has led to the suggestion that fractionation of the lanthanide series resulting from variation in metal-ligand stability is a useful probe of ligand-promoted biological weathering in the CZ (Vázquez-Ortega et al., 2015). A prior study in a granitic catchment showed that these elements are transported as colloidal material in streams, and that this process explained positive power law exponents in *C-Q* relations (Trostle et al., 2016). Results of the present study indicate that, in the volcanic terrain of La Jara catchment, REEs in streamwater occur as aqueous organic complexes that are tightly correlated with and potential controlled by DOC transport.

The last two groups (4 and 5) exhibited strong coefficients of variance in concentrations compared to discharge (i.e., high values of $CV_C/CV_Q$), and also showed large colloidal fractions throughout the snowmelt hydrograph (**Table 2** and **Figure 5**). In contrast to group 4 (Ti, Zr, Mn, and Al), Fe showed a high concentration flush and a positive C-Q trend in the first hydrograph limb (R1, **Table 2** and **Figure 4**), and a strong clockwise hysteresis in the first hydrograph peak, which led to it being distinguished as a separate solute group. The positive correlation of Fe with DOC during R1 ($R = 0.56$, $p < 0.001$), and large positive hysteresis pattern for the same period, suggests a rapid flush of small Fe-DOM colloids that accumulated over winter in the soil or riparian zones. Overall, the *C-Q* relations of elements in groups 4 and 5, are consistent with a dominant colloidal (<1.2 μm) control on aqueous filtrate concentrations, as was confirmed by direct cascade filtration (**Figure 5**). Previous studies have suggested increased fluid shear stress during lateral soil water flow is the dominant mechanism for colloid detachment and transport from soils and hyporheic zones to the stream (Bradford et al., 2002; Wörman et al., 2002; Trostle et al., 2016). Therefore, elements that transport to streams as colloids may demonstrate pronounced positive *C-Q* relations (Trostle et al., 2016). The fact that components of groups 4 (Ti, Zr, Mn, and Al) and 5 (Fe) did not show consistent and clear positive power law exponents in the present study (**Table 2** and **Figure 4**) despite being dominantly present in colloidal form (**Figure 5**) is consistent with the fact that the Jemez CZ is deeper and more complex than that of the Catalina site studied by Trostle et al. (2016). In the LJ catchment, colloids mobilized from soils may be subsequently immobilized in pores and fractures of the deep vadose and saturated zones.

## CONCLUSION

The La Jara catchment is representative of the high elevation, mountain headwaters of the Rio Grande, which serves as the principal water source for Albuquerque, El Paso and other cities. Monitoring of pore waters and surface waters in the LJ catchment during spring snowmelt identified five distinct groups of *C-Q* behaviors that are distinguished on the basis of their sourcing and transport behavior in the CZ. Probing multiple CZ compartments, including soil water, groundwater and surface water, enabled the establishment of linkages between *C-Q* behavior of these groups and CZ processes. Si and DIC (group 1) derive from a groundwater source, as their contribution to surface waters become more dominant when shallow subsurface flows

(soil) decreased during the descending limb of the hydrograph. Lanthanide series elements and DOC (group 3), had stronger positive *C-Q* trends and clockwise hysteresis patterns that were more pronounced compared with other tested elements. The *C-Q* behavior of these solutes suggest that they are useful signals of soil biologically influenced weathering reactions (e.g., strong positive chemodynamic behavior). Non-hydrolyzing cations and strong acid anions (group 2) demonstrated mostly positive *C-Q* trends and a clockwise hysteresis pattern. These trends imply flushing of a limited reservoir of solutes that accumulated under the snowpack. Endmembers of this group included $Na^+$, which showed some similarity to DIC and Si, suggesting contribution from deep subsurface weathering, and $K^+$, which exhibited *C-Q* behavior transitional to REEs and DOC, consistent with its sourcing from decomposing organic materials and active bio-cycling role. Groups 4 and 5 comprise metals that exhibit higher coefficients of variance (CV) for concentration relative to discharge, with generally poor fits to the power law function. These groups also had high colloidal fractions in surface water, demonstrating that adhesion and shearing effects that control colloid transport in complex geological settings are not strongly correlated with discharge. Although Fe had much in common with these other hydrolyzing metals and also comprised a significant colloidal component, it was represented by a separate group (5) due to its apparent complexation with DOM and transport to the stream as a metal-organic complex during the first rise of the hydrograph.

Frequent sampling of surface and ground water further revealed a large pulse of Si in streams and wells of the LJ catchment that occurred during the second descending limb of the hydrograph. This pulse was linked to enhanced bioactivity (increased soil $P_{CO2}$ and HIX values) and vertical downward flow of DIC and DOC that promoted fast weathering of silicate minerals, likely including volcanic glass, which is an abundant and highly weatherable mineral present in the CZ at this volcanic site. Given that soil biological activities likely drive the DIC and DOC impacts on silicate weathering observed here, consideration of such effects would be useful for the ongoing development of reactive transport models of critical zone evolution (Li et al., 2017b).

## AUTHOR CONTRIBUTIONS

YO performed the data analysis, developed the conceptual framework, and wrote the manuscript with support from JC, JM, AW, and BM. JC and JM conceived the original idea. JC supervised the project.

## FUNDING

This research was funded by the National Science Foundation, Grant No. EAR-1331408, which supports the Catalina-Jemez Critical Zone Observatory, and through the Binational Agricultural Research and Development (BARD) program, which awarded a postdoctoral fellowship to YO (Grant No. FI-534-2015) and the National Science Foundation, Grant No. EAR-1331408, which supports the Catalina-Jemez Critical Zone Observatory.

## ACKNOWLEDGMENTS

All data utilized in this paper are available through the criticalzone.org website at http://criticalzone.org/catalina-jemez/data/. We are grateful to Mary Kay Amistadi, Rachel Nadine Burnett, Mark Losleben, and Adam Killebrew for assistance with laboratory chemical analyses and field work.

## SUPPLEMENTARY MATERIAL

The Supplementary Material for this article can be found online at: https://www.frontiersin.org/articles/10.3389/feart.2018.00181/full#supplementary-material

## REFERENCES

Balan, E., Blanchard, M., Pinilla, C., and Lazzeri, M. (2014). First-principles modeling of sulfate incorporation and 34S/32S isotopic fractionation in different calcium carbonates. *Chem. Geol.* 374–375, 84–91. doi: 10.1016/j.chemgeo.2014.03.004

Bao, C., Li, L., Shi, Y., and Duffy, C. (2017). Understanding watershed hydrogeochemistry: 1. Development of RT-Flux-PIHM. *Water Resour. Res.* 53, 2328–2345. doi: 10.1002/2016WR018934

Benettin, P., Bailey, S. W., Campbell, J. L., Green, M. B., Rinaldo, A., Likens, G. E., et al. (2015). Linking water age and solute dynamics in streamflow at the Hubbard Brook Experimental Forest, NH, USA. *Water Resour. Res.* 51, 9256–9272. doi: 10.1002/2015WR017552

Bouchez, J., Moquet, J. S., Espinoza, J. C., Martinez, J. M., Guyot, J. L., Lagane, C., et al. (2017). River mixing in the amazon as a driver of concentration-discharge relationships. *Water Resour. Res.* 53, 8660–8685. doi: 10.1002/2017WR020591

Bowes, M. J., Jarvie, H. P., Halliday, S. J., Skeffington, R. A., Wade, A. J., Loewenthal, M., et al. (2015). Characterising phosphorus and nitrate inputs to a rural river using high-frequency concentration-flow relationships. *Sci. Total Environ.* 511, 608–620. doi: 10.1016/j.scitotenv.2014.12.086

Bowes, M. J., Smith, J. T., and Neal, C. (2009). The value of high-resolution nutrient monitoring: a case study of the River Frome, Dorset, UK. *J. Hydrol.* 378, 82–96. doi: 10.1016/j.jhydrol.2009.09.015

Bradford, S. A., Yates, S. R., Bettahar, M., and Simunek, J. (2002). Physical factors affecting the transport and fate of colloids in saturated porous media. *Water Resour. Res.* 38, 63-1–63-12. doi: 10.1029/2002WR001340

Brooks, P. D., Williams, M. W., and Schmidt, S. K. (1996). Microbial activity under alpine snowpacks, Niwot Ridge, Colorado. *Biogeochemistry* 32, 93–113. doi: 10.1007/BF00000354

Calabrese, S., Porporato, A., and Parolari, A. J. (2017). Hydrologic transport of dissolved inorganic carbon and its control on chemical weathering. *J. Geophys. Res. Earth Surf.* 122, 2016–2032. doi: 10.1002/2017JF004346

Chanat, J. G., Rice, K. C., and Hornberger, G. M. (2002). Consistency of patterns in concentration-discharge plots. *Water Resour. Res.* 38, 22-1–22-10. doi: 10.1029/2001WR000971

Chipera, S. J., Goff, F., Goff, C. J., and Fittipaldo, M. (2008). Zeolitization of intracaldera sediments and rhyolitic rocks in the 1.25 Ma lake of Valles caldera, New Mexico, USA. *J. Volcanol. Geotherm. Res.* 178, 317–330. doi: 10.1016/j.jvolgeores.2008.06.032

Chorover, J., Derry, L. A., and McDowell, W. H. (2017). Concentration-Discharge relations in the critical zone: implications for resolving critical zone structure, function, and evolution. *Water Resour. Res.* 53, 8654–8659. doi: 10.1002/2017WR021111

Chorover, J., Troch, P. A., Rasmussen, C., Brooks, P. D., Pelletier, J. D., Breshears, D. D., et al. (2011). How water, carbon, and energy drive critical zone evolution: The Jemez–Santa Catalina critical zone observatory. *Vadose Zone J.* 10:884. doi: 10.2136/vzj2010.0132

Eusterhues, K., Rumpel, C., and Kogel-Knabner, I. (2005). Organo-mineral associations in sandy acid forest soils: importance of specific surface area, iron oxides and micropores. *Eur. J. Soil Sci.* 56, 753–763. doi: 10.1111/j.1365-2389.2005.00710.x

Evans, C., and Davies, T. D. (1998). Causes of concentration/discharge hysteresis and its potential as a tool for analysis of episode hydrochemistry. *Water Resour. Res.* 34, 129–137. doi: 10.1029/97WR01881

Fox, J., and Weisberg, S. (2011). *An {R} Companion to Applied Regression. Second*. Thousand Oaks, CA: Sage.

Gill, B. C., Lyons, T. W., and Frank, T. D. (2008). Behavior of carbonate-associated sulfate during meteoric diagenesis and implications for the sulfur isotope paleoproxy. *Geochim. Cosmochim. Acta* 72, 4699–4711. doi: 10.1016/j.gca.2008.07.001

Godsey, S. E., Kirchner, J. W., and Clow, D. W. (2009). Concentration-discharge relationships reflect chemostatic characteristics of US catchments. *Hydrol. Process.* 23, 1844–1864. doi: 10.1002/hyp.7315

Gu, B., Schmitt, J., Chen, Z., Liang, L., and McCarthy, J. F. (1994). Adsorption and desorption of natural organic matter on iron oxide: mechanisms and models. *Environ. Sci. Technol.* 28, 38–46. doi: 10.1021/es00050a007

Herndon, E. M., Dere, A. L., Sullivan, P. L., Norris, D., Reynolds, B., and Brantley, S. L. (2015). Landscape heterogeneity drives contrasting concentration-discharge relationships in shale headwater catchments. *Hydrol. Earth Syst. Sci.* 19, 3333–3347. doi: 10.5194/hess-19-3333-2015

Hoagland, B., Russo, T. A., Gu, X., Hill, L., Kaye, J., Forsythe, B., et al. (2017). Hyporheic zone influences on concentration-discharge relationships in a headwater sandstone stream. *Water Resour. Res.* 53, 4643–4667. doi: 10.1002/2016WR019717

Hooper, R. P. (2003). Diagnostic tools for mixing models of stream water chemistry. *Water Resour. Res.* 39, 1–13. doi: 10.1029/2002WR001528

Hulen, J. B., and Nielson, D. L. (1986). Hydrothermal alteration in the Baca geothermal system, Redondo dome, Valles Caldera, New Mexico (USA). *J. Geophys. Res.* 91, 1867–1886. doi: 10.1029/JB091iB02p01867

Kim, H., Bishop, J. K. B., Dietrich, W. E., and Fung, I. Y. (2014). Process dominance shift in solute chemistry as revealed by long-term high-frequency water chemistry observations of groundwater flowing through weathered argillite underlying a steep forested hillslope. *Geochim. Cosmochim. Acta* 140, 1–19. doi: 10.1016/j.gca.2014.05.011

Kim, H., Dietrich, W. E., Thurnhoffer, B. M., Bishop, J. K. B., and Fung, I. Y. (2017). Controls on solute concentration-discharge relationships revealed by simultaneous hydrochemistry observations of hillslope runoff and stream flow: the importance of critical zone structure. *Water Resour. Res.* 53, 1424–1443. doi: 10.1002/2016WR019722

Kirchner, J. W., and Neal, C. (2013). Universal fractal scaling in stream chemistry and its implications for solute transport and water quality trend detection. *Proc. Natl. Acad. Sci. U.S.A.* 110, 12213–12218. doi: 10.1073/pnas.1304328110

Lenth, R. (2015). *lsmeans: Least-Squares Means*. Available at: http://cran.r-project.org/package=lsmeans

Li, L., C. Bao, P. L. Sullivan, S. Brantley, Y. Shi, and C. Duffy (2017a), Understanding watershed hydrogeochemistry: 2. Synchronized hydrological and geochemical processes drive stream chemostatic behavior. *Water Resour. Res.* 53, 2346–2367, doi: 10.1002/2016WR018935

Li, L., Maher, K., Navarre-Sitchler, A., Druhan, J., Meile, C., Lawrence, C., et al. (2017b). Expanding the role of reactive transport models in critical zone processes. *Earth Sci. Rev.* 165, 280–301. doi: 10.1016/j.earscirev.2016.09.001

Liu, F., Bales, R. C., Conklin, M. H., and Conrad, M. E. (2008). Streamflow generation from snowmelt in semi-arid, seasonally snow-covered, forested catchments, Valles Caldera, New Mexico. *Water Resour. Res.* 44, 1–13. doi: 10.1029/2007WR006728

Maher, K. (2011). The role of fluid residence time and topographic scales in determining chemical fluxes from landscapes. *Earth Planet. Sci. Lett.* 312, 48–58. doi: 10.1016/j.epsl.2011.09.040

McIntosh, J. C., Schaumberg, C., Perdrial, J., Harpold, A., Vázquez-Ortega, A., Rasmussen, C., et al. (2017). Geochemical evolution of the critical zone across variable time scales informs concentration-discharge relationships: jemez River Basin critical zone observatory. *Water Resour. Res.* 53, 4169–4196. doi: 10.1002/2016WR019712

Murphy, K. R., Stedmon, C. A., Graeber, D., and Bro, R. (2013). Fluorescence spectroscopy and multi-way techniques. PARAFAC. *Anal. Methods* 5:6557. doi: 10.1039/c3ay41160e

Musolff, A., Schmidt, C., Selle, B., and Fleckenstein, J. H. (2015). Catchment controls on solute export. *Adv. Water Resour.* 86, 133–146. doi: 10.1016/j.advwatres.2015.09.026

Nils Christophersen, R. P. H. (1992). Multivariate analysis of stream water chemical data: the use of principal components analysis for the end-member mixing problem. *Water Resour. Res.* 28, 99–107.

Ohno, T. (2002). Fluorescence inner-filtering correction for determining the humification index of dissolved organic matter. *Environ. Sci. Technol.* 36, 742–746. doi: 10.1021/es0155276

Perdrial, J., Brooks, P. D., Lohse, K. A., Harpold, A. A., Zapata-rios, X., Meixner, T., et al. (2018). Biogeochemistry A net ecosystem carbon budget for snow dominated forested headwater catchments: linking water and carbon fluxes to critical zone carbon storage. *Biogeochemistry* 138, 225–243. doi: 10.1007/s10533-018-0440-3

Perdrial, J. N., McIntosh, J., Harpold, A., Brooks, P. D., Zapata-Rios, X., Ray, J., et al. (2014). Stream water carbon controls in seasonally snow-covered mountain catchments: impact of inter-annual variability of water fluxes, catchment aspect and seasonal processes. *Biogeochemistry* 118, 273–290. doi: 10.1007/s10533-013-9929-y

Pinheiro, J., Bates, D., DebRoy, S., Sarkar, D., and R Core Team (2017). *{nlme}: Linear and Nonlinear Mixed Effects Models*. Available at: https://cran.r-project.org/package=nlme

Pokrovsky, O. S., Schott, J., and Dupré, B. (2006). Trace element fractionation and transport in boreal rivers and soil porewaters of permafrost-dominated basaltic terrain in Central Siberia. *Geochim. Cosmochim. Acta* 70, 3239–3260. doi: 10.1016/j.gca.2006.04.008

R Core Team (2017). *R: A Language and Environment for Statistical Computing*. Available at: https://www.r-project.org/

Reale, J. K., Van Horn, D. J., Condon, K. E., and Dahm, C. N. (2015). The effects of catastrophic wildfire on water quality along a river continuum. *Freshw. Sci.* 34, 1426–1442. doi: 10.1086/684001

Schmidt, S. K., and Lipson, D. A. (2004). Microbial growth under the snow: Implications for nutrient and allelochemical availability in temperate soils. *Plant Soil* 259, 1–7.

Stumm, W., and Morgan, J. J. (1981). *Aquatic Chemistry: An Introduction Emphasizing Chemical Equilibria in Natural Waters*. Hoboken, NJ: Wiley.

Thompson, S. E., Basu, N. B., Lascurain, J., Aubeneau, A., and Rao, P. S. C. (2011). Relative dominance of hydrologic versus biogeochemical factors on solute export across impact gradients. *Water Resour. Res.* 47, 1–20. doi: 10.1029/2010WR009605

Tripler, C. E., Kaushal, S. S., Likens, G. E., and Todd Walter, M. (2006). Patterns in potassium dynamics in forest ecosystems. *Ecol. Lett.* 9, 451–466. doi: 10.1111/j.1461-0248.2006.00891.x

Trostle, K. D., Ray Runyon, J., Pohlmann, M. A., Redfield, S. E., Pelletier, J., McIntosh, J., et al. (2016). Colloids and organic matter complexation control trace metal concentration-discharge relationships in Marshall Gulch stream waters. *Water Resour. Res.* 52, 7931–7944. doi: 10.1002/2016WR019072

Vaughan, M. C. H., Bowden, W. B., Shanley, J. B., Vermilyea, A., Sleeper, R., Gold, A. J., et al. (2017). High-frequency dissolved organic carbon and nitrate measurements reveal differences in storm hysteresis and loading in relation to land cover and seasonality. *Water Resour. Res.* 53, 5345–5363. doi: 10.1002/2017WR020491

Vazquez-Ortega, A., Hernandez-Ruiz, S., Amistadi, M. K., Rasmussen, C., and Chorover, J. (2014). Fractionation of dissolved organic matter by (Oxy)Hydroxide-coated sands: competitive sorbate displacement

during reactive transport. *Vadose Zone J.* 13:7. doi: 10.2136/vzj2013.10.0179

Vázquez-Ortega, A., Huckle, D., Perdrial, J., Amistadi, M. K., Durcik, M., Rasmussen, C., et al. (2016). Solid-phase redistribution of rare earth elements in hillslope pedons subjected to different hydrologic fluxes. *Chem. Geol.* 426, 1–18. doi: 10.1016/j.chemgeo.2016.01.001

Vázquez-Ortega, A., Perdrial, J., Harpold, A., Zapata-Ríos, X., Rasmussen, C., McIntosh, J., et al. (2015). Rare earth elements as reactive tracers of biogeochemical weathering in forested rhyolitic terrain. *Chem. Geol.* 391, 19–32. doi: 10.1016/j.chemgeo.2014.10.016

Wickham, H. (2009). *ggplot2: Elegant Graphics for Data Analysis*. New York, NY: Springer-Verlag.

Winnick, M. J., Carroll, R. W. H., Williams, K. H., Maxwell, R. M., Dong, W., and Maher, K. (2017). Snowmelt controls on concentration-discharge relationships and the balance of oxidative and acid-base weathering fluxes in an alpine catchment, East River, Colorado. *Water Resour. Res.* 53, 2507–2523. doi: 10.1002/2016WR019724

Wörman, A., Packman, A. I., Johansson, H., and Jonsson, K. (2002). Effect of flow-induced exchange in hyporheic zones on longitudinal transport of solutes in streams and rivers. *Water Resour. Res.* 38, 2-1–2-15. doi: 10.1029/2001WR000769

Wymore, A. S., Brereton, R. L., Ibarra, D. E., Maher, K., and McDowell, W. H. (2017). Critical zone structure controls concentration-discharge relationships and solute generation in forested tropical montane watersheds, *Water Resour. Res.* 53, 6279–6295. doi: 10.1002/2016WR020016

Zapata-Rios, X., Brooks, P. D., Troch, P. A., McIntosh, J., and Guo, Q. (2016). Influence of terrain aspect on water partitioning, vegetation structure and vegetation greening in high-elevation catchments in northern New Mexico. *Ecohydrology* 9, 782–795. doi: 10.1002/eco.1674

Zapata-Rios, X., McIntosh, J., Rademacher, L., Troch, P. A., Brooks, P. D., Rasmussen, C., et al. (2015). Climatic and landscape controls on water transit times and silicate mineral weathering in the critical zone. *Water Resour. Res.* 51, 6036–6051. doi: 10.1002/2015WR017018

**Conflict of Interest Statement:** The authors declare that the research was conducted in the absence of any commercial or financial relationships that could be construed as a potential conflict of interest.

frontiers in Earth Science

ORIGINAL RESEARCH
published: 09 November 2018
doi: 10.3389/feart.2018.00193

# Regolith Weathering and Sorption Influences Molybdenum, Vanadium, and Chromium Export via Stream Water at Four Granitoid Critical Zone Observatories

*Justin B. Richardson*[1,2]* *and Elizabeth K. King*[3]

[1] Department of Geosciences, University of Massachusetts Amherst, Amherst, MA, United States, [2] Earth and Atmospheric Sciences, College of Agriculture and Life Sciences, Cornell University, Ithaca, NY, United States, [3] Department of Earth, Ocean, and Atmospheric Sciences, University of British Columbia, Vancouver, BC, Canada

OPEN ACCESS

**Edited by:**
*Julia Perdrial,*
*University of Vermont, United States*

**Reviewed by:**
*Angelica Vazquez-Ortega,*
*Bowling Green State University, United States*
*Dragos George Zaharescu,*
*Georgia Institute of Technology, United States*

***Correspondence:**
*Justin B. Richardson*
*Soilbiogeochemist@gmail.com*

**Specialty section:**
*This article was submitted to Biogeoscience, a section of the journal Frontiers in Earth Science*

**Received:** *20 June 2018*
**Accepted:** *19 October 2018*
**Published:** *09 November 2018*

**Citation:**
*Richardson JB and King EK (2018) Regolith Weathering and Sorption Influences Molybdenum, Vanadium, and Chromium Export via Stream Water at Four Granitoid Critical Zone Observatories. Front. Earth Sci. 6:193. doi: 10.3389/feart.2018.00193*

Understanding the fate of oxyanions in the Critical Zone is important because of their biological significance and the potential for their use as geochemical tracers in terrestrial environments and subsurface systems. This study assessed the partitioning and transport of a suite of oxyanion metals (Mo, V, and Cr) in regolith profiles and stream waters from four granitoid Critical Zone Observatories (CZOs) (Boulder Creek, Calhoun, Luquillo, and Southern Sierra). For regolith profiles, we compared Mo, V, and Cr in total digestions and two extractions targeting oxyanions adsorbed to organic matter and amorphous oxides ($H_2O_2$ + 0.1 M acetic acid) and secondary Fe oxides (citrate–bicarbonate–dithionite). Total Mo, V, and Cr ranged from 0.4 to 2.5 mg $kg^{-1}$, 16 to 208 mg $kg^{-1}$, and 0.2 to 55 mg $kg^{-1}$, respectively. The greatest concentrations of the oxyanions did not occur in surface soil samples, nor deepest regolith samples (7–10 m in depth), but instead in subsurface peaks that corresponded with secondary Fe oxides and total organic carbon. The average organic and amorphous oxide bound phase was 0.1–3.5% while the secondary Fe oxide fraction was 4–27% of the respective total concentrations for oxyanions, suggesting that secondary Fe oxides were an important phase across the regolith profile. Stream water Mo, V, and Cr concentrations ranged from 0.02 to 0.25 $\mu g\ L^{-1}$, 0.2 to 1.8 $\mu g\ L^{-1}$, and 0.08 to 0.44 $\mu g\ L^{-1}$, respectively. Our results demonstrate that the deep regolith (2–7 m in depth) play an active role in both sourcing and retention of oxyanions. In addition, we observed that increased weathering intensity at warmer, wetter climates does not always lead to increased depletion in regolith or stream water export, which implies the importance of transport processes within regolith. Further quantification of oxyanion export from regolith can aid in developing their use as geochemical tools for global weathering.

**Keywords: deep regolith, oxyanions, stream export, Critical Zone, weathering profile, soil biogeochemistry**

## INTRODUCTION

The Critical Zone (CZ) is the thin region on Earth's surface where the atmosphere, hydrosphere, lithosphere, and biosphere interact through chemical, biological, and physical processes (e.g., Brantley et al., 2007; Chorover et al., 2007; Giardino and Houser, 2015). Exploring the natural processes that govern the CZ is important as they ultimately sustain terrestrial life and exert controls on the biotic and abiotic cycling of energy and nutrients (Amundson et al., 2007). However, the CZ exhibits substantial variations in climate, lithology, and biogeography, both across landscapes and with depth. It is paramount to understand and quantify the mechanisms, particularly the poorly understood processes occurring at depth, that influence the CZ's development and function (Brantley and Lebedeva, 2011; Giardino and Houser, 2015).

The biological importance of oxyanion metals is twofold as they can serve as micronutrients in a number of life-sustaining processes, but may also have toxic effects on organisms at elevated concentrations. For example, plant growth can be negatively impacted by total V concentrations greater than 0.8 mg $L^{-1}$ in soil solution (Larsson et al., 2013) and total Cr water concentrations greater than 5 mg $L^{-1}$ is considered hazardous to plants and animals (Singh et al., 2013). In this study, we investigate how lithology and climate influence the retention of oxyanions in the regolith and mobilization to stream water. We focus on molybdenum (Mo), chromium (Cr), and vanadium (V) because of their role as essential micronutrients and potential toxicity for organisms.

In addition to toxicity, the unique geochemistry and speciation patterns of oxyanions allows them to be proxies for various environmental parameters, particularly oxidation-reduction reactions and weathering. Molybdenum is a key component for a number of enzymatic processes that occur during nitrogen and sulfur metabolism and is also responsible for the biosynthesis of plant hormones (Kaiser et al., 2005). Of particular interest, Mo is a cofactor for the nitrogenase enzyme required for nitrogen fixation and can become a limiting micronutrient in forest soils (e.g., Barron et al., 2008). Low concentrations of Mo are required by plants, with typical foliar values ranging between 0.03 and 1.61 mg $kg^{-1}$ (Adriano, 2001). At concentrations exceeding 100 ppm in soils Mo can become toxic for plants, and at concentrations exceeding 10 mg $kg^{-1}$ in vegetation humans and animals are susceptible to molybdenosis (Gupta, 1997; Adriano, 2001).

Vanadium (V) is another trace metal oxyanion that enhances plant growth and serves as a micronutrient for a variety of biological processes. At low concentrations (<2 mg $kg^{-1}$), V has been shown to enhance chlorophyll synthesis and nitrogen fixation in plant tissues; however, higher concentrations may cause chlorosis and stunted growth (Kabata-Pendias, 2011). Due to similarities in their ionic radii, V can substitute for Ca and Mg, inhibiting chlorophyll generation, protein production, ATP formation, cellular pH, and enzymatic activities at high abundance within plant tissues (Cantley et al., 1977, 1978; Marschner et al., 1986; Crans et al., 1995; Larsson et al., 2013). Nevertheless, V toxicity in plants are uncommon due to its poor translocation from belowground to aerial tissues in plants (Adriano, 2001). There is no significant data to conclude that V is a necessary part of nutrition for humans (Imtiaz et al., 2015).

The biological importance of Cr is highly dependent on its oxidation state. Chromium(VI) does not serve any known roles for plants or animals, is a highly toxic carcinogen for humans (Kotaś and Stasicka, 2000; Dayan and Paine, 2001; Levina et al., 2003). Chromium (III), however, is essential for humans as it has been shown to be a cofactor for biologically active molecules that enhance the effects of insulin on target tissues; Cr(III) deficiencies include abnormal glucose utilization and increased insulin requirements (see Kotaś and Stasicka, 2000; Dayan and Paine, 2001). Chromium toxicity in plants is possible in very acidic soils with <5 pH, but is uncommon in soils with >5 pH due to low bioavailable concentrations (Adriano, 2001).

The retention and mobility of oxyanions (Mo, V, and Cr) are largely controlled by climate, weathering, and sorption reactions, all of which are variable in the Critical Zone. Molybdenum concentrations across all rock types range from 0.3 to 300 mg $kg^{-1}$ (Adriano, 2001), and all soil types range from 0.01 to 17 mg $kg^{-1}$ (Kabata-Pendias, 2011). Molybdenum exists in oxic soils primarily as the molybdate oxyanion ($MoO_4^{2-}$, +VI oxidation state) with molybdic acid ($H_2MoO_4$) and its oxyanion ($HMoO_4^-$) becoming increasingly present below pH 4, (Adriano, 2001; Alloway, 2013). Vanadium concentrations in rocks range from 20 to 250 mg $kg^{-1}$ while soils have a broader range of 3–500 mg $kg^{-1}$ depending on the initial concentration of their parent material (Adriano, 2001; Kabata-Pendias, 2011). Vanadium can be present as V(IV), mainly as $VO_2$ (vanadyl), whereas V(V) exists as the oxyanions $H_2VO_4^{-1}$ or as $HVO_4^{-2}$ (collectively referred to as vanadate), depending on the pH and oxidation status. Vanadate is considered the most toxic vanadium species (Martin and Kaplan, 1998; Larsson et al., 2013). Chromium concentrations in soils range from 2 to 150 mg $kg^{-1}$ and is found mainly in two oxidation states, the trivalent Cr(III) and the hexavalent Cr(VI) (Adriano, 2001).

The terrestrial geochemistry of Mo, V, and Cr is a function of sorption processes and chemical speciation. Under oxic conditions, Mo, V, and Cr oxyanion sorption onto soil solids is determined by Fe and Al oxides, clay minerals and organic matter, of which most are pH dependent (e.g., Gäbler et al., 2009; Pérez et al., 2014; Wisawapipat and Kretzschmar, 2017). As an example, adsorption of $MoO_4^{2-}$ ions from soil solution onto positively charged metal oxides occurs between pH 4 and 5 (Riley et al., 1987; Gupta, 1997; Xu et al., 2013). In acidic soils, molybdate, vanadate, and chromate anions are sorbed onto positively charged Fe, Mn, and Al oxides as well as clay minerals and organic matter (Grove and Ellis, 1980; Pérez et al., 2014; King et al., 2016; Larsson et al., 2017; Wisawapipat and Kretzschmar, 2017). In addition, sorption to primary minerals such as inherited clay minerals like illite can also occur. In three Swedish soils, V(IV) was predominantly bound to primary minerals (Gäbler et al., 2009; Larsson et al., 2015; Wisawapipat and Kretzschmar, 2017). Oxyanion sorption to organic matter, Al and Fe oxides, and clay minerals in soils is important as it directly controls the retention and export of Mo, Cr, and V to stream waters (Kerr et al., 2008).

The influence of deep regolith—the unconsolidated layer of physically and chemically weathered rock that overlies unweathered bedrock—on oxyanion biogeochemistry in the Critical Zone is largely unconstrained below 2 m depth. Previous studies of Mo, Cr, and V sourcing to stream waters have primarily focused on surface soils <0.3 m depth (e.g., Salvador-Blanes et al., 2006; Gäbler et al., 2009; Wichard et al., 2009; Pérez et al., 2014; Morrison et al., 2015; Larsson et al., 2017; Wisawapipat and Kretzschmar, 2017) or only aqueous systems (e.g., Kerr et al., 2008; Gardner et al., 2017). However, regolith underlying soils at depths >1 m may be an important source of metals to surface waters and may also influence their immobilization. Here, we investigated the importance of regolith on oxyanion geochemistry at four Critical Zone Observatories (CZOs) developed on monolithic granitoid parent material, spanning a diverse climatic gradient (wet, hot tropical forest to cold, dry mountain-steppe). We hypothesized that CZOs with more secondary Fe oxide phases will have greater oxyanion sorption deeper within their profiles (>1 m depth) beyond the typical depth of surface soils (<0.3 m depth). Illuminating the role of the deep CZ is essential to capture its control on soil and surface water geochemistry.

# MATERIALS AND METHODS

## Critical Zone Observatories (CZOs)

### Boulder Creek CZO

Boulder Creek CZO is located in Arapahoe National Forest at the front range of the Rocky Mountains in north central Colorado, (**Figure 1**). Regolith samples were collected by borehole drilling in June 2014 from Gordon Gulch, a valley with low topographic relief, within the Boulder Creek CZO. Eight regolith samples were collected over a 7.0 m depth profile with samples collected every 0.5 m for the top 2.5 m and one deep sample at 7.0 m. Gordon Gulch is characterized by a montane-steppe climate with a mean annual temperature (MAT) of 4°C and a mean annual precipitation (MAP) of 735 mm year$^{-1}$, with the majority of precipitation occurring between March and May (**Table 1**) (Dethier and Bove, 2011; Aguirre et al., 2017). The lithology of Gordon Gulch is dominated by biotite-gneiss (Dethier and Bove, 2011) and is forested with evergreen vegetation, primarily lodgepole pine (*Pinus contorta*) and ponderosa pine (*Pinus ponderosa*) (Dethier and Bove, 2011; Barnes et al., 2012). Despite the low MAP, Boulder Creek CZO regolith is moderately weathered, on the basis of Ca, K depletion and presence of neoformed kaolinite (Condie et al., 1995; Dethier and Bove, 2011). Stream water samples were collected under baseflow conditions from the permanent flowing river in Gordon Gulch in March and April of 2017, using acid washed HDPE bottles following USGS water sampling techniques (United States Geological Survey [USGS], 2006).


**FIGURE 1 |** Map of Boulder Creek, Calhoun, Luquillo, and Southern Sierra CZOs investigated in this study.

### Calhoun CZO

The Calhoun CZO is located in the Southern Piedmont in South Carolina (**Figure 1**), within the Calhoun Experimental Forest, and has been extensively studied to inform researchers about land and water degradation caused by agricultural uses (e.g., Richter and Markewitz, 2001). The sampling location at Calhoun CZO is on a low relief hill, derived from granitic-gneiss. The climate is subtropical with a MAT of 16°C and a MAP of 1,250 mm year$^{-1}$ (**Table 1**). Vegetation is dominated by loblolly pine (*Pinus taeda*), mixed hardwoods (primarily oak, *Quercus* spp.), and hickory (*Carya* spp.) (Richter and Markewitz, 2001). This study focused on samples collected every 0.6 m within a 7.6 m weathering profile collected from Research Area 1. Details of the collection and processing of drill core samples can be found in Bacon et al. (2012). In brief, soil samples (0–6.0 m) were collected from three cores while regolith was sampled with a three-wing auger bit (6.1–18.3 m). Samples were crushed, sieved to <2 mm, and air-dried. Bacon et al. (2012) has noted regolith at Calhoun CZO is intensively weathered, on the basis of Ca, K depletion in the upper 10 m. Stream water samples were collected under baseflow conditions from the nearest flowing surface water source, Watershed 4 stream, in March and April, 2017 using acid washed HDPE bottles following USGS water sampling techniques (United States Geological Survey [USGS], 2006).

### Luquillo CZO

The Luquillo CZO is located in the El Yunque National Forest in northeastern Puerto Rico (**Figure 1**), and has also been studied as a Long-Term Ecological Research site and a USGS Water, Energy, and Biogeochemical Budgets (WEBB) site. The Luquillo CZO is a tropical montane forest and has a MAT of 21°C (Murphy et al., 2012). Precipitation increases with elevation from 2,500 to 4,500 mm year$^{-1}$ (Garcia-Martino et al., 1996). This paper focuses on the Guaba study site, a montane ridge that receives a MAP of 4,200 mm year$^{-1}$ and is located 680 m.a.s.l. in the Rio Icacos watershed (**Table 1**) (Murphy et al., 2017). The most abundant tropical vegetation at the Guaba study site were *Dacryodes excelsa*, *Prestoea montana*, *Sloanea berteroana*, *Cordia borinquensis*, *Manilkara bidentata*, *Schefflera morototoni*, *Cecropia schreberiana*, *Micropholis garciniifolia*, *Henriettea squamulosa*, and *Quararibea turbinate* (Weaver and Gould, 2013). Surface soil (top 0.3 m of regolith) and upper regolith samples were collected in 2017 down to 1.8 m depth. Deeper regolith samples were subsampled in 2010 from archived material from site LG1 (Buss et al., 2005, 2017) and borehole LGW1 (Buss and White, 2012; Orlando et al., 2016). In total, eleven regolith samples were analyzed. Samples were spaced

**TABLE 1 |** Climate, ecosystem, and geologic properties of sampling sites for the four Critical Zone Observatories (CZO).

| Study area | | Mean elevation m.a.s.l | Latitude | Longitude | MAT °C | MAP mm year$^{-1}$ | Vegetation | Soil | Bedrock |
|---|---|---|---|---|---|---|---|---|---|
| Boulder Creek CZO | Gordon gulch watershed | 2,716 | 40° 01′ 09″ N | 105° 28′ 39″ W | 4 | 735 | Evergreen forest | Inceptisols | Granite-gneiss |
| Calhoun CZO | Research Area 1 – Watershed 1 | 124 | 34° 36′ 23.6″ N | 81° 43′ 24.8″ W | 16 | 1,250 | Pine-hardwood | Ultisols | Granitic gneiss |
| Luquillo CZO | Rio Icacos watershed | 680 | 18° 17′ 02″ N | 65° 47′ 20″ W | 21 | 4,200 | Tropical forest | Inceptisols | Quartz diorite |
| Southern Sierra CZO | Providence Creek – P301 | 1,250 | 37° 03′ 36″ N | 119° 11′ 27″ W | 9 | 1,100 | Coniferous | Inceptisols | Granodiorite |

every 0.4 m down to 1.8 m depth, with three deeper samples collected at 3.1 m, 4.2 m, and 8.6 m depth. An intact regolith sample was collected from 1.8 m depth, at the surface soil-regolith interface. Regolith at Luquillo CZO is intensively weathered, on the basis of Fe and base cation depletion throughout the upper 6 m (Buss et al., 2005, 2017). Stream water samples were collected under baseflow conditions (White et al., 1998; Pett-Ridge et al., 2009) from the Rio Icacos in February and March of 2017 using acid washed HDPE bottles following USGS water sampling techniques (United States Geological Survey [USGS], 2006).

### Southern Sierra CZO

The Southern Sierra CZO is located in Fresno County, California (**Figure 1**), within the Kings River Experimental Watershed (KREW), a long-term research site established by the Pacific Southwest Research Station of the United States Forest Service (Hunsaker and Eagan, 2003). The Southern Sierra CZO lies outside the limits of recent glaciation and is characterized by a sequence of parallel ridges and valleys, with alternating steep and gentle terrain of granitic bedrock. We focused on site P301 at the head of Providence Creek, which has a montane-steppe climate with a MAT of 9°C and a MAP of 1,100 mm year$^{-1}$ (**Table 1**). The topography is a 0.75 km wide valley with moderate to steep relief. Vegetation is dominated by a mixed-coniferous forest consisting of *Abies concolor*, *Pinus ponderosa*, *Pinus jeffreyi*, *Quercus kelloggii*, *Pinus lambertiana*, and *Calocedrus decurrens*, with intermixed chaparral. Eleven samples were collected using a Geoprobe® every 1.0 m down to 11.0 m in 2011 (Holbrook et al., 2014). Based upon the shallow depth of soil and high variability in regolith depth consistent with chemical weathering-limited regolith formation, we consider regolith at Southern Sierra CZO to be weak to moderately weathered (Bales et al., 2011). Stream water samples were collected above baseflow conditions from Providence Creek 301 in March and April of 2017 (see Godsey and Kirchner, 2014) using acid washed HDPE bottles following USGS water sampling techniques (United States Geological Survey [USGS], 2006).

## Elemental Analyses

### Extractions and Total Digestions of Regolith Samples

A two-step sequential extraction was performed to quantify organic bound and secondary oxide fractions. Subsamples of regolith from the four CZOs were dried at 105°C and then pulverized in a boron carbide mortar and pestle to <100 μm. Two grams of regolith was weighed into 50 mL centrifuge tubes. First, organic matter and amorphous oxide bound elements were collected by adding 5 mL of 30% $H_2O_2$ to oxidize organic matter and then extracting the soil solution with 10 mL of 0.01 M acetic acid to target amorphous and short-range-ordered Al-, Mn-, and Fe- (oxyhydr)oxides. The solution was centrifuged at 7,000 rpm for 45 min and decanted. This was repeated with two washes of 10 mL of deionized water, which were added to the total extract. For the secondary Fe oxide fraction of Mo, Cr, and V, the remaining soil was treated with citrate–bicarbonate–dithionite (CBD) following the methods described in Mehra and Jackson (1960), which focuses on the dissolution of crystalline Fe oxides such as goethite and hematite without dissolution of Fe-bearing silicates. In brief, 40 mL of analytical grade 0.3 M sodium citrate and 5 mL of analytical grade 1 M sodium bicarbonate was added to the dry samples. The tubes were heated to 60°C and 1 g of analytical grade sodium dithionite was added. After 45 min of reaction, samples were centrifuged at 3,500 rpm for 30 min and the supernatant was collected, filtered to <0.4 μm, and diluted with deionized water. For every batch of samples, a blank, duplicate, and a standard reference material (SRM) was included. Montana Soil 2711 from the National Institute of Standards and Technology was used as a standard reference material (SRM).

For total sample digestion, 100 mg of dried, pulverized regolith were dissolved in 5 mL of 25 M HF acid and 5 mL of distilled 16 M $HNO_3$ (Trace metal grade, VWR Analytical, Radnor, PA, United States) at 130°C in sealed 30 mL Teflon PFA vials for 48 h or longer as needed with quartz-rich samples. After complete digestion of visible materials, samples were dried to a powder and redissolved in 0.5 M $HNO_3$. For every batch of samples, a blank, duplicate, and two SRMs [W-2 diabase and G-2 granite from the United States Geological Survey (USGS)] were included with every 20 samples to monitor reproducibility.

### ICP-MS Analyses

Regolith digests and extracts were diluted with deionized water and analyzed for trace metals with an Element 2 ICP-MS (Thermo-Scientific, Waltham, MA, United States). Recoveries for total digests of Mo, V, Cr, Fe, and Ti were 81–103% of certified values. The variation between intra-sample duplicates was <6% and Ti

concentrations in the preparation blank samples were $<0.01\ \mu g\ g^{-1}$.

Stream water samples were collected from each CZO under baseflow conditions between February and April 2017. Stream water samples were collected using acid-washed LDPE plastic bottles, filtered to $<0.45\ \mu m$ and acidified to pH 1 with trace metal grade $HNO_3$. Stream water samples were analyzed for trace metals using an Agilent 8800 triple quadrupole (QQQ) ICP-MS at the Dartmouth College Trace Element Analysis Laboratory (Agilent Technologies, Santa Clara, CA, United States). The QQQ-ICP-MS was calibrated using NIST traceable single and multi-element standards containing Sc, Ge, Y, In, Rh, Te, and Bi as internal standards. Ten point calibration curves were constructed for each analyte with correlation coefficient criteria $>0.99$. The calibration was followed by an Initial Calibration Blank (IBC) and an Initial Calibration Verification (ICV). Acceptance criteria for the ICV and CCV are $\pm 10\%$. The CCV was run after every 10 samples. Analytical duplicates and spikes were performed every 20 samples. Spike recoveries were 93–101% for Mo, 91–99% for Cr, and 95–102% for V. Coefficient of variations (CVs) for duplicates were <5% for Mo, Cr V, Fe, and Ti.

### Micro X-Ray Fluorescence Mapping

The goal of the synchrotron-based Micro X-ray Fluorescence analysis (μ-XRF) was to elucidate whether V and Cr were located in primary minerals or secondary Fe oxide minerals. Molybdenum was not imaged due to its low concentration. Intact regolith samples were only collected from the Guaba Ridge site of the Luquillo CZO in February 2017 at the soil-regolith interface (1.8 m depth). The regolith sample was oven dried at 70°C and cemented in place using a room-temperature-curing epoxy-resin (EPO-TEK 301-2FL). The hardened soil columns were cut into 15 mm thick sections and wet polished using silicon carbide starting at 240 grit. Minimizing the amount of deionized water and decreasing the total amount of time samples spent wet-polished were taken to limit dissolution or disturbance of minerals, particularly the weathered rind, and water soluble elements. The weathering zone of the regolith was analyzed by μ-XRF imaging at the Cornell High Energy Synchrotron Source (CHESS) on the F3 bending-magnet beamline. At CHESS, a 20 μm beam (incident energy of 17 KeV) with an incident flux of $\sim 3 \times 10^9$ photons $s^{-1}$ at the sample was used. The detector was mounted at 90° with respect to the incident X-ray beam and samples were mounted at 45° to the incident beam and scanned through the X-ray beam. The Vortex silicon drift detector with a Digital X-ray Processor (DXP) for digital signal processing to detect fluorescent X-rays. X-ray spectra were fitted for elements and quantified using the PyMCA software package (Solé et al., 2007).

### Total Carbon Quantification

Soil carbon data was obtained for each CZO: Calhoun (Fimmen et al., 2008; Bacon et al., 2012), Luquillo (Buss et al., 2005), and Southern Sierra (Tian, 2018). Total organic C (TOC) concentrations in soil and regolith samples were measured for Boulder Creek CZO samples using a Carlo-Erba Elemental Analyzer. In brief, $6 \pm 1$ mg subsamples <0.5 mm were combusted. Every 20 samples included one blank, one Atropine SRM, and a duplicate. TOC concentrations in Atropine SRMs were within 3% of its certified value and <10% relative percent difference. Soils were treated with 0.1 mM HCl acid to remove C from carbonates. Values for Boulder Creek CZO were comparable with surface soils from Eilers et al. (2012).

## Data Analyses

We tested the associations of TOC and secondary Fe oxide with total Mo, V, and Cr concentrations and concentrations within secondary Fe oxide phase using linear regressions for each CZO. All regressions were performed using Matlab (Matlab, 2016, Mathworks, Natick, MA, United States). For elemental concentrations, error bars were propagated based upon the coefficient of variation for each sample measurement and the standard error measured through duplicate and triplicate samples.

Mass transfer coefficients (τ) of Mo, V, and Cr were calculated to assess the degree of chemical weathering for specific elements using Ti as an index element (Brantley and Lebedeva, 2011). Mass transfer coefficients are defined for the element of interest (Mo, V, and Cr) (*j*) in the soil or regolith sample normalized to an immobile index element Ti (*i*) in the parent material:

$$\tau_{j,w} = \frac{C_{j,w} C_{i,p}}{C_{j,p} C_{i,w}} - 1 \quad (1)$$

where $C_{j,w}$ and $C_{i,w}$ are total concentrations of the element of interest (Mo, V, and Cr) and Ti in the soil and regolith samples, respectively, and $C_{j,p}$ and $C_{i,p}$ are the element of interest and index element concentrations in the least weathered regolith material (e.g., Brimhall and Dietrich, 1987; Kraepiel et al., 2015). Negative τ values indicate a net loss of an element from a specific soil depth due to leaching. Positive τ values indicate a net enrichment of an element. Although Ti can be mobilized at strongly acidic, heavily weathered tropical soils (Kurtz et al., 2000), application of Ti-based mass transfer coefficients is effective for estimating relative losses and gains in the CZOs of our study.

Stream water concentrations were grouped across collection dates and compared across the four CZOs using the Kruskal–Wallis non-parametric tests. Using measured watershed area and mean annual stream discharge, we calculated the export of Mo, V, and Cr at each of the four CZOs. To accomplish this, we obtained the total watershed area, MAP, and mean annual discharge for each of the four CZOs from existing online data[1] (accessed May 2018). Stream water Mo, V, and Cr concentrations were multiplied by total discharge to estimate export rates for each element.

[1] criticalzone.org

# RESULTS

## Regolith Profiles

Regolith profiles exhibited a range of TOC and secondary oxide Fe with depth across the four CZOs. Overall, %TOC decreased with depth from approximately 1% down to 0.1% with subsurface peaks present at all four CZOs (**Figure 2**). Calhoun CZO had <0.1 %TOC below 2 m depth, which was lower than the other three CZOs (**Figure 2**). Total Fe was relatively constant with depth at Boulder Creek and Southern Sierra CZOs. Subtropical Calhoun CZO had low total Fe concentrations in the surface soils while tropical Luquillo CZO had higher total Fe concentrations above 2 m depth (**Figure 2**). Secondary oxide Fe concentrations were highest throughout the regolith profile at Luquillo CZO by nearly two orders of magnitude compared to Boulder Creek and Southern Sierra CZOs (**Figure 2**). Calhoun CZO had a subsurface peak of secondary oxide Fe concentration between 1 and 1.5 m depth (**Figure 2**).

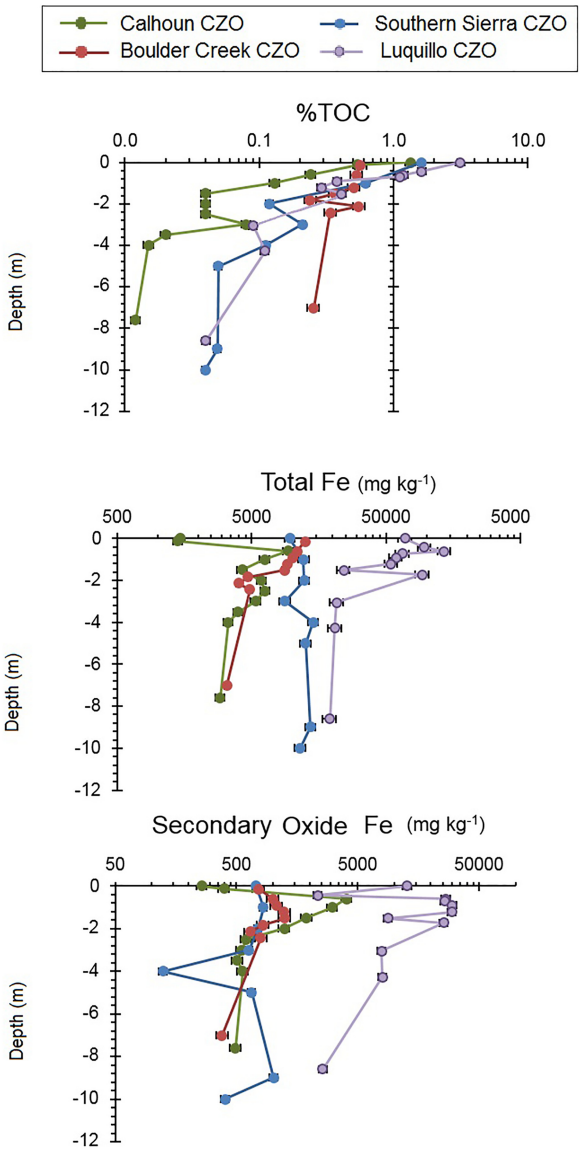


**FIGURE 2 |** Regolith profiles of Mo, V, and Cr concentrations in total digests and two extractions of secondary Fe oxide bound (citrate–bicarbonate–dithionate) and organic + amorphous oxide bound at the four CZOs. Error bars are coefficients of variation for each measurement. Please note each scale is different for each phase fraction.

Total Mo profile concentrations ranged from 0.4 to 2.5 mg $kg^{-1}$ across the four CZOs (**Figure 3** and **Supplementary Table 1**). The highest total Mo concentrations at the Calhoun and Luquillo CZOs were in the surface soils, at 0.6 m and 0.4 m in depth, respectively. The colder, higher elevation Boulder Creek and Southern Sierra CZOs had their highest total Mo concentrations deeper in the regolith, at 2.4 m and 4 m in depth, respectively. Total V profiles exhibited two orders of magnitude variation in concentrations across regolith profiles. Total V concentrations were highest in the top meter for Boulder Creek, Luquillo, and Calhoun CZOs, and were generally consistent with depth at the Southern Sierra CZO. Total Cr concentrations at the Calhoun CZO had subsurface peaks of total Cr between 2.0 and 4.0 m. Boulder Creek exhibited a significant total Cr peak between 1.0 and 2.0 m, which decreased with depth. Southern Sierra and Luquillo CZO exhibited nearly homogeneous (±3 mg $kg^{-1}$) total Cr profiles with depth.

In the regolith, organic matter and amorphous oxide bound Mo, V, and Cr were substantially lower than their respective secondary oxide and total concentrations. Across the four CZOs, organic matter and amorphous oxide bound Mo ranged between 0.01 and 0.13 mg $kg^{-1}$ (**Supplementary Table 2**), which on average was 0.5–0.9% of the total Mo concentration (**Supplementary Table 4**). The organic matter and amorphous oxide bound fraction of Mo were greatest near the surface (<1 m depth) for Calhoun and Southern Sierra CZOs while Boulder Creek and Luquillo CZOs had subsurface peaks (>2 m depth). Vanadium varied between 0.11 and 3.1 mg $kg^{-1}$ (**Supplementary Table 2**), which on average was 0.3–2.1% of the total V concentration (**Supplementary Table 4**). The organic matter and amorphous oxide bound fraction of V were greatest near the surface (<1 m depth) for Luquillo and Southern Sierra CZOs while Boulder Creek and Calhoun CZOs exhibited subsurface peaks (**Figure 3**). Organic bound Cr concentrations ranged between 0.01 and 1.07 mg $kg^{-1}$ (**Supplementary Table 2**), which on average was 0.9–3.5% of the total Cr concentration (**Supplementary Table 4**). Organic matter and amorphous oxide bound Cr was greatest in the top 2 m of regolith at Luquillo and Southern Sierra CZOs but were greater below 2 m in depth at Boulder Creek and Calhoun CZOs (**Figure 3**).

Secondary Fe oxide Mo concentrations ranged between 0.02 and 0.68 mg $kg^{-1}$ (**Supplementary Table 3**), which on average was 6.6–40.1% of the total Mo concentration (**Supplementary Table 5**). Vanadium concentrations in the secondary Fe oxide ranged between 1 and 52 mg $kg^{-1}$ (**Supplementary Table 3**), which on average was 6.0–39.7% of the total V concentration (**Supplementary Table 5**). Secondary Fe oxide Cr concentrations varied between 0.2 and 8.7 mg $kg^{-1}$, which on average was 13.0–40.5% of the total Cr concentrations (**Supplementary Table 5**).

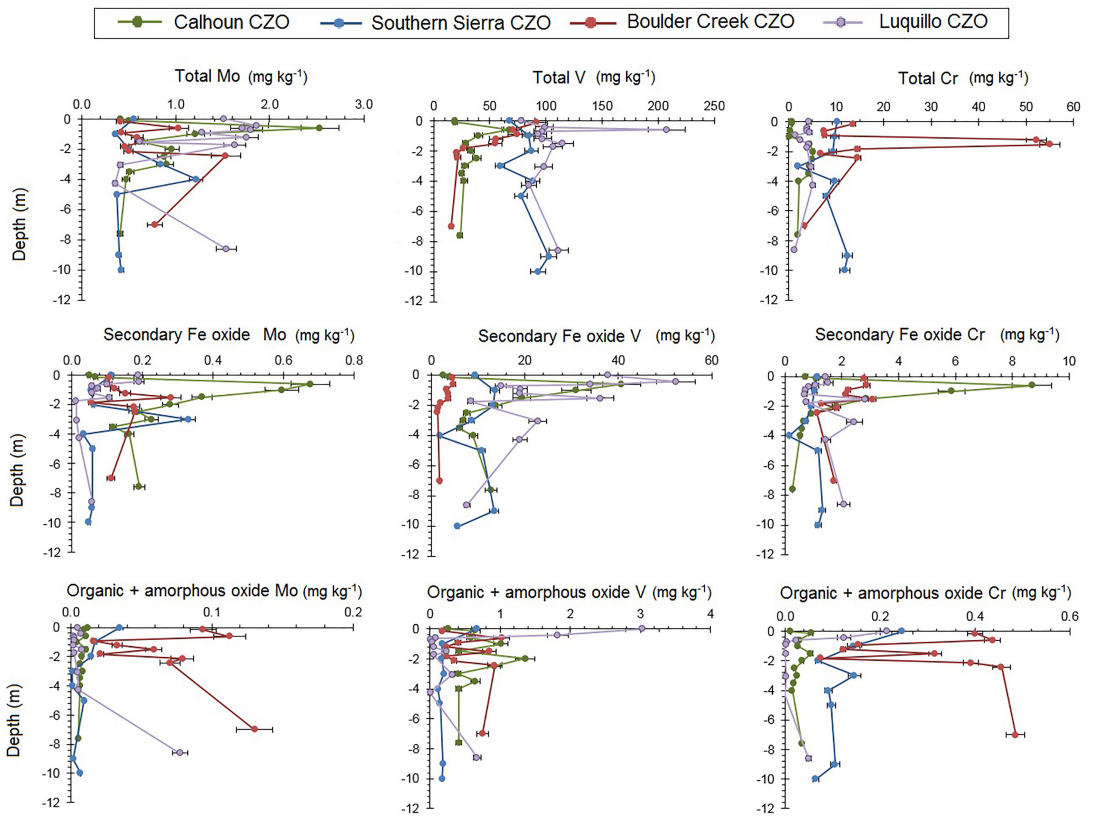


**FIGURE 3 |** Regolith profiles of TOC, total Fe, and secondary oxide Fe concentrations in total digests and secondary oxide extractions (citrate–bicarbonate–dithionate) at four CZOs. Note the different logarithmic scales for *X*-axes. Error bars are coefficients of variation.

Using Pearson correlations, we observed that total Mo, V, and Cr were correlated with secondary oxide Fe concentrations [a proxy for long-range ordered to crystalline Fe oxy(hydr)oxides] (**Table 2**). At Calhoun CZO, secondary oxide and total Mo, V, and Cr concentrations were positively correlated with secondary oxide Fe concentrations. For Southern Sierra CZO, secondary oxide V and Cr were positively correlated with secondary oxide Fe concentrations. At Boulder Creek CZO, secondary oxide and total concentrations of V and Cr were negatively correlated with both secondary oxide Fe and TOC. At Luquillo CZO, secondary oxide Mo and V were positively correlated with %TOC.

## Mass Transfer Coefficients and μ-XRF Mapping

Calculated tau values for Mo, V, and Cr show both net enrichment and depletion across the CZOs (**Figure 4**). At the montane coniferous Boulder Creek CZO, regolith down to 2.0 m depth were depleted in Mo and V, but Cr was enriched below 1.0 m

**TABLE 2 |** Pearson correlation coefficients for linear regressions between secondary Fe oxide and %TOC with secondary Fe oxide and total Mo, V, and Cr at each of the four CZOs.

| Study area | | Secondary oxide Mo | Secondary oxide V | Secondary oxide Cr | Mo total | V total | Cr total |
|---|---|---|---|---|---|---|---|
| Calhoun CZO | Secondary oxide Fe | 1.0** | 1.0** | 1.0** | 0.9** | 0.9** | 0.6* |
| | % TOC | −0.3 | −0.2 | −0.1 | −0.1 | −0.3 | −0.3 |
| Southern Sierra CZO | Secondary oxide Fe | 0.1 | 0.9** | 0.8* | −0.7* | 0.5* | 0.5* |
| | % TOC | 0.1 | 0.1 | 0.2 | −0.1 | −0.4 | 0.1 |
| Boulder Creek CZO | Secondary oxide Fe | 0.4 | 0.6* | 0.5* | −0.1 | 0.5* | 0.7* |
| | % TOC | 0.1 | 0.6* | 0.6* | −0.2 | 0.6* | 0.6* |
| Luquillo CZO | Secondary oxide Fe | −0.1 | −0.2 | −0.8* | 0.4 | 0.3 | −0.2 |
| | % TOC | 0.8* | 0.6* | −0.2 | 0.4 | 0.0 | 0.3 |

** *indicates* $P < 0.01$ *and* * *indicates* $P < 0.05$.

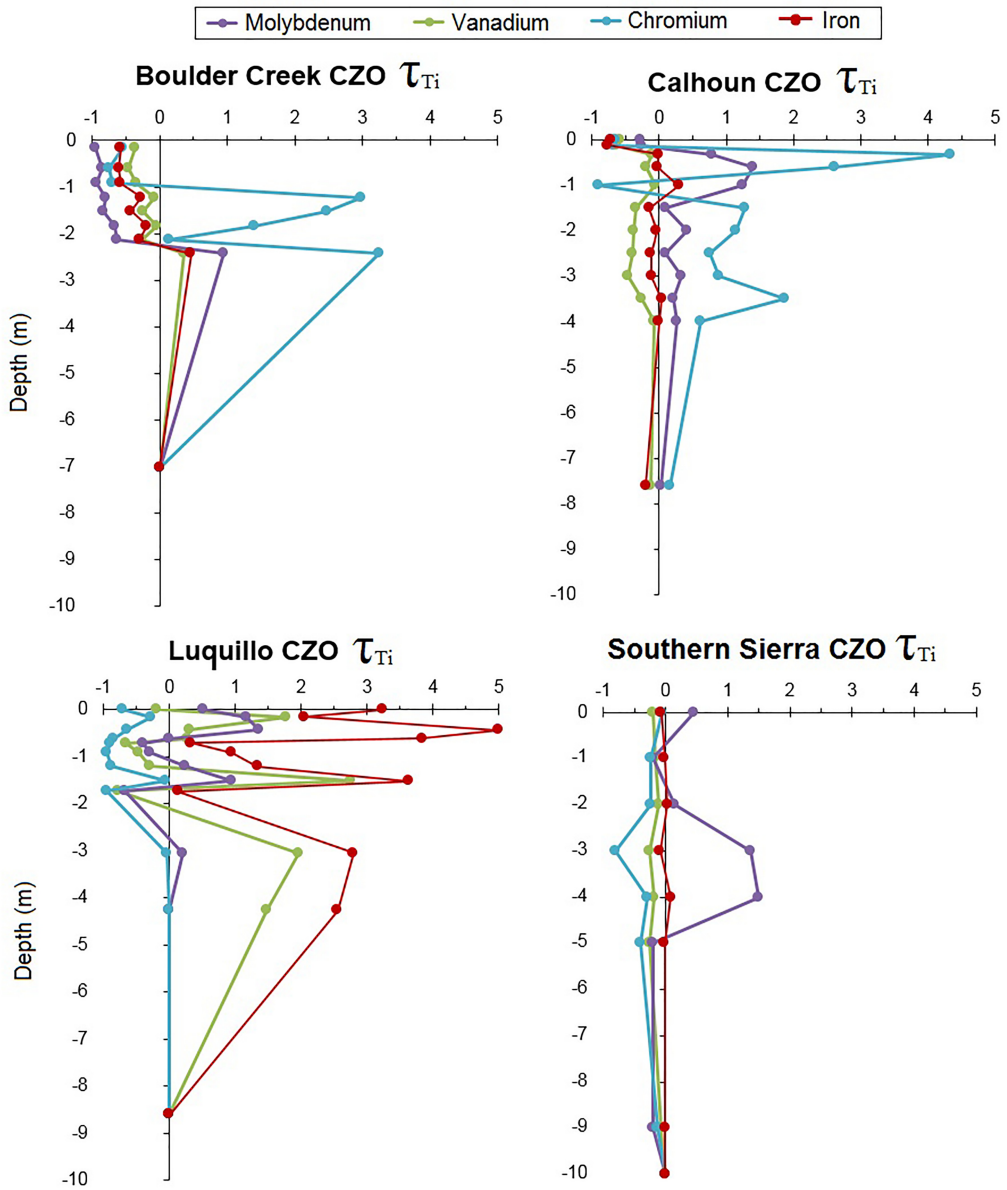


**FIGURE 4 |** Mass transfer coefficients (τ) for Mo, V, Cr, and Fe for regolith profiles at each CZO, using Ti as the indexing element.

depth. At the subtropical Calhoun CZO, V was depleted while Mo and Cr were enriched throughout the regolith profile. The tropical Luquillo CZO showed a wide variation but overall Cr was depleted throughout the entire profile while Mo and V were enriched at certain depths. The Southern Sierra CZO regolith profile was depleted in V and Cr but enriched in the surface and subsurface between 2.0 and 5.0 m depth.

Analysis of the μ-XRF spectra for the weathered regolith from Luquillo CZO showed Fe, V, and Cr coinciding together in hornblende and biotite primary minerals (Buss et al., 2005, 2017). This is particularly observable in the upper left-hand corner of the images and the outlines of the hornblende minerals are distinguishable in all four images. Moreover, Fe, V, and Cr also correspond with each other in the Fe oxide weathering rind on the right side of the image (**Figure 5**). More information on the weathering rinds of quartz diorite from Luquillo CZO is available in Buss et al. (2008).

## Stream Water Concentrations

Overall, stream water concentrations of oxyanions were generally comparable across CZOs (**Table 3** and **Figure 6**), but there were a few significant differences. Stream water V concentrations were similar across CZOs and ranged between 0.04 and 0.70 μg $L^{-1}$ (**Figure 6**). Stream water Cr concentrations at Calhoun and Boulder Creek CZOs were significantly than at the Southern

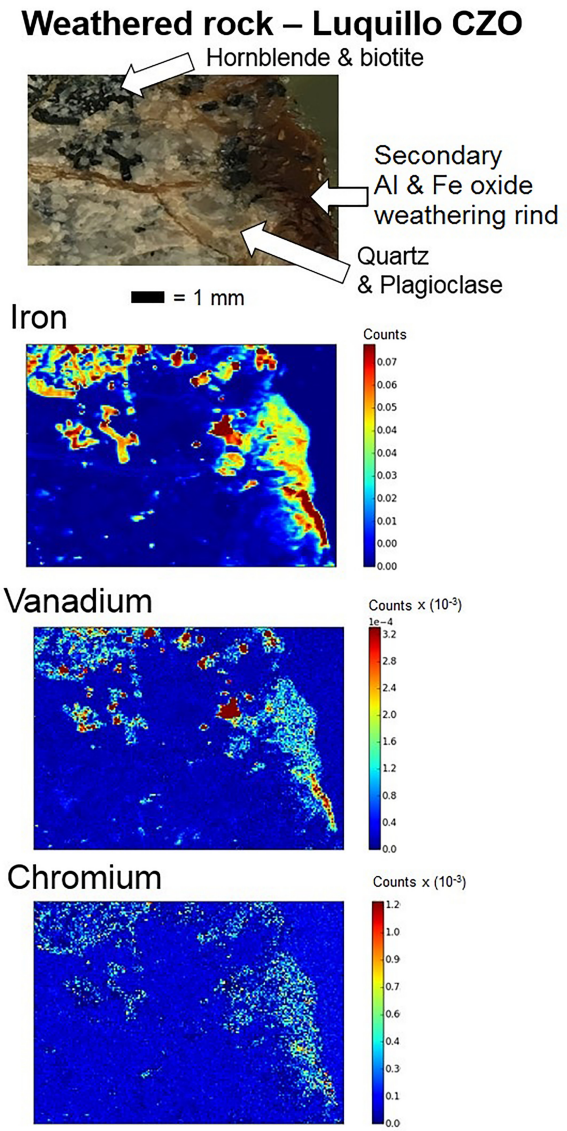


**FIGURE 5 |** Images of intact regolith from Luquillo CZO at 1.6 m depth and μ-XRF maps of Fe, V, and Cr using Synchrotron radiation at the Cornell High Energy Synchrotron Source (CHESS) Beamline F3. Molybdenum was not imaged.

Sierra and Luquillo CZOs (**Table 3** and **Figure 6**) using the non-parametric Kruskal–Wallis Test ($p < 0.05$). Stream water Mo concentrations were significantly higher at Boulder Creek and Calhoun CZOs compared to Southern Sierra CZO ($p < 0.05$, **Table 3** and **Figure 6**).

We compared the concentration of oxyanions in the stream water to the deepest, least weathered regolith to determine if variations in lithology explained the differences in stream water concentrations across CZOs and among oxyanions. In **Figure 7**, Mo stream water to regolith ratios were significantly greater at subtropical Calhoun and tropical Luquillo CZOs than montane Southern Sierra and Boulder Creek CZOs. In addition, Mo stream water to regolith ratios at Calhoun, Luquillo, and Southern Sierra CZOs were significantly greater than V and Cr ratios. Stream water to regolith ratios for V were not significantly different for Boulder Creek, Calhoun, and Luquillo CZOs but were greater than at Southern Sierra CZO. In addition, Stream water to regolith ratios for V were generally lower than Mo and Cr across CZOs (**Figure 7**). Stream water to regolith ratios for Cr were significantly higher at Calhoun CZO than the other three CZOs. Similarly, stream water to regolith ratios for Cr were significantly higher at Boulder Creek CZO than Luquillo and Southern Sierra CZOs.

# DISCUSSION

## Weathering and Partitioning of Mo, V, and Cr

Our results support the hypothesis that deep regolith play a substantial role in sorption of oxyanions. Overall, both surface soils (<0.3 m depth) and deeper regolith served as important sources and retainers of oxyanions. We observed many peaks in Mo, V, and Cr in both the organic matter and amorphous oxide and the secondary Fe oxide extractions at depths are far deeper than typical 0.3–1 m depth investigated for oxyanion sorption and weathering in soils (e.g., Shiller and Mao, 2000; Wichard et al., 2009; Wisawapipat and Kretzschmar, 2017). For example, at the montane regolith of Southern Sierra CZO had >39% of Mo and Cr were in the secondary Fe oxide fraction from 3 to 4 m in depth and the tropical forest Luquillo CZO, 52% of Cr and 23% of V were in the secondary Fe oxide fraction at 3 m in depth.

In addition, enrichment and depletion of oxyanions >2 m in depth indicated that regolith played both a significant role in the sorption and retention of oxyanions (**Figure 4**). Except for Cr, Boulder Creek CZO demonstrated the most depletion of oxyanions, extending down 2 m in depth (**Figure 4**). This is particularly important as the mountain-steppe Boulder Creek CZO has the least intensive weathering environment with the lowest MAP and MAT, but due to its long exposure, has been moderate to extensively weathered. The more tropical regolith profiles at Calhoun and Luquillo CZOs show much more complicated patterns of accumulation and depletion (**Figure 4**), likely due to variations in retention as described later in this section.

These results support other weathering observations by Dethier and Bove (2011) at Boulder Creek CZO, Bacon et al. (2012) at Calhoun CZO, and Buss et al. (2005) at Luquillo CZO. Subtropical Calhoun CZO and tropical Luquillo CZO were the most weathered regolith profiles and had the highest accumulations of secondary Fe oxides (**Figure 2**), consisting of hematite and goethite as observed by Buss et al. (2005); Fimmen et al. (2008), and Dethier and Bove (2011). In addition, neoformed kaolinite was present at the previously mentioned CZOs at >4% by mass (Fimmen et al., 2008 at Calhoun CZO; Dethier and Bove, 2011 at Boulder Creek CZO; Buss et al., 2017 at Luquillo CZO) demonstrating their extensive weathering history. The extent of weathering corresponded with the sorption of oxyanions throughout the regolith profiles. Southern Sierra had

**TABLE 3 |** Stream water export estimates for dissolved Mo, V, and Cr across the four CZOs.

| | Boulder Creek CZO Gordon Gulch watershed | Calhoun CZO Watershed 4 | Luquillo CZO Rio Icacos watershed | Southern Sierra CZO Providence Creek |
|---|---|---|---|---|
| Watershed size ($km^2$) | 2.77 | 0.07 | 3.14 | 0.99 |
| Mean annual precipitation (m) | 0.74 | 1.25 | 4.20 | 1.10 |
| Water annual flux ($m^3$) | $2.4 \times 10^5 \pm 1.2 \times 10^5$ | $2.5 \times 10^4 \pm 1.7 \times 10^4$ | $1.3 \times 10^7 \pm 3.1 \times 10^6$ | $4.0 \times 10^5 \pm 3.4 \times 10^4$ |
| Mean Mo concentrations ($\mu g\ L^{-1}$) | $0.06 \pm 0.01$ | $0.08 \pm 0.02$ | $0.06 \pm 0.03$ | $0.02 \pm 0.01$ |
| Mean V concentrations ($\mu g\ L^{-1}$) | $0.50 \pm 0.04$ | $0.43 \pm 0.0$ | $0.60 \pm 0.24$ | $0.33 \pm 0.05$ |
| Mean Cr concentrations ($\mu g\ L^{-1}$) | $0.27 \pm 0.02$ | $0.18 \pm 0.03$ | $0.08 \pm 0.02$ | $0.10 \pm 0.01$ |
| Mo flux† (mg $year^{-1}$) | $9.8 \times 10^2 \pm 4.3 \times 10^2$ | $1.9 \times 10^3 \pm 5.1 \times 10^2$ | $1.2 \times 10^6 \pm 4.1 \times 10^5$ | $8.0 \pm 2.5$ |
| V flux† (mg $year^{-1}$) | $8.4 \times 10^3 \pm 2.9 \times 10^3$ | $1.1 \times 10^4 \pm 3.1 \times 10^3$ | $7.8 \times 10^6 \pm 2.2 \times 10^6$ | $1.3 \times 10^2 \pm 4.9 \times 10^1$ |
| Cr flux† (mg $year^{-1}$) | $9.3 \times 10^3 \pm 3.7 \times 10^3$ | $4.4 \times 10^3 \pm 1.2 \times 10^3$ | $6.5 \times 10^5 \pm 3.4 \times 10^5$ | $40 \pm 18$ |

*Averages are given ± one standard error. †The flux estimates are based upon baseflow oxyanion concentrations. Here, we assumed oxyanions were isostatic, which may not necessarily be applicable for each element at all of the CZOs.*

lower secondary Fe oxide fractions of Mo, Cr, and V compared to the other three CZOs. Moreover, secondary oxide Mo, Cr, and V were greater in regolith with higher secondary Fe oxide concentrations at much warmer and wetter Calhoun and Luquillo CZOs when compared to the colder and drier Boulder Creek CZO. Thus, we conclude that weathering has influenced the formation and retention of oxyanions with secondary Fe oxides.

A generalized trends across the three oxyanions were present, demonstrating some linkages between weathering intensity and climate with the sorption of oxyanions to secondary Fe oxides. Total Mo, secondary Fe-bound Mo and organic and amorphous oxide bound Mo concentrations were comparable across the four CZOs, suggesting weathering intensity nor lithology did not strongly influence Mo in the soil and regolith profiles. Secondary oxides did not appear to play a dominant role for Mo retention at Luquillo CZO as total Mo was not correlated with secondary Fe oxides. Instead secondary oxide Mo was correlated with %TOC despite the fact that organic matter and amorphous oxide bound Mo was not a substantial fraction of the total Mo concentrations at any of the CZOs, generally ranging below 5%. This largely agrees with previous studies that the sorption and retention of Mo is dominated by both, secondary Fe oxides and organic compounds (e.g., Wichard et al., 2009; King et al., 2016, 2018). Due to the relatively small range in %TOC, there may not have been enough variability to capture the relationship between Mo and TOC.

Total V concentrations varied significantly across the CZOs (**Supplementary Table 1**), suggesting lithologic controls on the sourcing of V to the soil and regolith profiles. Secondary Fe oxide fraction of V, however, coincided with weathering intensity. Average secondary Fe oxide concentrations were highest for the more tropical Calhoun (14 mg $kg^{-1}$) and Luquillo CZO (26 mg $kg^{-1}$) compared to mountain-steppe Southern Sierra (9 mg $kg^{-1}$) and Boulder Creek CZOs (3 mg $kg^{-1}$). Vanadium exhibited significant linear relationships with secondary Fe oxide at Calhoun, Boulder Creek, and Southern Sierra CZOs. The substitution of V(III) for Fe(III) in minerals has been widely observed (Schwertmann and Pfab, 1996; Shiller and Mao, 2000; Wisawapipat and Kretzschmar, 2017) and V(II) and V(III) for Fe(II) and Fe(III) in primary Fe-silicate minerals during magmatic crystallization (e.g., Goldschmidt, 1954). Even though this relationship was not clearly observed at Luquillo CZO as with the other three CZOs using linear regressions with secondary Fe oxide, we did observe this relationship in μ-XRF maps of regolith samples. Our μ-XRF imaging of V in an intact weathering rind sample from Luquillo demonstrates its spatial distribution with Fe, both in primary minerals like hornblende and biotite and in secondary Fe oxides within regolith at Luquillo CZO.

Chromium concentrations exhibited a pattern similar to V. Total Cr concentrations were varied strongly with lithology but Cr concentrations in secondary Fe oxides appeared to be climate influenced. The more tropical Calhoun and Luquillo CZOs had higher % Cr in the secondary Fe oxide fraction than the montane-steppe Southern Sierra and Boulder Creek CZOs, suggesting intensive weathering promotes Cr sorption by secondary Fe oxides. The sorption of Cr by secondary Fe oxides and organic matter has been well observed by previous studies (e.g., Gustafsson et al., 2014; Pérez et al., 2014; Saputro et al., 2014).

Some potential variables that may explain the variation of oxyanions not explored here are the effects of erosion, atmospheric inputs, hydrological properties, and other source of sorption such as clay minerals and other oxides. Luquillo CZO differs from the other three CZOs due to its substantially greater annual precipitation (**Table 1**), which could not only flush and dissolve solutes at rates that may prevent sorption (see Dosseto et al., 2012) but also lead to increased atmospheric inputs of oxyanions in the surface soils (Marks et al., 2015; King et al., 2016). This may also influence τ values by enriching oxyanions at the surface and a net depletion due to leaching losses with depth. Nevertheless, the effect of atmospheric inputs on the deep regolith is likely minimal. In addition, Luquillo CZO undergoes more erosion in the form of landslides and surface soil erosion than the other three CZOs (Larsen, 2012). Lastly, Luquillo CZO also had much greater clay content in its soils and upper regolith than Calhoun, Boulder Creek, and Southern Sierra CZOs. Clays can provide an unaccounted source of oxyanion sorption capacity (Goldberg et al., 1996).

Our study observed low fractions of oxyanions in the organic bound and amorphous oxide phase and poor correlations

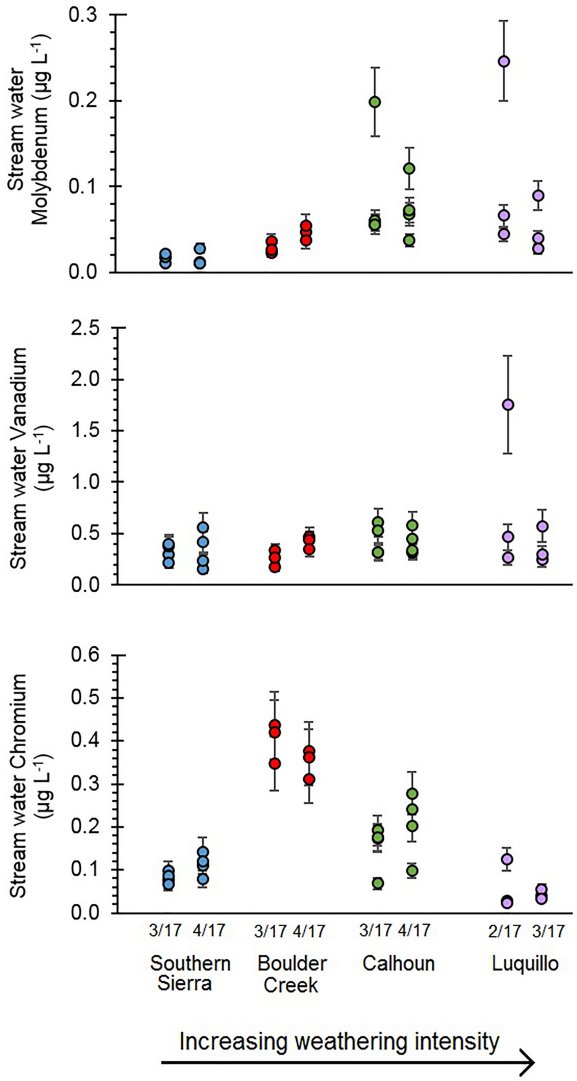


**FIGURE 6 |** Stream water oxyanions (Mo, V, and Cr) concentrations in solution. Samples were filtered to <0.45 µm. Error bars are coefficients of variation for each measurement.

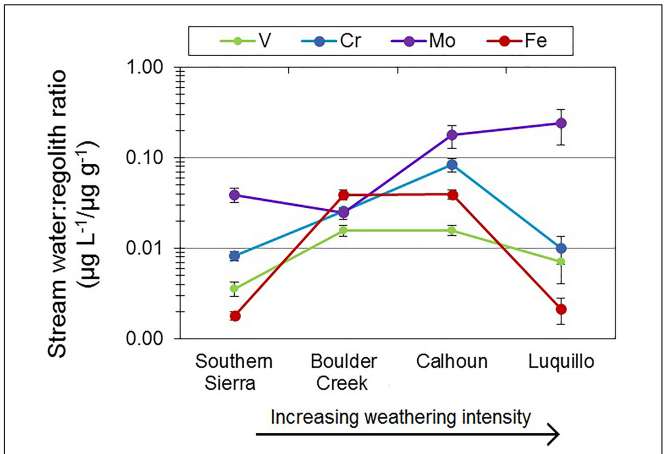


**FIGURE 7 |** Ratios of dissolved oxyanions in stream water to their respective concentrations in the least weathered regolith sample. Error bars are standard error.

between %TOC and oxyanion concentrations in the deep regolith. However, this conclusion should not be extrapolated to surface soils. Many previous studies have observed a significant relationship in surface soils and oxyanion concentrations (see Grove and Ellis, 1980; Wichard et al., 2009; King et al., 2014, 2016, 2018; Pérez et al., 2014; Marks et al., 2015; Siebert et al., 2015; King, 2017; Larsson et al., 2017; Wisawapipat and Kretzschmar, 2017). Therefore, sorption of oxyanions with organic matter may be most important spatially but not with depth into deep regolith (>2 m).

## Stream Water Export of Mo, V, and Cr

Oxyanion concentrations and export from the Critical Zone via stream water varied substantially across CZOs. The most intensively weathered regolith had higher average Mo concentrations in stream water (**Table 3** and **Figure 6**). However, Mo concentrations were generally comparable across CZOs when removing the outlier samples at Calhoun and Luquillo CZOs. Calhoun and Luquillo CZOs had higher Mo stream water to regolith ratios compared to V and Cr (**Figure 7**). This implies that Mo had lower relative retention in regolith, increasing its export by stream water compared to V and Cr at Calhoun and Luquillo CZOs. Alternatively, the stream water to regolith ratios increase with increasing MAP across the CZO (**Table 1** and **Figure 7**). This suggests that atmospheric inputs of Mo via precipitation (Marks et al., 2015; Siebert et al., 2015; King et al., 2016) may lead to increased export of Mo from the regolith. There may be additional transport processes influencing Mo transport such as colloidal Al, Fe, and Mn oxides and dissolved organic matter (Pearce et al., 2010; Trostle et al., 2016; Prouty et al., 2017), which can enhance its transport through soil. Furthermore, fine colloids <0.45 µm in solution may also be responsible for the two elevated Mo concentrations at Calhoun and Luquillo CZOs. When these high concentrations are not considered, Mo concentrations were similar. Thus, there is not a strong trend in Mo concentrations with weathering intensity but potential variability due to colloids was greatest at the most intensively weathered CZOs.

Few studies have examined the controls on V concentrations in stream water (Shiller and Boyle, 1987; Shiller, 1997; Shiller and Mao, 2000; Strady et al., 2009). Stream water V concentrations were not significantly different across the four CZOs (**Table 3**). The similarity in stream water to regolith ratio for V suggests that regolith at Boulder Creek, Calhoun, and Luquillo CZOs are weathering and exporting V at consistent rates. Further, the stream water to regolith V ratios were lower than Mo and Cr, suggesting that V is the least mobile of the three oxyanions during weathering (**Figure 7**). The elevated stream water V concentration measured in one sample at Luquillo CZO may be due to colloids, particularly DOC and Al and Fe particulates. Stream water to regolith ratios for V was not significantly different than Fe for each CZO, suggesting V export is directly

controlled with Fe movement. This may be as either dissolved or fine colloids <0.45 μm, the size of the filter pores used in this study (e.g., Pokrovsky and Schott, 2002; Gardner et al., 2017). Stream water Cr concentrations exhibited the greatest variation among the four CZOs. Boulder Creek CZO had the highest stream water Cr concentrations (**Table 3**). Moreover, Boulder Creek CZO had significantly higher stream water to regolith ratio, despite having the lowest MAT and lowest MAP compared with the other four CZOs in this study (**Figure 7**).

Using measured watershed area and mean annual stream discharge, we calculated the export of Mo, V, and Cr at each of the four CZOs. Luquillo CZO had Mo, V, and Cr fluxes ($10^5$ to $10^6$ mg year$^{-1}$) up to four orders of magnitude greater than the other CZOs ($10^2$ to $10^4$ mg per year) due to $10^2$ to $10^3$ times greater stream discharge than the other three CZOs. We observed that Boulder Creek CZO had greater Mo, V, and Cr fluxes than Southern Sierra CZOs, despite having lower MAP. Even when scaled for different watersheds size, Boulder Creek had >10× greater export of oxyanions per km$^2$. This highlights the importance that more weathered systems (based upon interpretation of mass transfer coefficients) export more oxyanions at greater rates than fresher regolith. It must be noted these approximations are based upon oxyanion concentrations in baseflow conditions. While this assumption might not hold for each of the oxyanions at the four CZOs, previous studies such as Shiller and Mao (2000), Aguirre et al. (2017) have found oxyanions can be isostatic with respect to concentration-discharge (CQ) dynamics. However, this provides an estimate in the variation of Mo, V, and Cr export via stream waters across different watershed with contrasting climates.

## CONCLUSION

Our study has shown that retention and sourcing of Mo, V, and Cr from regolith extends far below the depth that most typical soil studies examine. Depletion of Mo, V, and Cr extends several meters in depth at all four CZOs, from the montane-steppe Boulder Creek CZO to the tropical rainforest Luquillo CZO. Moreover, secondary Fe oxides containing Mo, V, and Cr are present beyond surface soils, extending down >8 m in depth and were important fraction of the total percentage. In particular, >25% of total Cr and V were in the secondary Fe oxide fraction at Luquillo and Calhoun CZO between 0 and 2 m depth.

Each of the three oxyanions exhibited a unique pattern in stream water samples. Total concentrations and regolith to stream water ratios of Mo and Cr exhibited significant variation among the four CZOs while V concentrations were similar across CZOs. Our regolith and stream water results highlight that each oxyanion has different geochemical pathways but share unifying principles across weathering and climate gradients. Identifying the upland causes for different oxyanion retention is key for developing Mo, V, and Cr as geochemical tools for understanding contemporary and paleo-terrestrial and marine global biogeochemical cycles.

## AUTHOR CONTRIBUTIONS

JR conducted laboratory experiments, analyzed, and interpreted data and shaped discussion. EK analyzed and interpreted data and shaped discussion.

## FUNDING

This work was made possible by the National Science Foundation Grant (NSF-1360760) to the Critical Zone Observatory Network National Office. Funding from the National Science Foundation for each CZO was also instrumental for each CZO studied in this project: Boulder Creek (NSF-1331828), Calhoun (NSF-1331846), Luquillo (NSF-1331841), and Southern Sierra (NSF-1331939).

## ACKNOWLEDGMENTS

We are thankful for help with obtaining samples from Erin Stacy (UC Merced), Stephen Hart (UC Merced), Scott Hynek (Penn State), Sue Brantley (Penn State), and Andy Kurtz (Boston University). We are thankful for the UC Angelo Coast Range Reserve and the analytical help from Brian Jackson (Dartmouth College). CHESS is supported by the NSF and NIH/NIGMS via NSF award DMR-1332208, and the MacCHESS resource is supported by NIH/NIGMS award GM-103485.

## SUPPLEMENTARY MATERIAL

The Supplementary Material for this article can be found online at: https://www.frontiersin.org/articles/10.3389/feart.2018.00193/full#supplementary-material

## REFERENCES

Adriano, D. C. (2001). *Trace Elements in Terrestrial Environments*. New York, NY: Springer, 219–261. doi: 10.1007/978-0-387-21510-5

Aguirre, A. A., Derry, L. A., Mills, T. J., and Anderson, S. P. (2017). Colloidal transport in the Gordon Gulch catchment of the Boulder Creek CZO and its effect on C-Q relationships for silicon. *Water Resour. Res.* 53, 2368–2383. doi: 10.1002/2016WR019730

Alloway, B. (2013). *Heavy Metals in Soil: Trace Metals and Metalloids in Soil and Their Bioavailability*. Reading: Springer. doi: 10.1007/978-94-007-4470-7

Amundson, R., Richter, D. D., Humphreys, G. S., Jobbágy, E. G., and Gaillardet, J. (2007). Coupling between biota and earth materials in the critical zone. *Elements* 3, 327–332. doi: 10.2113/gselements.3.5.327

Bacon, A. R., Richter, D. D., Bierman, P. R., and Rood, D. H. (2012). Coupling meteoric 10Be with pedogenic losses of 9Be to improve soil residence time estimates on an ancient North American interfluve. *Geology* 40, 847–850. doi: 10.1130/G33449.1

Bales, R. C., Conklin, M. H., Kerkez, B., Glaser, S., Hopmans, J. W., Hunsaker, C. T., et al. (2011). "Sampling strategies in forest hydrology and biogeochemistry," In *Forest Hydrology and Biogeochemistry: Synthesis of Past Research and Future*

*Directions*, eds D. F. Levia, D. Carlyle-Moses, and T. Tanaka (Dordrecht: Springer), 29–44. doi: 10.1007/978-94-007-1363-5_2

Barnes, R. T., Smith, R. L., and Aiken, G. R. (2012). Linkages between denitrification and dissolved organic matter quality, boulder creek watershed, Colorado. *J. Geophys. Res.* 117:G01014. doi: 10.1029/2011JG001749

Barron, A. R., Wurzburger, N., Bellenger, J. P., Wright, S. J., Kraepiel, A. M. L., and Hedin, L. O. (2008). Molybdenum limitation of asymbiotic nitrogen fixation in tropical forest soils. *Nat. Geosci.* 2, 42–45. doi: 10.1038/ngeo366

Brantley, S. L., Goldhaber, M. B., and Ragnarsdottir, K. V. (2007). Crossing disciplines and scales to understand the critical zone. *Elements* 3, 307–314. doi: 10.2113/gselements.3.5.307

Brantley, S. L., and Lebedeva, M. (2011). Learning to read the chemistry of regolith to understand the critical zone. *Annu. Rev. Earth Planet. Sci.* 39, 387–416. doi: 10.1146/annurev-earth-040809-152321

Brimhall, G. H., and Dietrich, W. E. (1987). Constitutive mass balance relations between chemical composition, volume, density, porosity, and strain in metasomatic hydrochemical systems: results on weathering and pedogenesis. *Geochim. Cosmochim. Acta* 51, 567–587. doi: 10.1016/0016-7037(87)90070-6

Buss, H. L., Bruns, M. A., Schultz, M. J., Moore, J., Mathur, C. F., and Brantley, S. L. (2005). The coupling of biological iron cycling and mineral weathering during saprolite formation, Luquillo Mountains, Puerto Rico. *Geobiology* 3, 247–260. doi: 10.1111/j.1472-4669.2006.00058.x

Buss, H. L., Chapela Lara, M., Moore, O. W., Kurtz, A. C., Schulz, M. S., and White, A. F. (2017). Lithological influences on contemporary and long-term regolith weathering at the Luquillo critical zone observatory. *Geochim. Cosmochim. Acta* 196, 224–251. doi: 10.1016/j.gca.2016.09.038

Buss, H. L., Sak, P. B., Webb, S. M., and Brantley, S. L. (2008). Weathering of the Rio Blanco quartz diorite, Luquillo Mountains, Puerto Rico: coupling oxidation, dissolution, and fracturing. *Geochim. Cosmochim. Acta* 72, 4488–4507. doi: 10.1016/j.gca.2008.06.020

Buss, H. L., and White, A. F. (2012). "Weathering processes in the Icacos and Mameyes watersheds in eastern Puerto Rico," in *Water Quality and Landscape Processes of Four Watersheds in Eastern Puerto Rico*, eds S. F. Murphy and R. F. Stallard (Reston, VA: U. S. Geological Survey), 249–262. doi: 10.3133/pp1789I

Cantley, L. C., Cantley, L. G., and Josephson, L. (1978). A characterization of vanadate interactions with the (Na, K)-ATPase. Mechanistic and regulatory implications. *J. Biol. Chem.* 253, 7361–7368.

Cantley, L. C., Josephson, L., Warner, R., Yanagisawa, M., Lechene, C., and Guidotti, G. (1977). Vanadate is a potent (Na, K)-ATPase inhibitor found in ATP derived from muscle. *J. Biol. Chem.* 252, 7421–7423.

Chorover, J., Kretzschmar, R., Garcia-Pichel, F., and Sparks, D. L. (2007). Soil biogeochemical processes within the critical zone. *Elements* 3, 321–326. doi: 10.2113/gselements.3.5.321

Condie, K. C., Dengate, J., and Cullers, R. L. (1995). Behavior of rare earth element in a paleoweathering profile. *Geochim. Cosmochim. Acta* 59, 279–294. doi: 10.1016/0016-7037(94)00280-Y

Crans, D. C., Mahroof-Tahir, M., and Keramidas, A. D. (1995). "Vanadium chemistry and biochemistry of relevance for use of vanadium compounds as antidiabetic agents," in *Vanadium Compounds: Biochemical and Therapeutic Applications*, eds A. K. Srivastava and J. L. Chiasson (Boston, MA: Springer), 17–24.

Dayan, A. D., and Paine, A. J. (2001). Mechanisms of chromium toxicity, carcinogenicity and allergenicity: review of the literature from 1985 to 2000. *Human Exp. Toxicol.* 20, 439–451. doi: 10.1191/096032701682693062

Dethier, D. P., and Bove, D. J. (2011). Mineralogic and geochemical changes from alteration of granitic rocks, boulder creek catchment, Colorado. *Vadose Zone J.* 10, 858–866. doi: 10.2136/vzj2010.0106

Dosseto, A., Buss, H. L., and Suresh, P. O. (2012). Rapid regolith formation over volcanic bedrock and implications for landscape evolution. *Earth Planet. Sci. Lett.* 337, 47–55. doi: 10.1016/j.epsl.2012.05.008

Eilers, K. G., Debenport, S., Anderson, S., and Fierer, N. (2012). Digging deeper to find unique microbial communities: the strong effect of depth on the structure of bacterial and archaeal communities in soil. *Soil Biol. Biochem.* 50, 58–65. doi: 10.1016/j.soilbio.2012.03.011

Fimmen, R. L., Vasudevan, D., Williams, M. A., and West, L. T. (2008). Rhizogenic Fe–C redox cycling: a hypothetical biogeochemical mechanism that drives crustal weathering in upland soils. *Biogeochemistry* 87, 127–141. doi: 10.1007/s10533-007-9172-5

Gäbler, H. E., Glüh, K., Bahr, A., and Utermann, J. (2009). Quantification of vanadium adsorption by German soils. *J. Geochem. Explor.* 103, 37–44. doi: 10.1016/j.gexplo.2009.05.002

Garcia-Martino, A. R., Warner, G. S., Scatena, F. N., and Civco, D. L. (1996). Rainfall, runoff and elevation relationships in the Luquillo Mountains of Puerto Rico. *Caribb. J. Sci.* 32, 413–424.

Gardner, C. B., Carey, A. E., Lyons, W. B., Goldsmith, S. T., McAdams, B. C., and Trierweiler, A. M. (2017). Molybdenum, vanadium, and uranium weathering in small mountainous rivers and rivers draining high-standing islands. *Geochim. Cosmochim. Acta* 219, 22–43. doi: 10.1016/j.gca.2017.09.012

Geological Survey, U. S. (2006). *Collection of Water Samples (Ver. 2.0)*. Reston, VA: U.S. Geological Survey,

Giardino, J. R., and Houser, C. (2015). *Principles and Dynamics of the Critical Zone*, Vol. 19. Waltham, MA: Elsevier.

Godsey, S. E., and Kirchner, J. W. (2014). Dynamic, discontinuous stream networks: hydrologically driven variations in active drainage density, flowing channels and stream order. *Hydrol. Process.* 28, 5791–5803. doi: 10.1002/hyp.10310

Goldberg, S., Forster, H. S., and Godfrey, C. L. (1996). Molybdenum adsorption on oxides, clay minerals, and soils. *Soil Sci. Soc. Am. J.* 60, 425. doi: 10.2136/sssaj1996.03615995006000020013x

Goldschmidt, V. M. (1954). *Geochemistry*. Oxford: Oxford University Press, 730.

Grove, J. H., and Ellis, B. G. (1980). Extractable chromium as related to soil pH and applied chromium. *Soil Sci. Soc. Am. J.* 44, 238–242. doi: 10.2136/sssaj1980.03615995004400020005x

Gupta, U. C. (ed.). (1997). *Molybdenum in Agriculture*. Cambridge: Cambridge University Press, 276. doi: 10.1017/CBO9780511574689

Gustafsson, J. P., Persson, I., Oromieh, A. G., van Schaik, J. W. J., Sjostedt, C., and Kleja, D. B. (2014). Chromium(III) complexation to natural organic matter: mechanisms and modeling. *Environ. Sci. Technol.* 48, 1753–1761. doi: 10.1021/es404557e

Holbrook, W. S., Riebe, C. S., Elwaseif, M., Hayes, J. L., Basler-Reeder, K., Harry, D. L., et al. (2014). Geophysical constraints on deep weathering and water storage potential in the Southern Sierra critical zone observatory. *Earth Surf. Process. Landf.* 39, 366–380. doi: 10.1002/esp.3502

Hunsaker, C. T., and Eagan, S. M. (2003). "Small stream ecosystem variability in the Sierra Nevada of California," in *First Interagency Conference on Research in the Watersheds*, eds K. G. Renard, S. A. McElroy, W. J. Gburek, H. E. Canfield, and R. L. Scott (Benson, AZ: U.S. Department of Agriculture), 716–721.

Imtiaz, M., Rizwan, M. S., Xiong, S., Li, H., Ashraf, M., Shahzad, S. M., et al. (2015). Vanadium, recent advancements and research prospects: a review. *Environ. Int.* 80, 79–88. doi: 10.1016/j.envint.2015.03.018

Kabata-Pendias, A. (2011). *Trace Elements in Soils and Plants*. Boca Raton, FL: Taylor and Francis Group.

Kaiser, B. N., Gridley, K. L., Brady, J. N., Phillips, T., and Tyerman, S. D. (2005). The role of molybdenum in agricultural plant production. *Ann. Bot.* 96, 745–754. doi: 10.1093/aob/mci226

Kerr, S. C., Shafer, M. M., Overdier, J., and Armstrong, D. E. (2008). Hydrologic and biogeochemical controls on trace element export from northern Wisconsin wetlands. *Biogeochemistry* 89, 273–294. doi: 10.1007/s10533-008-9219-2

King, E. K. (2017). *Understanding Molybdenum Isotope Dynamics in Terrestrial Environments*. Ph.D. thesis, Oregon State University, Corvallis, OR.

King, E. K., Perakis, S. S., and Pett-Ridge, J. C. (2018). Molybdenum isotope fractionation during adsorption to organic matter. *Geochim. Cosmochim. Acta* 222, 584–598. doi: 10.1016/j.gca.2017.11.014

King, E. K., Thompson, A., Chadwick, O. A., and Pett-Ridge, J. C. (2016). Molybdenum sources and isotopic composition during early stages of pedogenesis along a basaltic climate transect. *Chem. Geol.* 445, 54–67. doi: 10.1016/j.chemgeo.2016.01.024

King, E. K., Thompson, A., Hodges, C., and Pett-Ridge, J. C. (2014). Towards understanding temporal and spatial patterns of molybdenum in the critical zone. *Procedia Earth Planet. Sci.* 10, 56–62. doi: 10.1016/j.proeps.2014.08.011

Kotaś, J., and Stasicka, Z. (2000). Chromium occurrence in the environment and methods of its speciation. *Environ. Pollut.* 107, 263–283. doi: 10.1016/S0269-7491(99)00168-2

Kraepiel, A. M. L., Dere, A. L., Herndon, E. M., and Brantley, S. L. (2015). Natural and anthropogenic processes contributing to metal enrichment in surface soils of central Pennsylvania. *Biogeochemistry* 123, 265–283. doi: 10.1007/s10533-015-0068-5

Kurtz, A. C., Derry, L. A., Chadwick, O. A., and Alfano, M. J. (2000). Refractory element mobility in volcanic soils. *Geology* 28, 683–686. doi: 10.1130/0091-7613(2000)28<683:REMIVS>2.0.CO;2

Larsen, M. C. (2012). "Landslides and sediment budgets in four watersheds in Eastern Puerto Rico," in *Water Quality and Landscape Processes of Four Watersheds in Eastern Puerto Rico: US Geological Survey Professional Paper*, eds S. F. Murphy and R. F. Stallard (Reston, VA: U.S. Geological Survey), 153–178. doi: 10.3133/pp1789F

Larsson, M. A., Baken, S., Gustafsson, J. P., Hadialhejazi, G., and Smolders, E. (2013). Vanadium bioavailability and toxicity to soil microorganisms and plants. *Environ. Toxicol. Chem.* 32, 2266–2273. doi: 10.1002/etc.2322

Larsson, M. A., D'Amato, M., Cubadda, F., Raggi, A., Öborn, I., Kleja, D. B., et al. (2015). Long-term fate and transformations of vanadium in a pine forest soil with added converter lime. *Geoderma* 259, 271–278. doi: 10.1016/j.geoderma.2015.06.012

Larsson, M. A., Hadialhejazi, G., and Gustafsson, J. P. (2017). Vanadium sorption by mineral soils: development of a predictive model. *Chemosphere* 168, 925–932. doi: 10.1016/j.chemosphere.2016.10.117

Levina, A., Codd, R., Dillon, C. T., and Lay, P. A. (2003). Chromium in biology: toxicology and nutritional aspects. *Prog. Inorg. Chem.* 51, 145–250.

Marks, J. A., Perakis, S. S., King, E. K., and Pett-Ridge, J. C. (2015). Soil organic matter regulates molybdenum storage and mobility in forests. *Biogeochemistry* 125, 167–183. doi: 10.1007/s10533-015-0121-4

Marschner, H., Römheld, V., Horst, W. J., and Martin, P. (1986). Root-induced changes in the rhizosphere: importance for the mineral nutrition of plants. *J. Plant Nutr. Soil Sci.* 149, 441–456. doi: 10.1002/jpln.19861490408

Martin, H. W., and Kaplan, D. I. (1998). Temporal changes in cadmium, thallium, and vanadium mobility in soil and phytoavailability under field conditions. *Water Air Soil Pollut.* 101, 399–410. doi: 10.1023/A:1004906313547

Mehra, O. P., and Jackson, M. L. (1960). "Iron oxide removal from soils and clays by a dithionite–citrate system buffered with sodium bicarbonate," in *Proceedings of the Seventh National Conference on Clays and Clay Minerals*, Washington, DC.

Morrison, J. M., Goldhaber, M. B., Mills, C. T., Breit, G. N., Hooper, R. L., Holloway, J. M., et al. (2015). Weathering and transport of chromium and nickel from serpentinite in the Coast Range ophiolite to the Sacramento Valley, California, USA. *Appl. Geochem.* 61, 72–86. doi: 10.1016/j.apgeochem.2015.05.018

Murphy, S. F., Stallard, R. F., Larsen, M. C., and Gould, W. A. (2012). "Physiography, geology, and land cover of four watersheds in eastern Puerto Rico," in *Water Quality and Landscape Processes of Four Watersheds in Eastern Puerto Rico: US Geological Survey Professional Paper 1789*, eds S. F. Murphy and R. F. Stallard (Reston, VA: U.S. Geological Survey), 1–23.

Murphy, S. F., Stallard, R. F., Scholl, M. A., González, G., and Torres-Sánchez, A. J. (2017). Reassessing rainfall in the Luquillo Mountains, Puerto Rico: local and global ecohydrological implications. *PLoS One* 12:e0180987. doi: 10.1371/journal.pone.0180987

Orlando, J., Comas, X., Hynek, S. A., Buss, H. L., and Brantley, S. L. (2016). Architecture of the deep critical zone in the Rio Icacos watershed (Luquillo critical zone observatory, Puerto Rico) inferred from drilling and ground penetrating radar (GPR). *Earth Surf. Process. Landf.* 41, 1826–1840. doi: 10.1002/esp.3948

Pearce, C. R., Burton, K. W., Pogge von Strandmann, P. A. E., James, R. H., and Gíslason, S. R. (2010). Molybdenum isotope behaviour accompanying weathering and riverine transport in a basaltic terrain. *Earth Planet. Sci. Lett.* 295, 104–114. doi: 10.1016/j.epsl.2010.03.032

Pérez, C., Antelo, J., Fiol, S., and Arce, F. (2014). Modeling oxyanion adsorption on ferralic soil, part 2: chromate, selenate, molybdate, and arsenate adsorption. *Environ. Toxicol. Chem.* 33, 2217–2224. doi: 10.1002/etc.2581

Pett-Ridge, J. C., Derry, L. A., and Barrows, J. K. (2009). Ca/Sr and 87Sr/86Sr ratios as tracers of Ca and Sr cycling in the Rio Icacos watershed, Luquillo Mountains, Puerto Rico. *Chem. Geol.* 267, 32–45. doi: 10.1016/j.chemgeo.2008.11.022

Pokrovsky, O. S., and Schott, J. (2002). Iron colloids/organic matter associated transport of major and trace elements in small boreal rivers and their estuaries (NW Russia). *Chem. Geol.* 190, 141–179. doi: 10.1016/S0009-2541(02)00115-8

Prouty, N. G., Swarzenski, P. W., Fackrell, J. K., Johannesson, K., and Palmore, C. D. (2017). Groundwater-derived nutrient and trace element transport to a nearshore Kona coral ecosystem: experimental mixing model results. *J. Hydrol. Reg. Stud.* 11, 166–177. doi: 10.1016/j.ejrh.2015.12.058

Richter, D. D. Jr., and Markewitz, D. (2001). *Understanding Soil Change: Soil Sustainability Over Millennia, Centuries, and Decades*. New York, NY: Cambridge University Press.

Riley, M. M., Robson, A. D., Gartrell, J. W., and Jeffery, R. C. (1987). The absence of leaching of molybdenum in acidic soils from Western Australia. *Soil Res.* 25, 179–184. doi: 10.1071/SR9870179

Salvador-Blanes, S., Cornu, S., Bourennane, H., and King, D. (2006). Controls of the spatial variability of Cr concentration in topsoils of a central French landscape. *Geoderma* 132, 143–157. doi: 10.1016/j.geoderma.2005.05.003

Saputro, S., Yoshimura, K., Matsuoka, S., Takehara, K., Narsito, A. J., and Tennichi, Y. (2014). Speciation of dissolved chromium and the mechanisms controlling its concentration in natural water. *Chem. Geol.* 364, 33–41. doi: 10.1016/j.chemgeo.2013.11.024

Schwertmann, U., and Pfab, G. (1996). Structural vanadium and chromium in lateritic iron oxides: genetic implications. *Geochim. Cosmochim. Acta* 60, 4279–4283. doi: 10.1016/S0016-7037(96)00259-1

Shiller, A. M. (1997). Dissolved trace elements in the Mississippi River: seasonal, interannual, and decadal variability. *Geochim. Cosmochim. Acta* 61, 4321–4330. doi: 10.1016/S0016-7037(97)00245-7

Shiller, A. M., and Boyle, E. A. (1987). Dissolved vanadium in rivers and estuaries. *Earth Planet. Sci. Lett.* 86, 214–224. doi: 10.1016/0012-821X(87)90222-6

Shiller, A. M., and Mao, L. (2000). Dissolved vanadium in rivers: effects of silicate weathering. *Chem. Geol.* 165, 13–22. doi: 10.1016/S0009-2541(99)00160-6

Siebert, C., Pett-Ridge, J. C., Opfergelt, S., Guicharnaud, R. A., Halliday, A. N., and Burton, K. W. (2015). Molybdenum isotope fractionation in soils: influence of redox conditions, organic matter, and atmospheric inputs. *Geochim. Cosmochim. Acta* 162, 1–24. doi: 10.1016/j.gca.2015.04.007

Singh, H. P., Mahajan, P., Kaur, S., Batish, D. R., and Kohli, R. K. (2013). Chromium toxicity and tolerance in plants. *Environ. Chem. Lett.* 11, 229–254. doi: 10.1007/s10311-013-0407-5

Solé, V. A., Papillon, E., Cotte, M., Walter, P., and Susini, J. (2007). A multiplatform code for the analysis of energy-dispersive X-ray fluorescence spectra. *Spectrochim. Acta Part B* 62, 63–68. doi: 10.1016/j.sab.2006.12.002

Strady, E., Blanc, G., Schäfer, J., Coynel, A., and Dabrin, A. (2009). Dissolved uranium, vanadium and molybdenum behaviours during contrasting freshwater discharges in the Gironde Estuary (SW France). *Estuar. Coast. Shelf Sci.* 83, 550–560. doi: 10.1016/j.ecss.2009.05.006

Tian, Z. (2018). *Soil and Weathered Bedrock Evolution Along an Elevation Gradient in the Southern Sierra Nevada, California*. Doctoral dissertation, University of California, Davis.

Trostle, K. D., Ray Runyon, J., Pohlmann, M. A., Redfield, S. E., Pelletier, J., McIntosh, J., et al. (2016). Colloids and organic matter complexation control trace metal concentration-discharge relationships in Marshall Gulch stream waters. *Water Resour. Res.* 52, 7931–7944. doi: 10.1002/2016WR019072

Weaver, P. L., and Gould, W. A. (2013). "Forest vegetation along environmental gradients in northeastern Puerto Rico," in *Ecological Gradient Analyses in a Tropical Landscape*, Vol. 54, eds G. González, M. R. Willig, and R. B. Waide (Oxford: John Wiley & Sons), 43–66.

White, A. F., Blum, A. E., Schulz, M. S., Vivit, D. V., Stonestrom, D. A., Larsen, M., et al. (1998). Chemical weathering in a tropical watershed, Luquillo Mountains, Puerto Rico: I. Long-term versus short-term weathering fluxes. *Geochim. Cosmochim. Acta* 62, 209–226. doi: 10.1016/S0016-7037(97)00335-9

Wichard, T., Mishra, B., Myneni, S. C., Bellenger, J. P., and Kraepiel, A. M. (2009). Storage and bioavailability of molybdenum in soils increased by organic matter complexation. *Nat. Geosci.* 2, 625–629. doi: 10.1038/ngeo589

Wisawapipat, W., and Kretzschmar, R. (2017). Solid phase speciation and solubility of vanadium in highly Weathered soils. *Environ. Sci. Technol.* 51, 8254–8262. doi: 10.1021/acs.est.7b01005

Xu, N. A. N., Braida, W., Christodoulatos, C., and Chen, J. (2013). A review of molybdenum adsorption in soils/bed sediments: speciation, mechanism, and model applications. *Soil Sediment Contam.* 22, 912–929. doi: 10.1080/15320383.2013.770438

**Conflict of Interest Statement:** The authors declare that the research was conducted in the absence of any commercial or financial relationships that could be construed as a potential conflict of interest.

frontiers in Earth Science

ORIGINAL RESEARCH
published: 21 February 2019
doi: 10.3389/feart.2019.00024

# Solute Fluxes Through Restored Prairie and Intensively Managed Critical Zones in Nebraska and Iowa

*Ashlee L. Dere[1]*, Andrew W. Miller[2], Amy M. Hemje[2], Sara K. Parcher[1], Courtney A. Capalli[3] and E. Arthur Bettis III[3]*

*[1] Department of Geography/Geology, University of Nebraska Omaha, Omaha, NE, United States, [2] Department of Chemistry, University of Nebraska Omaha, Omaha, NE, United States, [3] Department of Earth and Environmental Sciences, University of Iowa, Iowa City, IA, United States*

Agricultural activities in the Midwestern United States have potentially altered geochemical fluxes within the critical zone (CZ) compared to native prairie systems that previously dominated the region. To quantify the impact of agricultural land use on soil and stream solute behavior, we are studying two watersheds in the region: Glacier Creek Preserve (GCP) in eastern Nebraska and the Intensively Managed Landscapes Critical Zone Observatory (IML-CZO) in eastern Iowa. Both watersheds were initially under agricultural land use for over 100 years, but part of each watershed was restored to prairie 20 – 50 years ago. Soils at both sites formed in thick Peoria loess (≥6 m) overlying glacial till with similar mean annual temperatures (~10°C) but slightly higher mean annual precipitation in Iowa (89 cm) compared to Nebraska (78 cm). At both sites, soil pore water and precipitation were collected every 2–4 weeks to measure anions, cations, and alkalinity; stream waters draining either restored prairie or agriculture were sampled similarly in Nebraska. Both soil moisture content and electrical conductivity were consistently higher in the upper one meter of agricultural soils compared to prairie soils in Nebraska, implying slower drainage and higher solute concentrations in the agricultural soils. At both sites, soil pore water $Ca^{2+}$ and $Mg^{2+}$ concentrations and annual fluxes were significantly higher in agricultural soils compared to restored prairie. Conversely, streams draining restored prairie have significantly higher $Ca^{2+}$ and $Mg^{2+}$ concentrations than the agricultural streams. Fluxes from agricultural streams, however, were higher than the prairie, pointing to a potential dilution effect of runoff from the agricultural land use. These observations lead to a conceptual model where deeply infiltrating water in restored prairie soils interacts with minerals present deeper in the soil before reaching the stream whereas in agricultural soils water does not infiltrate as deeply and thus experiences more shallow flowpaths to the stream. Furthermore, changes in geochemical and hydrologic fluxes have been realized in just a few decades since switching land use from agriculture to prairie. Thus, intensive agricultural land use may alter soil function and solute transport to streams compared to critical zones hosting tallgrass prairie vegetation.

**Keywords: agriculture, soil pore water, loess, water quality, discharge, stream**

OPEN ACCESS

***Edited by:***
*Alexandra V. Turchyn, University of Cambridge, United Kingdom*

***Reviewed by:***
*Justin Byron Richardson, University of Massachusetts Amherst, United States*
*Joel Moore, Towson University, United States*

****Correspondence:***
*Ashlee L. Dere*
*adere@unomaha.edu*

***Specialty section:***
*This article was submitted to Biogeoscience, a section of the journal Frontiers in Earth Science*

***Received:*** *04 September 2018*
***Accepted:*** *04 February 2019*
***Published:*** *21 February 2019*

***Citation:***
*Dere AL, Miller AW, Hemje AM, Parcher SK, Capalli CA and Bettis EA III (2019) Solute Fluxes Through Restored Prairie and Intensively Managed Critical Zones in Nebraska and Iowa. Front. Earth Sci. 7:24. doi: 10.3389/feart.2019.00024*

## INTRODUCTION

The Midwestern United States hosts an impressively thick critical zone (CZ), the layer of the Earth that encompasses groundwater to vegetation (Brantley et al., 2007), with loess deposits exceeding 40 m deep in some areas (Bettis et al., 2003). Historically, the region hosted extensive prairie vegetation, but the landscape has been largely converted to agricultural land use since the 1800s (Sampson and Knopf, 1994; Wright and Wimberly, 2013). Soils in this region sustain intensive agriculture, store large quantities of carbon, and filter water as it recharges groundwater and streams (Banwart, 2011), but how intensive agriculture influences CZ processes, including water and nutrient fluxes, and how long intensive land use can be maintained while sustaining high productivity, is unclear (Foley et al., 2005). Land disturbance from agriculture is widespread throughout the Midwestern United States and can have far reaching impacts on stream chemistry. Streams serve as integrators of CZ processes and, in the Midwest, ultimately deliver dissolved and particulate material to the Gulf of Mexico, impacting both the nutrient status and biology of waterways (Rabalais et al., 2010). Furthermore, there is evidence that intensive agriculture has altered the flow (Zhang and Schilling, 2006) and alkalinity (Raymond et al., 2008) of the Mississippi River, the largest river in North America. Despite the agronomic and environmental importance of the Midwestern CZ (Richardson and Kumar, 2017), we still know little about how activities at the surface influence CZ processes such as soil water fluxes and chemistry that are linked to streams.

Previous studies measuring soil and stream solute chemistry have largely focused on managed systems, such as row crop agriculture and pasture, and few studies have aimed to connect soil solute chemistry to stream chemistry in intensively managed systems. For example, previous studies investigating soil solutions under agricultural and grassland cover have primarily focused only on nitrate leaching (e.g., Masarik et al., 2014) and have been predominantly studied in sandy soils rather than finer textured soils (Singh et al., 2018). Furthermore, few studies involving *in situ* soil solution extractions concurrently use sensors to quantify soil moisture to investigate both soil solution chemistry and hydrology (Singh et al., 2018). Studies focused on stream fluxes from agricultural or restored prairie watersheds have also focused predominantly on nitrate and anion fluxes (e.g., Schilling, 2002; Aubert et al., 2013). Tallgrass prairie soils in the Midwest region have been most notably studied at the Konza Prairie Long Term Ecological Research (LTER) site in northeast Kansas, where soil water and gas fluxes through limestone and shale parent material have been linked to shallow groundwater chemistry (e.g., Tsypin and Macpherson, 2012; Vero et al., 2018). Previous work explicitly linking soil solute and stream water chemistry has largely focused on undisturbed forested systems (e.g., Jin et al., 2011; Hinckley et al., 2014) rather than row crop agriculture and prairie CZs.

To examine human influence on landscape connectivity and fluxes of water, sediment and nutrients in agroecosystems, the Intensively Managed Landscapes Critical Zone Observatory (IML CZO) was established (Kumar et al., 2018; Wilson et al., 2018). The CZO includes sites in Iowa, Illinois, and Minnesota, representing a region characterized by thick surficial deposits from multiple glaciations (Anders et al., 2018) that has transitioned from transforming to transporting energy and matter under current human management practices (Kumar et al., 2018). Previous research at the IML CZO in the Clear Creek Watershed in Iowa has focused on hillslope (Papanicolaou et al., 2015a,b, 2018) and stream bank (Neal and Anders, 2015; Papanicolaou et al., 2017) erosion that delivers sediments and associated nutrients directly to streams. Meanwhile, groundwater monitoring has highlighted that baseflow discharge to the connected stream accounts for the majority of nitrate loads exported by the stream, 95% of which is derived from row crop areas (Schilling et al., 2018). However, soils represent an intermediate step in transmitting such nutrients to groundwater or streams, yet direct measurements of soil and stream solute chemistry are still needed (Singh et al., 2018; Wilson et al., 2018).

Here we present data on precipitation, soil pore water, and stream water chemistry, along with soil moisture and electrical conductivity (EC), under both corn-soybean row crop agriculture and restored prairie vegetation in loess parent material at sites in eastern Nebraska and eastern Iowa. The two study sites have similar topography, duration of soil formation, mean annual temperatures (∼10°C), and a slight precipitation gradient (78 and 89 cm mean annual precipitation in Nebraska and Iowa, respectively). Both sites were used for agriculture for at least 100 years before portions of the sites were restored to prairie 20–50 years ago, thereby marking a substantial change in the aboveground vegetation and management. Given the similar environmental conditions between the two sites, we hypothesized that land use would be the main factor influencing soil hydrology and geochemistry, which in turn would impact stream chemistry. Solute measurements in this study focused on cations ($Na^+$, $K^+$, $Mg^{2+}$, and $Ca^{2+}$) and anions ($Cl^-$, $NO_2^-$, $NO_3^-$, $SO_4^{2-}$, and $PO_4^{3-}$) in precipitation, soil pore water, and stream water as well as some metals ($Al^{3+}$, $Fe^{2+}$, $Fe^{3+}$, and $Mn^{2+}$) in stream water. Using these geochemically relevant ion concentrations from the different water sample types, combined with soil and stream hydrologic characterization (soil moisture, soil EC, and stream discharge), we present an initial conceptual model demonstrating impacts of intensive agriculture and prairie land use on soil hydrology, geochemistry, and ultimately stream chemistry. Although the mechanisms driving these changes are yet unclear, the land use impacts on soil processes appear to alter the elemental fluxes from each land use despite less than 50 years since land use changed.

## MATERIALS AND METHODS

### Study Sites

#### Glacier Creek Preserve

Glacier Creek Preserve (GCP) is located in eastern Nebraska 20 km northwest of Omaha, NE, United States (**Table 1** and **Figures 1A,B**). The 4 $km^2$ preserve encompasses the entire first order Glacier Creek watershed and includes both restored tallgrass prairie and agricultural land use on the gently rolling topography (slopes < 15%). The site was used entirely for

**TABLE 1 |** Sampling locations in Nebraska (NE) and Iowa (IA) agriculture and restored prairie study sites.

| Site | | Latitude | Longitude | Elev. |
|---|---|---|---|---|
| | | | | m |
| NE Agriculture | | 41.3455 | −96.1414 | 363 |
| NE Prairie | | 41.3373 | −96.1414 | 371 |
| IA Agriculture | | 41.7390 | −91.9475 | 264 |
| IA Prairie | | 41.7403 | −91.7322 | 248 |
| NE Stream | GC2 | 41.3412 | −96.1405 | 322 |
| | GC3 | 41.3414 | −96.1413 | 320 |
| | GC4 | 41.3416 | −96.1421 | 323 |
| | GC5 | 41.3408 | −96.1429 | 328 |
| | GC6 | 41.3404 | −96.1448 | 348 |

agriculture from approximately 1870 until 1970, when the southern 0.54 km$^2$ of the preserve were reseeded to native tallgrass prairie (**Figure 1C**). The prairie vegetation is managed with a 3 year fire return interval with one third of the area burned each year. The northern portion of the site (0.32 km$^2$) continues to be used for minimal till corn (*Zea mays L.*) and soybean [*Glycine max (L.)*] agriculture; tilling practices switched from intensive to minimal tillage around 1970. In 2017 soybeans were grown in the study area and broadcast phosphorous and potassium fertilizer was applied the previous fall following a corn harvest.

Parent material at the site is dominated by Peoria loess in the upland areas (>10 m thick) and pre-Illinoian glacial till underlies the creek that runs through the center of the watershed. Soils on the ridgetop topographic position, where soil sensors and soil pore water were collected, are mapped as Contrary-Monona-Ida Complex (Soil Survey Staff, 2018). On the agricultural side of the watershed, soils are Contrary silt loam (Fine-silty, mixed, superactive, mesic Dystric Eutrudepts) while prairie soils are Monona silt loam (Fine-silty, mixed, superactive, mesic Typic Hapludolls). Mean annual temperature is 10°C and mean annual precipitation is 78 cm. In 2017, average air temperature was 11.8°C and precipitation in the watershed totaled 78 cm.

## Intensively Managed Landscapes Critical Zone Observatory

The Intensively Managed Landscapes Critical Zone Observatory (IML CZO) is located approximately 30 km northwest of Iowa

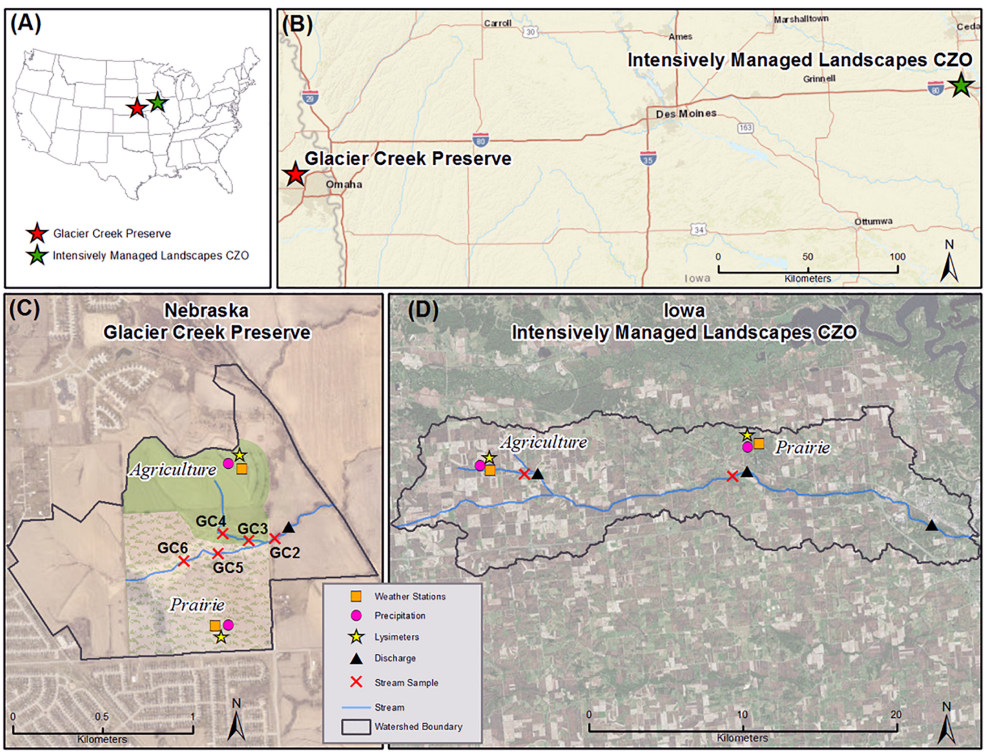


**FIGURE 1 |** Glacier Creek Preserve (GCP) and the Intensively Managed Landscapes Critical Zone Observatory (IML CZO) located in the Midwestern United States **(A)** approximately 400 km apart in eastern Nebraska (NE) and eastern Iowa (IA) **(B)**. The 4 km$^2$ watershed in Nebraska is drained by Glacier Creek which has forks draining restored prairie on the south side of the watershed (hatched green shading) and agriculture on the north side (solid green shading) **(C)**. The Iowa site lies in the 270 km$^2$ Clear Creek watershed and is drained by Clear Creek **(D)**. This site includes an agricultural study site toward the headwaters and a restored prairie study site on the northern edge of the watershed. In both Nebraska and Iowa, restored prairie and agricultural soils are equipped with weather stations, soil sensors, soil pore water samplers at four depths, and precipitation collectors. Glacier Creek is equipped with a stream discharge sensor and five stream locations were regularly sampled. Clear Creek has three discharge sensors monitored by the Iowa Flood Information System (IFIS) (from west to east: Homestead, Oxford, and Coralville), but the stream is not routinely sampled for solute chemistry.

City, IA (**Table 1** and **Figures 1A,B**). The 270 km$^2$ HUC 10 watershed is drained by Clear Creek and land use is dominated by roughly 100 years of agricultural land use across the gently rolling topography (slopes < 18%) (**Figure 1D**). The agricultural study site is located on a farm in the northwest corner of the watershed where minimal tillage practices replaced more intensive chisel plow tillage in the 1990s (Papanicolaou et al., 2015b). In 2017 corn was grown in the study area with an application of broadcast phosphorous and potassium fertilizer and anhydrous ammonium following harvest of the soybean crop in 2016. Parent material at the site is Peoria loess (∼6 m thick) overlying Sangamon age glacial till. Soils are mapped as Tama silty clay loam (Fine-silty, mixed, superactive, mesic Typic Argiudolls) (Soil Survey Staff, 2018).

A small restored tallgrass prairie (0.06 km$^2$) is located approximately 16 km to the east of the agricultural site in F.W. Kent Park. The prairie was originally forested prior to clearing for agriculture in the late 1800s; conventional corn-soybean row crop agriculture ceased in 1997. The site was left fallow until 2009 then reseeded with prairie grass mix; prairie vegetation is currently maintained through controlled burns every ∼5 years. Parent material at the site is thin Peoria loess (∼ 1.6 m thick) overlying Sangamon age glacial till; soils at the site are Fayette silt loam (Fine-silty, mixed, superactive, mesic Typic Hapludalfs) (Soil Survey Staff, 2018). Mean annual temperature in the Clear Creek watershed is 9°C and mean annual precipitation is 89 cm. In 2017, average air temperature was 12.1°C and 123 cm of precipitation was recorded near the agricultural study area.

## Sensor Data

### Meteorological Stations and Soil Sensors

At the Nebraska study site, two meteorological stations were installed on ridgetop topographic positions, one in the restored prairie and one in the agricultural field. Both stations provided hourly measurements of atmospheric and soil parameters at 10, 25, 50, and 100 cm depth (**Figure 1C**). The Campbell Scientific (Logan, UT, United States) meteorological stations recorded data on a CR1000 datalogger with the following sensors: anemometer (R.M. Young's 03002 Wind Sentry Set), all season pyranometer (SP230), precipitation sensor (Texas Electronics Tipping Bucket Rain Gages), temperature and relative humidity sensor (HC2S3), barometer (CS106), and soil moisture, temperature and electrical conductivity (EC) sensors (CS655).

At the IML CZO in Iowa, a meteorological station recorded atmospheric parameters on a ridgetop topographic position at the agricultural study site (**Figure 1D**). The Meter (Pullman, WA, United States) meteorological station collected data with EM50 dataloggers including precipitation (ECRN-100 tipping bucket), wind speed and direction (Davis Cup anemometer), and relative humidity and temperature (VP-3) at 1 min. intervals. Soil parameters at 10, 20, and 60 cm depth were measured at both the agricultural and restored prairie sites every 15 min. Soil moisture and temperature were measured with a 5TM Moisture/Temperature sensor at the agricultural site and a GS3 Soil Moisture/Temperature/EC sensor at the restored prairie site.

### Stream Water Quality

General stream water quality parameters were collected in the field at the Nebraska site using Xylem (Rye Brook, NY, United States) ProDSS handheld sensors. The parameters included pH/oxidation reduction potential (ORP, 626904), temperature/conductivity (626902), turbidity (626901), and optical dissolved oxygen (626900). Measurements were taken approximately every 2 weeks at each of five sampling sites (**Figure 1C**). Each probe was calibrated with relevant calibration solutions on the day of sampling. Before taking a measurement, the probes were placed in the stream for several minutes to allow the probes to equilibrate and allow fresh water to displace any sediment disturbed by the placement of the probes.

### Stream Discharge

A SonTek Xylem IQ *in situ* stream discharge sensor was placed in Glacier Creek at the Nebraska study site downstream of the GC2 sampling site in May 2017 (**Figure 1C**). The IQ system simultaneously measured the flow velocity and the stream channel dimensions using sound waves, which was then converted to volumetric flow. The IQ was programmed to log flow data every 15 min. In Iowa, several discharge sensors along Clear Creek recorded hourly discharge at the Homestead, Oxford and Coralville gaging stations[1] (**Figure 1D**).

## Solute Sampling

### Stream Water

Stream water samples were collected approximately monthly from all five sites in Glacier Creek in Nebraska beginning in April through December 2017. For data analysis purposes, four of the sampling locations were sorted based on physical proximity to either prairie or agricultural land uses. Locations GC3 and GC4 are physically closest to active agriculture and are located on the north fork of Glacier Creek, which drains predominantly agricultural land. Locations GC5 and GC6 are physically closest to the restored prairie and are located in the south fork of Glacier Creek, which drains the majority of the restored prairie. Site GC2 is located just below the convergence of the two forks, and was used for mass balance calculations described below. At each site, a grab sample was removed from the stream with a conditioned sampling beaker. The sample was filtered through a 0.45 μm PVDF syringe filter and then split. One split was left unacidified for anion and alkalinity analysis, the other split was acidified to pH < 2 with concentrated HCl. All samples were refrigerated at 4°C prior to analysis.

Clear Creek in the Iowa IML watershed predominantly drains agricultural land use in the headwaters and mixed urban and agricultural land use toward the mouth of the watershed, but does not have a stream draining predominantly restored prairie like in Nebraska. Grab samples from the Homestead gaging station (westernmost triangle in **Figure 1D**), which is located near the agriculture study site, were collected on two dates (2015-06-25 and 2016-12-01) and analyzed for cations and anions as described below.

[1] http://ifis.iowafloodcenter.org/ifis/app/

### Soil Pore Water

Suction cup pore water samplers with a silicon carbide cup (SIC20) (UMS brand; Munich, Germany) were installed at four different depths in both restored prairie and agricultural land use at the Nebraska and Iowa study sites. Samplers were installed in spring – summer of 2016 to allow time for porous cups to equilibrate with soil conditions (Singh et al., 2018). Pore water samplers were inserted at an approximately 20° angle away from vertical into a hand-drilled hole using a custom gouge auger (TB-20 and TBE-100). In Nebraska, pore water samplers were installed at 10, 25, 50, and 100 cm depth; in Iowa, samplers were installed at 20, 60, 80, and 150 cm depth. Pore water samplers were connected to 500 ml glass sampling bottles (SF-500) and stored in an insulated plastic box (SF-box) buried in the ground. Sample bottles were evacuated down to ∼0.5 bar using a hand-operated vacuum floor pump (VPS-2) in Nebraska and an automated portable vacuum (VacuPorter) in Iowa. The vacuum was removed from all samplers and the site covered in straw from December to March to avoid frost damage to the pore water samplers.

Soil pore water was collected approximately every 2 weeks from May through November and the sample volume, pH, and electric conductivity were recorded in the field. Samples were filtered through a 0.45 μm PVDF syringe filter and then split. One split was left unpreserved for anion and alkalinity analysis, the other split was acidified to pH $< 2$ with concentrated nitric acid for cation analysis. All samples were refrigerated at 4°C prior to analysis. At both sites, insufficient sample volume limited some or all chemical analyses, especially during the driest parts of the year in late summer (**Supplementary Tables 1–4**).

### Precipitation

Precipitation was collected every 2 weeks at the Iowa agriculture and prairie sites and at the Nebraska prairie site. The collection vessel included a plastic funnel covered by wire mesh connected by zip ties to a 250 ml plastic separatory funnel. A thin layer of mineral oil was added to prevent evaporation. A subsample was collected and filtered through a 0.45 μm PVDF syringe filter and then split and preserved in the same manner as the pore water samples. On some occasions, the volume of rainwater exceeded the capacity of the collection vessel or the addition of bird fecal matter contaminated precipitation samples and precluded their inclusion in the dataset (**Supplementary Table 5**).

## Chemical Analyses

### Cations and Anions

For all water samples, bulk ions ($Na^+$, $K^+$, $Mg^{2+}$, $Ca^{2+}$, $Cl^-$, $NO_2^-$, $NO_3^-$, $SO_4^{2-}$, and $PO_4^{3-}$) were determined using a Dionex Aquion ion chromatograph using CS12A analytical and guard columns for cation analysis, and AS23 analytical and guard columns for anion analysis (**Supplementary Tables 1–10**). Trace metal analysis ($Al^{3+}$ and $Mn^{2+}$) was completed on a Varian inductively coupled plasma mass spectrometer (ICP-MS) (Walnut Creek, CA, United States). Total dissolved iron ($Fe^{2+}$ and $Fe^{3+}$) was determined through complexation with phenanthroline on an Agilent Technologies Cary 8454 UV-Vis spectrophotometer (Santa Clara, CA, United States). For the instrumental methods, initial method validation was completed using sample spikes, dilutions, and replicate samples. For each analytical run, calibration standards and check standards were analyzed to ensure data quality.

### Alkalinity

Stream sample alkalinity determinations were completed within 24 h of sampling. Potentiometric alkalinity titrations were completed on 50 mL aliquots of stream samples using a Hannah Instruments (Woodsocket, RI, United States) autotitrator with standardized HCl. When possible, titrations were completed on pore water samples. Due to sample volume limitations, only 7 mL of sample were used.

## Data Analyses

### Flux Calculations

Since stream flow rate was only directly measured after the south fork (prairie) and north fork (agriculture) of Glacier Creek had converged (**Figure 1C**), mass balance calculations using conservative ions were used to split the total flow on the date of sampling into flow rates for each fork of the creek. Concentrations of several different ion pairs (Na/Cl, K/Cl, and Ca/Cl) from sampling positions just above and just below fork convergence were used to estimate the two fork flows (Davis and Cornwell, 1998). Once the flow for each fork was known, the flow was multiplied by the stream concentration and normalized to drainage area at the most downgradient sampling point on both the south fork and north fork to determine the elemental flux emanating from the prairie and agricultural land uses, respectively. During the driest parts of the year (fall/winter) total stream flow was frequently too low to be reliably measured. For months where the IQ sensor was not accurately capturing the total flow rate (September, October, and December), average monthly flow for each fork was estimated by averaging July, August, and November monthly discharges, which were considered to represent baseflow conditions at the site (i.e., not influenced by spring flush) (**Supplementary Table 11**).

Similarly, soil pore water fluxes were determined for each sample by multiplying elemental concentration by the collected volume and dividing by the area over which each pore water sampler suction cup captures water (25 $cm^2$) and the sampling period (∼14 days) (**Supplementary Tables 12–14**) (Weihermuller et al., 2007). Soil pore water fluxes were averaged over all depths for the year at each site to determine an average flux by site and land use.

### Speciation

All speciation calculations were completed using PHREEQC (Parkhurst and Appelo, 2013). For stream samples, where all major ions had been directly measured for every sample, the ion concentrations and basic water quality parameters (pH, dissolved oxygen, temperature) were used as input to calculate the error in the charge balance, saturation indices for relevant mineral species, and the partial pressure of $CO_2$ ($P_{CO2}$). Each stream water sample was speciated individually, and the annualized results from the prairie or agricultural stream

locations were averaged for analysis. For the pore water samples, volume limitations precluded direct determination of all ion concentrations in every sample. Some samples had either anion or cation analysis but not both, many were missing alkalinity values, and no samples had trace metal analysis (Fe, Mn, or Al). Since each sample could not be speciated individually, the annual average concentration for each measured ion was used instead. Pore water samples were averaged by land use type in Nebraska and Iowa; individual ion concentrations from all prairie related samples were averaged and individual ion concentrations from all agricultural samples were also averaged. To remove any outliers from consideration, concentrations larger than two standard deviations above the mean were not included. Non-detectable ion concentrations were also omitted from averaging. Non-detectable concentrations were common for $NO_2^-$ and $PO_4^{3-}$, while the other major ions were more consistently detected.

### Statistics

Differences between agriculture and restored prairie solute concentrations, soil moisture and soil EC were analyzed for significant differences using a two-sample student *t*-test ($\alpha = 0.05$) using OriginLab software (Wellesley Hills, MA, United States). The statistical test compared the agriculture and restored prairie data at each site individually (e.g., Nebraska prairie vs. Nebraska agriculture, Iowa prairie vs. Iowa agriculture).

## RESULTS

### Soil Moisture and Electrical Conductivity

Soil moisture (volumetric water content) throughout the year was higher overall in agricultural soils in Nebraska compared to prairie soils, especially March through May (**Figure 2A**). Prairie soil moisture responded rapidly to precipitation events in the upper 25 cm but an increase in soil moisture was often observed down to 100 cm following a precipitation event. In contrast, the agricultural soil responded rapidly to precipitation events predominantly in the upper 25 cm, but soil moisture at deeper depths tended to show no immediate response to incoming precipitation. Iowa soil moisture was higher overall throughout the year in the prairie soil compared to the agricultural soil, but at all depths soil moisture tended to increase immediately following a precipitation event (**Figure 2B**). In Nebraska, the average soil moisture was significantly lower ($p < 0.05$) in the upper 25 cm of restored prairie soils compared to agricultural soils (**Supplementary Table 15** and **Figure 3A**). The opposite was observed in Iowa, where average soil moisture at all depths was greater in prairie soils than agricultural soils (**Figure 3B**).

Soil electrical conductivity (EC), an indication of the dissolved solutes present in the soil water, was higher at all depths in Nebraska agricultural soils compared to prairie soils, especially during the summer months (**Figure 2A**). The agricultural soil EC showed an annual trend whereby EC increased steadily March through June and then slowly decreased through the rest of the year. In Iowa, where only prairie soil EC data were available, EC was relatively constant throughout the year, increasing in response to fall precipitation following the driest part of summer (**Figure 2B**). Soil EC was significantly higher ($p < 0.05$) at all depths in the agricultural soil than the prairie soils in Nebraska, with average EC increasing with depth under both land uses (**Figure 3C**). In Iowa, average EC at 10 and 60 cm depth was similar within uncertainty to EC measured in Nebraska prairie

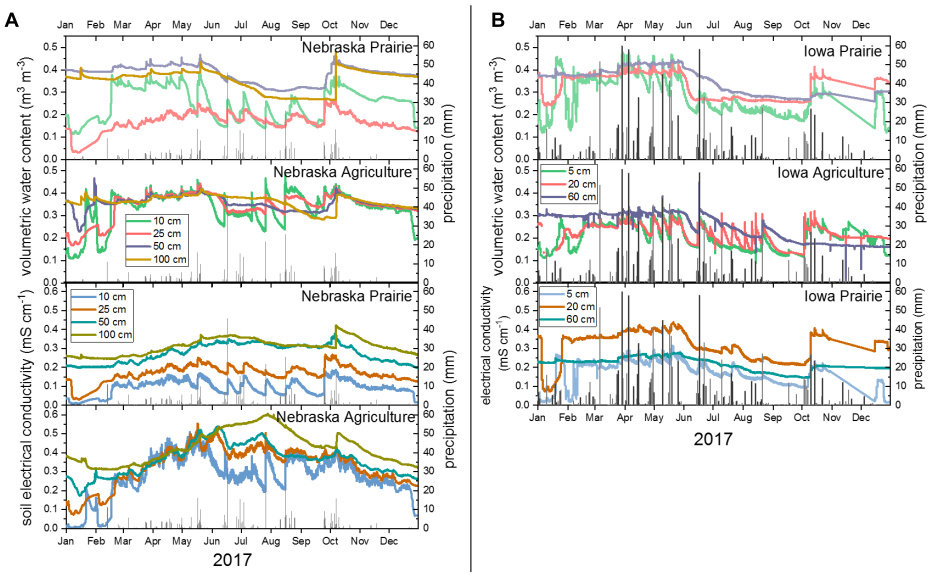


**FIGURE 2 |** Annual time series data for soil moisture (volumetric water content), soil electrical conductivity, and precipitation in Nebraska **(A)** and Iowa **(B)** restored prairie and agricultural sites. Colored lines indicate different measurement depths at each site and gray bars represent precipitation events. No soil electrical conductivity data is available at the Iowa agricultural site.

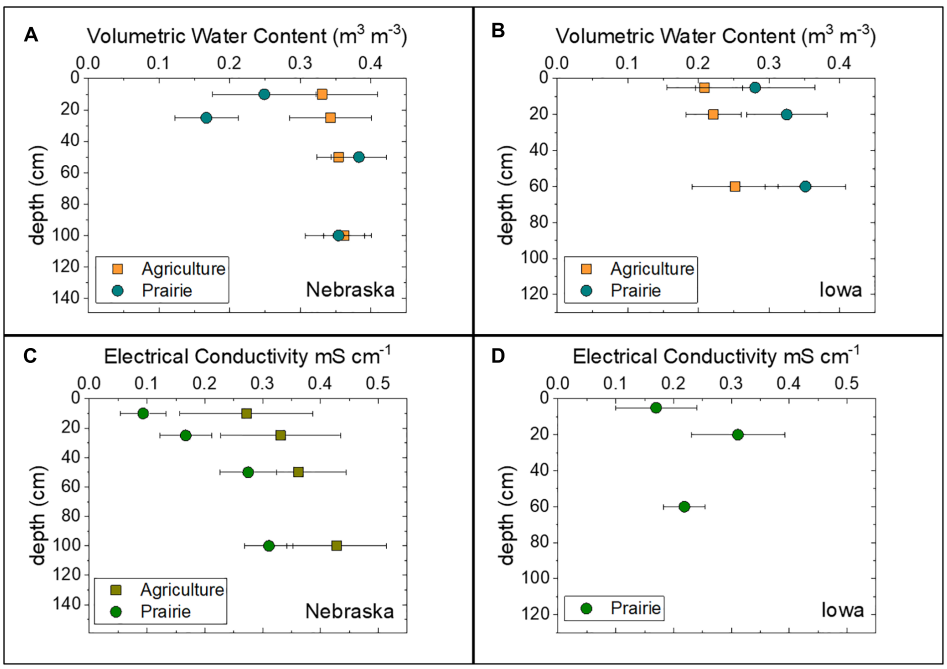


**FIGURE 3 |** Annual average soil volumetric water content and electrical conductivity with depth at the Nebraska **(A,C)** and Iowa **(B,D)** study sites for both agriculture and restored prairie land use. Black bars indicate one standard deviation around the mean.

soils, with a measurable increase then decrease in EC with depth (**Figure 3D**).

## Discharge

The average total stream flow for the studied period was 0.0113 $m^3$ $sec^{-1}$ with a median flow rate of 0.0060 $m^3$ $sec^{-1}$. The flow was <0.003 $m^3$ $sec^{-1}$ 10% of the time, and <0.023 $m^3$ $sec^{-1}$ 90% of the time. Based on the mass balance calculations, the south fork of Glacier Creek accounted for an average of 22% of the total flow (range: 12–31%) while the north fork accounted for an average of 78% of the total flow (range: 59–88%). There did not appear to be a relationship between total flow and the flow distribution between the two forks. The highest flows occurred in May and June; lowest flows occurred in September to December.

## Solute Chemistry

### Cations

In the agricultural soils, pore water annual average cation concentrations were significantly higher ($p < 0.05$) for $Ca^{2+}$ and $Mg^{2+}$, but not $Na^+$ and $K^+$, in both Nebraska and Iowa (**Figures 4A,B**). As with the concentrations, annual average $Ca^{2+}$ and $Mg^{2+}$ elemental fluxes in agricultural soil pore waters were higher at both Nebraska and Iowa, but the difference is significant only in Iowa (**Figures 4C,D**). At all measured depths, soil pore water cation concentrations were lower in prairie than agricultural soils (**Supplementary Figure 1**).

For stream water concentrations in Nebraska, all of the major cations except for $Na^+$ were significantly higher ($p < 0.05$) in stream locations draining restored prairie compared to stream locations draining agricultural fields (**Table 2** and **Figure 5**). Conversely, $Na^+$ was significantly lower in streams draining prairie land use. However, the cation fluxes in the stream were higher in water draining agricultural fields (**Table 3**). The concentrations of redox active species (Fe/Mn) were also significantly higher in the prairie locations. Aluminum concentrations were consistently just above the detection limit for the ICP-MS (0.7 ppb), and were not different between the prairie and agriculture associated sections of the stream. Stream fluxes for the major cations associated with agriculture were higher than the elemental fluxes from prairie (**Figure 5**).

### Anions

Soil pore water $Cl^-$ and $NO_3^-$ concentrations were higher overall in Nebraska compared to Iowa, but only $NO_3^-$ concentrations were significantly higher ($p < 0.05$) in agricultural soils compared to prairie soils in Nebraska; anion concentrations were not significantly different amongst soil pore waters in Iowa (**Figure 6**). Very little $NO_3^-$ (<1 mg $L^{-1}$) was detected in either agriculture or prairie soil pore waters in Iowa. Masarik et al. (2014) measured mean annual $NO_3^-$-N leachate concentrations of 12.2 mg $L^{-1}$ under no till corn crops and <0.1 mg $L^{-1}$ under restored prairie vegetation in silty loess soils with a similar climate to our study. The Iowa site has much lower $NO_3^-$ concentrations under agriculture than the Masarik et al. (2014) data, while the average under Nebraska agriculture is much higher (42 ± 51 mg $L^{-1}$), although highly variable. The concentrations under the prairie land use at both locations are within an order of magnitude of Masarik et al. (2014). At this point it is not clear if the

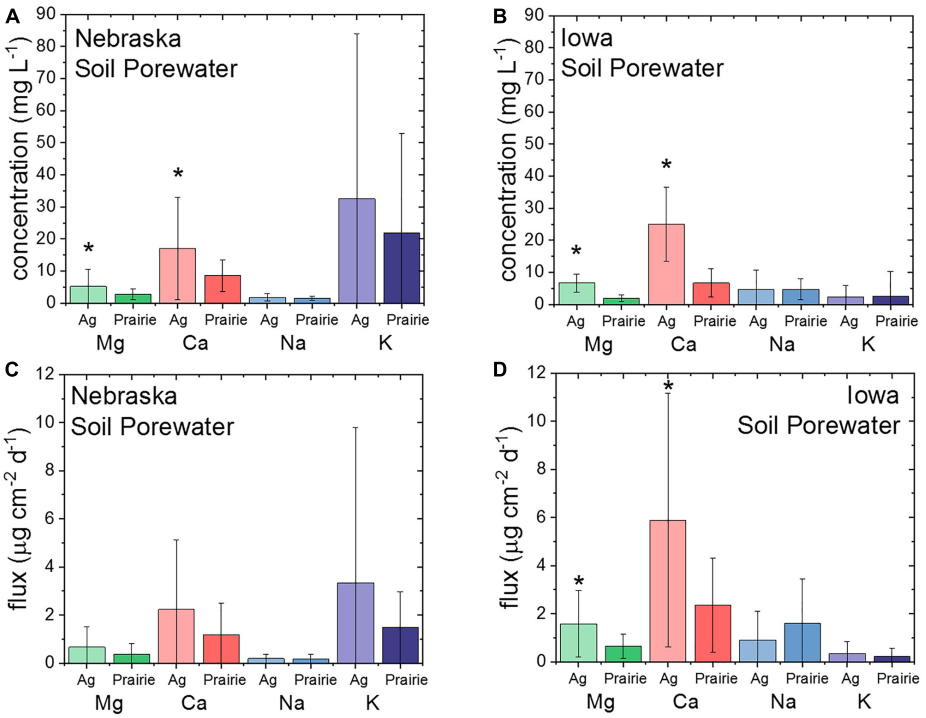


**FIGURE 4 |** Annual average soil pore water cation concentrations and fluxes at the Nebraska **(A,C)** and Iowa **(B,D)** study sites for both agriculture and restored prairie land use. Stars indicate significant differences ($p < 0.05$) between land uses at that site and black bars indicate one standard deviation around the mean.

variability in concentrations are related to fertilizer application rates or varied biogeochemical cycling rate of nitrogen at the different sites.

Similar to the cations, major stream anion concentrations ($Cl^-$ and $SO_4^{2-}$) were significantly higher ($p < 0.05$) in the prairie locations than they were in the agricultural stream (**Figure 6**). The minor anions ($NO_2^-$, $PO_4^{3-}$) were frequently non-detectable. Nitrate concentrations were more reliably detected, but were not significantly different between streams draining prairie and agriculture in Nebraska. When detectable in Nebraska stream samples, $NO_3^-$ concentrations were typically $< 0.4$ mg $L^{-1}$. In both the prairie and agricultural stream stretches, there was a pulse ($>10$ mg $L^{-1}$) of $NO_3^-$ in early spring (March for agriculture, and April for prairie) (**Supplementary Tables 6–10**). The juxtaposition in time implies a spring flush of $NO_3^-$ from both systems, but longer time scales are needed to confirm the large episodic $NO_3^-$ exports. Nitrite concentrations were typically too low to be detected (<11 ppb), but they generally followed the $NO_3^-$ concentrations. Phosphate was also generally too low to be detected (<19 ppb). When it was detected, the SI for hydroxyapatite was generally undersaturated (SI range: −4.8 to −0.08) implying a non-mineral control on $PO_4^{3-}$ concentrations.

### Alkalinity

The alkalinity was significantly higher in the stream waters associated with the prairie (**Tables 4**, **5**). Unlike other major ions, the pore water data was not consistent between agriculture and prairie between the two study sites. In Nebraska, the pore waters had slightly higher alkalinity under the prairie, but in Iowa the alkalinity was noticeably lower under the prairie.

## Speciation

The results from the speciation calculations are shown in **Table 5**. For stream samples, the average error in the charge balance for all speciated samples was 5.8% (with excess anions), indicating the combination of analyses was likely complete and accurate. For pore waters, the average error in the charge balance was 6.9%, also with excess anions.

# DISCUSSION

Using the collected data, a conceptual model is constructed below that shows soil hydrology and geochemistry, and ultimately stream chemistry, differ based on land use. The data point to a model where precipitation drains more rapidly and deeper under prairie land use, and much slower and shallower under agricultural land use. It also appears that some of the precipitation falling on agricultural soils does not infiltrate at all, and instead runs off directly to the stream. The differences in soil hydrology influence soil pore water chemistry, especially $Ca^{2+}$ and $Mg^{2+}$ fluxes, which in turn impact stream chemistry. Such changes in geochemical and hydrologic fluxes have been realized in just a few decades since switching land use from agriculture to prairie.

**TABLE 2 |** Average cation concentrations for stream waters, pore waters, and precipitation from Nebraska and Iowa study sites under agriculture and restored prairie land use.

| | Precipitation | | Pore Water | | Stream Water | | | | |
|---|---|---|---|---|---|---|---|---|---|
| | Agriculture | Prairie | Agriculture | Prairie | | Agriculture | | Prairie | |
| **Ion** | | | | | **GC2** | **GC3** | **GC4** | **GC5** | **GC6** |
| **Nebraska** | | | | | | | | | |
| *n* | – – – | 6 | 30 | 31 | 10 | 10 | 11 | 11 | 10 |
| $Na^+$ (mg/L) | – – – | 0.498 (0.48) | 1.79 (1.2) | 1.55 (0.64) | 19.9 (5.9) | 20.6 (6.2) | 21.8 (7.8) | 18.9 (8.4) | 18.5 (10) |
| $K^+$ (mg/L) | – – – | 3.80 (4.3) | 32.6 (51) | 21.8 (31) | 2.15 (0.39) | 2.02 (0.30) | 1.40 (0.50) | 3.37 (0.82) | 4.0 (1.2) |
| $Mg^{2+}$ (mg/L) | – – – | 1.08 (2.3) | 5.18 (5.3) | 2.69 (1.7) | 23.8 (2.6) | 23.0 (1.8) | 23.4 (3.0) | 30.6 (3.3) | 31.0 (1.9) |
| $Ca^{2+}$ (mg/L) | – – – | 3.45 (3.1) | 17.0 (16) | 8.62 (4.9) | 84.3 (8.9) | 80.4 (4.8) | 78.6 (8.4) | 99.8 (12) | 111.2 (5.3) |
| $Fe_{Total}$ (μg/L) | – – – | – – – | – – – | – – – | 215 (106) | 633 (1056) | 179 (67) | 2030 (1720) | 1110 (1550) |
| $Mn^{2+}$ (μg/L) | – – – | – – – | – – – | – – – | 211 (134) | 289 (263) | 284 (203) | 1090 (794) | 3160 (1737) |
| $Al^{3+}$ (μg/L) | – – – | – – – | – – – | – – – | 2.3 (3.8) | 0.87 (1.3) | 2.1 (3.4) | 1.1 (1.6) | 1.3 (1.5) |
| **Iowa** | | | | | | | | | |
| *n* | 7 | 5 | 13 | 15 | – – – | – – – | – – – | – – – | – – – |
| $Na^+$ (mg/L) | 0.672 (0.86) | 0.497 (0.41) | 4.70 (6.0) | 4.74 (3.2) | – – – | – – – | – – – | – – – | – – – |
| $K^+$ (mg/L) | 1.70 (3.1) | 0.396 (0.21) | 2.32 (3.6) | 2.55 (7.8) | – – – | – – – | – – – | – – – | – – – |
| $Mg^{2+}$ (mg/L) | 0.421 (0.41) | 0.571 (0.40) | 6.73 (2.8) | 1.87 (1.1) | – – – | – – – | – – – | – – – | – – – |
| $Ca^{2+}$ (mg/L) | 2.38 (1.0) | 1.75 (1.5) | 24.9 (12) | 6.70 (4.4) | – – – | – – – | – – – | – – – | – – – |

*One standard deviation around the mean is given in parentheses. A dash indicates variable was not measured and n indicates the number of samples collected per site for each sample type.*

## Geochemical Fluxes

For $Ca^{2+}$ and $Mg^{2+}$ in the pore waters, the likely control on concentration is the dissolution of carbonates. The speciation calculations showed undersaturation with respect to both calcite and dolomite under both land uses at both study sites, implying a kinetic control on dissolution (**Table 5**). Based on the pH and the activities of the carbonate aqueous species in the pore water samples, the calcite dissolution rate would be expected to be about 6% faster in the prairie soils compared to the agricultural soils in Nebraska and 8% faster in Iowa (Plummer et al., 1978). However, at both locations, the saturation index for calcite was more negative in the prairie soils suggesting less calcite has dissolved compared to the agricultural soil. Since chemical equilibrium was not attained, and the calculated rates of dissolution do not match the amount of dissolution observed, the control on carbonate solubility is likely not a chemical constraint. Instead, it is more likely a hydrological constraint where the pore water under agriculture is moving more slowly and has more time to interact with the soil matrix thereby moving slightly closer to equilibrium despite slower kinetics (Jin et al., 2008). The same saturation state relationships were also seen for dolomite.

In the Nebraska soils, the differences in the saturation indices were smaller than those in Iowa, yet the calculated $P_{CO2}$ was noticeably higher in prairie soils (**Table 5**). Since the $CO_2$ in the pore space from mineral sources was at least similar between agriculture and prairie soils at each site, the larger $P_{CO2}$ is likely due to more biological respiration occurring in the prairie soils (Raich and Tufekcioglu, 2000). Despite the increased $P_{CO2}$ and decreased pH in prairie soil from respiration leading to the expected faster dissolution rate, the rate of water drainage appears to more strongly affect the total amount of carbonate dissolution in the two soils (Egli and Fitze, 2001). However, unlike the Nebraska soils, there was a much larger difference between the agricultural and prairie saturation indices in Iowa, and the $P_{CO2}$ was larger in the agricultural soils. In this case, the larger $P_{CO2}$ in agriculture is more likely driven by either the larger amounts of carbonate dissolution or by the distinct soil types associated with the Iowa site in Nebraska, discussed below. Between the pore water samplers and the stream, conditions shift such that in both the prairie and agricultural setting, the carbonates are essentially at equilibrium and are controlling $Ca^{2+}$ and $Mg^{2+}$ fluxes.

Relative to the pore waters, stream water elemental fluxes appear to be driven by flow. Even though the concentrations

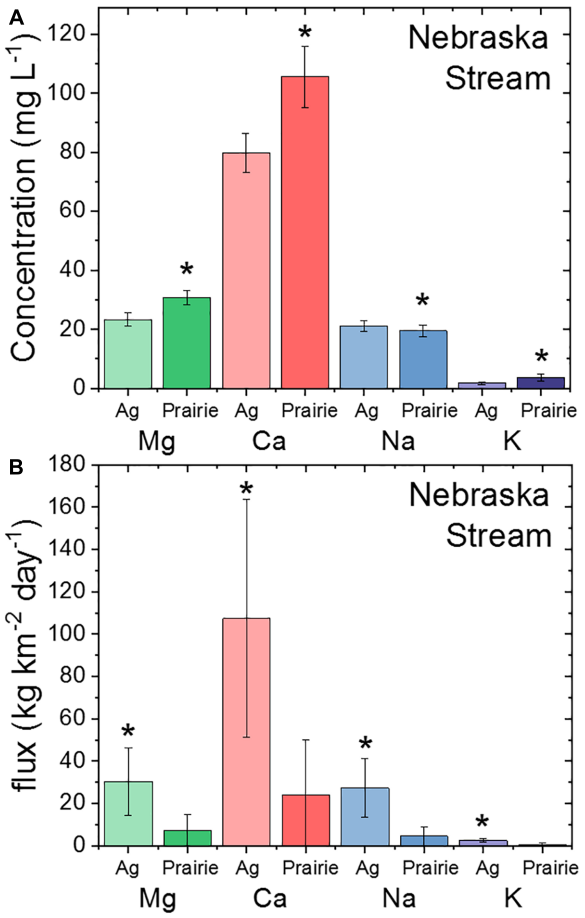


**FIGURE 5 |** Annual average cation concentrations **(A)** and fluxes **(B)** from streams draining restored prairie or agricultural land use in Nebraska. Stars indicate significant differences ($p < 0.05$) between land uses at that site and black bars indicate one standard deviation around the mean.

of $Ca^{2+}$ and $Mg^{2+}$ were higher in the stretches associated with the prairie in Nebraska, the much higher flow rate from the agricultural setting led to larger elemental fluxes associated with agriculture. Similar relationships have been widely observed, for example by Godsey et al. (2009) who analyzed weathering-derived solutes (Si, Ca, and Mg) in 59 watersheds and showed that solute fluxes were proportional to discharge. Pore water fluxes are more typically concentration driven. Extractable pore water volumes under both land uses were at least comparable, such that larger concentrations under agriculture also led to larger fluxes.

Although no stream water was routinely sampled for solute chemistry in Iowa, two grab samples from Clear Creek near the agricultural study site were collected in June 2015 and December 2016 (westernmost triangle in **Figure 1D**). Average concentrations from these two collection dates were $26.5 \pm 0.38$ mg $L^{-1}$ of $Mg^{2+}$, $58 \pm 22$ mg $L^{-1}$ of $Ca^{2+}$, $7.8 \pm 1.0$ mg $L^{-1}$ of $Na^{+}$, and $0.73 \pm 0.12$ mg $L^{-1}$ of $K^{+}$, values that are similar in magnitude to concentrations measured in the Nebraska stream. Although there is no stream draining prairie in Iowa to compare cation concentrations, the Iowa stream draining agriculture appears to have similarly high concentrations of $Ca^{2+}$ and $Mg^{2+}$ relative to $Na^{+}$ and $K^{+}$.

## Hydrologic Connectivity

From the chemical and data analysis, interpretations of hydrologic flowpaths can be made. From the pore water analysis, it appears that water drains more slowly within the top 1 m of the agricultural soil compared to the prairie soils, which caused the water chemistry to move closer to equilibrium with respect to calcite and dolomite in agricultural soils. The larger drainage rate under the prairie soils is consistent with other work showing that more deeply rooted prairie perennials make better connections between pore spaces in the soil than do the annual plants planted in agricultural settings (Udawatta et al., 2008). However, comparing the relative stream concentrations to the pore water concentrations implies a disconnect under the agricultural setting. Despite the higher relative concentrations in the agricultural pore waters, the relative stream concentrations were lower, implying a second water source that does not interact with the soils thereby diluting the stream concentrations. A likely interpretation is that some amount of the precipitation that falls on the agricultural soils does not infiltrate, but instead runs off more directly to the stream (Schilling et al., 2008). Furthermore, $Cl^{-}$ concentrations were roughly four times lower in agricultural stream water compared to the soil pore water, suggesting possible preferential flowpaths contributing to the agricultural stream (**Table 4**) (Aubert et al., 2013). The high soil pore water $Cl^{-}$ concentrations, although extremely variable, may also point to longer residence time for shallow water in the agricultural soils compared to prairie soils (Kirchner et al., 2010).

Under the prairie setting in Nebraska, there was no evidence of increased runoff, and precipitation instead infiltrates rapidly through the upper 50 cm of the soil profile, resulting in overall lower soil moisture than the agricultural soil that receives the same amount of precipitation (**Figure 3A**). Furthermore, prairie soil moisture increased at all depths in response to precipitation events, especially in the fall when grasses have senesced (**Figure 2A**). In contrast, a study by Masarik et al. (2014) on similar silty loess soils and climate to our study reported higher soil matric potential measurements in prairie soils compared to agricultural soils, indicating prairie soils did not dry out as much as soils planted with corn, and overall drainage through restored prairie soils was 57 – 69% lower than agriculture soils. The authors attributed this difference to the ability of perennial grass vegetation with established root networks to take up water earlier in the season and later into the year than corn vegetation. Although it is likely that differences in water use between crops and prairie grasses exist at our sites, the differences we observed in soil moisture and EC persisted even in fall after crops were removed and grasses senesced, so moisture removal by prairie vegetation is not likely to entirely explain the different patterns in soil moisture and EC.

In contrast, average soil moisture at the Iowa study site was greater in prairie soils at all depths compared to agricultural soils (**Figure 3B**). This is likely due to differences in soil genesis between these sites: the restored prairie site was forested prior

**TABLE 3 |** Average daily solute fluxes for stream and pore water in Nebraska (NE) and Iowa (IA) agriculture or restored prairie land use.

| | $Na^+$ | $Ca^{2+}$ | $K^+$ | $Mg^{2+}$ | $Cl^-$ | $NO_3^-$ | $SO_4^{2-}$ |
|---|---|---|---|---|---|---|---|
| Stream waters | ——————————— kg $km^{2-}$ $day^{-1}$ ——————————— | | | | | | |
| NE Agriculture | 27.3 (14) | 107 (56) | 2.56 (0.95) | 30.3 (16) | 3.38 (2.6) | 0.153 (0.15) | 6.98 (4.3) |
| NE Prairie | 4.48 (4.6) | 24.1 (26) | 0.665 (0.45) | 7.27 (7.6) | 9.06 (9.0) | 0.0731 (0.14) | 2.00 (2.2) |
| Pore waters | ——————————— μg $cm^{2-}$ $day^{-1}$ ——————————— | | | | | | |
| NE Agriculture | 0.186 (0.18) | 2.23 (2.9) | 3.35 (6.4) | 0.662 (0.86) | 4.25 (11) | 2.88 (3.0) | 0.588 (0.70) |
| NE Prairie | 0.183 (0.18) | 1.19 (1.3) | 1.48 (1.5) | 0.380 (0.43) | 1.75 (1.7) | 0.0208 (0.026) | 1.40 (2.1) |
| IA Agriculture | 0.912 (1.2) | 5.89 (5.3) | 0.351 (0.51) | 1.58 (1.4) | 2.00 (2.2) | 0.275 (0.41) | 2.98 (3.2) |
| IA Prairie | 1.61 (1.8) | 2.36 (2.0) | 0.223 (0.35) | 0.639 (0.51) | 0.286 (0.37) | 0.198 (0.28) | 2.82 (3.3) |

*One standard deviation around the mean is given in parentheses.*

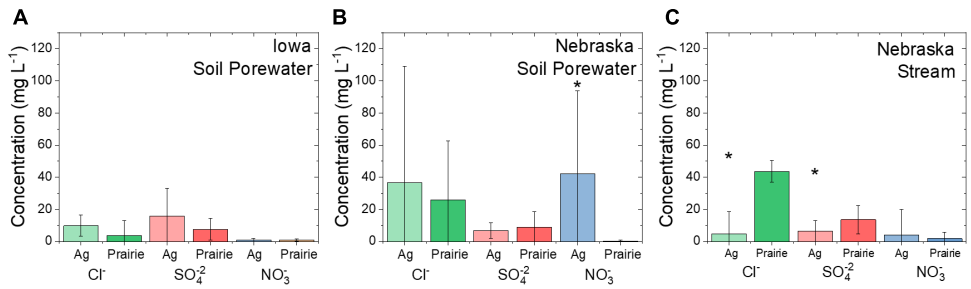


**FIGURE 6 |** Average annual soil pore water anion concentrations at the Iowa **(A)** and Nebraska **(B)** study sites and annual average stream water anion concentrations at the Nebraska study site **(C)** for both agriculture and restored prairie land use. Stars indicate significant differences ($p < 0.05$) between land uses at that site and black bars indicate one standard deviation around the mean.

to cultivation, which led to the formation of Alfisols, a soil that typically forms under hardwood forest in humid areas and is characterized by clay-enriched subsoil and relatively thin accumulations of organic matter (Soil Survey Staff, 1999). In contrast, the agricultural site hosted tallgrass prairie prior to cultivation, which resulted in the formation of Mollisols, or soils characterized by high organic matter accumulation (Soil Survey Staff, 1999). Clay content was overall slightly higher in the restored prairie soil (∼26% clay in the upper 50 cm) compared to the agricultural site (∼22% clay in the upper 50 cm), perhaps as a result of the soil previously forming under forest vegetation rather than prairie vegetation. Water retention is greater for clay-sized soil particles (Saxton and Rawls, 2006), which could account for the higher moisture content in the more clay-rich restored prairie soil. However, despite the different soil forming conditions prior to cultivation between the Iowa restored prairie and agricultural soils, the patterns with respect to soil pore water chemistry were similar to observations at the Nebraska site.

There was evidence in the Nebraska prairie of water interactions with mineral phases much deeper in the subsurface. At the stream sampling locations draining prairie (G5 and G6 in **Figure 1C**), the concentration of the redox active $Fe^{2+/3+}$ and $Mn^{2+}$ were significantly higher than found in the stream draining agriculture (G3 and G4 in **Figure 1C**). Further, large amounts of iron flocs were consistently present in the prairie sampling locations, and they were not present at the agricultural locations, despite similar ranges of saturation indices for ferrihydrite [prairie saturation index (SI) range: 1.61–2.79, agriculture SI range: 0.16–2.28]. The larger concentrations of the redox active metals suggests a water source that is separated from the atmosphere. For all four stream sampling locations in Nebraska, the effective $P_{CO2}$ was also much higher than equilibrium with the atmosphere (GC3 = 3.8E-2, GC4 = 2.6E-2, GC5 = 2.3E-2, GC6 = 6.0E-2, atmospheric $P_{CO2}$ = ∼4E-4, all values in atm). The highest value was at position GC6 in the prairie, which again implies a water source that is separated from the atmosphere. Between GC6 and GC5, there is a small cascade where $CO_2$ is likely being lost. The stream section connecting GC4 (upstream) to GC3 (downstream) is quite flat so de-gassing is at a minimum. The stream $P_{CO2}$ values are essentially the same order of magnitude as values found in groundwater associated with limestone host rock (Macpherson et al., 2008).

**TABLE 4 |** Average anion concentrations for stream waters, pore waters and precipitation from Nebraska and Iowa study sites under agriculture and restored prairie land use.

| | Precipitation | | Pore water | | Stream water | | | | |
|---|---|---|---|---|---|---|---|---|---|
| | Agriculture | Prairie | Agriculture | Prairie | | Agriculture | | Prairie | |
| **Ion** | | | | | **GC2** | **GC3** | **GC4** | **GC5** | **GC6** |
| **Nebraska** | | | | | | | | | |
| *N* | --- | 6 | 34 | 36 | 10 | 10 | 11 | 11 | 10 |
| $Cl^-$ (mg/L) | --- | 2.98 (2.6) | 36.7 (72) | 25.8 (37) | 9.06 (5.7) | 8.17 (20) | 1.17 (0.53) | 39.6 (5.1) | 47.3 (5.6) |
| $NO_2^-$ (mg/L) | --- | 0.0708 (0.028) | 0.207 (0.28) | 0.0609 (0.092) | 0.017 (0.006) | 0.024 (0.016) | 0.020 (0.004) | 0.017 (0.017) | 4.38 (6.3) |
| $NO_3^-$ (mg/L) | --- | 3.06 (3.5) | 42.3 (51) | 0.321 (0.56) | 3.18 (2.1) | 0.266 (0.45) | 0.724 (0.84) | 0.412 (0.53) | 4.38 (6.3) |
| $SO_4^{2-}$ (mg/L) | --- | 1.74 (2.1) | 6.86 (4.8) | 8.92 (9.6) | 8.42 (3.1) | 7.18 (7.0) | 5.81 (6.6) | 9.89 (11.3) | 17.2 (3.7) |
| $PO_4^{3-}$ (mg/L) | --- | 0.0156 (0.17) | 0.368 (0.82) | 0.298 (0.71) | 0.089 (0.018) | 0.113 (0.059) | 0.069 (0.027) | ND | 0.063 (0.062) |
| Alkalinity (mg/L as $CaCO_3$) | --- | --- | 14.7 (7.9) | 20.5 (10) | 354 (18) | 355 (18) | 355 (24) | 390 (24) | 413 (30) |
| **Iowa** | | | | | | | | | |
| *n* | 8 | 7 | 14 | 16 | --- | --- | --- | --- | --- |
| $Cl^-$ (mg/L) | 0.730 (0.62) | 0.748 (0.44) | 9.74 (6.6) | 3.76 (9.1) | --- | --- | --- | --- | --- |
| $NO_2^-$ (mg/L) | 0.0546 (0.045) | 0.518 (1.1) | 0.032 (0.027) | 0.169 (0.23) | --- | --- | --- | --- | --- |
| $NO_3^-$ (mg/L) | 1.16 (0.55) | 0.518 (1.1) | 0.922 (1.0) | 0.968 (0.76) | --- | --- | --- | --- | --- |
| $SO_4^{2-}$ (mg/L) | 1.15 (0.41) | 1.87 (2.09) | 15.8 (17) | 7.52 (6.8) | --- | --- | --- | --- | --- |
| $PO_4^{3-}$ (mg/L) | 1.42 (1.9) | 0.639 (0.82) | 1.42 (2.0) | 0.193 (0.25) | --- | --- | --- | --- | --- |
| Alkalinity (mg/L as $CaCO_3$) | 12.0 (5.7) | 17.1 (6.5) | 88.8 (33) | 32.3 (16) | --- | --- | --- | --- | --- |

*One standard deviation around the mean is given in parentheses. ND means that ion was never detected in samples from that site. A dash indicates variable was not measured and n indicates the number of samples collected per site for each sample type.*

## Conceptual Model

The observations reported here lead to a conceptual model whereby agricultural land use has altered soil hydrology, and in turn soil chemistry, and those alterations were propagated to changes in nearby stream chemistry. Precipitation appears to infiltrate agricultural soils slowly, allowing more time for mineral-water interaction (**Figure 7**). The agricultural soil waters were enriched in ions, especially $Ca^{2+}$ and $Mg^{2+}$, but rather than flushing the dissolved solutes deeper into the soil profile, the solutes appear to be routed rapidly to the nearby stream where they influence stream chemistry. In contrast, precipitation entering a soil dominated by prairie vegetation appears to infiltrate rapidly, limiting time for mineral-water interactions near the surface. Thus, soil pore water chemistry more closely resembles dilute precipitation and infiltrates deeper into the soil before entering the stream.

A likely explanation for differences in hydrology between agriculture and restored prairie, and in turn the soil water chemistry, is reduced pore connectivity in agricultural systems due to limited rooting depths and densities of corn and soybean crops as well as compaction by agricultural equipment that destroys soil structure. Prairie systems, however, are known for extensive and deep root networks (Jackson et al., 1996) that create

**TABLE 5 |** Water chemistry measured and calculated values for stream and pore waters in Nebraska (NE) and Iowa (IA) agriculture or restored prairie land use.

| | pH | Alkalinity (mg $L^{-1}$ as $CaCO-_3$) | $P_{CO2}$ (atm) | Calcite SI | Dolomite SI |
|---|---|---|---|---|---|
| **Stream waters** | | | | | |
| NE Agriculture | 7.06 (0.2) | 355 (21) | 3.2E-2 | −0.035 | −0.31 |
| NE Prairie | 6.94 (0.3) | 402 (30) | 4.1E-2 | 0.12 | 0.058 |
| **Pore waters** | | | | | |
| NE Agriculture | 6.83 (0.4) | 14.7 (7.9) | 1.2E-3 | −2.6 | −4.6 |
| NE Prairie | 6.59 (0.7) | 20.5 (10) | 4.3E-3 | −2.8 | −5.8 |
| IA Agriculture | 7.04 (0.6) | 88.8 (33) | 5.9E-3 | −0.79 | −1.9 |
| IA Prairie | 7.24 (0.3) | 32.3 (16) | 2.9E-3 | −2.1 | −4.4 |

*For directly measured values, one standard deviation around the mean is given in parentheses, all other values were calculated in PHREEQC.*

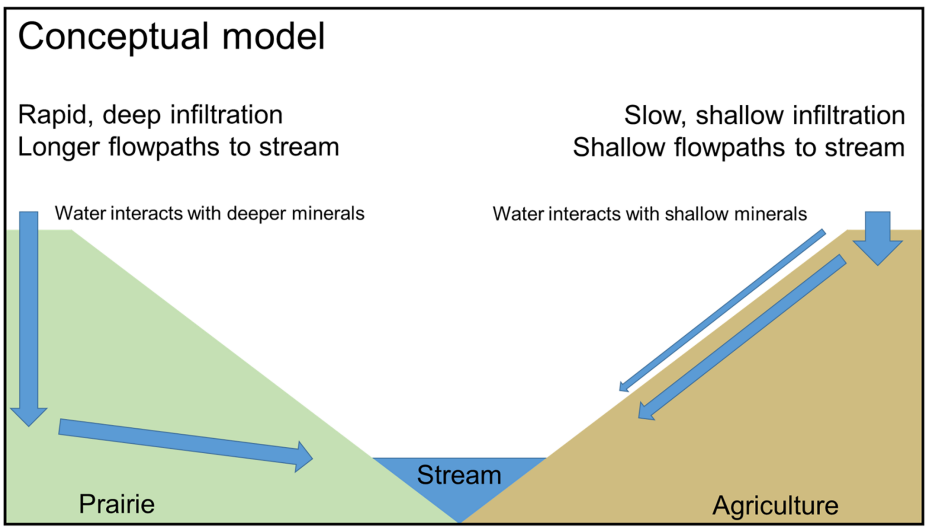


**FIGURE 7 |** Conceptual model of hydrologic fluxes influencing soil and stream chemistry in intensively managed landscapes.

preferential flowpath and enhance soil aggregation (Udawatta et al., 2008), providing pathways for water and oxygen to infiltrate more deeply into the soil. Directly quantifying differences in pore networks is a logical future step for investigating hydrologic and geochemical connectivity in these intensively managed systems.

Furthermore, an intriguing observation is the relatively short time needed to observe differences in soil hydrology and chemistry between land uses. In Nebraska, both soil sampling locations were farmed until roughly 50 years ago when agriculture ceased in one part of the watershed. In Iowa, the site was farmed until 20 years ago. Thus, the changes in pore connectivity and hydrologic fluxes have been realized in just a few decades, and the influence on soil and stream chemistry is already distinguishable. Such results point to a highly dynamic system that can be influenced by land use not just at the surface, where direct management occurs, but deeper into the critical zone and ultimately into streams.

## CONCLUSION

Clear chemical differences in both the pore and stream waters were detected under two land uses (row crop agriculture and restored prairie) at two study sites (Nebraska and Iowa) that are representative of the Midwestern USA region. Similarly, clear differences were observed between soil moisture and EC under the two land uses. From these differences we constructed a conceptual model describing likely hydrological processes within the CZ at the Nebraska field site. It appears that within just a few decades, restored prairie can re-establish much of the deeper pore connectivity that tends to be destroyed under agriculture. The restoration of connectivity leads to alterations of soil and mineral weathering patterns within the pore spaces of the soil. The altered dissolution of the minerals based on surficial land use is transferred downslope as the pore waters drain into the connected stream. Under prairie land use, it appears that this draining is likely direct, proceeding downward to the impermeable till and surfacing in the stream. Under agriculture land use, the draining of pore water is likely indirect, with the water perching in the shallow sub-surface before flowing with associated runoff into the connected stream. Future research will focus on identifying the mechanisms driving contrasting hydrologic and geochemical behavior between land use types.

## DATA AVAILABILITY STATEMENT

The meteorological, soil sensor, and discharge datasets generated from this study can be found in the EarthChem Library (http://earthchem.org/library).

## AUTHOR CONTRIBUTIONS

AD, AM, and EB conceptualized the research. AD, AM, EB, SP, CC, and AH collected and processed samples. AM and AH completed laboratory analysis and speciation calculations. AD, AM, and EB analyzed the data. AD, AM, and EB prepared the manuscript.

## FUNDING

This work was supported by NSF Grant EAR-1331906 for the Intensively Managed Landscapes Critical Zone Observatory (PI P. Kumar), Douglas County Environmental Services, the Sherwood Foundation Teacher-Researcher Partnership Program grant (ID #5444), the University of Nebraska at Omaha University Committee on Research and Creative Activity (UCRCA), and the generous support of B. Hayes and T. Bragg at Glacier Creek Preserve.

## ACKNOWLEDGMENTS

We would like to thank the Maas Family and FW Kent State Park for supporting research on their properties, as well as Barbi Hayes and Tom Bragg for their support of research at Glacier Creek Preserve. We also thank Tracy Coleman for field instrumentation support at Glacier Creek Preserve, Chris Jackson for assistance collecting and analyzing samples, Katie Goff and Will Boyd for their help sampling Iowa sites, and Paul Hunt for assistance generating site maps. Additional field and laboratory assistance was provided by: R. Benzoni, R. Burns, M. Cain, D. Dere, J. Felix, T. Frederick, K. Gerdes, B. Greco, L. LeGrand, D. Klein, K. Knapp, J. Lopez, S. Nath, M. O'Malley, S. Rodie, S. Sterner, L. Stover, B. Terrell, and T. Webb. We also greatly appreciate the insightful suggestions provided by the reviewers.

## SUPPLEMENTARY MATERIAL

The Supplementary Material for this article can be found online at: https://www.frontiersin.org/articles/10.3389/feart.2019.00024/full#supplementary-material

## REFERENCES

Anders, A. M., Bettis, E. A. III, Grimley, D. A., Stumpf, A. J., and Kumar, P. (2018). Impacts of quaternary history on critical zone structure and processes: examples and a conceptual model from the intensively managed landscapes critical zone observatory. *Front. Earth Sci.* 6:24. doi: 10.3389/feart.2018.00024

Aubert, A. H., Gascuel-Odoux, C., Gruau, G., Akkal, N., Faucheux, M., Fauvel, Y., et al. (2013). Solute transport dynamics in small, shallow groundwater-dominated agricultural catchments: insights from a high-frequency, multisolute 10 yr-long monitoring study. *Hydrol. Earth Syst. Sci.* 17, 1379–1391. doi: 10.5194/hess-17-1379-2013

Banwart, S. (2011). Save our soils. *Nature* 474, 151–152. doi: 10.1038/474151a

Bettis, E. A. III, Muhs, D. R., Roberts, H. M., and Wintle, A. G. (2003). Last glacial loess in the conterminous USA. *Quat. Sci. Rev.* 22, 1907–1946. doi: 10.1016/S0277-3791(03)00169-0

Brantley, S. L., Goldhaber, M. B., and Ragnarsdottir, K. V. (2007). Crossing disciplines and scales to understand the critical zone. *Elements* 3, 307–314. doi: 10.2113/gselements.3.5.307

Davis, M. L., and Cornwell, D. A. (1998). *Introduction to Environmental Engineering*, 3rd Edn. Boston, MA: McGraw-Hill.

Egli, M., and Fitze, P. (2001). Quantitative aspects of carbonate leaching of soils with differing ages and climates. *Catena* 46, 35–62. doi: 10.1016/S0341-8162(01)00154-0

Foley, J. A., DeFries, R., Asner, G. P., Barford, C., Bonan, G., Carpenter, S. R., et al. (2005). Global consequences of land use. *Science* 309, 570–574. doi: 10.1126/science.1111772

Godsey, S. E., Kirchner, J. W., and Clow, D. W. (2009). Concentration-discharge relationships reflect chemostatic characteristics of US catchments. *Hydrol. Process.* 23, 1844–1864. doi: 10.1002/hyp.7315

Hinckley, E.-L. S., Barnes, R. T., Anderson, S. P., Williams, M. W., and Bernasconi, S. M. (2014). Nitrogen retention and transport differ by hillslope aspect at the rain-snow transition of the colorado front range. *J. Geophys. Res. Biogeo.* 119, 1281–1296. doi: 10.1002/2013JGE002588

Jackson, R. B., Canadell, J., Ehleringer, J. R., Moonery, H. A., Sala, O. E., and Schulze, E. D. A. (1996). Global analysis of root distributions for terrestrial biomes. *Oecologia* 108, 389–411. doi: 10.1007/BF00333714

Jin, L., Andrews, D. M., Holmes, G. H., Lin, H., and Brantley, S. L. (2011). Opening the "Black Box": water chemistry reveals hydrological controls on weathering in the susquehanna shale hills critical zone observatory. *Vadose Zone J.* 10, 928–942. doi: 10.2136/vzj2010.0133

Jin, L., Williams, E. L., Szramek, K. J., Walter, L. M., and Hamilton, S. K. (2008). Silicate and carbonate mineral weathering in soil profiles developed on pleistocene glacial drift (Michigan, USA): mass balances based on soil water geochemistry. *Geochim. Cosmochim. Acta* 72, 1027–1042. doi: 10.1016/j.gca.2007.12.007

Kirchner, J. W., Tetzlaff, D., and Soulsby, C. (2010). Comparing chloride and water isotopes as hydrological tracers in two Scottish catchments. *Hydrol. Process.* 24, 1631–1645. doi: 10.1002/hyp.7676

Kumar, P., Le, P. V. V., Papanicolaou, A. N., Rhoads, B. L., Anders, A. M., Stumpf, A., et al. (2018). Critical transition in critical zone of intensively managed landscapes. *Anthropocene* 22, 10–19. doi: 10.1016/j.ancene.2018.04.002

Macpherson, G. L., Roberts, J. A., Blair, J. M., Townsend, M. A., Fowle, D. A., and Beisner, K. R. (2008). Increasing shallow groundwater CO2 and limestone weathering, Konz Prairie, USA. *Geochim. Cosmochim. Acta* 72, 5581–5599. doi: 10.1016/j.gca.2008.09.004

Masarik, K. C., Norman, J. M., and Brye, K. R. (2014). Long-term drainage and nitrate leaching below well-drained continuous corn agroecosystems and a prairie. *J. Environ. Protect.* 5, 240–254. doi: 10.4236/jep.2014.54028

Neal, C. W. M., and Anders, A. M. (2015). Suspended sediment supply dominated by bank erosion in a low-gradient agricultural watershed, Wildcat Slough, Fisher, Illinois, United States. *J. Soil Water Conserv.* 70, 145–155. doi: 10.2489/jswc.70.3.145

Papanicolaou, A. N., Abban, B. K., Dermisis, D. C., Giannopoulos, C. P., Flanagan, D. C., Frankenberger, J. R., et al. (2018). Flow resistance interactions on hillslopes with heterogeneous attributes: effects on runoff hydrograph characteristics. *Water Resour. Res.* 54, 359–380. doi: 10.1002/2017WR021109

Papanicolaou, A. N., Elhakeem, M., Wilson, C. G., Burras, C. L., West, L. T., Lin, H., et al. (2015a). Spatial variability of saturated hydraulic conductivity at the hillslope scale: understanding the role of land management and erosional effect. *Geoderma* 24, 58–68. doi: 10.1016/j.geoderma.2014.12.010

Papanicolaou, A. N., Wacha, K. M., Abban, B. K., Wilson, C. G., Hatfield, J. L., Stanier, C. O., et al. (2015b). From soilscapes to landscapes: a landscape-oriented approach to simulate soil organic carbon dynamics in intensively managed landscapes. *J. Geophys. Res. Biogeo.* 120, 2375–2401. doi: 10.1002/2015JG00.078

Papanicolaou, A. N. T., Wilson, C. G., Tsakiris, A. G., Sutarto, T. E., Bertrand, F., Rinaldi, M., et al. (2017). Understanding mass fluvial erosion along a bank profile: using PEEP technology for quantifying retreat lengths and identifying event timing. *Earth Surf. Process. Landforms* 42, 1717–1732. doi: 10.1002/esp.4138

Parkhurst, D. L., and Appelo, C. A. J. (2013). *Description of Input and Examples for PHREEQC Version 3–A Computer Program for Speciation, Batch- Reaction, One-dimensional Transport, and Inverse Geochemical Calculations*. Available at: http://pubs.usgs.gov/tm/06/a43 [accessed August 27, 2018] doi: 10.3133/tm6A43

Plummer, L. N., Wigley, T. M. L., and Parkhurst, D. L. (1978). The kinetics of calcite dissolution in CO2-water systems at 5°C to 60°C and 0.0 to 1.0 ATM CO2. *Am. J. Sci.* 278, 179–216. doi: 10.2475/ajs.278.2.179

Rabalais, N. N., Diaz, R. J., Levin, L. A., Turner, R. E., Gilbert, D., and Zhang, J. (2010). Dynamics and distribution of natural and human-caused hypoxia. *Biogeo* 7, 585–619. doi: 10.5194/bg-7-585-2010

Raich, J. W., and Tufekcioglu, A. (2000). Vegetation and soil respiration: correlations and controls. *Biogeochemistry* 48, 71–90. doi: 10.1023/A:1006112000616

Raymond, P. A., Oh, N. H., Turner, R. E., and Broussard, W. (2008). Anthropogenically enhanced fluxes of water and carbon from the Mississippi River. *Nature* 451, 449–452. doi: 10.1038/nature06505

Richardson, M., and Kumar, P. (2017). Critical zone services as environmental assessment criteria in intensively managed landscapes. *Earths Fut.* 5, 617–632. doi: 10.1002/2016EF000517

Sampson, F., and Knopf, F. (1994). Prairie conservation in North America. *BioScience* 44, 418–421. doi: 10.2307/1312365

Saxton, K. E., and Rawls, W. J. (2006). Soil water characteristic estimates by texture and organic matter for hydrologic solutions. *Soil Sci. Soc. Am. J.* 70, 1569–1578. doi: 10.2136/sssaj2005.0117

Schilling, K. E. (2002). Chemical transport from paired agricultural and restored prairie watersheds. *J. Environ. Q.* 31, 1184–1193. doi: 10.2134/jeq2002.1184

Schilling, K. E., Manoj, K. J., Zhang, Y. K., Gassman, P. W., and Wolter, C. F. (2008). Impact of land use and land cover change on the water balance of a large agricultural watershed: historical effects and future directions. *Water Resour. Res.* 44:W00A09. doi: 10.1029/2007WR006644

Schilling, K. E., Streeter, M. T., Bettis, E. A. III, Wilson, C. G., and Papanicolaou, A. N. (2018). Groundwater monitoring at the watershed scale: an evaluation of recharge and nonpoint source pollutant loading in the clear creek watershed, Iowa. *Hydrol. Process.* 32, 562–575. doi: 10.1002/hyp.11440

Singh, G., Kaur, G., Williard, K., Schoonover, J., and Kang, J. (2018). Monitoring of water and solute transport in the vadose zone: a review. *Vadose Zone J.* 17:160058. doi: 10.2136/vzj2016.07.0058

Soil Survey Staff (1999). *Soil Taxonomy: A Basic System of Soil Classification for Making and Interpreting Soil Surveys. Agriculture Handbook 436. Natural Resources Conservation Service*, 2nd Edn. Washington, DC: USDA.

Soil Survey Staff (2018). *Natural Resources Conservation Service, United States Department of Agriculture. Web Soil Survey*. Available at: https://websoilsurvey.sc.egov.usda.gov/ [accessed 08/27/2018].

Tsypin, M., and Macpherson, G. L. (2012). The effect of precipitation events on inorganic carbon in soil and shallow groundwater, konza prairie lter site, NE Kansas, USA. *Appl. Geochem.* 27, 2356–2369. doi: 10.1016/j.apgeochem.2012.07.008

Udawatta, R. P., Anderson, S. H., Gantzer, C. J., and Garrett, H. E. (2008). Influence of prairie restoration on CT-measured soil pore characteristics. *J. Environ. Q.* 37, 219–228. doi: 10.2134/jeq2007.0227

Vero, S. E., Macpherson, G. L., Sullivan, P. L., Brookfield, A. E., Nippert, J. B., Kirk, M. F., et al. (2018). Developing a conceptual framework of landscape and hydrology on tallgrass prairie: a critical zone approach. *Vadose Zone J.* 17:170069. doi: 10.2136/vzj2017.03.0069

Weihermuller, L., Siemens, J., Deurer, M., Knoblauch, S., Rupp, H., Gottlein, A., et al. (2007). In situ soil water extraction: a review. *J. Environ. Qual.* 36, 1735–1748. doi: 10.2134/jeq2007.0218

Wilson, C., Keefer, L., Abban, B., Wacha, K., Dermisis, D., Giannopoulos, C., et al. (2018). The intensively managed landscape critical zone observatory: a scientific testbed for agroecosystem functions and services. *Vadose Zone J.* 17:180088. doi: 10.2136/vzj2018.04.0088

Wright, C., and Wimberly, M. (2013). Recent land use change in the western corn belt threatens grassland and wetlands. *Proc. Natl. Acad. Sci. U.S.A.* 10, 4134–4139. doi: 10.1073/pnas.1215404110

Zhang, Y. K., and Schilling, K. E. (2006). Increasing streamflow and baseflow in Mississippi River since the 1940s: effect of land use change. *J. Hydrol.* 324, 412–422. doi: 10.1016/j.jhydrol.2005.09.033

**Conflict of Interest Statement:** The authors declare that the research was conducted in the absence of any commercial or financial relationships that could be construed as a potential conflict of interest.

frontiers in Earth Science

ORIGINAL RESEARCH
published: 05 March 2019
doi: 10.3389/feart.2018.00246

# Does Stream Water Composition at Sleepers River in Vermont Reflect Dynamic Changes in Soils During Recovery From Acidification?

*Jesse R. Armfield[1], Julia N. Perdrial[1]*, Alex Gagnon[1], Jack Ehrenkranz[1], Nicolas Perdrial[1], Malayika Cincotta[1], Donald Ross[2], James B. Shanley[3], Kristen L. Underwood[4] and Peter Ryan[5]*

[1] Environmental Biogeochemistry Laboratory, Geology Department, The University of Vermont, Burlington, VT, United States, [2] Plant and Soil Science Department, The University of Vermont, Burlington, VT, United States, [3] United States Geological Survey, Montpelier, VT, United States, [4] Department of Civil and Environmental Engineering, The University of Vermont, Burlington, VT, United States, [5] Geology Department, Middlebury College, Middlebury, VT, United States

Stream water pH and composition are widely used to monitor ongoing recovery from the deposition of strong anthropogenic acids in many forested headwater catchments in the northeastern United States. However, stream water composition is a function of highly complex and coupled processes, flowpaths, and variations in soil and bedrock composition. Spatial heterogeneity is especially pronounced in headwater catchments with steep topography, potentially limiting stream water composition as an indicator of changes in critical zone (CZ) dynamics during system recovery. To investigate the link between catchment characteristics, landscape position, and stream water composition we used long-term data (1991–2015) from the Sleepers River Research Watershed (SRRW) in northeastern Vermont. We investigated trends with time in stream water and trends with time, depth, and landscape position (upslope, midslope, and riparian zone) in groundwater (GW) and soil solution. We further determined soil elemental composition and mineralogy on archived (1996) and modern (2017) soil samples to assess changes in composition with time. SRRW is inherently well-buffered by calcite in bedrock and till, but soils had become acidified and are now recovering from acidification. Although base cations, especially Ca, decrease progressively with time in GW, riparian soils have become more enriched in Ca, due to a mixture of lateral and vertical transfers. At the same time stream water Ca fluxes increased over the past two decades, likely due to the leaching of (transient) legacy Ca from riparian zones and increased water fluxes. The stream water response therefore reflects the dynamic changes in soil chemistry, flow routing and water inputs.

**Keywords: weathering, recovery, acid impact, Sleepers River, carbonate**

OPEN ACCESS

***Edited by:***
*Samuel Abiven,*
*University of Zurich, Switzerland*

***Reviewed by:***
*Patrick Durand,*
*INRA Centre Bretagne-Normandie, France*
*Lei Duan,*
*Tsinghua University, China*

***Correspondence:**
*Julia N. Perdrial*
*Julia.Perdrial@uvm.edu*

***Specialty section:***
*This article was submitted to Biogeoscience, a section of the journal Frontiers in Earth Science*

***Received:*** *27 July 2018*
***Accepted:*** *18 December 2018*
***Published:*** *05 March 2019*

***Citation:***
*Armfield JR, Perdrial JN, Gagnon A, Ehrenkranz J, Perdrial N, Cincotta M, Ross D, Shanley JB, Underwood KL and Ryan P (2019) Does Stream Water Composition at Sleepers River in Vermont Reflect Dynamic Changes in Soils During Recovery From Acidification? Front. Earth Sci. 6:246. doi: 10.3389/feart.2018.00246*

## INTRODUCTION

Streams indicate critical zone (CZ) function, because they represent an integrated signal of watershed processes (Frisbee et al., 2011) including internal stream processes (Mulholland and Hill, 1997; Dawson et al., 2001) and processes occurring at the interfaces (i.e., riparian or hyporheic zones) (Bishop et al., 2004; Winterdahl et al., 2011). For example, the effects of acid deposition,

especially prevalent in the northeastern United States (Likens et al., 1972), have been monitored using stream water observations (Newell and Skjelkvåle, 1997; Amiotte-Suchet et al., 1999; Huang et al., 2017).

Acid deposition forms when emission-derived sulfur dioxide and nitrogen oxides interact with precipitation, which impacts the entire CZ through a multitude of complex and coupled processes, including declining tree and soil quality due to low pH and base cation leaching (Matzner and Murach, 1995; Driscoll et al., 2001; Raddum et al., 2007). The ensuing stream water signals are typically sensitive to these effects and showed low pH, increased concentrations of acid anions (sulfate and nitrate), and increased effluxes of base cations (e.g., Ca and Na) from many acid-impacted systems (Newell and Skjelkvåle, 1997; Driscoll et al., 2001; Garmo et al., 2014). In the United States, legislation passed in 1970 and 1990 led to reductions in emissions that caused a slow increase in precipitation pH as well as a decrease in the acid anion content across affected regions, and stream water composition has since been monitored closely for signs of recovery (Newell and Skjelkvåle, 1997; Driscoll et al., 2001; Skjelkvåle, 2003; Rice and Herman, 2012; Rogora et al., 2013; Garmo et al., 2014; Kopáček et al., 2016).

However, because streams merge water and solutes from various sources, the attribution of changes in stream water chemistry to specific process locations without detailed investigations of the CZ is difficult. For example, one CZ process strongly affected by the presence of strong acids (mostly $H_2SO_4$ and $HNO_3$) is weathering, i.e., the breakdown of bedrock and regolith through physical and chemical processes (Jin et al., 2010). Chemical weathering includes simple dissolution reactions (typical for carbonates) and hydrolysis (typical for silicates). Both processes are driven by proton availability and in the case of most silicate minerals weathering reactions are incongruent, i.e., they generate dissolved weathering products and form secondary minerals (Strawn et al., 2015). As such, weathering and soil development continuously change the composition of the solid CZ and the composition of percolating waters [e.g., soil solution and groundwater (GW)]. Another important process is the leaching of base cations from acid-impacted soils that lead to declines in soil health. These changes can be clear in headwater catchments with pronounced topography, even within just a few decades of changes in precipitation chemistry due to the transfer of soluble materials to deeper soil layers, GW (vertical transfer), and/or via lateral transfer to low-lying landscape positions (Johnson et al., 2000; Nezat et al., 2004; Brantley et al., 2007; Bailey et al., 2014; Lawrence et al., 2015; Lybrand and Rasmussen, 2015).

Stream water composition is therefore strongly affected by flowpaths that intersect different layers of a heterogeneous CZ. Accordingly, backtracking to identify specific processes requires information on soils as well as subsurface waters. We attempt this backtracking to identify signals of recovery in streams and soils using the well-studied Sleepers River Research Watershed (SRRW) in northeastern Vermont as a testbed. SRRW received strong acids through wet and dry deposition but, unlike many other watersheds in the NE, contains carbonate-bearing parent material that buffers the pH of percolating water. The impact of acid deposition on the CZ is therefore less dramatic but potentially visible due to the sensitivity of carbonates to only small changes in acid inputs.

In order to investigate how the CZ at SRRW responds to changes in precipitation chemistry in the stream signal and how compositional differences by landscape position influence this signal, we analyzed long-term stream water (1991-present), soil solution (2004–2013), and GW composition (2004–2013) at various landscape positions. Data analyzed include: pH, acid anions (nitrate and sulfate), base cations (Na and Ca) and Si. To test for changes in soil composition with time we investigated soil elemental composition (Si, Al, Na, and Ca) and mineralogy data from archived (1996) and modern (2017) soil samples of varying landscape position.

Because silicate weathering at the watershed scale is a slow process, we hypothesize that changes in acid deposition are not recorded as significant trends of silicate weathering products in the stream over our 24-year study period. However, we hypothesize that carbonate weathering and base cation leaching slowed, leading to decreases in Ca flux in the stream since 1991. We further hypothesize that topographically induced transfer of base cations led to depletions in shallow horizons at upslope and midslope locations while near-stream soils led to enrichments in base cations, especially Ca.

# MATERIALS AND METHODS

## Field Site

The SRRW comprises a series of nested catchments with varying land use in northeastern VT (**Figure 1**). The forested headwater watershed, W-9, is the focus of this study and is underlain by the Waits River Formation, which includes a quartz-mica phyllite member interbedded with calcareous granulite (Ferry, 1991; Ratcliffe et al., 2011). This formation is covered by up to 4 m of dense silty basal till from the last glaciation, (Shanley, 2000) which itself is sourced from the underlying Waits River Formation (53%) and the nearby Gile Mountain Formation (25%; Hornbeck et al., 1997). The presence of carbonates in bedrock and till contributes to the high buffering capacity and high pH in stream waters, despite historic acid deposition (Hornbeck et al., 1997; Shanley, 2000).

Annual precipitation averages 1320 mm, of which up to 30% falls as snow. The average maximum snow water equivalent approaches 280 mm, and the annual spring snowmelt is a dominant hydrologic event (Shanley et al., 2004). Decades-long research on the hydrology and biogeochemistry of W-9 has provided insights into water routing and stream flow contribution (Hornbeck et al., 1997; Shanley et al., 2015). Saturation-excess overland flow is an important contribution to streamflow generation, stored catchment water typically controls stream response, and convergent landscape positions especially contribute to event stream waters (McGlynn et al., 1999; Shanley et al., 2015). Because this area was a till deposition zone for the SE-moving Wisconsinan glaciation, the shallow aquifer is dominated by till with fine silt texture and a low saturated hydraulic conductivity that increases from near 0.1 mm/hr within

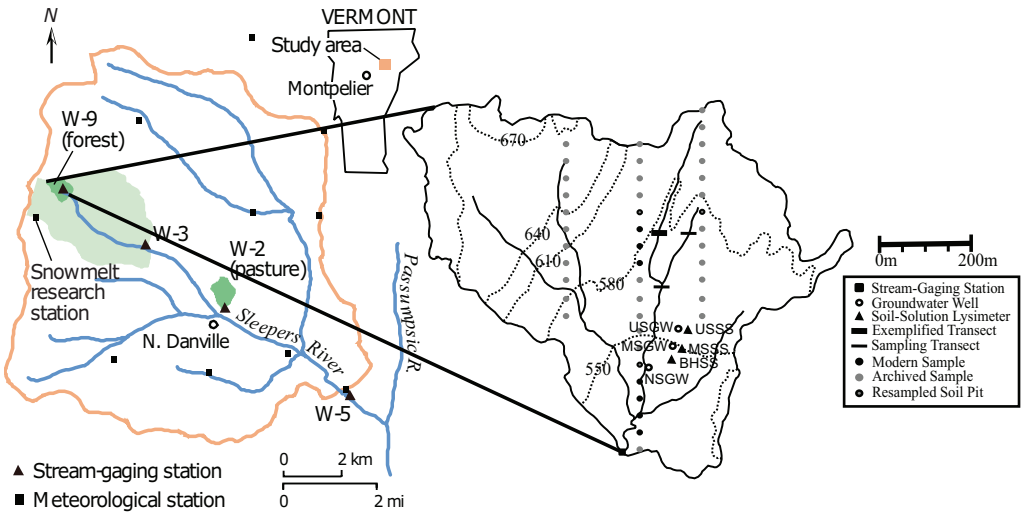


**FIGURE 1 |** Location of the Sleepers River watershed and nested subwatershed in Vermont with locations of well, soil pits and augered transects (modified after Kendall et al., 1999; Shanley, 2000, with permission).

the till to as much as 100 mm/hr in some surficial soils (Kendall et al., 1999). Streamflow has a relatively flashy response to precipitation, but water stored in the till sustains base flow such that W-9 has never ceased to flow, while comparable size watersheds in the region, including Hubbard Brook New Hampshire, routinely dry up in summer. This stored water helps contribute to an "old-water" dominated response in streamflow during events (Shanley et al., 2002).

Elevation at W-9 ranges from 519 to 678 m, and the terrain presents a mix of slopes of varying steepness and gently dipping riparian areas and wetlands. Because of this setting, landscape position strongly influences soils in W-9: Inceptisols (most prevalent) and Spodosols dominate on well-drained upland areas such as upslope and midslope areas (Shanley et al., 2004). Histosols are mostly found in poorly drained riparian areas and are often located where GW upwelling occurs (Shanley et al., 2004). The catchment is completely forested with second-growth northern hardwoods such as sugar maple, yellow birch, white ash and American beech, but softwood species (balsam fir and red spruce) are also present (Shanley et al., 2004). Like other catchments in the Northeastern United States, SRRW has been impacted by acid deposition that caused forest decline (branch dieback, some declining crown vigor) and low soil pH (Shanley et al., 2004). However, due to emissions regulations, SRRW is experiencing reduced acid inputs (Stoddard et al., 1999; Burns et al., 2005). In particular, sulfate concentrations in precipitation have been decreasing at SRRW (Shanley et al., 2004) and the NE more generally (Miles et al., 2012). Stream water dissolved organic matter has been measured weekly at SRRW since 1991 and increased steadily by 0.027 mg $L^{-1}$ $yr^{-1}$ (Cincotta et al., this special issues).

## Sampling Methods

In order to assess trends in soil-, ground- and stream water composition, we used existing data on discharge, pH, sulfate, nitrate, Si, Ca, and Na that have been collected weekly and during events at SRRW over 24 years (chemistry database doi: 10.5066/P9380HQG, flow database doi: 10.5066/P929KMVK). For soil solution, we used data from 3 sets of nested zero-tension lysimeters that occupy three main landscape positions (upslope, midslope, and base of the hill) and sample at 15 cm (shallow), and 50 cm (deep). Groundwater wells screened at various depths (**Table 1**) occupy the same landscape positions as lysimeters and were used to monitor changes in GW composition. Both soil solution and GW compositions were determined on approximately biweekly samples between 2004 and 2013 but due to intermittently dry conditions, soil solution samples were obtained less frequently. Stream water composition for the same solutes was available from approximately weekly grab sample collection between 1991 and 2015 at the stream gauge at the base of the watershed (**Figure 1**).

In addition to existing data, we collected samples from lysimeters, wells and the stream in the fall of 2017 for dissolved inorganic carbon (DIC) isotope analysis to test for carbonate weathering signals. Lysimeters and wells were pumped and

**TABLE 1 |** Screened intervals (wells) and sampling depth (lysimeters).

| Installation | Top (cm) | Bottom (cm) |
|---|---|---|
| Near stream GW (NSGW) | 170 | 245 |
| Near stream GW (NSGW) | 90 | 170 |
| Near stream GW (NSGW) | 25 | 100 |
| Upslope GW (USGW) | 160 | 310 |
| Midslope GW (MSGW) | 70 | 220 |
| Shallow lysimeters (US-, MS-, BH-, and SS) | 15 | |
| Deep lysimeters (US-, MS-, BH-, and SS) | 50 | |

*US, upslope; MS, midslope; BH, base of the hill; NS, near stream; GW, groundwater; SS, soil solution. All values are depth below land surface.*

allowed to recharge prior to sampling and all samples were capped immediately with no headspace, placed in a cooler, and shipped to the UC Davis Stable Isotope Facility within 24 h of collection.

To investigate landscape position controls on soil composition, we took soil samples every 1–3 m in three transects that spanned from upslope to midslope to near stream areas (**Figure 1**). Two transects cut across the two main tributaries, and one transect cut across a few meters below the confluence of the tributaries (**Figure 1**). These transect samples were taken using a bucket auger in 15-cm depth increments until 90 cm or depth of refusal.

To increase the statistical power of results and to allow for an in-depth analysis of compositional changes in soil with depth and landscape position, we additionally sampled each of the three soil orders from soil pits by taxonomic horizon in various locations throughout W-9 in 2017 (**Figure 1**). In order to allow for comparison with soils prior to recovery, we also analyzed archived samples (stored at room temperature in the dark in sealed glass vials) collected as part of a soil survey in 1996 ($n$ = 156). We used average values of soil composition in archived (1996) and modern (2017) samples, some of which were re-sampled in the same approximate location (**Figure 1**).

## Sample Processing and Analyses

Soil samples prepared for XRF and powder XRD were air dried (4–5 days), sieved (<2 mm), ground and homogenized in a ball mill, and stored dry prior to analysis. Soil elemental composition was determined on both archived samples ($n$ = 156) and modern transect samples (n = 121) as well as samples from representative landscape positions of modern ($n$ = 43) and archived soils ($n$ = 78) using a Thermo Scientific Niton XL3t X-Ray Fluorescence Analyzer and a Thermo Scientific ARL QUANT'X X-Ray Fluorescence Spectrometer in the Geology Department at the University of Vermont and Middlebury College, respectively. From these data we calculated mass transfer coefficients (MTC) to determine the pedogenetic behavior of selected elements (Si, Al, Na, Ca; Brimhall and Dietrich, 1987; Brantley et al., 2007). For parent material we did not use bedrock or till, but the deepest sampled horizon (i.e., partially weathered till) because parent material composition in this area varies greatly across the watershed. MTC values therefore only show depletion vs. enrichment relative to the deepest accessible horizon. We used Ti as an immobile element because of its normal distribution in the parent material. All data from each soil order of the 1996 survey as well as the representative data from 2017 were averaged by horizon to assess the variability of each horizon of each soil order. Relative MTC was calculated as:

$$MTC_{I,M} = \frac{C_{W,M}}{C_{P,M}} * \frac{C_{P,I}}{C_{W,I}}$$

where MTC (dimensionless) is the ratio of the concentration (C) of an element of interest (subscript M) relative to an immobile element (subscript I) in the weathered soil (subscript W) and the parent material (subscript P). Soil mineralogy was identified using X-ray diffraction (XRD) on random powder mounts from modern soil samples from each resampled pit. In order to identify secondary clay minerals, samples from the lowest horizon (till) were also analyzed using oriented texture preparations of the <2 μm fraction that was separated by decantation (Poppe et al., 2001). Suspensions were pipetted on glass slide preparations and allowed to air-dry. This approach allows for an orientation of crystallites that restricts diffraction in the crystallographic c-direction and hence only the (00l) intervals are visible (Lagaly, 1993; Moore and Reynolds, 1997). The clay fraction was analyzed air-dried (AD), treated with ethylene glycol (EG) to test for presence of swelling clay, and heat-treated (HT, 400 and 550°C) to collapse the chlorite peaks to test for overlap with the kaolinite reflections (Moore and Reynolds, 1997). XRD analysis of all samples was conducted on a Rigaku Miniflex II Powder Diffractometer with CuKα radiation, operated at 30 kV and 15 mA. Scanning parameters were set at 0.02 step width and a count time of 10 s per step between 3 and 5–65 °2θ.

## Statistical Methods

All statistical analyses were completed in R (R Core Development Team, 2017). Stream flux was calculated to evaluate trends in recovery (sulfate, nitrate) and weathering (Si, Na, and Ca). All stream flux calculations were completed using the USGS LoadEst functions (Runkel et al., 2004) implemented within the LoadFlex package and trend analyses were conducted using the Kendall and trend packages (McLeod, 2011; Appling et al., 2015; R Core Development Team, 2017; Pohlert, 2018). LoadEst requires daily time steps, therefore concentration and discharge of highly sampled storm events were entered as daily averages. The best of the 9 predefined LoadEst models was then selected based on how accurately it predicted measured values and was applied to the discharge record for annual flux calculation.

Flow adjusted residuals of the concentration-discharge relationship were then evaluated and, if they were not normally distributed, a Mann-Kendall trend analysis was conducted and the Sen slope was calculated. Baseflow composition was determined by calculating the mean stream composition during discharge conditions lower than the 20th percentile and storm flow composition was determined by calculating the mean stream composition during the of discharge conditions greater than the 80th percentile. Baseflow and stormflow composition were also computed at less than the 5th percentile and greater than 95th percentile.

The significance of trends in soil solution and GW composition with time and space were evaluated using several methods. For temporal trends in GW, linear regressions on raw data were used first as this method is powerful and if significance is established no more statistical analyses are needed to draw conclusions (Meals et al., 2011). Temporal trends in GW concentration were evaluated using data from the well with the most complete record (the well at the upslope). In the case of highly variable seasonal compositions, regressions on annual averages were implemented. When large parts of the datasets (>1/3 of the record) were missing or other tests failed to establish a trend, Welch's 2 sample $t$ tests were used to evaluate any differences in composition (Meals et al., 2011; Derrick and White, 2016). Trends in space were evaluated by calculating the average

and standard error at each depth and landscape position. If averages were within error of one another, Welch's 2 sample *t* test was used to determine whether the data sets were significantly different (Derrick and White, 2016).

# RESULTS

## Trends in Stream Water Composition and Flux

Discharge showed large variations (ranging from $7.4*10^4$ $m^3$ $yr^{-1}$ in 2001 to $1.5*10^5$ $m^3$ $yr^{-1}$ in 2011) and increased slightly but significantly (**Figure 2A**). Stream water pH values showed large, mostly seasonal, variations between 1991 and 2004 with values ranging from 6.7 up to 8.6 with less variability thereafter (**Figure 2B** and **Supplementary Materials**). Annual stream water sulfate flux decreased more than 30% since 1991 (from 870 to 580 kg $yr^{-1}$, **Figure 2C**) and Mann Kendall trend analysis on flow adjusted model residuals indicated a significant negative trend in sulfate concentration ($\tau = -0.442$, Sens Slope = −0.007, $p < 0.05$). The annual nitrate flux showed large interannual variability (between 60 and 105 kg $NO_3^-$ per year) but no significant increase or decrease over time (**Figure 2D**).

Both Si and Na stream water flux showed large interannual variability (ranging from 750 to 1400 kg $yr^{-1}$ for Si and from 180 to 330 kg $yr^{-1}$ for Na, **Figures 2E,F**). Mann Kendall trend analyses showed no significant trends in Si and Na concentration. The flux of Ca showed similarly large variations (ranging from 3450 and 6450 kg $yr^{-1}$) and a slight increase that was significant ($\tau = 0.078$, Sens Slope = 0.002, $p < 0.05$). The great interannual variability in fluxes is in agreement with the interannual variability in discharge (**Figure 2A**), showing very wet years in 1996, 2008 and 2011 and much drier years in 1995, 2001, and 2012.

## Temporal and Spatial Trends in Groundwater and Soil Water Composition

We also investigated groundwater and soil water composition for trends with time, depth, and landscape position (upslope vs. midslope vs. base of the hill). Temporal trends are exemplified for selected years with typical annual precipitation (i.e., years 2004, 2008, and 2012). Significance was established using linear regression on the entire time series (see **Supplementary Material Figure S1** for complete time series of GW composition).

Soil solution pH increased over time especially in deep and some shallow soil solution and was generally greater at depth and with proximity to the stream (**Figure 3A**). GW pH in the upslope well increased from an annual average of 7.9 ± 0.3 in 2004 to an annual average of 8.1 ± 0.2 in 2012, which is higher than the average stream water pH at base flow (7.8 ± 0.2, **Table 2**).

Sulfate concentrations generally decreased with time but were greater at depth and with proximity to the stream (**Figure 3B**). For example, the average sulfate concentration in all shallow soil water decreased from 3.2 ± 1.5 mg $L^{-1}$ in 2004 to 1.6 ± 1.1 mg $L^{-1}$ in 2008 and is in agreement with the general trend of decreasing sulfate over the years. GW sulfate decreased from an average of 5.3 ± 0.7 mg $L^{-1}$ in 2004 to 4.4 ± 0.3 mg $L^{-1}$ in 2012. The trend of increasing sulfate concentrations with depth was observed at the upslope position where the sulfate concentration in GW was up to 2.5 times higher than in soil water. The average stream water sulfate concentration at baseflow (<20%, 8.1 ± 2.3 mg $L^{-1}$) was the highest mean sulfate concentration of any water source (**Table 2**).

Nitrate concentrations did not change significantly over time and were lower at depth and closer to the stream (**Figure 3C**). Annual average nitrate concentrations in shallow soil solution ranged from as low as 0.02 ± 0.01 mg $L^{-1}$ at the base of the hill in 2004 to as high as 0.26 ± 0.12 mg $L^{-1}$ at the hilltop position in

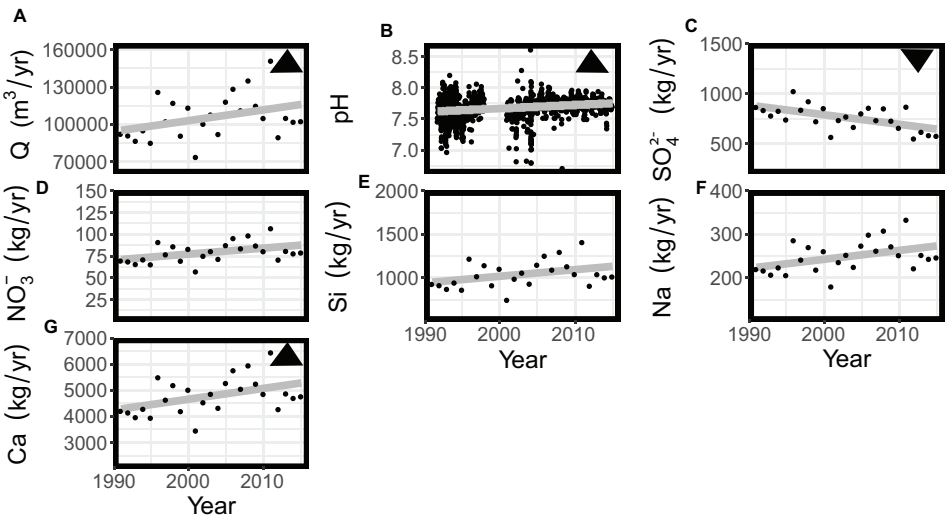


**FIGURE 2 |** Complete time series for **(A)** discharge (Q), for the water year **(B)** pH measurements, and **(C–G)** annual flux of selected solutes (calendar year). Triangles in the top right corner indicate the directionality of statistically significant trends of linear regression.

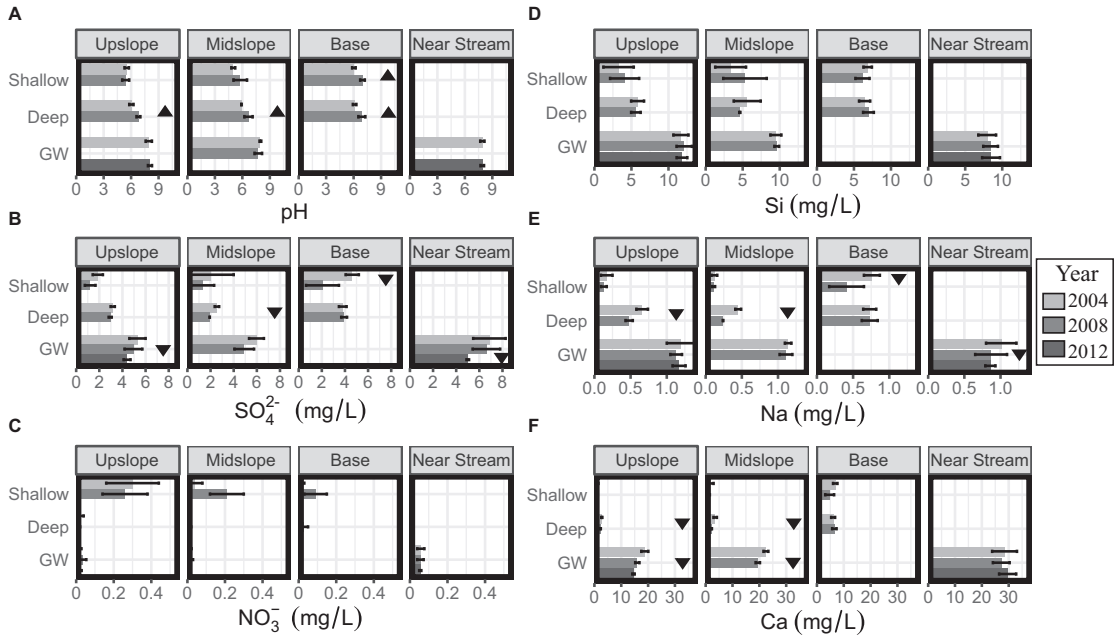


**FIGURE 3 |** Mean annual **(A)** pH and **(B–F)** concentrations of selected solutes in soil water (shallow = 15 cm and deep = 50 cm) and GW at four landscape positions (upslope, slope, base, and near stream) between 2004 and 2012. Base of the hill (soil solution samples) and near stream (GW well) are in proximity to each other. Triangles indicate the directionality of statistically significant trends on the complete time series of data for each depth and landscape position.

**TABLE 2 |** Average stream water pH and concentration of selected solutes (mg/L) during baseflow and stormflow conditions from 1991 to 2015.

| Measurement | Baseflow (<20%) | *SD* | Baseflow (<5%) | *SD* | Stormflow (>80%) | *SD* | Stormflow (>95%) | *SD* |
|---|---|---|---|---|---|---|---|---|
| pH | 7.74 | 0.15 | 7.77 | 0.14 | 7.53 | 0.22 | 7.34 | 0.17 |
| Sulfate | 8.07 | 2.28 | 8.73 | 2.69 | 4.64 | 1.3 | 3.77 | 1.40 |
| Nitrate (as $NO_3^-$) | 0.14 | 0.08 | 0.11 | 0.05 | 0.25 | 0.16 | 0.30 | 0.19 |
| Silicon | 3.21 | 0.42 | 3.56 | 0.28 | 2.00 | 0.29 | 1.74 | 0.25 |
| Calcium | 27.83 | 3.88 | 31.24 | 3.19 | 15.02 | 2.97 | 12.32 | 1.99 |
| Sodium | 0.84 | 0.14 | 0.98 | 0.14 | 0.46 | 0.09 | 0.38 | 0.07 |

2008 (**Figure 3C**). Compared to upslope, nitrate concentrations at the base of the hill were slightly lower and similar to base flow stream water concentrations (**Table 2**).

Average annual soil and groundwater Si concentrations did not show significant changes with time but, like pH and sulfate, concentrations were generally greater with depth and proximity to the stream (**Figure 3D**). For example, Si in GW at the upslope position remained relatively constant since 2004 at an average value of 12 ± 0.2 mg $L^{-1}$ (**Figure 3D**). Soil water Si concentrations were generally greater (6.7 ± 0.8 mg $L^{-1}$) at the base of the hill than upslope. In contrast, near stream GW Si concentrations (8.4 ± 1.2 mg $L^{-1}$) were almost 30% lower than upslope GW concentrations, (12.0 ± 0.8 mg $L^{-1}$) which is still almost 3 times higher than stream water base flow concentrations (**Table 2**).

Annual average Na concentrations decreased with time in deep soil solution at the upslope and midslope positions and were generally lowest in upslope soil waters (as low as 0.6 ± 0.1 mg $L^{-1}$) and largest in GW, which was similar to stream water composition at base flow (**Table 2**).

Ca concentrations generally decreased through the study period but were greater at depth and proximal to the stream (**Figure 3F**). Upslope GW Ca concentrations decreased significantly from 18.8 ± 1.3 mg $L^{-1}$ in 2004 to 16.0 ± 0.8 mg $L^{-1}$ in 2012 (**Figure 3F**) and were generally greater at depth (1.0 ± 0.7 mg $L^{-1}$ in shallow soil water vs. 16.4 ± 2.4 mg $L^{-1}$ in GW). Stream water Ca concentrations at base flow were similar to GW concentrations (**Table 2**).

The isotopic composition of DIC was determined for soil solution and GW. The mean $\delta^{13}$C-DIC of soil solution (−20.8 ‰ ± 1.2) was significantly lower than that of GW (−14.5 ‰ ± 1.5), and $\delta^{13}$C-DIC values also generally increased with proximity to the stream (**Table 3**).

## Spatial and Temporal Trends of Selected Elements in Soil

Spatial trends on transect samples generally showed depletions at upslope and midslope locations and accumulations in riparian areas (**Figure 4** and **Supplementary Figures S2, S3**). The exception was Si that was, relative to the parent material, variably

**TABLE 3 |** $\delta C^{13}$ of dissolved organic carbon and concentrations in soil solution (SS) and groundwater (GW) at different landscape positions and depths.

| Landscape position | Depth (cm) | $\delta^{13}C_{VPDB}$ ‰ | mg/L |
|---|---|---|---|
| Upslope (SS) | 50 | −22.07 | 4.7 |
| Upslope (SS) | 15 | −21.06 | 6.6 |
| Upslope (GW) | 160–310 | −14.75 | 13.4 |
| Base of the hill (GW) | 70–220 | −17.24 | 17.9 |
| Near stream (SS) | 40 | −19.18 | 13.7 |
| Near stream (GW) | 25–100 | −14.06 | 19.8 |
| Near stream (GW) | 90–170 | −13.33 | 17.0 |
| Near stream (GW) | 170–245 | −13.12 | 14.3 |

enriched or depleted in upslope and midslope positions (MTC values ranging from −0.51 to 0.64). Al was mildly depleted from upslope soils (−0.10 to −0.39) and accumulated in the top 45 cm of the profile closest to the stream. The base cations Na and Ca were typically depleted from the upslope soils (e.g., MTC values ranging from −0.86 to −0.08 for Ca) and accumulated in near stream soils, especially in the top 30 cm (up to 31.2 for Ca, **Figure 4**).

Temporal trends in soil elemental composition were investigated by comparing MTC values from archived and modern samples (**Figures 5**–**7**). The variability in typical upslope soils (mostly Spodosols) was great, as indicated by the broad shaded areas (**Figure 5**), but generally showed a combined accumulation-depletion pattern (**Figure 5**). For example, MTC values for Si indicated mild enrichments (e.g., archived mean = 0.12 ± 0.36 in the O horizon) in the upper horizons (O, A, E) and depletions in lower horizons (e.g., archived mean = −0.28 ± 0.11 for the BC horizon). Aluminum also showed an addition-depletion profile where MTC values were negative at the surface and positive in the spodic horizon. Base cations were generally enriched and highly variable in the O horizon but depleted in underlying mineral soil (e.g., archived mean up to −0.58 ± 0.19 for Na). The differences between archived and modern samples were not significant for any of the investigated elements except Ca, which was generally more enriched in the top horizons of archived soils.

Midslope Inceptisol composition in the study area was less variable compared to Spodosols (shaded areas are less broad, **Figure 6**). Overall, Si was depleted throughout the profile (archived means between −0.04 ± 0.25 and −0.16 ± 0.17, **Figure 6**), while Al in archived samples was somewhat depleted in upper horizons and was depleted in lower horizons in modern samples. MTC values for base cations, especially Ca, were highly variable in the O horizon (e.g., archived mean = 3.65 ± 4.18 for Ca). As for Spodosols, differences between archived and modern samples was only significant for Ca in the top horizons, where Ca MTC values were significantly higher in archived soils.

The variability of riparian soil composition in the study area was high for most elements, especially in archived samples. For example, MTC values were generally positive for Si, negative for Al (especially in modern samples; **Figure 7**). Base cation MTC values were generally positive, especially for Ca, in the two uppermost organic horizons (32.1 ± 33.6 and 19.9 ± 29.7). Again, the differences between archived and modern samples was significant for Ca in the top horizons, where Ca MTC values were significantly higher in archived soils.

## Mineralogy of Till and Soils

The deepest horizons (weathered till) contained primary minerals of the Waits River and Gile Mountain Formations including micas (with a prominent peak at 10.0 Å), chlorite (14.2/7.1/3.5 Å), pyroxenes (e.g., at 3.0 Å), feldspars (e.g., at 3.1 Å), quartz (at 3.34/4.26 Å), amphibole (at 8.5 Å), oxides (rutile or spinel at

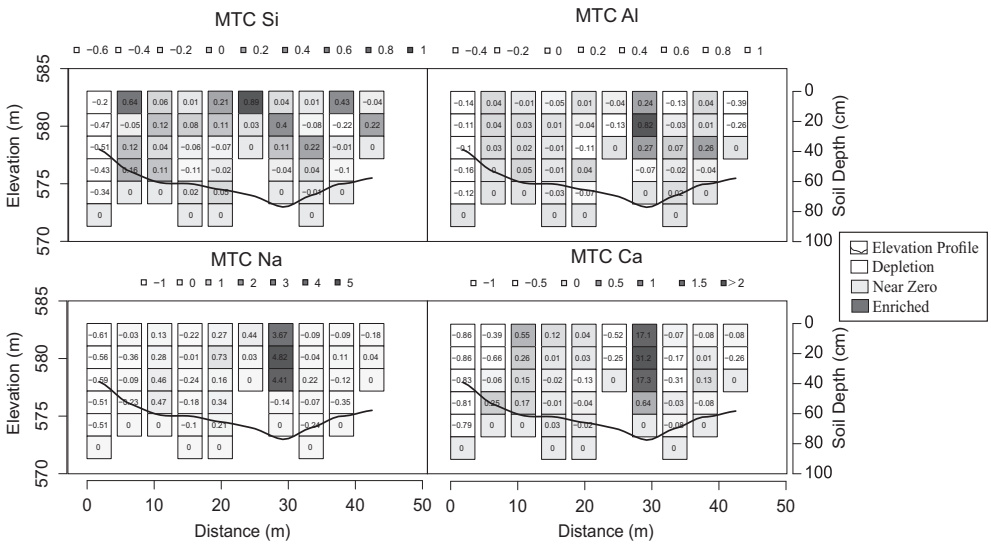


**FIGURE 4 |** Mass transfer coefficient (MTC) values for selected elements on the exemplified transect with the greatest relief. Upslope soils are located on each end of the elevation contour, near stream soils are located at the lowest elevation, and all other soils are defined as midslope soils. The color ramp ranges from white to black indicating depletions (white), near zero values (gray), and enrichments (black).

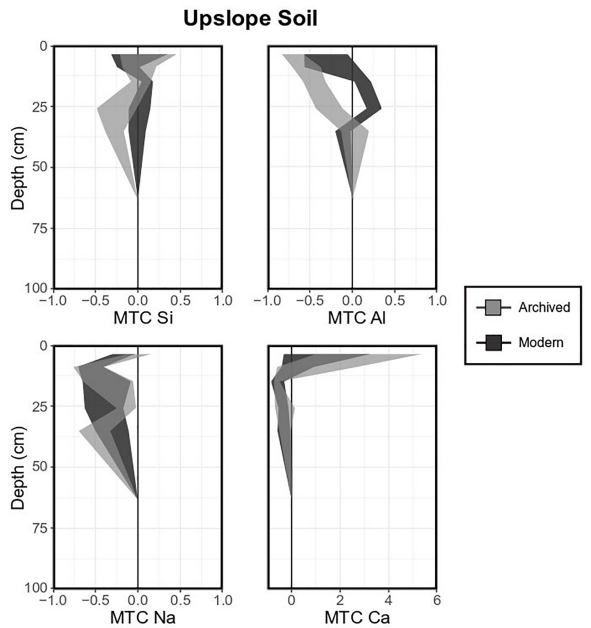


**FIGURE 5 |** Mass transfer coefficient (MTC) values of selected elements for a typical upslope soil (Spodosol). Light gray shaded areas indicate means and standard deviations for each element measured in 1996 (8 pits), dark gray shaded areas indicate means and standard deviations for each element measured in 2017 (3 pits).

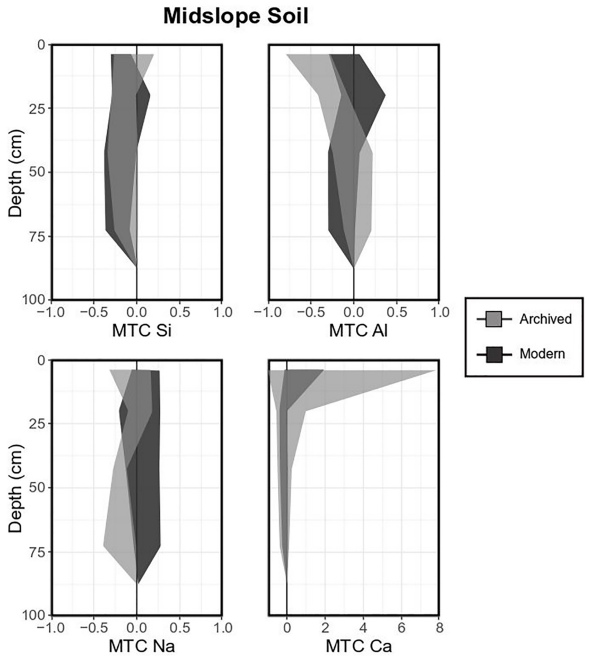


**FIGURE 6 |** Mass transfer coefficient (MTC) values of selected elements for a typical midslope soil (Inceptisol). Light gray shaded areas indicate standard deviations of means for each element measured in archived samples (1996, 18 pits), dark gray shaded areas indicate standard deviations of means for each element of modern samples (2017, 4 pits).

2.5 Å), and apatite (2.8 Å, see **Supplementary Materials** for diffractograms). Representative soils for all landscape positions (Spodosol for upslopes, Inceptisols for most midslopes and Histosols for riparian zones) showed most peaks for the primary minerals associated with contributing bedrock formations, but several of these peaks changed or disappeared toward upper horizons (**Supplementary Figures S4–S6**). For example, quartz peaks decreased in intensity toward shallower horizons, whereas feldspar, muscovite, amphibole and pyroxene peaks varied but became difficult to resolve in the organic horizon of all soils. Primary chlorite is present in all soils (intense peak at 14.2 Å in powder samples). The secondary swelling clay mineral smectite (confirmed by EG treatment, **Supplementary Figures S4–S6**) and illite were found in deeper horizons of most soils. Smectite was most prominent in Spodosols and not well resolved in the riparian Histosol. In contrast, calcite was only identified in the lowest horizons of the riparian Histosol.

# DISCUSSION

## Streams as Indicators of Recovery From Acidification

Changes in stream water composition can indicate changes in CZ dynamics (Meybeck, 1993; Maher, 2011; McIntosh et al., 2017). However, a multitude of complex and coupled processes in the watershed and the stream itself can make the identification of specific processes or source locations difficult. Using the acid-impacted SRRW as a testbed, we investigated the potential and limitations of stream water composition as an indicator of watershed recovery from acidification and explored whether changes in soil composition contributed to a recovery signal.

Generally, decreasing stream water nitrate and sulfate fluxes and overall increases in stream water pH are typical indicators of chemical recovery at the watershed scale (Newell and Skjelkvåle, 1997; Driscoll et al., 2001; Skjelkvåle et al., 2001, 2005; Rogora et al., 2013; Garmo et al., 2014). At SRRW, sulfate fluxes in the stream indeed decreased significantly (**Figure 2C**) despite the fact that GW sulfate concentrations are high due to pyrite weathering at greater depth (Mayer et al., 2010). Over the past decades precipitation increased an average of 14 mm/yr (Shanley et al., 2016), which is reflected in the overall increase in discharge (**Figure 2A**). If sulfate still had a significant source in precipitation or release from soil stores, increases in annual precipitation may have led to stream sulfate flux increases, not decreases. The actual decreases in sulfate flux indicate that the stream is responding to the substantial reduction in sulfate deposition in the area (Shanley et al., 2004; Miles et al., 2012). In contrast, stream water nitrate flux did not change significantly, a finding that is consistent with the strong control of vegetation in a system that is not N saturated and the slower decrease in nitrate deposition (Burns et al., 2005). Stream water pH never dropped below 6.7, due to the high buffering capacity of the bicarbonate-rich waters (Shanley, 2000; Shanley et al., 2004)

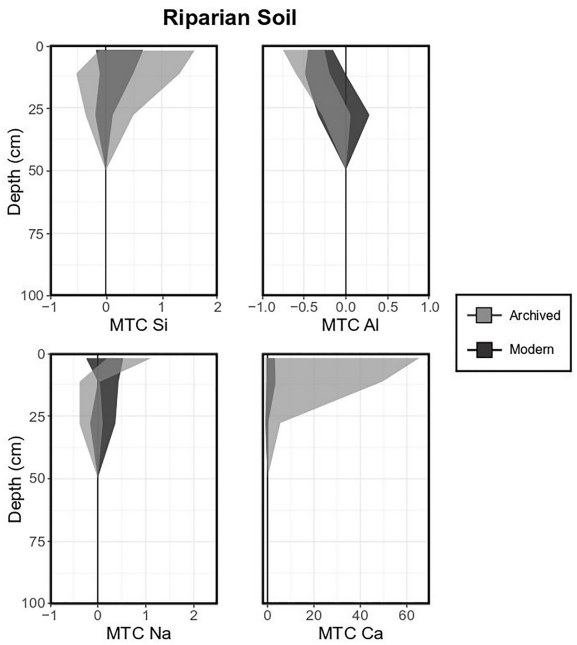


**FIGURE 7 |** Mass transfer coefficient (MTC) values of selected elements for a typical base of the hill soil (Histosol). Light gray shaded areas indicate standard deviations of means for each element measured in archived samples (1996, 11 pits), dark gray shaded areas indicate standard deviations of means for each element of modern samples (2017, 3 pits).

but the magnitude of pH variation decreased, especially after 2004 (**Figure 2B**).

Because the reduction of acid deposition reduces proton availability, we had hypothesized that stream water fluxes of Ca from base cation leaching would decrease significantly. Indeed, many recovering watersheds in the region show a substantial reduction in base cation fluxes including Ca and Na (Newell and Skjelkvåle, 1997; Stoddard et al., 1999; Burns et al., 2005; Garmo et al., 2014). However, SRRW Na (and Si) fluxes remained unchanged, whereas Ca fluxes increased (**Figures 2E–G**).

Because GW can indicate subsurface processes more directly than stream water (Peters and Aulenbach, 2009), we investigated temporal trends in GW Ca, Na and Si concentrations and found that the concentrations of Si remained stable, Na decreased slightly and that Ca decreased by over 30% since 2004 (**Figures 3D–F**). The relatively high $\delta^{13}$C-DIC values measured in GW are typical for a mixture of pedogenic DIC and carbonate weathering, confirming that carbonate is still actively weathering (Cerling, 1984; Amiotte-Suchet et al., 1999). Coupled with the decreases in GW Ca concentrations on the upslope and midslope, the isotopic patterns are consistent with either decreased carbonate weathering or increased plant Ca uptake during recovery, but they do not explain the increased Ca flux in stream water. We will discuss the potential role of Ca accumulation in the riparian zone as a mechanism to explain this pattern (section "The Riparian Zone: Integrator of Flow Paths and Soil Processes").

## From Subsurface to Stream: Changes in Soil and Water Composition by Landscape Position

We had hypothesized that long-term lateral transfer of leached base cations would lead to depleted shallow horizons, especially at upslope or midslope locations, while the accumulation of base cations, especially Ca, would be largest in near stream locations. Indeed, base cation and Si concentrations in soil water generally increased with depth and also increased toward low-lying landscape positions, which might reflect a combination of vertical and lateral transfer through shallow flowpaths and supply from GW when water tables rise (Sommer, 2006). Highly variable Si MTC values at all landscape positions and in all soil horizons (**Figure 4**) might reflect a combination of unweathered quartz high in the profile as well as transfer of Si from the weathering of less stable aluminosilicates (**Figure 4**). Aluminum, at upslope locations, showed a typical Spodosol depletion-enrichment pattern due to pH driven changes in Al solubility (Cronan and Schofield, 1979) but had significant enrichment in riparian soil horizons. XRD analyses indicate the weathering of aluminosilicate phases (especially amphiboles and pyroxenes) in most horizons and many of these minerals were still present in mineral soil horizons (**Supplementary Figures S4–S6**). Together with the high soil solution concentrations of Si (and partially for Na as well) these results indicate active silicate weathering in these soils.

Solid phase analyses of Na and Ca revealed negative MTC values for these elements in upslope and midslope soils but showed, again, substantial enrichment in riparian soils (**Figures 5–7**), a pattern that was also present in soils taken in transects associated with these landscape positions (**Figure 4**). E.g., Ca and Na were generally depleted in upslope-Spodosols (except for top horizons), relatively stable in the midslope-Inceptisols and enriched in riparian-Histosols, especially in top layers (**Figure 4**). Organic rich horizons tend to have less Ti, and hence the normalization to this otherwise immobile element to calculate MTC values can overestimate enrichments. However, riparian Histosol Ca content reaches up to 72000 mg $kg^{-1}$, compared to a mean of 26000 $\pm$ 13000 mg $kg^{-1}$ for midslope soils. XRD analyses of these soils explain most of these patterns through weathering and disappearance of amphiboles, chlorite, apatite, and pyroxenes. The lack of calcite in the till at upslope and midslope locations indicates that the carbonate weathering front is much lower than the silicate weathering front (i.e., in the deep till). The lack of significant amounts of secondary Ca-bearing minerals in near-stream locations further suggests that the large amounts of Ca are not accommodated in crystalline phases.

## The Riparian Zone: Integrator of Flow Paths and Soil Processes

At SRRW, the riparian zones are areas of confluence where shallow and deep flow paths converge, GW discharges and base cations accumulate, hence the riparian zone has a high potential for impacting stream water composition for these solutes.

Si and Na concentrations were similarly high in GW at upslope and midslope locations, however, concentrations were

significantly lower in riparian zone waters and even lower in stream water [e.g., base flow stream water Si concentrations were almost 6 mg $L^{-1}$ lower than riparian GW (**Figure 3** and **Table 2**)], an observation consistent with previous research (Kendall et al., 1999). The missing Si and Na might be stored in secondary minerals, such as smectites that were identified in weathered till (**Supplementary Figures S4–S6**). However, as mentioned above, we cannot explain the high riparian soil Ca content through only the accumulation of secondary minerals.

Cincotta et al. (this special issues) found riparian soils at SRRW were rich in both Ca and organic carbon. Ca is common in biofilms, and is the dominant exchangeable cation in organic soils with high pH and cation exchange capacity. As a divalent cation, Ca can help bridge charges between negative soil particles (Perdrial et al., 2009). Organic matter readily forms complexes with free $Ca^{2+}$ ions (Ong and Bisque, 1968; Temminghoff et al., 1995), leading to DOM coagulation that, when Ca concentrations are high, is not pH dependent (Tipping and Ohnstad, 1984; Temminghoff et al., 1995). Therefore, Ca in riparian soils is likely associated with and stabilized by organic materials in soil aggregates. Cincotta et al. (this special issues) also showed that recovery from acidification can lead to the breakup of soil aggregates and the release of associated organic matter into soil solution. Their study did not investigate Ca release, but if Ca is associated with organic matter it would be liberated in the same process. Indeed, annual discharge has slightly increased since 1992 (**Figure 2A**) and so has stream water DOC flux (Schuster et al., 2007; Sebestyen et al., 2008; Cincotta et al., this special issues). Thus, the slight but significant increase in stream water Ca flux (**Figure 2G**) could have the same origin as the stream DOC increase, i.e., release from soil aggregates that served as transient store. Both indicate riparian processes driven by changes in aggregate stability and solubility (not increased carbonate weathering), with the result that Ca is effectively flushed into the stream. This effect is exacerbated by increased discharge (**Figure 2A**) and increased abundance of high intensity events (Peters et al., 2006), advectively transferring soil-derived material into the stream.

Furthermore, our results from modern vs. archived soil samples are in agreement with a gradual, recovery-induced, leaching of legacy Ca from riparian soils. The Ca concentration of the riparian soils decreased measurably between archived (1996) and modern samples (2017) throughout the study area as well (**Figure 7**). We illustrate the strong impact of riparian soils and near stream waters vs. midslopes on stream water in a mixing diagram of Na-normalized mole ratios (**Figure 8**). Here, composition of upslope and midslope soils have overall lower Ca/Na ratios than the riparian soils, which again have lower ratios than GW or stream water. These results confirm that riparian zones are highly reactive parts of the CZ and exert a strong control on stream composition (Peters and Aulenbach, 2009; Vidon et al., 2010; Lidman et al., 2017). In the case of SRRW, the complex interactions among base cation leaching, converging flow paths, GW upwelling (providing changes in pH and further accumulation of more reactants), temporal solute storage (i.e., transient legacy), and interaction with organics, produce a highly reactive zone that responds to the same driver (decrease of acid inputs) in fundamentally different ways than the midslopes.

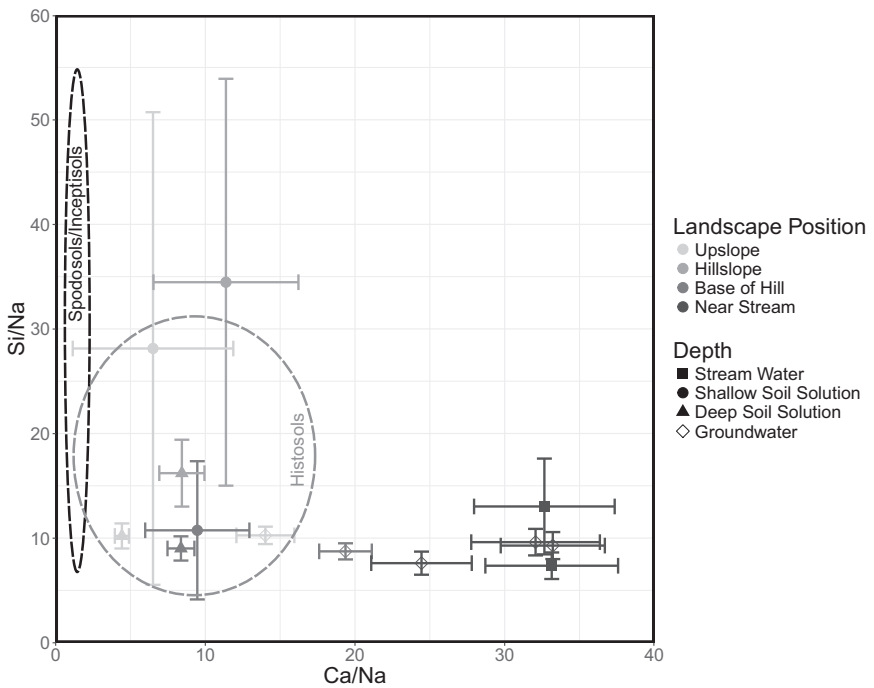


**FIGURE 8 |** Mixing diagram of Na-normalized mean molar ratios and standard error for water composition by source (symbols) and landscape position (gray shades). Black dashed lines indicate the range of molar ratios in Spodosols and Inceptisols while gray dashed line represents this range in Histosols.

## PERMISSION TO REUSE AND COPYRIGHT

**Figure 1** was modified from Hydrological Processes, 29, Shanley, James B., Stephen D. Sebestyen, Jeffrey J. McDonnell, Brian L. McGlynn, and Thomas Dunne. 'Water's Way at Sleepers River watershed – revisiting flow generation in a post-glacial landscape, VT, United States,' 3447-59, Copyright 2014, with permission from John Wiley and Sons and from Journal of Hydrology, 219, 'a hydrometric and geochemical approach to test the transmissivity feedback hypothesis during snowmelt,' 188–205, Copyright 1999, with permission from Elsevier.

## AUTHOR CONTRIBUTIONS

JA was responsible for sample collection, preparation, and analyses as well as figure production, table production, and primary authorship. JP as MS thesis advisor aided in interpretation, authorship, field work, lab work, lab training, as well as allowed lab use. AG and JE assisted with field sampling and lab work. NP contributed through interpretations, authorship, and lab training. MC assisted with field sampling, lab work, and interpretations through research published in this issue. DR assisted in interpretations and editing. JS provided soil solution, groundwater, and stream composition data as well as archived soil samples and also introduced authors to watershed installations, aided in interpretations and provided pre-research consulting. KU aided in statistical processing and interpretations as well as provided example R scripts. PR allowed the use of and provided training on the XRF at Middlebury College.

## FUNDING

Funding supporting this research was made available through the Geology Department at the University of Vermont.

## ACKNOWLEDGMENTS

Scott Bailey provided pre-research consulting and archived soil samples. USGS participation was funded by the Land Change Science Program. USGS-collected data used in this paper is available at doi: 10.5066/P929KMVK (flow database) and doi: 10.5066/P9380HQG (chemistry database). Use of trade, product, or firm names is for informational purposes and does not imply endorsement by the United States Government.

## SUPPLEMENTARY MATERIAL

The Supplementary Material for this article can be found online at: https://www.frontiersin.org/articles/10.3389/feart.2018.00246/full#supplementary-material

## REFERENCES

Amiotte-Suchet, P., Aubert, D., Probst, J. L., Gauthier-Lafaye, F., Probst, A., Andreux, F., et al. (1999). δ13C pattern of dissolved inorganic carbon in a small granitic catchment: the Strengbach case study (Vosges mountains, France). *Chem. Geol.* 159, 129–145. doi: 10.1016/S0009-2541(99)00037-6

Appling, A. P., Leon, M. C., and McDowell, W. H. (2015). Reducing bias and quantifying uncertainty in watershed flux estimates: the R package loadflex. *Ecosphere* 6:art269. doi: 10.1890/ES14-00517.1

Bailey, S. W., Brousseau, P. A., McGuire, K. J., and Ross, D. S. (2014). Influence of landscape position and transient water table on soil development and carbon distribution in a steep, headwater catchment. *Geoderma* 226–227, 279–289. doi: 10.1016/j.geoderma.2014.02.017

Bishop, K., Seibert, J., Köhler, S., and Laudon, H. (2004). Resolving the Double Paradox of rapidly mobilized old water highly variable responses in runoff chemistry. *Hydrol. Process.* 18, 185–189. doi: 10.1002/hyp.5209

Brantley, S. L., Goldhaber, M. B., and Ragnarsdottir, K. V. (2007). Crossing disciplines and scales to understand the critical zone. *Elements* 3, 307–314. doi: 10.2113/gselements.3.5.307

Brimhall, G. H., and Dietrich, W. E. (1987). Constitutive mass balance relations between chemical composition, volume, density, porosity, and strain in metasomatic hydrochemical systems: results on weathering and pedogenesis. *Geochim. Cosmochim. Acta* 51, 567–587. doi: 10.1016/0016-7037(87)90070-6

Burns, D. A., McHale, M. R., Driscoll, C. T., and Roy, K. M. (2005). Response of surface water chemistry to reduced levels of acid precipitation: comparison of trends in two regions of New York, USA. *Hydrol. Process.* 20, 1611–1627. doi: 10.1002/hyp.5961

Cerling, T. E. (1984). The stable isotopic composition of modern soil carbonate and its relationship to climate. *Earth Planet. Sci. Lett.* 71, 229–240. doi: 10.1016/0012-821X(84)90089-X

Cronan, C. S., and Schofield, C. L. (1979). Aluminum leaching response to Acid precipitation: effects on high-elevation watersheds in the northeast. *Science* 204, 304–306. doi: 10.1126/science.204.4390.304

Dawson, J. J., Bakewell, C., and Billett, M. F. (2001). Is in-stream processing an important control on spatial changes in carbon fluxes in headwater catchments? *Sci. Total Environ.* 265, 153–167. doi: 10.1016/S0048-9697(00)00656-2

Derrick, B., and White, P. (2016). Why Welch's test is Type I error robust. *Tutor. Quant. Methods Psychol.* 12, 30–38. doi: 10.20982/tqmp.12.1.p030

Driscoll, C. T., Lawrence, G. B., Bulger, T. J., Cronan, C. S., Eagar, C., Lambert, K. F., et al. (2001). *Acid Rain Revisited: Advances in Scientific Understanding Since the Passage of the 1970 and 1990 Clean Air Act Amendments*. Thornton, CO: Hubbard Brook Research Foundation.

Ferry, J. M. (1991). Regional metamorphism of the waits river formation, eastern vermont: delineation of a new type of giant metamorphic hydrothermal system. *J. Petrol.* 33, 45–94. doi: 10.1093/petrology/33.1.45

Frisbee, M. D., Phillips, F. M., Campbell, A. R., Liu, F., and Sanchez, S. A. (2011). Streamflow generation in a large, alpine watershed in the southern Rocky Mountains of Colorado: is streamflow generation simply the aggregation of hillslope runoff responses? *Water Resour. Res.* 47:W06512. doi: 10.1029/2010WR009391

Garmo, Ø. A., Skjelkvåle, B. L., de Wit, H. A., Colombo, L., Curtis, C., Fölster, J., et al. (2014). Trends in surface water chemistry in acidified areas in Europe and North America from 1990 to 2008. *Water Air Soil Pollut.* 225:1880. doi: 10.1007/s11270-014-1880-6

Hornbeck, J., Bailey, S., Buso, D., and Shanley, J. (1997). Streamwater chemistry and nutrient budgets for forested watersheds in New England: variability and management implications. *For. Ecol. Manag.* 93, 73–89. doi: 10.1016/S0378-1127(96)03937-0

Huang, Q. B., Qin, X. Q., Liu, P. Y., Zhang, L. K., and Su, C. T. (2017). Impact of sulfuric and nitric acids on carbonate dissolution, and the associated deficit of $CO_2$ uptake in the upper-middle reaches of the Wujiang River, China. *J. Contam. Hydrol.* 203, 18–27. doi: 10.1016/j.jconhyd.2017.05.006

Jin, L., Ravella, R., Ketchum, B., Bierman, P. R., Heaney, P., White, T., et al. (2010). Mineral weathering and elemental transport during hillslope evolution at the

Susquehanna/Shale Hills Critical Zone Observatory. *Geochim. Cosmochim. Acta* 74, 3669–3691. doi: 10.1016/j.gca.2010.03.036

Johnson, C. E., Driscoll, C. T., Siccama, T. G., and Likens, G. E. (2000). Element fluxes and landscape position in a northern hardwood forest watershed ecosystem. *Ecosystems* 3, 159–184. doi: 10.1007/s100210000017

Kendall, K., Shanley, J., and McDonnell, J. (1999). A hydrometric and geochemical approach to test the transmissivity feedback hypothesis during snowmelt. *J. Hydrol.* 219, 188–205. doi: 10.1016/S0022-1694(99)00059-1

Kopáček, J., Hejzlar, J., Kaňa, J., Porcal, P., and Turek, J. (2016). The sensitivity of water chemistry to climate forested, nitrogen-saturated catchment recovering from acidification. *Ecol. Indic.* 63, 196–208. doi: 10.1016/j.ecolind.2015.12.014

Lagaly, G. (1993). "Reaktionen des tonminerale," in *Tonminerale und Tone: Struktur, Eigenschaften und Einsatz in Industrie und Umwelt*, eds K. Jasmund and G. Lagaly (Darmstadt: Steinkopff Verlag), 89–167. doi: 10.1007/978-3-642-72488-6_3

Lawrence, G. B., Hazlett, P. W., Fernandez, I. J., Ouimet, R., Bailey, S. W., Shortle, W. C., et al. (2015). Declining acidic deposition begins reversal of forest-soil acidification in the northeastern U.S. and Eastern Canada. *Environ. Sci. Technol.* 49, 13103–13111. doi: 10.1021/acs.est.5b02904

Lidman, F., Boily, A., Laudon, H., and Köhler, S. J. (2017). From soil water to surface water – how the riparian zone controls element transport from a boreal forest to a stream. *Biogeosciences* 14, 3001–3014. doi: 10.5194/bg-14-3001-2017

Likens, G. E., Bormann, F. H., and Johnson, N. M. (1972). Acid rain. *Environ. Sci. Policy Sustain. Dev.* 14, 33–40. doi: 10.1080/00139157.1972.9933001

Lybrand, R. A., and Rasmussen, C. (2015). Quantifying climate and landscape position controls on soil development in semiarid ecosystems. *Soil Sci. Soc. Am. J.* 79, 104–116. doi: 10.2136/sssaj2014.06.0242

Maher, K. (2011). The role of fluid residence time and topographic scales in determining chemical fluxes from landscapes. *Earth Planet. Sci. Lett.* 312, 48–58. doi: 10.1016/j.epsl.2011.09.040

Matzner, E., and Murach, D. (1995). Soil changes induced by air pollutant deposition and their implication for forests in central Europe. *Water Air Soil Pollut.* 85, 63–76. doi: 10.1007/BF00483689

Mayer, B., Shanley, J. B., Bailey, S. W., and Mitchell, M. J. (2010). Identifying sources of stream water sulfate after a summer drought in the Sleepers River watershed (Vermont, USA) using hydrological, chemical, and isotopic techniques. *Appl. Geochem.* 25, 747–754. doi: 10.1016/j.apgeochem.2010.02.007

McGlynn, B. L., McDonnell, J. J., Shanley, J. B., and Kendall, C. (1999). Riparian zone flowpath dynamics during snowmelt in a small headwater catchment. *J. Hydrol.* 222, 75–92. doi: 10.1016/S0022-1694(99)00102-X

McIntosh, J. C., Schaumberg, C., Perdrial, J., Harpold, A., Vázquez-Ortega, A., Rasmussen, C., et al. (2017). Geochemical evolution of the Critical Zone across variable time scales informs concentration-discharge relationships: Jemez River Basin Critical Zone Observatory. *Water Resour. Res.* 53, 4169–4196. doi: 10.1002/2016WR019712

McLeod, A. I. (2011). *Kendall: Kendall Rank Correlation and Mann-Kendall Trend Test*. Available at: http://CRAN.R-project.org/package=Kendall

Meals, D. W., Spooner, J., Dressing, S. A., and Harcum, J. B. (2011). "Statistical analysis for monotonic trends," in *Developed for U.S. Environmental Protection Agency* (Fairfax, VA: Tetra Tech, Inc.), 23. Available at: https://www.epa.gov/polluted-runoff-nonpoint-source-pollution/nonpoint-source-monitoring-technical-notes

Meybeck, M. (1993). Riverine transport of atmospheric carbon: sources, global typology and budget. *Water Air Soil Pollut.* 70, 443–463. doi: 10.1007/BF01105015

Miles, G., Mitchell, M., Mayer, B., Likens, G., and Welker, J. (2012). Long-term analysis of Hubbard Brook stable oxygen isotope ratios of streamwater and precipitation sulfate. *Biogeochemistry* 111, 443–454. doi: 10.1007/s10533-011-9670-3

Moore, D. M., and Reynolds, R. C. (1997). *X-Ray Diffraction and the Identification and Analysis of Clay Minerals*, 2nd Edn. New York, NY: Oxford University Press.

Mulholland, P. J., and Hill, W. R. (1997). Seasonal patterns in streamwater nutrient and dissolved organic carbon concentrations: separating catchment flow path and in-stream effects. *Water Resour. Res.* 33, 1297–1306. doi: 10.1029/97wr00490

Newell, A. D., and Skjelkvåle, B. L. (1997). Acidification trends in surface waters in the international program on acidification of rivers and lakes. *Water Air Soil Pollut.* 93, 27–57. doi: 10.1023/A:1022126704750

Nezat, C. A., Blum, J. D., Klaue, A., Johnson, C. E., and Siccama, T. G. (2004). Influence of landscape position and vegetation on long-term weathering rates at the Hubbard Brook Experimental Forest, New Hampshire, USA 11 Associate editor: K. L. Nagy. *Geochim. Cosmochim. Acta* 68, 3065–3078. doi: 10.1016/j.gca.2004.01.021

Ong, H. L., and Bisque, R. E. (1968). Coagulation of humic colloids by metal IonS. *Soil Sci.* 106, 220–224. doi: 10.1097/00010694-196809000-00011

Perdrial, J. N., Warr, L. N., Perdrial, N., Lett, M.-C., and Elsass, F. (2009). Interaction between smectite and bacteria: implications for bentonite as backfill material in the disposal of nuclear waste. *Chem. Geol.* 264, 281–294. doi: 10.1016/j.chemgeo.2009.03.012

Peters, N. E., Shanley, J. B., Aulenbach, B. T., Webb, R. M., Campbell, D. H., Hunt, R., et al. (2006). Water and solute mass balance of five small, relatively undisturbed watersheds in the U.S. *Sci. Total Environ.* 358, 221–242. doi: 10.1016/j.scitotenv.2005.04.044

Peters, N., and Aulenbach, B. (2009). *Flowpath Contributions of Weathering Products to Stream Fluxes at the Panola Mountain Research Watershed, Georgia*. Reston, VA: U.S Geological Survey.

Pohlert, T. (2018). *trend: Non-Parametric Trend Tests and Change-Point Detection, R package version 0.0.1*.

Poppe, L. J., Paskevich, V. F., Hathaway, J. C., and Blackwood, D. S. (2001). *A Laboratory Manua for X-Ray Powder Diffraction (Open-File No. 1–41)*. Reston, VA: USGS.

R Core Development Team (2017). *R: A Language and Environment for Statistical Computing*. Vienna: R Foundation for statistical computing.

Raddum, G. G., Fjellheim, A., Erikson, L., Fott, J., Halvorsen, G. A., Heegaard, E., et al. (2007). "Biological recovery," in *Trends in Surface Water Chemistry and Biota; The Importance of Confounding Factors: Report 87/2007*, eds H. de Wit and B. L. Skjelkvale (Warsaw: ICP Waters), 50–63.

Ratcliffe, N., Stanley, R., Gale, M., Thompson, P., and Walsh, G. (2011). *Bedrock Geologic Map of Vermont. Scientific Investigations Series Map 3184*. Reston, VA: U.S. Geological Survey.

Rice, K. C., and Herman, J. S. (2012). Acidification of Earth: an assessment across mechanisms and scales. *Appl. Geochem.* 27, 1–14. doi: 10.1016/j.apgeochem.2011.09.001

Rogora, M., Colombo, L., Lepori, F., Marchetto, A., Steingruber, S., and Tornimbeni, O. (2013). Thirty years of chemical changes in alpine acid-sensitive lakes in the alps. *Water Air Soil Pollut.* 224:1746. doi: 10.1007/s11270-013-1746-3

Runkel, R. L., Crawford, C. G., and Cohn, T. A. (2004). "Load estimator (LOADEST): a FORTRAN program for estimating constituent loads in streams and rivers," in *USGS Techniques and Methods Book 4, Chapter A5*, eds S. M. Westenbroek, J. Doherty, J. F. Walker, and V. A. Kelson (Reston, VA: U.S. Geological Survey).

Schuster, P. F., Shanley, J., Marvin-Dipasquale, M., Reddy, M. M., Aiken, G. R., Roth, D. A., et al. (2007). Mercury and organic carbon dynamics during runoff episodes from a northeastern USA watershed. *Water Air Soil Pollut.* 187, 89–108. doi: 10.1007/s11270-007-9500-3

Sebestyen, S. D., Boyer, E. W., Shanley, J. B., Kendall, C., Doctor, D. H., Aiken, G. R., et al. (2008). Sources, transformations, and hydrological processes that control stream nitrate and dissolved organic matter concentrations during snowmelt in an upland forest. *Water Resour. Res.* 44:W12410. doi: 10.1029/2008WR006983

Shanley, J. B. (2000). *Sleepers River Watershed – A USGS WEBB Program Site: U.S. Geological Survey Fact Sheet*. Reston, VA: US Geological Survey.

Shanley, J. B., Chalmers, A. T., Mack, T. J., Smith, T. E., and Harte, P. T. (2016). Groundwater level trends and drivers in two northern New England glacial aquifers. *JAWRA J. Am. Water Resour. Assoc.* 52, 1012–1030. doi: 10.1111/1752-1688.12432

Shanley, J. B., Kram, P., Hruska, J., and Bullen, T. D. (2004). A biogeochemical comparison of two well-buffered catchments with contrasting histories of acid deposition. *Water Air Soil Pollut. Focus* 4, 325–342. doi: 10.1023/B:WAFO.0000028363.48348.a4

Shanley, J. B., Schuster, P. F., Reddy, M. M., Roth, D. A., Taylor, H. E., and Aiken, G. R. (2002). Mercury on the move during snowmelt in Vermont. *EOS* 83, 45–48. doi: 10.1029/2002EO000031

Shanley, J. B., Sebestyen, S. D., Mcdonnell, J. J., Mcglynn, B. L., and Dunne, T. (2015). Water's Way at Sleepers River watershed – revisiting flow generation in a post-glacial landscape, Vermont USA. *Hydrol. Process.* 29, 3447–3459. doi: 10.1002/hyp.10377

Skjelkvåle, B. L. (2003). "The 15-year report: assessment and monitoring of surface waters in Europe and North America; acidification and recovery, dynamic modelling and heavy metals," in *NIVA Rep. 4716-2003, ICP Waters Report 73/2003*, (Reston, VA: US Geological Survey).

Skjelkvåle, B. L., Stoddard, J. L., and Andersen, T. (2001). Trends in surface water acidification in Europe and North America (1989–1998). *Water Air Soil Pollut.* 130, 787–792. doi: 10.1023/A:1013806223310

Skjelkvåle, B. L., Stoddard, J. L., Jeffries, D. S., Tørseth, K., Høgåsen, T., Bowman, J., et al. (2005). Regional scale evidence for improvements in surface water chemistry 1990–2001. *Environ. Pollut.* 137, 165–176. doi: 10.1016/j.envpol.2004.12.023

Sommer, M. (2006). Influence of soil pattern on matter transport in and from terrestrial biogeosystems—A new concept for landscape pedology. *Geoderma* 133, 107–123. doi: 10.1016/j.geoderma.2006.03.040

Stoddard, J. L., Jeffries, D. S., Lukewille, A., Clair, T. A., Dillon, P. J., Driscoll, C. T., et al. (1999). Regional trends in aquatic recovery from acidification in North America and Europe. *Nature* 401, 575–578. doi: 10.1038/44114

Strawn, D. G., Hinrich, B. L., and O'Connor, G. A. (2015). *Soil Chemistry*, 4th Edn. Hoboken, NJ: John Wiley & Sons, Ltd.

Temminghoff, E. J. M., Van der zee, S. E. A. T. M., and Haan, F. A. M. (1995). Speciation and calcium competition effects on cadmium sorption by sandy soil at various pHs. *Eur. J. Soil Sci.* 46, 649–655. doi: 10.1111/j.1365-2389.1995.tb01361.x

Tipping, E., and Ohnstad, M. (1984). Aggregation of aquatic humic substances. *Chem. Geol.* 44, 349–357. doi: 10.1016/0009-2541(84)90148-7

Vidon, P., Allan, C., Burns, D., Duval, T. P., Gurwick, N., Inamdar, S., et al. (2010). Hot spots and hot moments in riparian zones: potential for improved water quality management1. *JAWRA J. Am. Water Resour. Assoc.* 46, 278–298. doi: 10.1111/j.1752-1688.2010.00420.x

Winterdahl, M., Temnerud, J., Futter, M. N., Löfgren, S., Moldan, F., and Bishop, K. (2011). Riparian zone influence on stream water dissolved organic carbon concentrations at the Swedish integrated monitoring sites. *Ambio* 40, 920–930. doi: 10.1007/s13280-011-0199-4

**Conflict of Interest Statement:** The authors declare that the research was conducted in the absence of any commercial or financial relationships that could be construed as a potential conflict of interest.

frontiers in Earth Science

ORIGINAL RESEARCH
published: 13 March 2019
doi: 10.3389/feart.2019.00036

# Distinct Contributions of Eroding and Depositional Profiles to Land-Atmosphere $CO_2$ Exchange in Two Contrasting Forests

*Sharon A. Billings*[1]*, *Daniel de B. Richter*[2], *Susan E. Ziegler*[3], *Karen Prestegaard*[4] and *Anna M. Wade*[2]

[1] Department of Ecology and Evolutionary Biology, Kansas Biological Survey, University of Kansas, Lawrence, KS, United States, [2] Nicholas School of the Environment, Duke University, Durham, NC, United States, [3] Department of Earth Sciences, Memorial University, St. John's, NL, Canada, [4] Department of Geology, University of Maryland, College Park, MD, United States

OPEN ACCESS

**Edited by:**
Ashlee Dere,
University of Nebraska Omaha,
United States

**Reviewed by:**
Ronny Lauerwald,
Free University of Brussels, Belgium
Gary E. Stinchcomb,
Murray State University, United States

***Correspondence:**
Sharon A. Billings
sharon.billings@ku.edu

**Specialty section:**
This article was submitted to Biogeoscience, a section of the journal Frontiers in Earth Science

**Received:** 29 June 2018
**Accepted:** 14 February 2019
**Published:** 13 March 2019

**Citation:**
Billings SA, Richter DdB, Ziegler SE, Prestegaard K and Wade AM (2019) Distinct Contributions of Eroding and Depositional Profiles to Land-Atmosphere $CO_2$ Exchange in Two Contrasting Forests. Front. Earth Sci. 7:36. doi: 10.3389/feart.2019.00036

Lateral movements of soil organic C (SOC) influence Earth's C budgets by transporting organic C across landscapes and by modifying soil-profile fluxes of $CO_2$. We extended a previously presented model (Soil Organic C Erosion Replacement and Oxidation, SOrCERO) and present SOrCERODe, a model with which we can project how erosion and subsequent deposition of eroded material can modify biosphere-atmosphere $CO_2$ fluxes in watersheds. The model permits the user to quantify the degree to which eroding and depositional profiles experience a change in SOC oxidation and production as formerly deep horizons become increasingly shallow, and as depositional profiles are buried. To investigate the relative importance of erosion rate, evolving SOC depth distributions, and mineralization reactivity on modeled soil C fluxes, we examine two forests exhibiting distinct depth distributions of SOC content and reactivity, hydrologic regimes and land use. Model projections suggest that, at decadal to centennial timescales: (1) the quantity of SOC moving across a landscape depends on erosion rate and the degree to which SOC production and oxidation at the eroding profile are modified as deeper horizons become shallower, and determines the degree to which depositional profile SOC fluxes are modified; (2) erosional setting C sink strength increases with erosion rate, with some sink effects reaching more than 40% of original profile SOC content after 100 y of a relatively high erosion rate (i.e., 1 mm $y^{-1}$); (3) even large amounts of deposited SOC may not promote a large depositional profile C sink even with large gains in autochthonous SOC post-deposition if oxidation of buried SOC is not limited; and (4) when modeled depositional settings receive a disproportionately large amount of SOC, simulations of strong C sink scenarios mimic observations of modest preservation of buried SOC and large SOC gains in surficial horizons, suggesting that C sink scenarios have merit in these forests. Our analyses illuminate the importance of cross-landscape linkages between upland and depositional

environments for watershed-scale biosphere-atmosphere C fluxes, and emphasize the need for accurate representations and observations of time-varying depth distributions of SOC reactivity across evolving watersheds if we seek accurate projections of ecosystem C balances.

**Keywords: erosion, deposition, hillslope, floodplain soils, carbon fluxes, soil organic carbon, dynamic replacement, terrestrial carbon sink**

## INTRODUCTION

Lateral movement of soil organic C (SOC) due to erosion can influence regional and global C budgets (Doetterl et al., 2016), a phenomenon of increasing importance given human acceleration of soil transport across the globe (Syvitski et al., 2005; Wilkinson and McElroy, 2007; Haff, 2010; Hook et al., 2012). Soil erosion and subsequent deposition transports SOC, which locally depletes or augments profile SOC reservoirs, respectively. Erosion can also alter regional and global C budgets by influencing fluxes of $CO_2$ to and from the atmosphere (Stallard, 1998; Harden et al., 1999; Berhe et al., 2007; van Oost et al., 2007; Billings et al., 2010; Doetterl et al., 2015; Dialynas et al., 2016; Wang et al., 2017). Biosphere-atmosphere exchange of C can be influenced by erosion via SOC mineralization to $CO_2$ during transport of eroded material, and by alteration of SOC production and mineralization rates in both eroding and depositional profiles.

Mineralization of SOC to $CO_2$ during transport of eroded material (Jacinthe and Lal, 2001; Jacinthe et al., 2002) is perhaps the most obvious way that erosion can influence atmospheric $CO_2$. The fraction of eroded SOC subjected to mineralization during transport varies greatly, depending on the chemical and physical characteristics of eroded material (Hu and Kuhn, 2014). Assumptions about the fate of eroded SOC range from complete mineralization to complete preservation (Lal, 1995; Jacinthe and Lal, 2001; Smith et al., 2001). Difficulties with tracking the fate of eroded SOC make quantifying the eroded SOC that is lost as $CO_2$ during transport a challenging problem (Hu and Kuhn, 2014).

Erosion influences atmospheric $CO_2$ by influencing biosphere-atmosphere C exchange within the eroding profile. "Dynamic replacement" (Stallard, 1998) of SOC—the continued production of SOC at an eroding profile that can replenish the SOC removed via erosion—is an important driver of erosion's influence on global C cycling (van Oost et al., 2007; Wang et al., 2017). The degree to which SOC continues to be produced within an eroding profile via litterfall, root detritus, and root exudates depends on ecosystem productivity. Production of SOC may be maintained, but in natural, unfertilized systems SOC production may decrease with the onset of erosion given that eroded ecosystems typically exhibit lower productivity than those growing on intact soil profiles due to fertility losses (Lal, 1987, 1995; Lenka et al., 2017).

Soil erosion may also influence rates of SOC oxidation within eroding profiles. Though it is possible that deep, slow-turnover SOC retains its relatively slow mineralization rate as it becomes increasingly shallow upon erosion, its mineralization behavior is difficult to predict. As buried horizons become closer to the surface upon erosion, they are likely exposed to an increasingly more oxygenated environment. Soil at a new, shallower depth also may experience a greater rate of labile inputs than it would have *sans* erosion, which can promote mineralization of relatively persistent SOC (Fontaine et al., 2007). These processes may result in formerly deep, slow-turnover SOC experiencing mineralization to $CO_2$ at rates more similar to the SOC that previously resided at the shallower depths.

As a result of potentially altered SOC dynamics, each layer within a soil profile may exhibit SOC production ranging between some reduced rate and that occurring prior to erosion. Likewise, each layer may exhibit SOC oxidation ranging between its original rate and some new, enhanced rate similar to SOC oxidation of the layer that originally resided at that depth (i.e., SOC oxidation rates maintained at the pre-erosion rate). The integrated, eroded profile thus exhibits some $CO_2$ sink or source reflective of the combined influence of both of these phenomena. Indeed, model projections suggest that modifying both of these terms can result in significant changes to the eroding profile's C budget, and that eroding profiles can serve as significant, net C sinks (Billings et al., 2010). Note that these phenomena within the eroding profile—dynamic replacement of SOC (Stallard, 1998) at potentially lower rates and potentially maintained SOC oxidation rates—assume that profile depth is only influenced by erosion and not by bedrock weathering, a reasonable assumption for decadal-to-centennial timescales. "Dynamic replacement" of SOC thus does not consider longer-term processes linking erosion, weathering, and geochemical $CO_2$ consumption (Ebelman, 1845; Berner, 1999).

The same logic suggesting that soil removal via erosion can modify SOC production and oxidation at an eroding profile also suggests that deposition of eroded soil can modify analogous processes in terrestrial depositional profiles. If the eroded material is comprised of organic matter-rich topsoil, deposition of eroded soil can introduce a rich source of exogenous nutrients to depositional profiles (Liu et al., 2003; Quinton et al., 2010; Wang et al., 2014; Papanicolaou et al., 2015); even erosion of SOC from deep gullies (Nadeu et al., 2012) transports nutrients to depositional environments. This process can promote relatively high ecosystem productivity at many depositional environments (McKenney et al., 1995; Van Loo et al., 2017) and, presumably, SOC productivity rates as well. Because SOC buried in relatively low-oxygen environments can be preserved far longer than in surface environments, deposition of eroded material also may induce enhanced preservation of buried profiles at depositional settings (Berhe et al., 2008; Berhe and Kleber, 2013; Marín-Spiotta et al., 2014). The mechanisms driving such preservation remain unclear, but it is likely to greater frequency of reducing conditions

in deepening soils. Regardless of the mechanisms, the degree to which deposition of eroded material influences either SOC production or oxidation at depositional profiles remains poorly quantified. It is difficult to predict the relative dominance of simultaneously occurring SOC production and oxidation across profiles receiving varying amounts of eroded material.

Here, we present a modeling tool useful for assessing the influence of erosion and subsequent deposition on soil and atmospheric C budgets, conceptually depicted in **Figure 1**. The new model expands an existing 1-D model, Soil Organic C Erosion Replacement and Oxidation (SOrCERO; Billings et al., 2010), which focused on eroding profile C dynamics, to include depositional profiles (SOrCERODe), providing a tool to facilitate watershed-scale assessment of C budgets. Both models are spreadsheet-driven, providing a user-friendly interface and the ability to observe soil layers (i.e., spreadsheet rows) to vary in SOC content over time. The original SOrCERO model tests the influence of erosion rates and associated changes in SOC production and oxidation in an eroding soil profile with prescribed SOC characteristics on profile C stocks and atmospheric $CO_2$. Recently expanding these ideas, a spatially-explicit, hydrogeomorphic model (tRIBS-ECO; Dialynas et al., 2016) demonstrates the potential importance of time-varying erosion rates and small-scale (i.e., tens of meters) topographical differences in driving watershed-scale, erosion-induced C fluxes due to changes in SOC production and oxidation. SOrCERODe represents another expansion of SOrCERO's principles by allowing the user to specify depositional profile characteristics and the degree to which depositional profile SOC production and oxidation are modified upon deposition. Note that the depositional profile is assumed to be terrestrial, where SOC production can occur. Further, SOrCERODe allows the user to specify the fraction of eroded SOC that is deposited at the depositional profile. SOrCERODe does not explicitly account for differences in characteristics of soil organic matter that arrives at depositional profiles compared to the material that was eroded; because low density material tends to travel further, this can be an important driver of SOC transformations post-erosion (Berhe and Kleber, 2013; Hu and Kuhn, 2014; Papanicolaou et al., 2015). It also does not consider processes influencing total ecosystem C balance such as methane dynamics or volatile organic C or CO losses (Chapin et al., 2006). However, the user is able to evaluate the relative importance of (1) changes in SOC production and oxidation rates in the eroding profile *and* the depositional profile and (2) the fraction of eroded material arriving at the depositional profile in driving the influence of erosion and subsequent deposition on an integrated watershed's C budget.

We applied SOrCERODe in two contrasting forested ecosystems. Our objective was to assess the relative importance of erosion rate, oxidation of SOC during transport, deposition rate, and altered SOC production and oxidation in both eroding and depositional profiles as influences on ecosystem SOC balances. Our efforts represent one step toward constraining the watershed-scale C dynamics that result from the lateral movement of SOC across a landscape. One forest is a mesic, warm temperate forest supported by soils containing relatively low SOC content that have experienced anthropogenically enhanced erosion rates. This forest was the subject of our original explorations with SOrCERO of eroding profiles' influence on atmospheric $CO_2$ (Billings et al., 2010). It is leveraged here as representative of forest soils in the southeastern U.S. that experienced significant erosion upon conversion to agricultural land upon European settlement (Trimble, 2008), prompting widespread deposition of formerly upland soil materials in riparian areas (Trimble and Lund, 1982; James, 2013), some aided by mill dams (Walter and Merritts, 2008). The second forest is a mesic boreal forest with relatively high SOC content (Ziegler et al., 2017) that experiences relatively low erosion rates due to its closed canopy status, the low erosional impact of high latitude precipitation, and the snowmelt-dominated annual hydrographs. We employ these forests as contrasting environments (low SOC and high erosion rates, and high SOC and low erosion rates) to explore the influences of SOC erosion and deposition, and associated changes in SOC production and oxidation on soil profile and watershed SOC pools.

# METHODS

## The Model

Details of the original SOrCERO model are found in Billings et al. (2010). Briefly, the original model prompts users to parameterize initial conditions in any soil profile of interest with SOC contents at multiple, evenly-spaced depths. Each interval's thickness is dictated by a user-determined erosion rate. For example, an erosion rate of 1 mm $y^{-1}$ defines each soil layer as 1 mm thick. For each depth, the user provides SOC content (kg C $m^{-2}$) and initial rates of SOC oxidation ($k_{ox}$, $y^{-1}$) and production ($I$, kg C $m^{-2}$). These processes are held at steady state as an initial condition prior to the onset of erosion. Functions for smooth interpolations between known values are provided such that each layer, regardless of thickness, is populated. A key advance made by SOrCERO was the introduction of mixing coefficients that compute how SOC oxidation and production rates at the eroding profile change over time ($n_{ox}$ and $n_{prod}$, respectively). These mixing coefficients are provided by the model user, and reflect the user's assumptions about any changes in SOC oxidation and production at the eroding profile as erosion proceeds, an elusive value to estimate in soil profiles. The inclusion of these coefficients in the model allows the user to assess the importance of this knowledge gap. Values of $n_{ox}$ and $n_{prod}$ can vary between zero and one, inclusive, and are independent of each other. They reflect oxidation and production rates that are either absolute or relative, respectively. Absolute rates of SOC oxidation and production define rates as originally assigned to each soil layer in the profile, and remain unmodified throughout model runs even as layers become increasingly shallow as erosion occurs. In contrast, relative rates are those originally assigned to each depth increment, not each layer, and thus change for all layers as they become increasingly shallow upon the onset of erosion.

As erosion proceeds at the user-defined rate for the specified time period, the model modifies each layer's SOC content at the end of the previous time step (or, for the initial time step, from

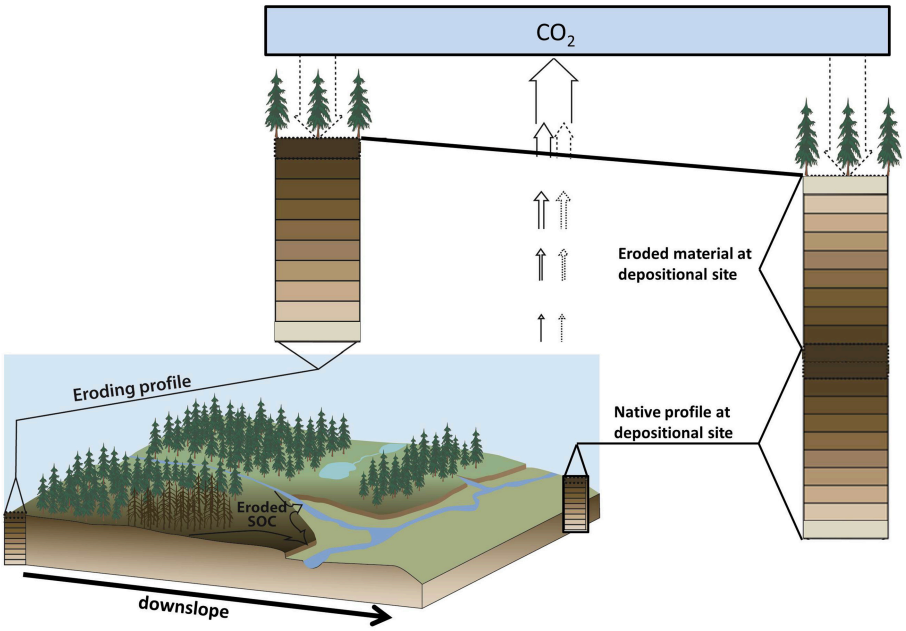


**FIGURE 1 |** Schematic of a landscape experiencing erosion (upslope) and deposition (downslope), as conceptualized by the Soil Organic C Erosion Replacement and Oxidation-Deposition (SOrCERODe) model. Shades of brown at each depth depict variation in SOC concentrations with depth. In the eroding profile and native profile at the depositional site, SOC concentrations decline with depth. In eroded material deposited at depositional site, colors are inverted to represent topsoil layers with relatively high SOC concentrations being deposited prior to formerly deep layers. Note that the coloring does not reflect new SOC production at the depositional setting. At both eroding and depositional sites, SOC production (dashed downward-facing arrows) occurs concurrently with SOC oxidation (solid, upward-facing arrows) and $CO_2$ production by autotrophs (dashed, upward-facing arrows). SOrCERODe allows the user to define the erosion rate, the deposition rate, and the degree to which SOC production and oxidation at each depth is influenced by erosion at the eroding site and by deposition at the depositional site. Figure adapted from Billings et al. (2010).

initial values) according to Equation (1):

$$C_t = C_{t-1} - ((n_{ox} \times C_{t-1}) \times e^{-k_{ox,R}t} + (1 - n_{ox}) \times C_{t-1} \times e^{-k_{ox,A}t}) + n_{prod} \times I_R + (1 - n_{prod}) \times I_A \quad (1)$$

where $C_t$ is the amount of SOC in the layer at the end of time step $t$, $k_{ox,R}$ is the new SOC oxidation rate constant assigned to the layer (relative), $k_{ox,A}$ is the SOC oxidation rate constant originally assigned to the layer (absolute), $t$ is the time step, $I_R$ is the SOC production rate newly assigned to the layer (relative), and $I_A$ is the SOC production rate originally assigned to the layer (absolute). Prior to the onset of erosion, the soon-to-be-eroded profile is assumed to be in steady state with respect to SOC inputs and outputs; this changes according to the user's designations of $n_{ox}$ and $n_{prod}$. Model outputs include changing profile SOC content over time, and the net $CO_2$ sink or source of the eroding profile in the specified time period.

The expanded SOrCERODe model is comprised of SOrCERO plus a new module that accounts for C dynamics in depositional profiles. Here, the depositional profile is assumed to be in steady state with respect to SOC inputs and outputs until eroded SOC is deposited. At that point, SOC content in a profile's layer at the end of time step $t$ ($C_{t(d)}$) will equal $C_{t-1(d)}$ minus the SOC oxidized plus SOC produced at the deposition profile during the time period specified, plus the SOC deposited. Both oxidation and production of SOC at the depositional profile are defined according to some combination of the originally-defined (absolute) and changing (relative) rates, as per user specification. These processes are defined in Equation (2):

$$C_{t(d)} = C_{t-1(d)} - \left((n_{ox(d)} \times C_{t-1(d)} \times e^{-k_{ox(d),A}t}) + (1 - n_{ox(d)}) \times C_{t-1(d)} \times e^{-k_{ox(d),R}t}\right) + n_{prod(d)} \times I_{(d),A} + (1 - n_{prod(d)}) \times I_{(d),R} + D \quad (2)$$

where subscripts $d$ refer to the depositional profile. Note that for the eroding profile, $n_{ox}$ and $n_{prod}$ prescribe SOC oxidation and production rates relative to those rates in the surface horizon, and for the depositional profile these mixing coefficients prescribe rates relative to those in the surface horizon of the buried profile; as a result, arriving SOC has the potential to enhance SOC production at the depositional profile, presumably via enhanced ecosystem productivity, and to mitigate oxidation of buried SOC. Any enhanced SOC production would presumably arise due to at least partial mineralization of, and associated $CO_2$ losses from, arriving soil organic matter. The final term in Equation (2), $D$, is the amount of SOC deposited immediately upon erosion at the specified time point. This term is derived from a user-defined fraction of the eroded material that reflects assumptions about the probability that eroded SOC arrives at the depositional

location instead of undergoing mineralization during transport, or export to streams; either scenario prevents eroded SOC from residing in a depositional profile. Depending on the user's intentions, $D$ also can be modified to reflect the proportion of eroding relative to depositional settings in the area of interest. The amount of eroded SOC subjected to those assumptions depends on the user's assigned values of $n_{ox}$ and $n_{prod}$ at the eroding profile. Note that though both erosion and deposition are phenomena distributed across landscapes, Equations (1, 2) treat both erosion and deposition as one-dimensional processes. However, by considering erosional and depositional functions in conjunction with each other, we can take a large step forward in understanding potential responses of watershed C fluxes to erosion.

## Model Limitations and Assumptions

There are multiple scenarios that can govern SOC fluxes into and out of soil profiles that SOrCERODe does not explicitly accommodate. For example, SOrCERODe does not account for leaching losses of dissolved organic C (DOC) or other known pathways of C loss from terrestrial ecosystems, which combined can represent a meaningful fraction of an ecosystem's C losses (Chapin et al., 2006). Another limitation of the model is that it offers no means of incorporating soil texture or lithologic discontinuities, both of which can be important drivers of SOC transit times within soil profiles (e.g., Nadeu et al., 2012) and SOC concentrations of eroded material (Papanicolaou et al., 2015). Similarly, phenomena responsible for non-monotonic depth distributions of SOC such as freeze-thaw events and animal burrowing (Matzner and Borken, 2008; Clark et al., 2016) are not explicitly accounted for in the model, and size separation during overland transport (Hu and Kuhn, 2014) is not explicitly defined. However, by prescribing each soil layer's SOC production and oxidation functions, the user can prescribe input parameters that implicitly account for such features. It also is important to note that SOrCERODe is best suited for assessing the influence of SOC erosion and deposition on ecosystem C dynamics when erosion rates are relatively constant. If event-based erosion temporally interspersed with longer-term, slower erosion rates is of interest, the user must concatenate model runs defined by varying erosion rates and erosion duration. Given the stochastic arrival of sediment packages comprised of diverse soil textures in depositional settings (e.g., Wilson et al., 2012) and spatial heterogeneity in profile characteristics across watersheds (Dialynas et al., 2016), an important next step for model development is more elegant integration of temporal and spatial heterogeneity in delivery of sediment packages.

In addition to these limitations, SOrCERODe implicitly assumes several ecosystem features. First, current parameterization assumes equivalent depth distributions of SOC content and turnover characteristics and equivalent profile depths at both erosional and depositional sites prior to the onset of erosion, and that SOC inputs and losses from these profiles are at steady state prior to the onset of erosion. We parameterize the model in this way to permit exploration of landscape evolution (i.e., a deepening depositional profile) as the system departs from steady state. SOrCERODe also makes no explicit provisions for lighter SOC to escape terrestrial, depositional environments (e.g., into streams). Instead, the user must incorporate their assumption of how much eroded SOC is lost into the fraction of SOC arriving at the depositional setting. Additionally, the model assumes uniform, layer-by-layer erosion and deposition. In reality, overland transit can be a turbulent and stochastic process (Hu and Kuhn, 2014), with depositional profiles subjected to spatially and temporally heterogeneous inputs from erosional areas of varying magnitudes. Finally, though SOrCERODe is a one-dimensional model, we can upscale modeled results; however, we must know the proportion of eroding to depositional settings in a watershed, an idea explored in our analyses. In spite of these limitations, the model represents a step toward developing the process models needed to better constrain the dominant processes responsible for watershed-scale C balances as they evolve with landscape evolution over time.

## Model Application

We apply SOrCERODe in two contrasting forests. One is a hardwood stand within the Calhoun Critical Zone Observatory (CZO) in South Carolina, USA. Dominant species include white oak (*Quercus alba*), northern red oak (*Quercus rubra*), hickory (*Carya* spp.), sweetgum (*Liquidambar styraciflua*), and yellow poplar (*Liriodendron tulipifera*). Tree age derived from breast height cores averages 129 ± 21 (s.d.) y. Soils are Oxyaquic Kanhapludults on granitic gneiss; the surface mineral horizon is a sandy loam underlain by a clay-rich Bt horizon and regolith extends ∼38 m in depth (Bacon et al., 2012). We infer from multiple sources (W. Cook and D. Richter, pers. comm.) that soils in the forest stand employed in the current study have not been subjected to the plow, though the region experienced widespread, agriculturally accelerated erosion (Richter and Markewitz, 2001; Trimble, 2008). Thus, this forest's soils exhibit characteristics we take to be similar to those that experienced accelerated erosion upon clearing, a widespread historical phenomenon in this region (Richter and Markewitz, 2001). We consider these forest soils to be representative of those upslope of depositional, floodplain soils prior to European settlement in a ∼638 ha watershed where SOC depth distributions of depositional settings recently have been well-characterized, and where previous landscape-level work indicates that depositional settings comprise <10% of the landscape (K. Godsey and D.D. Richter, personal communication).

The second forest lies within the Newfoundland and Labrador Boreal Ecosystem Latitudinal Transect (NL-BELT) in eastern Canada, part of the Critical Zone Exploratory Network. The dominant overstory species is balsam fir (*Abies balsamifera*) averaging 47 y (±6 s.d.) at breast height. The forest has developed on post-glacial till and moderately coarse grained glaciofluvial materials (Ricketts, 2001). Soils in these forests are well-drained, humic ferric podzols (as designated by the Canadian Forest Service; Haplorthods in the U.S. system). These soils possess well-developed organic horizons (average thickness of 8 ± 1.5 cm) overlying sandy loam B horizons (A horizons are often not expressed and E horizons only weakly so) underlain by relatively shallow till (i.e., <50 cm; McCuaig, 2002). There is no evidence or

record of harvesting activity in these stands, and the major stand disturbance is insect outbreaks (D. Harris, pers. comm.). We consider these forest soils to be representative of those upslope of streambank soils in a ∼345 ha watershed. The forested headwater streams monitored in conjunction with these forest profiles exhibit clear waters even during storm events, with particulate organic matter representing a minor fraction of total organic matter concentrations (S. Ziegler, pers. comm.), consistent with relatively low erosion rates.

For both forests, we populated model input parameters for the eroding profile following the approach described in Billings et al. (2010). Briefly, we used depth distributions of bulk density and SOC concentrations obtained in both forests from previous work (Markewitz and Richter, 1998; Richter et al., 1999; Ziegler et al., 2017) to generate SOC content in each soil layer (**Figure 2**). In both forests, the first order oxidation rate constants $k_{ox}$ were derived from the inverse of estimated SOC mean residence times (MRT), which in turn were constrained by radiocarbon signatures of SOC stocks derived from previous studies (Richter et al., 1999; Ziegler et al., 2017) and as described in Billings et al. (2010). We appreciate that MRT estimates of SOC based on radiocarbon rely on several assumptions that are likely false in many forest soil profiles (Sierra et al., 2017) and employ these preliminary values as a simplified, first attempt to characterize these profiles' SOC dynamics. We defined MRT of SOC as 10 and 2,000 y at the surface and 100 cm depth, respectively, at the Calhoun CZO (i.e., 0.1 and 0.0005 $y^{-1}$, respectively). Values between these surface and deep estimates were interpolated following a function defined by the depth distribution of SOC fraction. At NL-BELT, estimates of MRT of SOC are much younger, exhibiting surprisingly modern values throughout the relatively shallow profiles: 33 and 62 y in surface O horizons and at 10 cm depth in the mineral soil, respectively (i.e., 0.030 and 0.016 $y^{-1}$, respectively); these estimated mineralization reactivities are discussed in Ziegler et al. (2017). We parameterized the model with no interpolation between these values, but instead an abrupt shift in value to reflect the sharp horizon distinction between O and mineral horizons. Within each forest, we assumed that eroding and depositional profiles exhibited identical depth distributions of SOC content and $k_{ox}$ prior to the onset of modeled erosion and deposition; in this way, we are able to observe the influence of erosion and deposition, *de novo*, on these profiles' depth distributions of SOC. Note that each layer's $k_{ox}$ value defines that layer's SOC input rate $I$ with the assumption that the eroding and depositional profiles are at steady state prior to erosion, and both $k_{ox}$ and $I$ are modified as erosion occurs according to user assumptions about $n_{ox}$ and $n_{prod}$.

These two forests contrast in ways relevant to erosion-induced changes in the C cycle. In the boreal forest, erosion of the shallow soil profiles is primarily driven by hydrologic flows of Oi sub-horizon material (∼47% C, that of recent plant litterfall) downslope to riparian areas. Hydrologic data from this and nine additional forests in the region indicate that runoff is a substantial fraction of incoming precipitation (S. Ziegler and K. Prestegaard, pers. comm.), but we assume low erosive precipitation in this closed-canopy, high latitude forest, and that erosion rates are very

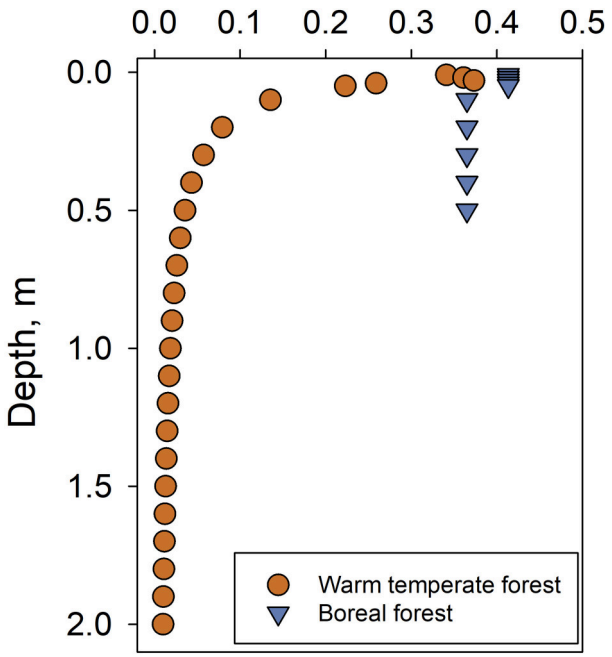


**FIGURE 2 |** Depth distributions of soil organic C (SOC) content in a warm temperate forest (Calhoun Critical Zone Observatory, South Carolina, USA) and a mesic boreal forest (Newfoundland and Labrador Boreal Ecosystem Latitudinal Transect, Canada) used as input parameters for the Soil Organic C Erosion Replacement and Oxidation-Deposition (SOrCERODe) model. Values are smoothed from actual values (Markewitz and Richter, 1998; Ziegler et al., 2017). Note that soil profiles in the boreal forest are shallower than in the warm temperate forest. In the current study, each forest's erosional and depositional profiles are assumed to exhibit these depth distributions prior to initiation of modeled erosion and deposition, allowing model users to investigate the influence of erosion, deposition, and SOC production and oxidation on profile SOC content post-erosion.

low in spite of the forests' mesic nature. In the warm temperate forest, O horizons are thinner, mineral soils are thicker and are less C-rich than in the boreal forest. The relatively high erosion rates that soils in the warm, temperate, southeastern U.S. experienced upon conversion of hardwood forest to agriculture in the late eighteenth, nineteenth, and early twentieth centuries resulted in relatively low-C mineral soil being transported rapidly to floodplains downslope, driven by highly erosive rainfall in conjunction with poor soil management practices (Richter and Markewitz, 2001). Thus, these two forests contrast in soil depth to bedrock, soil organic C concentrations, and erosion rates—all important features to consider when investigating the influence of erosion on C budgets over time.

Employing these two contrasting forests, we ran SOrCERODe for 100 y at two erosion rates broadly representative of or higher than either their current or historic erosional histories: 1 mm $y^{-1}$, which represents a conservative estimate of historical erosion rates in the warm temperate forest soils after conversion to

agriculture (Trimble, 2008; Billings et al., 2010), and 0.1 mmy$^{-1}$, an order of magnitude lower (though still higher than many natural systems as inferred over geologic timescales; Wilkinson and McElroy, 2007; Bacon et al., 2012). We also varied the fraction of eroded SOC that reaches the depositional profile. For each of these scenarios, we explored two combinations of $n_{ox}$ and $n_{prod}$ values. First, we set these terms to represent maximum SOC production for both eroding and depositional profiles in each forest. At the eroding profiles, we thus assumed that SOC production was maintained in spite of erosion, and that each profile layer's SOC oxidation was maintained in spite of a presumed increase in oxygen access as erosion occurs. At the depositional profiles, we assumed that SOC production was enhanced, and oxidation of buried SOC mitigated, upon deposition. Next, we set these terms to represent minimum SOC production and maximum oxidation for both eroding and depositional profiles in each forest. This combination of $n_{ox}$ and $n_{prod}$ values at the eroding profile corresponds to an assumption of reduced SOC production and each profile layer's SOC oxidation becoming enhanced upon erosion. At the depositional profiles, these $n_{ox}$ and $n_{prod}$ values correspond to no enhancement of SOC production, and maintenance of SOC oxidation in spite of its burial.

The boreal forest region invoked here has relatively shallow soils (**Figure 2**), so we limited our analyses to relatively shallow depths in this forest. In contrast, the warm temperate forest has a soil profile many meters deep (Bacon et al., 2012). For this forest, we present results for a soil profile truncated at the same depth as in the boreal forest (termed the shallow scenario) to allow for a direct comparison of the two forest types across the same depths. We also present results for warm temperate forest profiles >1 m deep (termed the deep scenario; this represents the original top meter in the depositional profile plus deposited material). These deeper modeled profiles more likely represent these warm temperate forests' C dynamics upon erosion and deposition. These shallow and deep scenarios are distinct only at the warm temperate forest depositional profile, where deposition can generate relatively deep profiles in some modeled scenarios, consistent with the concept of legacy sediments (James, 2013). For all model runs, we report net $CO_2$ source (+) or sink (–) strength at the eroding and depositional profiles and their combined influence.

The model simulations do not require the user to know the relative proportion of erosional vs. depositional areas within a watershed. This approach compares eroding and depositional settings that are equivalent in area (i.e., each m$^2$ of eroding profile contributes SOC to each m$^2$ of depositional profile). This is not reflective of most watersheds' geomorphologies, where depositional settings receive a disproportionately large amount of sediment from surrounding hillslopes (Anderson and Anderson, 2010). We thus also performed model runs that account for the additional annual SOC inputs that depositional profiles would receive given a specified proportion of eroding and depositional soil types in a given watershed. For these model runs, we leveraged recent estimates of upland and floodplain soils comprising 90 and 10% of the Calhoun CZO's warm temperate forests, respectively (D. Richter, personal communication); we applied these same values to the boreal forest watershed to provide a point of comparison. In these model runs, erosion rates of 1.0 and 0.1 mm y$^{-1}$ from 90% of a watershed prompt a maximum of 9.0 and 0.9 mm y$^{-1}$ to be deposited on 10% of the watershed's area (though recall that the user can modify the fraction of eroding SOC arriving at the depositional profile). Note that assuming that only 10% of the watershed receives eroding material thus generates deeper profiles than was previously modeled, an additional factor contributing to changing profile SOC content upon erosion. Specifically, these calculations assume that depositional profiles deepen by 0.09 and 0.9 m with a 0.1 and 1.0 mm y$^{-1}$ erosion rate, respectively. In both the boreal and the warm temperate forest, we report how accounting for these disproportionately large SOC inputs in modeled depositional profiles may modify watershed-scale SOC content after 100 y of erosion at these two rates.

# RESULTS

## Eroding Profile C Sinks and Sources

In both forests, model maximization of SOC production and minimization of SOC oxidation at the eroding profiles—i.e., enhancing each profile layer's SOC production while preventing its oxidation from increasing as it becomes shallower—resulted in stronger C sinks or weaker C sources, as would be expected (**Figure 3**, **Tables 1–3**). At both forests' eroding profiles, both the C sink and C source strengths increased with erosion rate, though potential sink strengths increased to a greater degree than potential source strengths (**Figure 3A** vs. **Figure 3B**).

If no eroded SOC undergoes oxidation during transport, 100 y of erosion at 0.1 mm y$^{-1}$ in the warm temperate forest resulted in a potential C sink strength of −1.3 kg C m$^{-2}$ (**Figure 3A**, left-most point of long-dash line) when SOC production is maximized and SOC oxidation is minimized upon erosion. This is equivalent to 19% of the original profile SOC content. In contrast, 100 y of erosion at 1 mm y$^{-1}$ in this same forest resulted in a potential C sink strength of −14.4 kg C m$^{-2}$ if no eroded SOC undergoes oxidation during transport and if SOC production is maximized and SOC oxidation is minimized upon erosion (**Figure 3B**, left-most point of long-dash line). This suggests that an increase in erosion rate by one order of magnitude can increase the sink potential of the eroding profile by more than one order of magnitude. Even if we assume that no eroded SOC is oxidized and SOC production is minimized and SOC oxidation is maximized, 100 y of erosion at 1 mm y$^{-1}$ in the warm temperate forest generated a C sink of −2.9 kg C m$^{-2}$, equivalent to 43% of the original profile SOC content.

In the boreal forest, potential C sources to the atmosphere after 100 y of erosion were highest for both erosion rates when SOC production was minimized and SOC oxidation was maximized, ranging from 0.6 to 5.5 kg C m$^{-2}$ at 0.1 and 1.0 mm y$^{-1}$, respectively (right-most point of dot-dash line in **Figures 3A,B**, respectively). When SOC production was maximized and SOC oxidation was minimized at the boreal forest eroding profile, the lower erosion rate always induced a net sink, the largest of which represented 7% of the original profile SOC content. The higher erosion rate only induced a net $CO_2$

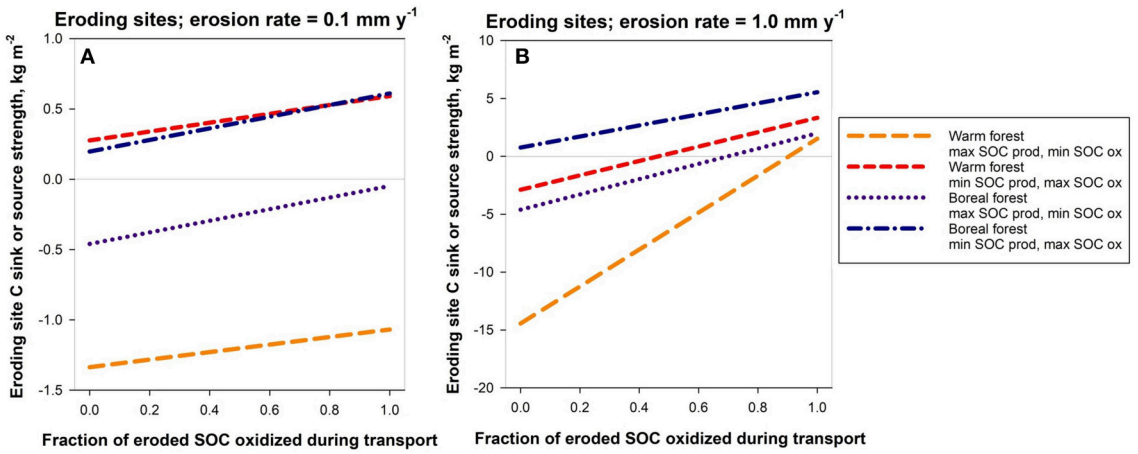


**FIGURE 3 |** The net C sink or source strength of eroding profiles as a function of the fraction of SOC oxidized during transport for a warm temperate forest and a boreal forest after 100 y of erosion at two specified erosion rates 0.1 mmy$^{-1}$ **(A)** and 1.0 mmy$^{-1}$ **(B)**. The two labeled scenarios represent contrasting assumptions about (1) potential enhancement of each depth's SOC oxidation rate as it nears the surface upon erosion, and (2) potential decline of SOC production rates for each depth as it nears the surface upon erosion. Negative values indicate net C sinks; positive values indicate net C sources to the atmosphere. Note change in Y axis scaling across erosion rates. Max, maximum; min, minimum. See text for model description and definitions of maximum and minimum SOC production and oxidation.

**TABLE 1 |** Boreal forest eroding and depositional sites' net $CO_2$ source (+) or sink (–) strengths, and their summed effects on the atmosphere, for given soil organic C oxidation and production characteristics at both sites and two potential fates of eroded material for model runs of 100 y duration.

| Eroding site | | Fate during transport | Depositional site | | Summed effect on atmosphere |
|---|---|---|---|---|---|
| | Net $CO_2$ source/sink | | | Net $CO_2$ source/sink | |
| **0.1 mm y$^{-1}$** | | | | | |
| Min prod, max ox | 0.61 | Oxidized | Maintains steady state | 0 | 0.61 |
| Min prod, max ox | 0.20 | Reaches dep'l site | Min prod, max ox | 1.44 | 1.64 |
| Max prod, min ox | −0.05 | Oxidized | Maintains steady state | 0 | −0.05 |
| Max prod, min ox | −0.46 | Reaches dep'l site | Max prod, min ox | 1.43 | 0.97 |
| **1.0 mm y$^{-1}$** | | | | | |
| Min prod, max ox | 5.55 | Oxidized | Maintains steady state | 0 | 5.55 |
| Min prod, max ox | 2.00 | Reaches dep'l site | Min prod, max ox | 1.70 | 3.70 |
| Max prod, min ox | 0.77 | Oxidized | Maintains steady state | 0 | 0.77 |
| Max prod, min ox | −4.61 | Reaches dep'l site | Max prod, min ox | 0.43 | −4.18 |

*Prior to erosion's onset, depth of both eroding and depositional profiles was set to 0.18 m, reflective of depth to glacial till in these forests. All values are in kg C m$^{-2}$; top section reflects erosion rate of 0.1 mm y$^{-1}$ and bottom section an erosion rate of 1.0 mm y$^{-1}$. Min, minimized; max, maximized. See text for description of these terms.*

source to the atmosphere when more than ∼70% of eroded SOC experienced oxidation post-erosion.

## Soil Organic C Arriving at Depositional Profiles

In the model, the mass of eroded SOC deposited at depositional profiles depends on two phenomena: the rate of erosion; and the rate of SOC production and oxidation within the eroding profile (i.e., $n_{ox}$ and $n_{prod}$ of eroding profiles), which dictate the concentration of SOC in the eroded material. When we assumed that no eroded SOC was oxidized during transport, boreal forest depositional profiles received 0.41 and 5.37 kg C m$^{-2}$ after 100 y of erosion when erosion rates were set at 0.1 and 1.0 mm y$^{-1}$, respectively, and eroding profile SOC production was maximized and oxidation was minimized (**Figure 4A**, middle bar). In contrast, when eroding profiles experienced lower SOC production and higher SOC oxidation, boreal forest depositional profiles received 0.41 and 3.55 kg C m$^{-2}$ for erosion rates of 0.1 and 1.0 mm y$^{-1}$, respectively (**Figure 5A**, middle bar).

When $n_{ox}$ and $n_{prod}$ at eroding profiles were set to maximize SOC production and minimize SOC oxidation, the warm temperate forest depositional profiles received 0.27 and 11.56 kg C m$^{-2}$ for erosion rates of 0.1 and 1.0 mm y$^{-1}$, respectively (**Figures 4B,C**, middle bars). Note that these values are constant regardless of the depth of the warm temperate forest depositional profile (**Figure 4B** vs. **Figure 4C**). When eroding profiles experienced lower SOC production and high SOC oxidation than prior to erosion, the warm temperate forest depositional profiles received 0.32 and 1.80 kg C m$^{-2}$ for erosion rates of 0.1 and 1.0 mm y$^{-1}$, respectively (middle bars in **Figures 5B,C**).

**TABLE 2 |** Warm temperate forest eroding and depositional sites' net $CO_2$ source (+) or sink (-) strengths, and their summed effects on the atmosphere, assuming that initial depth of both profiles was 0.18 m.

| Eroding site | | Fate during transport | Depositional site | | Summed effect on atmosphere |
|---|---|---|---|---|---|
| | Net $CO_2$ source/sink | | | Net $CO_2$ source/sink | |
| **0.1 mm $y^{-1}$** | | | | | |
| Min prod, max ox | 0.59 | Oxidized | Maintains steady state | 0 | 0.59 |
| Min prod, max ox | 0.28 | Reaches dep'l site | Min prod, max ox | 0.11 | 0.39 |
| Max prod, min ox | −1.07 | Oxidized | Maintains steady state | 0 | −1.07 |
| Max prod, min ox | −1.34 | Reaches dep'l site | Max prod, min ox | 0.07 | −1.27 |
| **1.0 mm $y^{-1}$** | | | | | |
| Min prod, max ox | 3.33 | Oxidized | Maintains steady state | 0 | 3.33 |
| Min prod, max ox | 1.54 | Reaches dep'l site | Min prod, max ox | −0.59 | 0.95 |
| Max prod, min ox | −2.88 | Oxidized | Maintains steady state | 0 | −2.88 |
| Max prod, min ox | −14.44 | Reaches dep'l site | Max prod, min ox | −2.91 | −17.35 |

*The initial depth setting permits direct comparisons to the boreal forest soil profile fluxes (see **Table 1**), though real profiles in the warm temperate forest were deeper. All values are in kg C $m^{-2}$ and represent given soil organic C oxidation and production characteristics at both sites, and two potential fates of eroded material, for model runs of 100 y duration. Top section reflects erosion rate of 0.1 mm $y^{-1}$ and bottom section 1.0 mm $y^{-1}$. Min, minimized; max, maximized. See text for description of these terms.*

**TABLE 3 |** Warm temperate forest eroding and depositional sites' net $CO_2$ source (+) or sink (-) strengths, and their summed effects on the atmosphere, assuming that initial depth of both profiles was 1.0 m.

| Eroding site | | Fate during transport | Depositional site | | Summed effect on atmosphere |
|---|---|---|---|---|---|
| | Net $CO_2$ source/sink | | | Net $CO_2$ source/sink | |
| **0.1 mm $y^{-1}$** | | | | | |
| Min prod, max ox | 0.59 | Oxidized | Maintains steady state | 0 | 0.59 |
| Min prod, max ox | 0.28 | Reaches dep'l site | Min prod, max ox | −0.73 | −0.45 |
| Max prod, min ox | −1.07 | Oxidized | Maintains steady state | 0 | −1.07 |
| Max prod, min ox | −1.34 | Reaches dep'l site | Max prod, min ox | −1.10 | −2.44 |
| **1.0 mm $y^{-1}$** | | | | | |
| Min prod, max ox | 3.33 | Oxidized | Maintains steady state | 0 | 3.33 |
| Min prod, max ox | 1.54 | Reaches dep'l site | Min prod, max ox | −1.17 | 0.37 |
| Max prod, min ox | −2.88 | Oxidized | Maintains steady state | 0 | −2.88 |
| Max prod, min ox | −14.44 | Reaches dep'l site | Max prod, min ox | −3.55 | −17.99 |

*All values are in kg C $m^{-2}$ and represent given soil organic C oxidation and production characteristics at both sites, and two potential fates of eroded material, for model runs of 100 y duration. Top section reflects erosion rate of 0.1 mm $y^{-1}$ and bottom section 1.0 mm $y^{-1}$. Min, minimized; max, maximized. See text for description of these terms.*

## Depositional Profile C Sinks and Sources

Depositional profiles were assumed to remain in steady state when all eroded SOC underwent oxidation during transport and no eroded material arrived at depositional profiles. Model runs depicting this scenario thus indicate that depositional profiles had no net influence as a $CO_2$ source or sink (**Table 1**, see rows in which depositional profile is designated as maintaining a steady state). In contrast, when eroded SOC reached depositional profiles (i.e., was not oxidized during transport), depositional profiles served as either a $CO_2$ sink or source (**Figures 4**, **5**, far right bars). Depositional profile sink or source strength depended on the mass of material deposited (section Soil Organic C Arriving at Depositional Profiles) and the degree to which deposition of SOC influenced SOC production and oxidation at the depositional profile (i.e., $n_{ox}$ and $n_{prod}$ at depositional profiles).

When eroded material reached the depositional profiles and SOC production was maximized and SOC oxidation was minimized at both eroding and depositional profiles, the boreal forest depositional profiles served as a small net $CO_2$ source to the atmosphere regardless of erosion rate after 100 y of erosion and deposition (1.43 kg C $m^{-2}$ at 0.1 mm $y^{-1}$ and 0.43 kg C $m^{-2}$ at 1.0 mm $y^{-1}$; **Figure 4A**). Under these same constraints, depositional profiles in the warm temperate forest served as either a small net $CO_2$ source to the atmosphere (0.07 kg C $m^{-2}$ at 0.1 mm $y^{-1}$) or a net $CO_2$ sink (−2.91 kg C $m^{-2}$ at 1.0 mm $y^{-1}$) when we considered a depositional profile the same depth as in the boreal forest (**Figure 4B**). When we deepened the depositional profile, the sink strength of the warm temperate forest depositional profile increased to −1.10 and −3.55 kg C $m^{-2}$ at 0.1 and 1.0 mm $y^{-1}$, respectively, under these same conditions of maximized SOC production

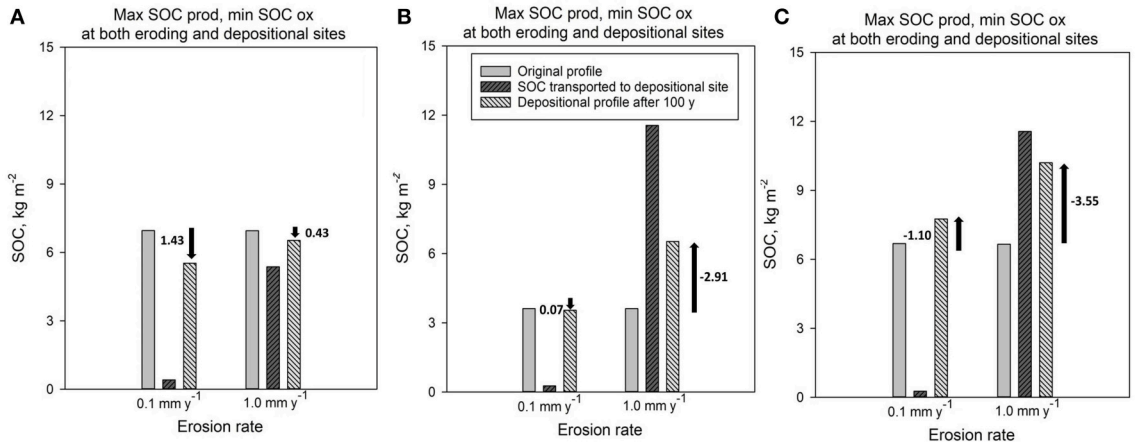


**FIGURE 4 |** Soil organic C content in depositional profiles prior to erosion onset (left most bar in each set), SOC content arriving at depositional sites (middle bar in each set), and SOC content in depositional profiles after 100 y (right-most bar in each set) at the specified erosion rates for boreal forest soils **(A)** and warm temperate forest soils **(B,C)**. In all scenarios, both eroding and depositional sites experienced maximized SOC production and minimized SOC oxidation upon erosion and deposition (see text for details of model parameterization). Boreal forest soil profiles **(A)** were 0.18 m deep prior to the onset of deposition, and 0.19 or 0.28 m deep after 100 y of deposition at 0.1 and 1.0 mm $y^{-1}$, respectively. In **(B)**, warm temperate forest soils were truncated at the same depth as the boreal forest soils **(A)** to enable direct comparison across these forests; **(C)** reflects the top 1.01 (0.1 mm $y^{-1}$) and 1.1 (1.0 mm $y^{-1}$) of depositional profiles in the warm temperate forest to enable projection of more realistic fluxes in these deep soils. Arrows reflect net SOC loss from profile (downward arrows) or net SOC gain to profile (upward arrows); numbers represent corresponding net SOC source to atmosphere or net SOC sink, respectively. Note that middle bars in each set remain constant across **(B,C)**, because SOC amount deposited does not depend on depositional site conditions.

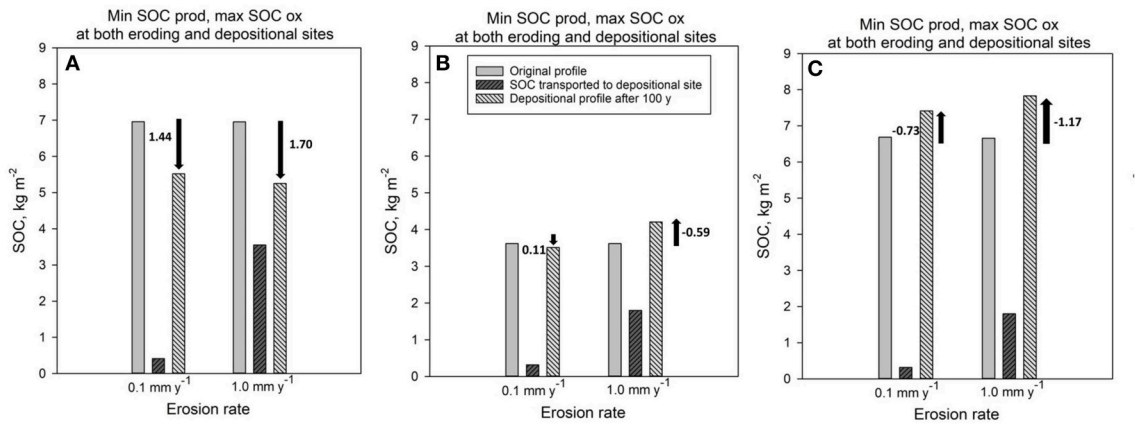


**FIGURE 5 |** Soil organic C content in depositional profiles prior to erosion onset (left most bar in each set), SOC content arriving at depositional sites (middle bar in each set), and SOC content in depositional profiles post-deposition (right-most bar in each set) at the specified erosion rates for boreal forest soils **(A)** and warm temperate forest soils **(B,C)**. In all scenarios, both eroding and depositional sites experienced minimized SOC production and maximized SOC oxidation upon erosion and deposition (see text for details of model parameterization). Boreal forest soil profiles **(A)** were 0.18 m deep prior to the onset of deposition, and 0.19 or 0.28 m deep after 100 y of deposition at 0.1 and 1.0 mm $y^{-1}$, respectively. Warm temperate forest soils were truncated at the same depth as the boreal forest soils in **(B)** to enable direct comparison across these forests; **(C)** considered the top 2 m of depositional profiles in the warm temperate forest to enable projection of more realistic fluxes in these deep soils. Arrows reflect net SOC loss from profile (downward arrows) or net SOC gain to profile (upward arrows); numbers represent corresponding net SOC source to atmosphere or net SOC sink, respectively. Note that middle bars in each set remain constant across **(B,C)**, because SOC amount deposited does not depend on depositional site conditions.

and minimized SOC oxidation at both eroding and depositional profiles (**Figure 4C**).

When we assigned $n_{ox}$ and $n_{prod}$ values that minimized SOC production and maximized SOC oxidation at both eroding and depositional profiles, 100 y of erosion and deposition induced a net $CO_2$ source in the boreal forest (1.44 and 1.70 kg C $m^{-2}$ at 0.1 and 1.0 mm $y^{-1}$, respectively; **Figure 5A**) and a small $CO_2$ source (0.11 kg C $m^{-2}$) or sink (−0.59 kg C $m^{-2}$) at 0.1 and 1.0 mm $y^{-1}$, respectively, in a similarly shallow warm temperate forest profile (**Figure 5B**). Deepening the warm temperate forest

depositional profile generated a consistent $CO_2$ sink regardless of erosion rate (−0.73 and −1.17 kg C $m^{-2}$ at 0.1 and 1.0 mm $y^{-1}$, respectively; **Figure 5C**).

## Assessing Whole-System C Sinks and Sources Resulting From Erosion and Deposition of SOC

The combined influence of eroding and depositional profiles on whole-system, net C uptake or loss after 100 y of erosion varied with forest type, erosion rate, and values of $n_{ox}$ *and* $n_{prod}$ at both eroding and depositional profiles (**Tables 1**–**3**). At the lower erosion rate (0.1 mm $y^{-1}$), the boreal forest eroding and depositional profiles, combined, generated a small net $CO_2$ sink (0.05 kg C $m^{-2}$) when no eroded SOC reached the depositional profiles and eroding profile SOC productivity was maximized and SOC oxidation was minimized (**Table 1**). This sink effect was exhibited entirely at the eroding profile. In all other scenarios, the combined effect of eroding and depositional profiles in the boreal forest was a net $CO_2$ source, ranging from 0.61 to 1.64 kg C $m^{-2}$. In the scenarios in which eroded SOC was not oxidized during transport, net $CO_2$ sources across the whole system were dominated by fluxes at the depositional profiles.

When the erosion rate increased to 1.0 mm $y^{-1}$, the combined erosional and depositional profiles exhibited greater variation in net $CO_2$ sinks and sources. Here, the influence of erosion and deposition ranged from a net $CO_2$ source of 5.55 kg C $m^{-2}$ to a net $CO_2$ sink of −4.18 kg C $m^{-2}$. In contrast with the lower erosion rate, the majority of these 100-y sinks and sources were exhibited at the eroding profile.

For the warm temperate forest's shallow and deep scenarios, we also observed less variation in summed eroding and depositional profiles' net $CO_2$ sink and source terms at the lower erosion rate (**Tables 2**, **3**). At 0.1 mm $y^{-1}$, the shallow scenario resulted in net $CO_2$ sinks and sources ranging from a net source of 0.59 kg C $m^{-2}$ to a net sink of −1.27 kg C $m^{-2}$ after 100 y (**Table 2**). At 1.0 mm $y^{-1}$, the shallow scenario ranged from a net source of $CO_2$ of 3.33 kg C $m^{-2}$ to a net sink of −17.35 kg C $m^{-2}$. When we allowed the depositional profile in the warm temperate forest to deepen from a starting depth of 1 m, the lower erosion rate resulted in values ranging from a maximum net source of $CO_2$ to the atmosphere of 0.59 kg C $m^{-2}$ to a maximum net sink of $CO_2$ from the atmosphere of −2.44 kg C $m^{-2}$ (**Table 3**). At the higher erosion rate, the deeper profile in the warm temperate forest exhibited a greater range of whole-system $CO_2$ fluxes, ranging from a small net $CO_2$ source of 0.37 kg C $m^{-2}$ to a net $CO_2$ sink of −17.99 kg C $m^{-2}$. In this warm temperate forest, the majority of the summed, net effect of erosional and depositional profiles on atmospheric $CO_2$ was dominated by fluxes at the eroding profile, particularly at the higher erosion rate when eroding profile SOC production was maximized and oxidation was minimized (**Table 3**).

## Model Simulations Assuming Disproportionately Large SOC Inputs at Depositional Settings

Though the warm temperate forest watershed under study is larger (∼638 ha) than the boreal forest watershed (∼345 ha), model estimates suggest that these forests contain similar quantities of SOC in their pre-eroded state (6.65 and 6.96 kg $m^{-2}$ or 4.24 and 2.40 Mg in each watershed, respectively; **Figure 6**). These values are influenced by assumptions of initial profile depths of 1.0 and 0.18 m in the warm temperate and boreal forest, respectively. Model runs that transferred nine times the eroding material to depositional profiles (i.e., assuming that 90% of both forests experience erosion and 10% receive eroded material) over 100 y of erosion at an erosion rate of 0.1 mm $y^{-1}$ resulted in a net $CO_2$ source to the atmosphere in both forests (lower post-erosion SOC content in both panels of **Figure 6A**). This was true regardless of whether the model was parameterized for the maximum possible $CO_2$ sink or maximum possible $CO_2$ source. The net $CO_2$ source, or net loss of SOC from the watersheds, ranged from 3.04 kg $m^{-2}$ (1.94 Mg) in the warm temperate forest to 3.16 kg $m^{-2}$ (1.09 Mg) in the boreal forest. However, when the modeled erosion rate increased, both forests' model runs exhibited a net $CO_2$ sink when parameterized for the maximum possible sink, ranging from −0.45 kg $m^{-2}$ (0.16 Mg) in the boreal forest to −4.46 kg $m^{-2}$ (2.85 Mg) in the warm temperate forest (**Figure 6B**). When parameterized for the maximum possible source at this higher erosion rate, $CO_2$ sources ranged from 2.76 kg $m^{-2}$ (1.76 Mg) to 4.90 kg $m^{-2}$ (1.69 Mg) in the warm temperate and boreal forests, respectively (**Figure 6B**).

# DISCUSSION

By using SOrCERODe to compare two forests with contrasting characteristics relevant to erosional C dynamics—high erosion rate and lower SOC concentrations vs. low erosion rate and higher SOC concentrations—we estimate how erosion rate, fraction of eroded SOC arriving in depositional settings, and changing rates of SOC production and oxidation at eroding and depositional profiles can govern profile- to watershed-scale net soil $CO_2$ sinks and sources. Some modeled $CO_2$ fluxes were of meaningful magnitude; net C sink and source strengths of eroding and depositional profiles of the two studied forests reach or surpass the same order of magnitude as measured dissolved organic C exports from the surface horizon to deeper horizons in these boreal forests (∼30 g C $m^{-2}$ $y^{-1}$; S. Ziegler, pers. comm.) and in the warm temperate forest (∼20 g C $m^{-2}$ $y^{-1}$; calculated from Markewitz et al., 1998).

## Eroding Profile $CO_2$ Source and Sink Strengths

The enhancement of eroding profile $CO_2$ sink strength when SOC production at the eroding profile is maintained (i.e., $n_{prod}$= 1) in spite of surficial horizon losses was exaggerated with a higher erosion rate, a phenomenon also observed after 150 y of modeled erosion in the original presentation of SOrCERO that invoked the same warm temperate forest (Billings et al., 2010). Model results from both forests in the current study are consistent with Stallard's (1998) idea of dynamic replacement of SOC. However, we note that the eroding system consistently exhibited a net $CO_2$ source for the boreal forest at both erosion rates when SOC production was minimized and oxidation was

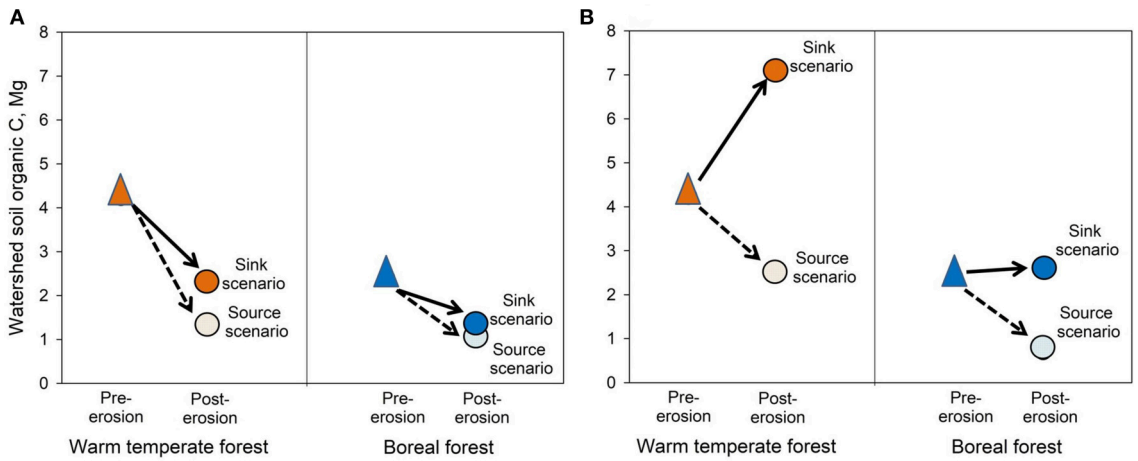


**FIGURE 6 |** Model estimates of soil organic C prior to the onset of modeled erosion (triangle in all panels), and after 100 y of erosion (post-erosion points in all panels) for two erosion rates: **(A)** 0.1 mm $y^{-1}$ and **(B)** 1 mm $y^{-1}$ in a warm temperate forest watershed and a boreal forest watershed, assuming that 90% of the watersheds experiences erosion and 10% experiences deposition. Values reflect watershed sizes of 638 and 345 ha for the warm temperate and boreal forests, respectively. The sink or source scenario terms refer to model runs generating the maximum possible $CO_2$ sink or source terms. Maximum sink scenario assumes maximized SOC production and minimized SOC oxidation; maximum source scenario assumes minimized SOC production and maximized SOC oxidation in both eroding and depositional settings. Differences between the warm temperate and boreal forest are most pronounced at high erosion rates **(B)**. Note that at low erosion rates **(A)**, even when the sink strength is maximized the SOC content post-erosion is lower than the pre-erosion content in both forests, and thus this scenario does not represent a true sink, but rather a smaller $CO_2$ source (i.e., greater SOC content relative to the maximum source scenario).

maximized (blue dot-dash lines, **Figures 3A,B**). Thus, in the extreme scenario of the eroding profile experiencing a decline in SOC production and increases in SOC oxidation of each layer of the profile as it becomes shallower, the boreal forest eroding profile serves as a small net $CO_2$ source to the atmosphere. Observations of intact woody and leaf material in high-latitude regions (e.g., France et al., 1996; Köhler et al., 2009; Guillemette et al., 2017) including this boreal forest's streams (S. Ziegler, pers. comm.) and in many streams, lakes, and coastal sediments (Hedges et al., 1982; Golladay, 1997) suggest that some fraction of eroded material in these ecosystems undergoes lateral export to non-terrestrial environments. Thus, C dynamics of eroded material in watershed aquatic systems along with eroding profile C dynamics are important focal points for understanding the influence of erosion on terrestrial C dynamics.

In contrast, the warm temperate forest serves as a net $CO_2$ sink from the atmosphere even when SOC production was minimized and oxidation was maximized at the higher erosion rate, when less than ∼50% of eroded SOC is oxidized post-erosion (orange dashed line, **Figure 3B**). Indeed, an increase in erosion rate of one order of magnitude increased the potential sink strength of the eroding profile by more than one order of magnitude in the warm temperate forest. This, in conjunction with the much stronger potential sink strength of the warm temperate forest relative to the boreal forest, highlights the importance of these forests' contrasting depth distributions of SOC reactivity in governing eroding profile $CO_2$ dynamics. In the boreal forest, the difference between estimates of SOC turnover time in surficial and the deepest modeled horizons was 29 y; in the warm temperate forest, that difference across equivalent depths was 785 y. The relatively greater reactivity of SOC in the boreal forest, even at depth, means that over a 100 y model run all original SOC in the boreal profiles has left those reservoirs, resulting in stronger net $CO_2$ sources and weaker net $CO_2$ sinks at eroding profiles in the boreal forest than in the warm temperate forest.

## Depositional Profile $CO_2$ Source and Sink Strengths

The frequent status of warm temperate forest depositional profiles as net $CO_2$ sinks across model runs was driven by two features. First, when arriving material fueled greater SOC production (presumably via enhanced ecosystem productivity), sink strength increased. This result is consistent with forests in riparian areas exhibiting high productivity when flood disturbances are not too frequent or severe (Petit et al., 2017). Second, when oxidation of buried SOC was slowed, $CO_2$ sources from native SOC at the depositional profile were mitigated. This is congruent with observations of buried paleo-A horizons in riparian areas at the Calhoun CZO (D. Richter, pers. comm.) and, more generally, preservation of SOC in buried profiles (van Oost et al., 2012; Marín-Spiotta et al., 2014). We emphasize that this second feature does not constitute a $CO_2$ sink, but rather dampens a potential source term.

In spite of the frequent net sink strength of depositional profiles in the warm temperate forest, there is evidence of significant SOC loss from these depositional profiles. Even when a significant quantity of SOC arrived at depositional profiles, depositional profile SOC content after 100 y (right-most bar, **Figures 4B,C**) could be less than the amount of arriving SOC (middle bar, **Figures 4B,C**). This feature highlights the lability—and thus the oxidative potential—of arriving SOC, consistent with eroded material being typically comprised of SOC-rich, A

horizon materials that are resource-rich for soil microbes (Berhe and Kleber, 2013). The dynamism of surface horizons is also highlighted by the relatively small difference in sink strength of shallow vs. deeper depositional profiles in the warm temperate forest. Incorporating relatively deep subsoils into assessments of depositional profile C dynamics can be relevant for accurate projections of C stocks (Doetterl et al., 2016), but in these forests' profiles, deepening the depositional profile enhanced sink potential less than might be expected of a linear system.

In contrast to the warm temperate forest, the boreal forest depositional profile was always a net $CO_2$ source to the atmosphere no matter the erosion rate or the oxidation or production characteristics of the depositional profile. Thus, depositional profile SOC content was always lower than the original depositional profile, even after 100 y of deposition. This counterintuitive result likely reflects two phenomena. First, the material eroded and then deposited in the boreal forest is either all O horizon material (at the lower erosion rate) or ∼80% O horizon material (at the higher erosion rate; O horizons in this forest average ∼8 cm deep). Thus, material arriving at the depositional profile has high oxidation potential (Li et al., 2011). Second, the <100 y turnover time estimates of this material dictates that all eroded material undergoes oxidation within our 100 y model run. This feature means that SOC production must overwhelm oxidation of all arriving SOC to generate a net $CO_2$ sink. We note that net $CO_2$ source strength of the boreal depositional profile was weaker when erosion rate increased. This suggests that as material is deposited at boreal forest depositional profiles, it mitigates SOC oxidation and promotes SOC production, as we might expect. However, these processes were not sufficient to outpace the relatively high reactivity—and thus $CO_2$ loss—of the highly labile deposited material.

## Contrasting and Linking Eroding and Depositional Profile Influences on Atmospheric $CO_2$

The generally increasing sink or source strength (i.e., increasing absolute values) for eroding and depositional profiles with an increase in erosion rate highlights the importance of erosion rate as a primary driver of C fluxes across landscapes. This was true in both forests, though the direction of the C flux varied widely. The potential for eroding profiles to serve as a strong C sink was heightened at eroding profiles in both forests as erosion rate increased, and in the warm temperate forest at depositional profiles as well. These observations particularly highlight the apparently strong influence of SOC's "dynamic replacement" (Stallard, 1998) at eroding profiles and, to a lesser extent, of eroding material's ability to promote SOC production at depositional profiles. This effect seems plausible when we consider that eroded and subsequently deposited material can be relatively nutrient-rich (Quinton et al., 2010; Kuhn, 2011), and thus that depositional profiles can experience nutrient enhancement over time. Indeed, downslope movement of organic matter is a significant contributor to organic carbon and nutrient stocks in depositional environments (Gregory et al., 1991; Köhler et al., 2009; Sanderman et al., 2009; James, 2013).

Summing the influence of erosional and depositional profiles on biosphere-atmosphere C fluxes allows us to estimate the influence of these processes at larger scales. Quantifying how SOC production and oxidation rates are modified upon erosion and deposition is notoriously difficult (van Oost et al., 2007; Billings et al., 2010), but we can make reasonable assumptions about other erosion-relevant factors in these forests to make valuable comparisons of their erosion-induced influence on atmospheric $CO_2$. There are two cross-forest comparisons of particular interest. First, we can compare boreal forest land-atmosphere C fluxes resulting from that forest's relatively low erosion rates to those that likely occurred to warm temperate forest soils prior to European settlement, when erosion rates were also relatively low. Second, we can compare boreal forest soil C fluxes to those in the warm temperate forest soils during their period of accelerated erosion as agricultural soils. For both of these comparisons, we use the deeper depositional scenario in the warm temperate forest, as it likely reflects that region's deep profiles more accurately. We initially consider scenarios in which depositional profiles receive SOC at the same rate at which SOC erodes. We then turn to scenarios in which depositional profiles receive a disproportionately large amount of SOC due to their small areal extent relative to eroding profiles. Combined, these scenarios represent the diverse ways in which SOrCERODe can be leveraged to investigate the influence of erosion on profile- and watershed-scale C dynamics.

### Land-Atmosphere C Fluxes With Relatively Low Erosion Rates in Two Contrasting Forests

In both forests at the lower erosion rate the summed, net effect of eroding and depositional profiles on system $CO_2$ exchange was low in most scenarios compared to those same scenarios at higher erosion rates (contrast top vs. bottom sections of **Tables 1**, **3**). This suggests that the low erosion rates typically observed on low to moderate hillslope gradients (Heimsath et al., 1997; Bacon et al., 2012) do not serve as large contributors to annual C fluxes. Indeed, summed erosional and depositional profile C fluxes after 100 y of erosion at the lower rate in both forests are a small fraction of estimated annual net primary productivity (NPP) for boreal (∼0.19 kg C $m^{-2}$ $y^{-1}$) and temperate (∼0.78 kg C $m^{-2}$ $y^{-1}$) forests (Schlesinger and Bernhardt, 2013).

The degree to which eroding vs. depositional soils governed whole-system C fluxes prompts important inferences about depositional profile dynamics in eroding landscapes. In both forests, lower erosion rates prompted depositional soils to comprise a greater fraction of whole-system C fluxes than eroding profiles, compared to higher erosion rates (compare top vs. bottom sections of **Tables 1**, **3**). The larger influence of the depositional profile on whole-system C dynamics at the lower erosion rate was dependent on assumptions about how depositional profile SOC production and oxidation were modified by the arriving material as well as the amount of material arriving at the profile, and was not due to the simpler, lateral movement of already-fixed SOC across the landscape. Though multiple studies either hint

or explicitly state that ecosystem C sinks can result from movement of fixed C from one pool to another, we emphasize that preservation of SOC, regardless of its position on the landscape, does not draw additional $CO_2$ from the atmosphere (Billings and Schlesinger, 2015).

### Land-Atmosphere C Fluxes in Two Forests Experiencing Contrasting Erosion Rates

Another relevant comparison across these forests is that of the higher erosion rate (1.0 mm $y^{-1}$) in the warm temperate forest, and the low erosion rate (0.1 mm $y^{-1}$) in the boreal forest. Comparing the values from these scenarios allows us to consider what two contrasting land use histories—one anthropogenically dominated with extremely high erosion rates for at least 100 y, the other far less so—may have meant for whole-system C fluxes. Perhaps the most salient feature of the higher erosion rate in the warm temperate forest is the strong, whole-system C sink it induced after 100 y. The annualized largest sink estimate of −17.99 kg C $m^{-2}$ over 100 y in the warm temperate forest (i.e., −0.18 kg C $m^{-2}$ $y^{-1}$) equates to ∼23% of annual temperate forest NPP (Schlesinger and Bernhardt, 2013). Though this flux was dominated by the sink strength of the eroding profile (bottom section, **Table 3**), model results also suggest that the eroding profile C sink was augmented by C uptake at the depositional profile (up to 20% of the whole-system flux). This enhancement of whole-system C flux by the depositional profile occurred even when SOC production at the depositional profile was minimized (bottom section **Table 3**).

In contrast, model results suggest that the same duration of erosion at a lower erosion rate in the boreal forest likely induced a small, whole-system C source to the atmosphere. Increasing the erosion rate in the boreal forest to an unrealistically high 1.0 mm $y^{-1}$ was not sufficient to enhance potential C sink strengths there. The difference in these forests' behavior stems from contrasting estimated depth distributions of SOC reactivity (Richter et al., 1999; Ziegler et al., 2017). Specifically, estimates of relatively low SOC reactivity near the surface in the warm temperate forest (i.e., estimated MRT of ∼1,700 y at 50 cm) translated to an eroding profile with low oxidation rates even as deeper soil became shallower upon erosion. This effect was far more muted at the boreal forest profile, where estimates of SOC reactivity were greater (Ziegler et al., 2017), and thus modeled SOC oxidation relatively greater, even at depth in this forest's shallow profiles.

## Leveraging Watershed Characteristics to Upscale SOC Content and Assess Model Accuracy

Until now, our discussion of erosional and depositional profiles has assumed that each $m^2$ of eroding area contributes to 1 $m^2$ of depositional area. However, depositional settings typically represent a smaller fraction of watersheds than do eroding uplands (Anderson and Anderson, 2010). We leveraged estimates from the Calhoun CZO of the areal extent of upland and floodplain soil types in both forests to estimate how disproportionately large amounts of SOC deposited in depositional settings can modify watershed-scale C dynamics. At the higher erosion rate, accounting for a relatively large area of eroding profiles in the watersheds prompted net gains of modeled SOC in both forests when SOC production was maximized and SOC oxidation was minimized (**Figure 6B**). With a lower erosion rate, both forests experienced modest net losses of SOC to the atmosphere, even in the maximum sink scenarios (**Figure 6A**). These results differ from those model runs that assume each $m^2$ of eroding soil contributes to each $m^2$ of depositional soil; with those model runs, when the warm temperate forest experienced relatively slow erosion, it served as a small net C sink (**Table 3**, top part). Such discrepancies result from two factors: when the model accounts for the distribution of eroding vs. depositional profiles, it weights eroding profile C dynamics more heavily than those at the depositional profiles (here, by a factor of nine), and it allows depositional profiles to deepen to a greater extent.

We can assess the accuracy of modeling disproportionate deepening of depositional profiles and surficial SOC dynamics by employing well-characterized SOC depth distributions in Calhoun CZO depositional settings (**Figure 7**). Buried A horizons are evident via relatively high SOC at depths ranging from ∼60 cm to ∼175 cm in some depositional profiles (**Figure 7A**). Congruent with this, modeled depositional profiles hint that preservation of SOC promoted by deposition of 0.9 m of soil (9 mm $y^{-1}$ for 100 y) extends through the top ∼0.5 m of the original profile (i.e., from 0.9 to 1.4 m in **Figure 7B**). The muted preservation of modeled, buried SOC compared to some profiles' higher SOC content at depth suggests that SOrCERODe may underestimate SOC preservation in some settings. This is consistent with stronger $CO_2$ source strengths and a dampening of $CO_2$ sink strengths when we assume that eroding profiles represent 90% of a watershed (**Figure 6**) than when model runs are conducted on a $m^2$-to-$m^2$ basis (**Table 3**). Surficial SOC dynamics were also captured by SOrCERODe: while the most surficial modeled horizon in the strongest sink scenario (orange triangles, **Figure 7B**) reflects an over-estimation of SOC content in that layer, the strongest sink scenario is similar in shape and content to multiple observed profiles (**Figure 7A**). Thus, although SOrCERODe does not account for the variable nature of the Calhoun CZO's historic erosion (Trimble and Lund, 1982; Walter and Merritts, 2008; James, 2013) or heterogeneity in the fraction of watershed area contributing to each depositional profile, these congruencies highlight how SOrCERODe simulations can reflect partial preservation of deep SOC and faithfully mimic post-deposition SOC formation in surficial layers.

## CONCLUSIONS

We investigate erosion-induced modifications to C inputs and losses in eroding and depositional profiles and associated watershed-scale C dynamics. We demonstrate how ecosystem C fluxes and storage are inextricably linked to landscape evolution on relatively short, centennial timescales. We also demonstrate the importance of eroded SOC retention in a terrestrial depositional setting vs. its escape via mineralization

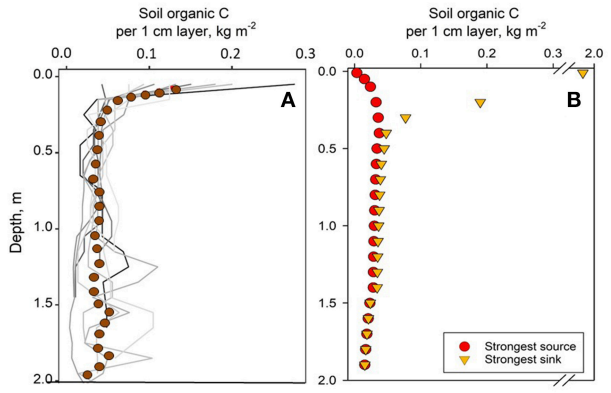


**FIGURE 7 |** Observed **(A)** and modeled **(B)** depth distributions of soil organic C (SOC) at depositional settings in the Calhoun Critical Zone Observatory, a warm temperate forest in South Carolina, USA. Lines in **(A)** represent observations in 10 profiles along a stream channel that have received eroded SOC prior to and post-European settlement at rates varying from extremely low up to ~1 mm $y^{-1}$; symbols in **(A)** represent a smoothed mean of all 10 profiles. Note evidence of buried, high-SOC content horizons (i.e., buried A horizons) in several observed profiles. Symbols in **(B)** represent model runs with contrasting assumptions about SOC production and oxidation in eroding and depositional profiles that result in varying magnitudes of land-atmosphere $CO_2$ fluxes. In the strongest source scenario, SOC oxidation is maximized and SOC production is minimized at eroding and depositional sites. In the strongest sink scenario, the opposite phenomena are assumed. In **(A,B)**, symbols represent SOC content in each 1 cm-thick layer; for clarity, not all 1 cm-thick layers are plotted. See text for model description and estimated influence of the described processes on land-atmosphere $CO_2$ fluxes.

or transport to an aquatic system for estimating a watershed's C balance. Our work reveals four key points:

- The quantity of SOC moving across a landscape depends on the erosion rate and the degree to which SOC production and oxidation at the eroding profile is modified as deeper horizons become shallower. The amount of eroded material arriving at the depositional profile determines the degree to which depositional profile SOC production and oxidation are modified, illuminating the importance of cross-landscape linkages between upland and depositional environments in determining watershed-scale, biosphere-atmosphere C fluxes.
- Changes in SOC formation and oxidation in eroding profiles can result in strong C sink effects in erosional settings that increase with erosion rate in most scenarios. Some model simulations indicate a sink strength at eroding profiles equivalent to more than 40% of the original profile's SOC content in a warm temperate forest experiencing relatively high erosion over 100 y. In a boreal forest, modeled eroding site SOC sink scenarios generally were smaller, reflecting greater SOC mineralization reactivity in those profiles compared to the warm temperate forest.
- Legacy sediments can comprise a meaningful fraction of depositional soils in contemporary landscapes (Walter and Merritts, 2008; James, 2013) and autochthonous SOC additions to depositional profiles can be large relative to initial depositional stocks. However, the current study demonstrates how even large amounts of SOC experiencing cross-landscape transport may not promote a large net C sink in depositional profiles, particularly if oxidation of buried SOC is not sufficiently retarded.
- When we assumed that depositional profiles received a disproportionately large amount of eroded SOC, simulations of depositional profiles reflect modest preservation of buried SOC, congruent with observed profiles in depositional settings. SOrCERODe also faithfully mimicked observed SOC gains in surficial horizon of depositional profiles when the model was parameterized for a strong potential C sink scenario.

Combined, these results suggest that model scenarios representing increasing C sink strength with increasing erosion rates have merit, and that SOrCERODe represents a step toward process modeling of the influence of erosion and deposition on watershed C fluxes. We illuminate the importance of cross-landscape linkages between upland and depositional environments in determining watershed-scale biosphere-atmosphere C fluxes, and emphasize the need for quantifying time-varying depth distributions of SOC reactivity across evolving watersheds if we seek accurate projections of ecosystem C balances.

## AUTHOR CONTRIBUTIONS

SB built and implemented the model, interpreted results, wrote the first draft of the manuscript, and serves as point of contact for model dissemination. AW and DR provided soil organic C data for **Figure 7A**. DR, SZ, KP, and AW assisted with interpreting results and writing the manuscript.

## FUNDING

NSF's grant EAR-1331846: funded modeling and empirical research conducted by SB, DR, and AW. Canada's NSERC Discovery and Strategic Project Grant #397494-10: funded SZ and KP's involvement.

## ACKNOWLEDGMENTS

We are grateful for engaging discussions with Daniel Markewitz and Darrell Harris, for Gil Ortiz's assistance with **Figure 1**, for the contributions of the two reviewers, and for funding from the NSF's grant EAR-1331846 and Canada's NSERC Discovery and Strategic Project Grant program (#397494-10).

## REFERENCES

Anderson, R. S., and Anderson, S. P. (2010). *Geomorphology: The Mechanics and Chemistry of Landscapes*. Cambridge: Cambridge University Press. doi: 10.1017/CBO9780511794827

Bacon, A. R., deB Richter, D., Bierman, P. R., and Rood, D. H. (2012). Coupling meteoric 10Be with pedogenic losses of 9Be to improve soil residence time

estimates on an ancient North American interfluve. *Geology* 40, 847–850. doi: 10.1130/G33449.1

Berhe, A. A., Harden, J. W., Torn, M. S., and Harte, J. (2008). Linking soil organic matter dynamics and erosion-induced terrestrial carbon sequestration at different landform positions. *J. Geophys. Res.* 113:G04039. doi: 10.1029/2008JG000751

Berhe, A. A., Harte, J., Harden, J. W., and Torn, M. S. (2007). The significance of the erosion-induced terrestrial carbon sink. *Bioscience* 57, 337–346. doi: 10.1641/B570408

Berhe, A. A., and Kleber, M. (2013). Erosion, deposition, and the persistence of soil organic matter: mechanistic considerations and problems with terminology. *Earth Surf. Proc. Landforms* 38, 908–912. doi: 10.1002/esp.3408

Berner, R. A. (1999). A new look at the long-term carbon cycle. *GSA Today* 9, 1–6.

Billings, S. A., Buddemeier, R. W., deB Richter, D., van Oost, K., and Bohling, G. (2010). A simple method for estimating the influence of eroding soil profiles on atmospheric $CO_2$. *Global Biogeochem. Cycles* 24:GB2001. doi: 10.1029/2009GB003560

Billings, S. A., and Schlesinger, W. (2015). Letter to the editor on "pyrogenic organic matter production from wildfires: a missing sink in the global carbon cycle." *Glob. Chang. Biol.* 28:2831. doi: 10.1111/gcb.12836

Chapin, F. S. III, Woodwell, G. M., Randerson, J. T., Rastetter, E. B., Lovett, G. M., Baldocchi, D. D., et al. (2006). Reconciling carbon-cycle concepts, terminology, and methods. *Ecosystems* 9, 1041–1050. doi: 10.1007/s10021-005-0105-7

Clark, K., Branch, L., Hierro, J., and Villarreal, D. (2016). Burrowing herbivores alter soil carbon and nitrogen dynamics in a semi-arid ecosystem, Argentina. *Soil Biol. Biochem.* 103, 253–261. doi: 10.1016/j.soilbio.2016.08.027

Dialynas, Y. G., Bastola, S., Bras, R. L., Marín-Spiotta, E., Silver, W. L., Arnone, E., et al. (2016). Impact of hydrologically driven hillslope erosion and landslide occurrence on soil organic carbon dynamics in tropical watersheds. *Water Resour. Res.* 52, 8895–8919. doi: 10.1002/2016WR018925

Doetterl, S., Berhe, A. A., Nadeu, E., Wang, Z., Sommer, M., and Fiener, P. (2016). Erosion, deposition and soil carbon: a review of process-level controls and experimental tools and models to address C cycling in dynamic landscapes. *Earth Sci. Rev.* 154, 102–122. doi: 10.1016/j.earscirev.2015.12.005

Doetterl, S., Cornelis, J. T., Six, J., Bodé, S., Opfergelt, S., Ooeckx, P., et al. (2015). Soil redistribution and weathering controlling the fate of geochemical and physical carbon stabilization mechanisms in soils of an eroding landscape. *Biogeosciences* 12, 1357–1371. doi: 10.5194/bg-12-1357-2015

Ebelman, J. J. (1845). Sur les produits de la decomposition des especes minerals de la famille des silicates. *Annales Mines* 7, 3–66.

Fontaine, S., Barot, S., Barre, P., Bdioui, N., Mary, B., and Rumpel, C. (2007). Stability of organic carbon in deep soil layers controlled by fresh carbon supply. *Nature* 450, 277–280. doi: 10.1038/nature06275

France, R., Culbert, H., and Peters, R. (1996). Decreased carbon and nutrient input to boreal lakes from particulate organic matter following riparian clear-cutting. *Environ. Manage.* 20, 579–583. doi: 10.1007/BF01474657

Golladay, S. W. (1997). Suspended particulate organic matter concentration and export in streams. *J. North Am. Benthol. Soc.* 16, 122–131. doi: 10.2307/1468245

Gregory, S. V., Swanson, F. J., McKee, W. A., and Cummins, K. W. (1991). An ecosystem perspective of riparian zones. *Bioscience* 41, 540–551. doi: 10.2307/1311607

Guillemette, F., von Wachenfeldt, E., Kothawala, D. N., Bastviken, D., and Tranvik., L. J. (2017). Preferential sequestration of terrestrial organic matter in boreal lake sediments. *J. Geophys. Res.* 122, 863–874. doi: 10.1002/2016JG003735

Haff, P. K. (2010). Hillslopes, rivers, plows, and trucks: mass transport or Earth's surface by natural and technological processes. *Earth Surf. Proc. Landforms* 35, 1157–1166. doi: 10.1002/esp.1902

Harden, J. W., Sharpe, J. M., Parton, W. J., Ojima, D. S., Fries, T. L., Huntington, T. G., et al. (1999). Dynamic replacement and loss of soil carbon on eroding cropland. *Global Biogeochem. Cycles* 13, 885–901. doi: 10.1029/1999GB900061

Hedges, J. I., Ertel, J. R., and Leopold, E. S. (1982). Lignin geochemistry of a late quaternary sediment core from Lake Washington. *Geochim. Cosmochim. Acta.* 46, 1869–1877. doi: 10.1016/0016-7037(82)90125-9

Heimsath, A. M., Dietrich, W. E., Nishiizumi, K., and Finkel, R. C. (1997). The soil production function and landscape equilibrium. *Nature* 388, 358–361. doi: 10.1038/41056

Hook, R., Martin-Duque, J. F., and Pedraza, J. (2012). Land transformation by humans: a review. *GSA Today* 22, 4–10. doi: 10.1130/GSAT151A.1

Hu, Y., and Kuhn, N. J. (2014). Aggregates reduce transport distance of soil organic carbon: are our balances correct? *Biogeosciences* 11, 6209–6219. doi: 10.5194/bg-11-6209-2014

Jacinthe, P. A., and Lal, R. (2001). A mass balance approach to assess carbon dioxide evolution during erosional events. *Land Degrad. Dev.* 12, 329–339. doi: 10.1002/ldr.454

Jacinthe, P. A., Lal, R., and Kimble, J. M. (2002). Carbon dioxide evolution in runoff from simulated rainfall on long-term no-till and plowed soils in southwestern Ohio. *Soil Tillage Res.* 66, 23–33. doi: 10.1016/S0167-1987(02)00010-7

James, L. (2013). Legacy sediment: definitions and processes of episodically produced anthropogenic sediment. *Anthropocene* 2, 16–26. doi: 10.1016/j.ancene.2013.04.001

Köhler, S. J., Buffam, I., Seibert, J., Bishop, K. H., and Laudon, H. (2009). Dynamics of stream water TOC concentrations in a boreal headwater catchment: controlling factors and implications for climate scenarios. *J. Hydrol.* 374, 44–56. doi: 10.1016/j.jhydrol.2009.04.012

Kuhn, N. (2011). Connecting the cycles: impact of sediment, carbon and nutrient erosion on GHG emissions. *Appl. Geochem.* 26:S63. doi: 10.1016/j.apgeochem.2011.03.030

Lal, R. (1987). Effects of soil-erosion on crop productivity. *Crit. Rev. Plant Sci.* 5, 303–367. doi: 10.1080/07352688709382244

Lal, R. (1995). Erosion-crop productivity relationships for soils of Africa. *Soil Sci. Soc. Am. J.* 59, 661–667. doi: 10.2136/sssaj1995.03615995005900030004x

Lenka, N. K., Satapathy, K. K., Lal, R., Singh, N. A. K., Singh, P. K., Agrawal, P. C., et al. (2017). Weed strip management for minimizing soil erosion and enhancing productivity in the sloping lands of north-eastern India. *Soil Tillage Res.* 170, 104–113. doi: 10.1016/j.still.2017.03.012

Li, J., Ziegler, S., Lane, C. S., and Billings, S. A. (2011). Warming-enhanced preferential microbial mineralization of humified boreal forest soil organic matter: interpretation of soil profiles along a climate transect using laboratory incubations. *J. Geophys. Res.* 117:G02008. doi: 10.1029/2011JG001769

Liu, S., Bliss, N., Sundquist, E., and Huntington, T. G. (2003). Modeling carbon dynamics in vegetation and soil under the impact of soil erosion and deposition. *Global Biogeochem. Cycles* 17:1074. doi: 10.1029/2002GB002010

Marín-Spiotta, E., Chaopricha, N. T., Plante, A. F., Diefendorf, A. F., Mueller, C. W., Grandy, A. S., et al. (2014). Long-term stabilization of deep soil carbon by fire and burial during early holocene climate change. *Nat. Geosci.* 7, 428–432. doi: 10.1038/ngeo2169

Markewitz, D., and Richter, D. D. (1998). The *bio* in aluminum and silicon geochemistry. *Biogeochemistry* 42, 235–252.

Markewitz, D., Richter, D. D., Allen, H. L., and Urrego, J. B. (1998). Three decades of observed soil acidification in the calhoun experimental forest: has acid rain made a difference? *Soil Sci. Soc. Am. J.* 62, 1428–1439. doi: 10.2136/sssaj1998.03615995006200050040x

Matzner, E., and Borken, A. (2008). Do freeze-thaw events enhance C and N losses from soils of different ecosystems? a review. *Eur. J. Soil Sci.* 59, 274–284. doi: 10.1111/j.1365-2389.2007.00992.x

McCuaig, S. J. (2002). *Quaternary Geology of the Alexis River Area, and the Blanc-Sablon To Mary's Harbour Road Corridor, Southern Labrador*. Current Research. Newfoundland Department of Mines and Energy, Geological Survey Branch, Report, 1–20.

McKenney, R., Jacobson, R. B., and Wetheimer, R. C. (1995). Woody vegetation and channel morphogenesis in low-gradient, gravel-bed streams in the Ozark Plateaus, Missouri and Arkansas. *Geomorphology* 13, 175–198. doi: 10.1016/0169-555X(95)00034-3

Nadeu, E., Berhe, A. A., de Vente, J., and Boix-Fayos, C. (2012). Erosion, deposition and replacement of soil organic carbon in Mediterranean catchments: a geomorphological, isotopic and land use change approach. *Biogeosciences* 9, 1099–1111. doi: 10.5194/bg-9-1099-2012

Papanicolaou, A. N., Wacha, K. M., Abban, B. K., Wilson, C. G., Hatfield, J. L., Stanier, C. O., et al. (2015). From soilscapes to landscapes: a landscape-oriented approach to simulate soil organic carbon dynamics in intensively managed landscapes. *J. Geophys. Res.* 120, 2375–2401. doi: 10.1002/2015JG003078

Petit, N. E., Naiman, R. J., Warfe, D. M., Jardine, T. D., Douglas, M. M., Bunn, S. E., et al. (2017). Productivity and connectivity in tropical riverscapes

of northern Australia: ecological insights for management. *Ecosystems* 20, 492–514. doi: 10.1007/s10021-016-0037-4

Quinton, J. N., Govers, G., van Oost, K., and Bardgett, R. D. (2010). The impact of agricultural soil erosion on biogeochemical cycling. *Nature Geosci.* 3, 311–314. doi: 10.1038/ngeo838

Richter, D. D., and Markewitz, D. (2001). *Understanding Soil Change*. New York, NY: Cambridge University Press.

Richter, D. D., Markewitz, D., Trumbore, S. E., and Wells, C. G. (1999). Rapid accumulation and turnover of soil carbon in a re-establishing forest. *Nature* 400, 56–58. doi: 10.1038/21867

Ricketts, M. J. (2001). *Granular Aggregate Mapping in NTS Map Areas 1N/2, 1N/11, 110/14 and 110/15*. Current Research, Newfoundland Department of Mines and Energy, Geological Survey, Report 200, 279–291.

Sanderman, J., Lohse, K. A., Baldock, J. A., and Amundson, R. (2009). Linking soils and streams: sources and chemistry of dissolved organic matter in a small coastal watershed. *Water Resourc. Res.* 45:W03418. doi: 10.1029/2008WR006977

Schlesinger, W. H., and Bernhardt, E. S. (2013). *Biogeochemistry: An Analysis of Global Change*. Cambridge, MA: Academic Press.

Sierra, C. A., Müller, M., Metzler, H., Manzoni, S., and Trumbore, S. E. (2017). The muddle of ages, turnover, transit, and residence times in the carbon cycle. *Glob. Chang. Biol.* 23, 1763–1773. doi: 10.1111/gcb.13556

Smith, S. V., Renwick, W. H., Buddemeier, R. W., and Crossland, C. J. (2001). Budgets of soil erosion and deposition for sediments and sedimentary organic carbon across the conterminous United States. *Global Biogeochem. Cycles* 15, 697–707. doi: 10.1029/2000GB001341

Stallard, R. F. (1998). Terrestrial sedimentation and the carbon cycle: coupling weathering and erosion to carbon burial. *Global Biogeochem. Cycles* 12, 231–257. doi: 10.1029/98GB00741

Syvitski, J. P., Vörösmarty, C. J., Kettner, A. J., and Green, P. (2005). Impact of humans on the flux of terrestrial sediment to the global coastal ocean. *Science* 308, 376–380. doi: 10.1126/science.1109454

Trimble, S., and Lund, S. (1982). *Soil Conservation and the Reduction of Erosion and Sedimentation in the Coon Creek Basin*. Washington, DC: Geological Survey Professional Paper. doi: 10.3133/pp1234

Trimble, S. W. (2008). *Man-Induced Soil Erosion on the Southern Piedmont, 1700–1970*. Ankeny, IA: Soil and Water Conservation Society.

Van Loo, M., Dusar, B., Verstraeten, G., Renssen, H., Notebaert, B., D'Haen, K., et al. (2017). Human induced soil erosion and the implications on crop yields in a small mountainous Mediterranean catchment (SW-Turkey). *Catena* 149, 491–504. doi: 10.1016/j.catena.2016.08.023

van Oost, K., Quine, T. A., Govers, G., De Gryze, S., Six, J., Harden, J. W., et al. (2007). The impact of agricultural soil erosion on the global carbon cycle. *Science* 318, 626–629. doi: 10.1126/science.1145724

van Oost, K., Verstraeten, G., Doetterl, S., Notebaert, B., Wiaux, F., Broothaerts, N., et al. (2012). Legacy of human-induced C erosion and burial on soil-atmosphere C exchange. *Proc. Natl. Acad. Sci. U.S.A.* 109, 19492–19497. doi: 10.1073/pnas.1211162109

Walter, R. C., and Merritts, D. J. (2008). Natural streams and the legacy of water-powered mills. *Science* 319, 299–304. doi: 10.1126/science.1151716

Wang, X., Cammeraat, E. L. H., Cerli, C., and Kalbitz, K. (2014). Soil aggregation and the stabilization of organic carbon as affected by erosion and deposition. *Soil Biol. Biochem.* 72, 55–65. doi: 10.1016/j.soilbio.2014.01.018

Wang, Z., Hoffmann, T., Six, J., Kaplan, J. O., Govers, G., Doetterl, S., et al. (2017). Human-induced erosion has offset one-third of carbon emissions from land cover change. *Nat. Clim. Chang.* 7, 345–349. doi: 10.1038/nclimate3263

Wilkinson, B. H., and McElroy, B. J. (2007). The impact of humans on continental erosion and sedimentation. *GSA Bulletin* 119, 140–156. doi: 10.1130/B25899.1

Wilson, C. G., Papanicolaou, A. N., and Denn, K. D. (2012). Partitioning fine sediment loads in a headwater system with intensive agriculture. *J. Soils Sed.* 12, 966–981. doi: 10.1007/s11368-012-0504-2

Ziegler, S. E., Benner, R., Billings, S. A., Edwards, K. A., Philben, M., Zhu, X., et al. (2017). Climate warming can accelerate carbon fluxes without changing soil carbon stocks. *Front. Earth Sci.* 5:2. doi: 10.3389/feart.2017.00002

**Conflict of Interest Statement:** The authors declare that the research was conducted in the absence of any commercial or financial relationships that could be construed as a potential conflict of interest.

frontiers in Earth Science

ORIGINAL RESEARCH
published: 05 April 2019
doi: 10.3389/feart.2019.00063

# Mineral Weathering and Podzolization Control Acid Neutralization and Streamwater Chemistry Gradients in Upland Glaciated Catchments, Northeastern United States

*Scott W. Bailey[1]*, Kevin J. McGuire[2], Donald S. Ross[3], Mark B. Green[4] and Olivia L. Fraser[5]*

*[1] Northern Research Station, United States Department of Agriculture Forest Service, North Woodstock, NH, United States, [2] Department of Forest Resources and Environmental Conservation, Virginia Water Resources Research Center, Virginia Tech, Blacksburg, VA, United States, [3] Department of Plant and Soil Science, University of Vermont, Burlington, VT, United States, [4] Northern Research Station, United States Department of Agriculture Forest Service, Center for the Environment, Plymouth State University, Plymouth, NH, United States, [5] Department of Natural Resources and the Environment, University of New Hampshire, Durham, NH, United States*

OPEN ACCESS

**Edited by:**
*Samuel Abiven,*
*University of Zurich, Switzerland*

**Reviewed by:**
*Jason Austin,*
*University of Georgia, United States*
*Pamela L. Sullivan,*
*The University of Kansas, United States*

***Correspondence:**
*Scott W. Bailey*
*swbailey@fs.fed.us*

**Specialty section:**
*This article was submitted to Biogeoscience, a section of the journal Frontiers in Earth Science*

**Received:** *27 July 2018*
**Accepted:** *14 March 2019*
**Published:** *05 April 2019*

**Citation:**
*Bailey SW, McGuire KJ, Ross DS, Green MB and Fraser OL (2019) Mineral Weathering and Podzolization Control Acid Neutralization and Streamwater Chemistry Gradients in Upland Glaciated Catchments, Northeastern United States. Front. Earth Sci. 7:63. doi: 10.3389/feart.2019.00063*

Headwater streams in the White Mountains, NH, United States have been shown to have downstream gradients of increasing pH and concentrations of base cations coupled with decreasing concentrations of aluminum. A two-stage acid neutralization model involving shallow soil exchange processes in headwaters coupled with deeper mineral weathering downstream had been proposed to explain these gradients. We conducted synoptic sampling of three headwater catchments in this region that showed variations in this longitudinal pattern, ranging from streams that remain acidic throughout their length to streams with circumneutral pH beginning at their source. To explain these differences, we mapped soils using a hydropedologic approach that emphasizes the influence of groundwater saturation frequency and water table regime on soil formation processes. Stream segments with lower pH and base cation concentrations, coupled with higher concentrations of dissolved organic carbon (DOC), aluminum, and in one case iron, were in subcatchments mapped with shallow to bedrock soils where eluvial soil forming processes dominated. In contrast, stream segments with higher pH and base cation concentrations coupled with low concentrations of DOC and aluminum were associated with subcatchments with deeper soils where illuvial processes were more dominant. Concentrations of sodium and silicon were relatively uniform across these gradients. Coupled with the higher concentrations of dissolved aluminum and small pools of exchangeable aluminum in the areas of bedrock outcrops and shallow soils, these data suggest that primary mineral dissolution is an important process influencing upper stream reaches, not just along longer, deeper flowpaths in downslope areas. In contrast, some stream reaches with obvious groundwater springs show a

more abrupt transition in pH and base cation concentrations higher along the stream, suggesting that neutralization along deeper flowpaths may play a role in upslope areas as well. These data suggest a new three stage model of stream chemistry evolution. First, organic acids are introduced by frequent flushing of organic soils on shallow bedrock along ridge areas. Second, upper acidic reaches are controlled by mineral dissolution coupled with eluvial soil development. Third, downstream reaches are influenced by illuviation as organometallic complexes precipitate in spodic soil horizons, removing organic acids, and acid-mobile metals from drainage waters. This new model highlights differences in critical zone evolution along hillslopes in glaciated catchments with implications for understanding gradients in water quality, soil fertility, and response and recovery from disturbances.

**Keywords: critical zone, streamwater, biogeochemistry, groundwater, soil development, podzolization, mineral weathering, glaciated catchments**

## INTRODUCTION

Surface water chemistry in forested catchments is highly regulated by the ecosystem/critical zone of the catchment, with concentrations of major solutes typically varying temporally by a factor or two or three while streamflow varies by five or more orders of magnitude (Likens et al., 1977; Godsey et al., 2009; Kim et al., 2017). Despite this tight temporal control of surface water chemistry (i.e., chemostatic behavior), much spatial variability in stream chemistry is commonly observed, as seen in longitudinal or synoptic stream sampling studies (Johnson et al., 1981; Bailey et al., 1987; Likens and Buso, 2006), with spatial chemical patterns stable over a broad range of catchment wetness or flow conditions (Zimmer et al., 2013; Abbott et al., 2018). The mechanisms by which catchments regulate surface water quality are important to understand in order to inform management of forests for reliable delivery of high quality water, of particular concern in the United States where approximately 50–70% of public water supplies, including nearly all larger municipal supplies in the Northeastern United States, are derived from surface waters flowing from forested lands (Brown et al., 2008; Barnes et al., 2009).

Variation in metal cations and overall acidity, reflected in pH, are commonly controlled by catchment scale processes and may reflect overall structure of the critical zone. Various studies have examined controls on spatial water quality patterns (e.g., Phillips and Stewart, 1990; Ross et al., 1994; Fitzhugh et al., 1999; Palmer et al., 2005; Ågren et al., 2014; Herndon et al., 2015a,b; Peralta-Tapia et al., 2015; Kim et al., 2017) and have interpreted controls from various properties such as stream connectivity with hillslopes, depth of flowpaths, amount of groundwater inputs, and depth and location of organic soils, particularly in riparian areas. While all of these explanations involve properties of soils or deeper portions of the critical zone, none of these studies included a coupled investigation of spatial variation in stream chemistry with a complete catchment-scale analysis of soil development processes.

At the Hubbard Brook Experimental Forest (HBEF), in central New Hampshire, United States, Johnson et al. (1981) studied longitudinal variation in the chemistry of Falls Brook, a second order tributary of Hubbard Brook and proposed a two stage acid neutralization model that explained the dominant longitudinal chemical gradient. In the headwaters, mineral acidity derived from atmospheric precipitation was partially replaced by aluminum (Al), which they interpreted as a soil cation exchange process. Further downstream, acidity from both hydrogen ion (H) and dissolved Al decreased, balanced by increasing concentrations of base cations (especially Ca, Mg, Na) interpreted to have been supplied by mineral dissolution reactions along longer hydrologic flowpaths. A follow up study of all of the ∼15 tributaries of Hubbard Brook by Likens and Buso (2006) found similar longitudinal patterns with gradients of pH (**Figure 1**) as well as total monomeric ($Al_m$) and base cations along most of the tributaries. However, a smaller number of tributaries remained acidic all the way to their mouth at the main stem of Hubbard Brook while a few other tributaries had circumneutral pH and higher concentrations of base cations from source to mouth. Little advancement of the conceptual model proposed by Johnson et al. (1981) has been offered by subsequent studies and an explanation for the contrasting longitudinal gradients shown by several of the streams has not been addressed.

While the Hubbard Brook tributary catchments are generally similar with respect to geologic substrate, soils, vegetation, and disturbance history (Likens et al., 1977), Bailey et al. (2014) showed strong hillslope-scale gradients in soil development that reflect variation in frequency and depth of groundwater incursions into the soil zone. Soils at HBEF are dominantly Spodosols, a common soil type in cool humid forested regions (Sauer et al., 2007) where primary mineral weathering and leaching and precipitation of Al and Fe complexed by organic acids are dominant soil forming processes. A hydropedologic soil classification (Gannon et al., 2014; **Table 1**), based on relationships between soil morphology and groundwater regime observed at the soil profile- and catena-scale distinguishes between soils formed primarily by vertical leaching processes, above the influence of the water table, and laterally formed soils that

reflect groundwater influence on soil development and lateral translocations between profiles at the hillslope scale (Bourgault et al., 2017; Gannon et al., 2017). Thus soil development patterns may be used to understand processes occurring along hydrologic flowpaths.

On portions of the hillslope where groundwater remains deeper in the subsoil, vertical leaching leads to a common horizon sequence (hence called a typical podzol), consisting of a thin E horizon at the top of the mineral soil, leached of organic matter, Al, and Fe. This overlies a zone of deposition showing a vertical gradient of illuviation, i.e., accumulated soil organic matter (SOM) composed of secondary Al and Fe organic complexes (i.e., spodic B horizons). In contrast to better drained profiles that show a gradient in the eluvial to illuvial development at the point scale, soil profiles influenced by lateral flow of shallow groundwater tend to have exaggerated thickness of one type of mineral horizon, displaying one dominant portion of the podzolization process, either eluvial or illuvial, depending on what portion of a hillslope they occur and the water table saturation frequency. Thus, an E podzol is dominated by a thick mineral layer leached of organic matter, Al, and Fe and may have no B horizon in the same profile while shortly downslope, a Bhs podzol may have little or no E horizon, instead primarily expressing a thick Bhs horizon high in SOM complexed with Al, and Fe (Bourgault et al., 2017). These functionally defined soil types occur in distinct portions of the catchment and their distribution is largely predictable by topographic analysis via a high resolution LiDAR derived terrain model (Gillin et al., 2015). Furthermore, initial sampling of groundwater wells used to characterize variation in water table fluctuations showed distinctions in the solute composition of groundwater among soil types (Zimmer et al., 2013), suggesting that varying contributions of groundwater from contrasting soils may explain spatial patterns seen in surface water chemistry.

The purpose of this study was to investigate the possibility that differences in the spatial dynamics of soil formation processes within and between catchments could explain longitudinal patterns in stream solute concentrations. We chose three catchments to study based on contrasting longitudinal stream chemistry gradients. We compiled groundwater data from previous studies at the site to evaluate differences in groundwater quality between soil types and extended the soil distribution model of Gillin et al. (2015) from Watershed3 (W3), where it was developed, to our other study catchments. Together with a detailed synoptic stream chemistry survey, these data allowed us to evaluate the hypothesis that differences in soil distribution, and resulting groundwater inputs to streams, explain chemical gradients in stream chemistry within and between catchments.

# MATERIALS AND METHODS

## Study Site

Hubbard Brook Experimental Forest is located in west-central New Hampshire, United States (43° 56′N, 71° 45′W; **Figure 1**) within the White Mountain National Forest. The climate is humid continental with a mean annual precipitation of 140 cm and stream runoff of 90 cm (Bailey A.S. et al., 2003). Much of the research is centered on nine headwater catchments located in the northern (W1–6) and southern (W7–9) portions of the experimental forest (**Figure 1**) where water and solute input and output is measured at a series of meteorological and stream gauging stations. This study focuses on catchments W3, and Watershed 9 (W9), which are maintained in a natural, unmanaged condition and serve as reference catchments, and the ungauged upper west branch of Zig Zag Brook (ZZ), a similar headwater catchment that is not gauged but maintained in a natural, unmanaged condition (**Figure 1**).

Land cover at HBEF is forest with northern hardwoods dominated by *Acer saccharum* Marsh. (sugar maple), *Betula alleghaniensis* Britt. (yellow birch), and *Fagus grandifolia* Ehrh. (American beech) on deeper and better drained soils; mixed conifers dominated by *Picea rubens* Sarg. (red spruce), *Abies balsamea* (L.) Mill. (balsam fir), and *Betula papyrifera* var. *cordifolia* (Regel) Fern. (mountain paper birch) occupy wetter sites and areas where soils are shallow to bedrock. Forests on the reference catchments are mature, mostly second growth following partial cutting in the period of 1890–1920, and partial blowdown during a hurricane in 1938. The study catchments have had no direct human disturbance or management since partial harvesting, which ended in the 1910s.

Bedrock in the portions of HBEF considered in this study is the Silurian Rangeley Formation, a sillimanite-grade metapelite consisting of mica schist with minor amounts of calc-silicate granulite (Burton et al., 2000). Bedrock is poorly exposed, outcropping mostly along ridges and in some stream channels, and is covered by a veneer of late Wisconsinan glacial drift. In the study watersheds, drift is thin and interspersed with exposed bedrock in the uppermost portion of the catchments, particularly along catchment divides while it is variable and up to 10 m thick in central to lower portions of the catchments. Catchment W9 is distinct in having much more bedrock outcrops while the remainder of the catchment is underlain by thin drift, with bedrock less than 1 m deep.

Glacial drift is dominated by granitic lithologies, transported from the north and west of the study catchments, with lesser contributions from local bedrock (Bailey S.W. et al., 2003), and is the parent material for soil development. Based on review of published bedrock mineralogy, till lithologic sources, and direct microprobe analyses of soil minerals (Hyman et al., 1998; Bailey S.W. et al., 2003), plagioclase feldspar is of composition oligoclase ($Ca_{0.2}Na_{0.8}Al_{1.2}Si_{2.8}O_8$) and a dominant source of calcium (Ca) and sodium (Na), as well as the most easily weathered source of aluminum (Al) and silicon (Si). Other relatively reactive minerals include minor amounts of biotite and hornblende and trace amounts of apatite. Bailey (2019a) showed that oligoclase is the major supply of Ca, Na, Al, and Si in mineral dissolution while biotite and hornblende are likely the major sources of dissolved Fe (Hyman et al., 1998; Bailey S.W. et al., 2003).

Where not confined by shallow bedrock, soils average 0.7 m to the top of the C-horizon, corresponding to the depth of major alteration of glacial drift by soil forming processes, as well as the limit of the rooting zone (Bailey et al., 2014).

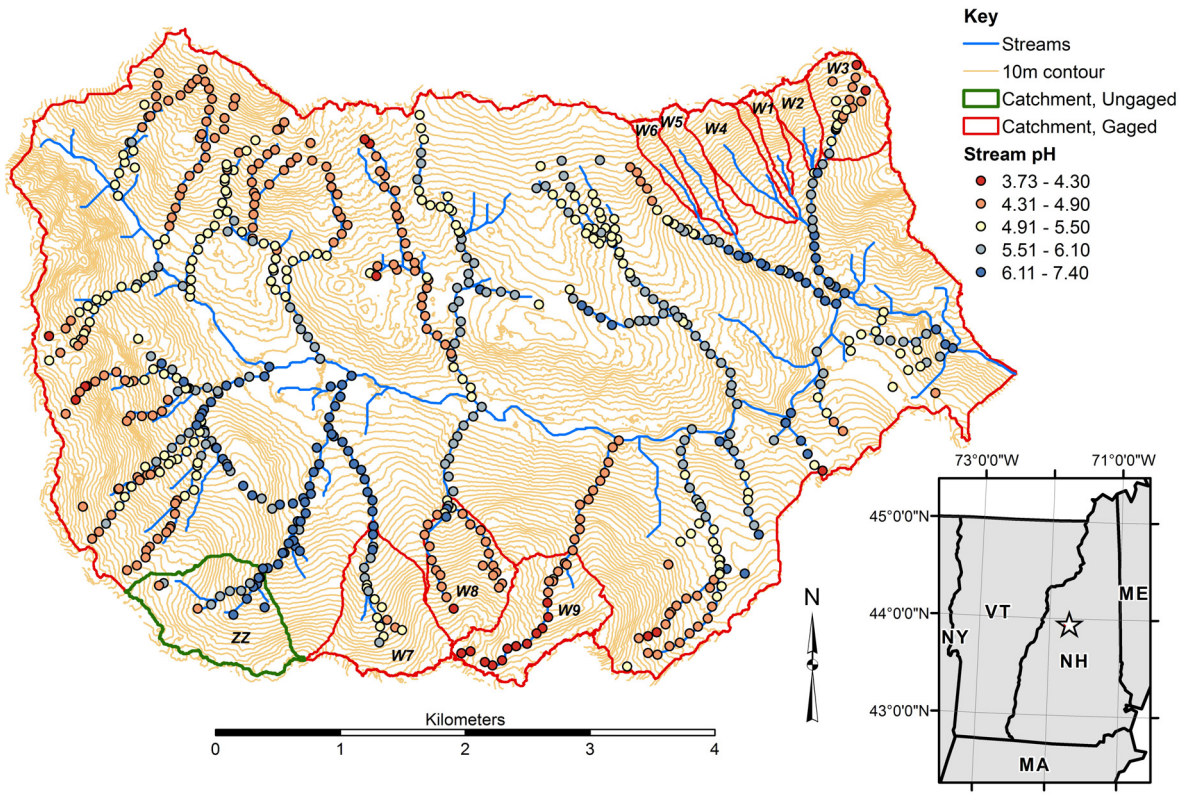


**FIGURE 1 |** Locus map and variation in surface water pH across the tributaries of Hubbard Brook. pH data are from Likens and Buso (2006), further described statistically by McGuire et al. (2014). Catchments considered in the present study include Zig Zag (ZZ) and Watershed 9 (W9) along the southern edge of the Hubbard Brook catchment and Watershed 3 (W3) at the northeastern edge.

Podzolization is a dominant soil forming process, with organic acids leaching iron (Fe) and Al from surficial mineral soil layers (eluviation) and depositing them as organic Fe and Al complexes in lower mineral soil layers (illuviation). Soil profiles vary in their expression of eluvial horizons, i.e., mineral soil low in organic matter and extractable metals, where leaching processes dominate, and illuvial horizons, with mineral surfaces coated by amorphous organometallic complexes, where precipitation processes dominate (Bourgault et al., 2015; **Table 1**). Presence and thickness of eluvial and illuvial horizons depends on thickness of the soil parent material, subsurface drainage limitations, and upslope drainage area (Bailey et al., 2014; Bourgault et al., 2017).

## Water Sampling and Analysis

Based on the variations in longitudinal stream chemical gradients seen by Likens and Buso (2006), we chose to investigate W3, the headwaters of Paradise Brook, as an example of a catchment with the longitudinal acid neutralization gradient described by Johnson et al. (1981). We chose W9, the headwaters of Cascade Brook, as an example of a more uniformly acidic catchment (Wellington and Driscoll, 2004), and ZZ, an ungauged catchment in the upper west branch of Zig Zag Brook, as an example of a more uniformly circumneutral catchment (Palmer et al., 2005). A synoptic surface water sampling campaign was conducted in W3 and W9 on July 22, 2015; the west branch of Zig Zag Brook was sampled the following day on July 23, 2015. Catchment conditions during the survey were relatively wet as a large rain event centered on July 19, 2015 left 117 and 109 mm of precipitation on W3 and W9, respectively. On the sampling date, daily streamflow was 2.43 and 1.78 mm (or daily flow exceedance 24 and 28%) for W3 and W9, respectively. As the streams were in recession from high flow earlier in the week, most of the intermittent portions of the stream network were actively flowing, allowing a relatively complete sampling of the channel network. We resampled sites in W3 established by Zimmer et al. (2013), at about half the sampling density of that earlier study, or about one sample site per 100 m of stream length. New sampling sites at a similar density were established in W9 and ZZ, with sites chosen to fall just above junctions or at breaks in channel slope or substrate type. Zimmer et al. (2013) showed that stream chemistry was relatively persistent spatially in W3 across flow exceedance probabilities from 0.2 to 87%.

Sampling sites were classified as stream sites if they were on a channel with obvious signs of sustained fluvial activity. A smaller number of sites were designated as seeps and are interpreted to be point discharge sites where groundwater returns to the surface. These included sites that were close to but not directly on the stream network, or channel heads where low water temperature or anomalously well-developed channels with

**TABLE 1 |** Summary of functional soil units showing the dominant horizons, carbon concentration, and general groundwater response in each.

| Soil unit | Bedrock outcrop | O horizon on bedrock | E podzol | Bhs podzol | Typical podzol | Bh podzol |
|---|---|---|---|---|---|---|
| Abbreviation | R | O | E | Bhs | Typical | Bh |
| Organic soil horizons | None; moss and lichens | Forest floor in varying levels of decomposition from fresh leaf litter through humus | | | | |
| Dominant mineral soil horizon | None | None | E | Bhs | Bs | Bh |
| Mean C concentration of dominant mineral horizon mg/g | – | – | 1.5 | 5.5 | 4.7 | 4.4 |
| Transient groundwater response | Saturated to near the soil surface during rain events; recession immediately following | | | Saturated to mid depth during rain events; recession 1–2 days afterward | Saturation rises to lower B/upper C horizon seasonally and following large rain events | Saturated into mid B horizon seasonally and following large rain events |

perennial flow at first flowing water suggested the importance of a groundwater spring.

Grab samples of surface water were collected in 0.5 L bottles and brought to the HBEF field laboratory for processing within an hour or two of collection. For this study, we focused on pH as a general indicator of acidity, dissolved organic carbon (DOC), Al, and Fe, as indicators of the podzolization process, and Na and Si as indicators of primary mineral dissolution (Bailey, 2019a). Fresh untreated samples were analyzed for pH. Subsamples were filtered through an ashed 0.45 μm glass microfiber filter and frozen for later analysis for DOC, refrigerated untreated for later analysis of $Al_m$, or acidified to pH 2 with nitric acid for later analysis of cations. pH was measured potentiometrically with a Thermo Scientific Orion 3-Star pH meter at HBEF. All other analyses were performed at the United States Department of Agriculture Forest Service, Forestry Sciences Laboratory, Durham, NH, United States. Dissolved metals, including Ca, Fe, Na, and Si were analyzed on a Varian Vista axial inductively coupled plasma spectrometer. Total monomeric Al ($Al_m$) was measured on a Lachat automated flow cell with the pyrocatechol violet technique. DOC was measured on a Shimadzu TOC-5000A. Other major solutes were measured but not reported here; complete analyses are available at Bailey et al. (2019).

Groundwater samples were collected across W3 from a suite of wells installed during 2008–2012 by Detty and McGuire (2010); Zimmer et al. (2013); and Gannon et al. (2014). Each well was constructed of SDR 21 PVC pipe (3.18 cm outer diameter) with a 31 cm screen length consisting of 0.025 cm width lateral slots with 0.32 cm spacing between slots. The wells were installed so the base of the screen was in the upper C horizon, between 40 and 100 cm deep. Wells were stratified into soil groups based on description of a nearby soil sampling pit or based on soil morphology observed during well installation. A battery-operated peristaltic pump was used to purge the wells of a minimum of two well volumes followed by collection of water samples for chemical analyses.

For the shallowest soils considered, consisting of a thin forest floor (O horizon) overlying shallow bedrock, construction of and sampling a well was not feasible. In this case, we cut a short section of a 10 cm diameter PVC pipe longitudinally in half and inserting it, concave side up, at the O horizon-bedrock interface. A cap at the downslope end of the half pipe was fitted with a tygon tube that ran down to a 0.5 L HDPE collection bottle. The collection bottle was installed when a rainfall event to be sampled was forecast and retrieved immediately at the end of the rain event. Groundwater samples were analyzed for the same parameters and with the same methods as surface water samples.

## Soil Mapping and Analysis

A soil map for W3 was produced by Gillin et al. (2015) and modified for the current study following a similar approach as described by Gillin et al. (2015). This map was made by using an ordination of soil morphology and topographic metrics derived from LiDAR analysis to identify metrics predictive of the various soil units (**Table 1**). Three soil units, bedrock outcrops (R), O horizon on bedrock (O), and E podzols (E), intermingle in bedrock-controlled portions of the catchment and were mapped as a complex of the three (R–O–E). A multinomial logistic regression was used to determine the probability of the presence of each soil unit at each grid cell in a 5 m raster. In 99% of the cells, one soil unit was predicted to have a greater than 50% probability of occurrence. The most probable soil present was assigned to each grid cell. This model had a 70% success rate in correctly classifying fifty soil profiles withheld from the analysis for validation (Gillin et al., 2015).

The map for W3 was updated for the present study by refining the procedure used to map bedrock outcrops and shallow soils. Field verification combined with visual interpretation of 1-m LiDAR derived hillshades illuminated from three different angles were used to update and delineate bedrock-controlled portions of the catchments. This procedure for bedrock outcrop delineation was used with model coefficients derived from the logistic regression analysis in W3 to predict soil distribution across W9 and ZZ. Over 75% of soil profile descriptions collected in W9 and ZZ, none of which were used in model development, were properly classified by the predictive soil map (Bailey, 2019b). The proportion of soil functional units R–O–E, Bhs podzol (Bhs), typical podzol (Typical), and Bh podzol

(Bh) were calculated for each catchment. The watershed tool from SAGA GIS (Conrad et al., 2015) was used to delineate subcatchments draining to each stream sampling point and then queried to determine the proportion of the four soil map units in each subcatchment. Subcatchments for seep sampling sites were not calculated as many of them did not lie directly along drainage ways and the GIS delineation failed. The perennial nature of the seeps, particularly at upper slope positions, suggests that their sources were not confined to topographically defined drainage areas.

Soil profiles were described and sampled by genetic horizon by Bailey et al. (2014) and Bourgault et al. (2017) in W3 to characterize the hydropedologically defined soil units. In the present study, the presence of the same soil units, and a prediction of their distribution via the model of Gillin et al. (2015) was confirmed by profile description and sampling in W9 ($n$ = 20 soil profiles) and ZZ ($n$ = 18 soil profiles; Bailey (2019b). Samples from previous studies in W3 were used to estimate salt extractable Al pools by soil type. Samples were air-dried, sieved through a 2 mm screen and subsampled for analysis. Total carbon content was analyzed by combustion. Extractable Al was measured in a 1 M solution of ammonium acetate buffered to pH 4.8. Similar to the water samples, soil analyses were made at the USFS laboratory in Durham, NH, United States. Exchangeable Al concentrations multiplied by horizon thickness and bulk density estimated by carbon content (Federer et al., 1993), and summed for each soil profile to obtain estimates of exchangeable Al pools on a per unit landscape area basis.

# RESULTS

## Synoptic Stream Survey

Stream chemical gradients in the three catchments were similar to those reported by Likens and Buso (2006) although we sampled the intermittent portions of the upper stream network more thoroughly and thus found a truncated gradient in stream acidity in the upper reaches of ZZ not seen by the earlier survey (**Figures 1**, **2**). W3 tributaries generally showed the strongest longitudinal gradient in pH, with stream heads starting at a pH in the mid fours and increasing to 5.8 at the catchment outlet. W9 tributaries remained quite acidic throughout their reaches, starting with pH in the range of 3.8–4.2 and increasing to 4.5 at the outlet. ZZ had the highest pH at its outlet, at a value of 6.3, with pH in the upper fives and sixes in much of the network. However, we did find acidic reaches in the uppermost intermittent portions of the network in ZZ, with the lowest pH recorded in the study of 3.79.

Several groundwater seeps were sampled in each catchment, and distinguished from regular stream sampling sites as being springs outside of the channel area, or channel sites with lower water temperature than stream sites and/or with channels with anomalously perennial conditions at or near channel heads. In W3, the seeps span the elevational range of the stream network and appear in a near-linear pattern in the central part of the catchment, subparallel to the central stream tributary (**Figure 2**). W3 seeps had pH in the sixes including one seep with a pH of 6.70, the highest pH measured in the study. W9 only had three sites identified as seeps, all in the lower eastern part of the catchment (**Figure 2**). All had pH in the mid to upper fives, higher than any of the stream sites in the catchment. ZZ had five sites classified as seeps. All occurred at mid to upper portions of tributary streams and had pH values in the sixes.

Spatial patterns of DOC, Al, and Fe (**Figures 3–5**) were examined as complexation, leaching, and subsequent deposition of Al and Fe organometallic complexes are predominant soil forming processes in Spodosols. DOC concentrations were mostly low in W3, between 80 and 500 μM, with several locations in the upper part of the network, particularly on the eastside showing higher concentrations up to 1200 μM. In contrast, the lowest concentrations in streams in W9 were in the range of 400–500 μM, with most sites >2500 μM and a peak of 4000 μM at one station. ZZ DOC concentrations were more similar to those seen in W3, typically less than 500 μM while the upper portions of most of the tributaries had concentrations up to 2400 μM. In all three catchments, seeps had low DOC concentrations, <500 μM (**Figure 3**).

Total monomeric Al concentrations (**Figure 4**) showed a range in each catchment, with concentrations >9 μM common in the upper part of W3, particularly on the eastside, throughout W9, including at the outlet, and along the upper parts of the tributaries in ZZ. Seeps had among the lowest concentrations of $Al_m$, generally below the method detection limit (MDL) of 0.6 μM, while some seeps and stream sites in W3 and ZZ had concentrations below the limit of quantification (LOQ) of 2 μM. Fe concentrations were very low in W3 (**Figure 5**), with most stream and all seep sites either less than the MDL of 0.6 μM or the LOQ of 1.8 μM. In contrast, many stream sites in W9, particularly in mid to upper portions of the network had Fe concentrations in excess of 10 μM with a peak concentration of 33 μM. Some of the uppermost sites in ZZ had concentrations in the 10–20 μM range.

Spatial patterns of Na and Si were examined as indicators of primary mineral dissolution (**Figures 6**, **7**) as these solutes are less impacted by other ecosystem processes. Concentrations of Na in all catchments were generally in similar ranges and increased slightly moving downstream, with concentrations 12–20 μM typical of headwaters, tending to increase to 20–30 μM in the lower catchment. Na concentrations were highest in seeps, modestly higher, in a range of 30–40 μM in W9 seeps and 40–60 μM in W3 and ZZ seeps. Si concentrations were more variable longitudinally within the catchments, with concentrations in a range of 20–100 μM seen in upper and lower portions of all catchments, except that lowest concentrations in ZZ were about 60 μM. Concentrations of Si in a range of 100–150 μM were seen in the three seeps in W9 and in two stream sites, and in most of the seeps and a larger number of stream sites in ZZ. One seep in ZZ and two seeps in W9 had concentrations in the range of 150–200 μM Si (**Figure 7**).

## Soil Distribution

The catchments differed in the proportion of hydropedologically defined soil units present in each. W9 had the greatest contribution, 70%, of the shallowest soils, including bedrock outcrops, O horizon on bedrock, and E podzols (together mapped

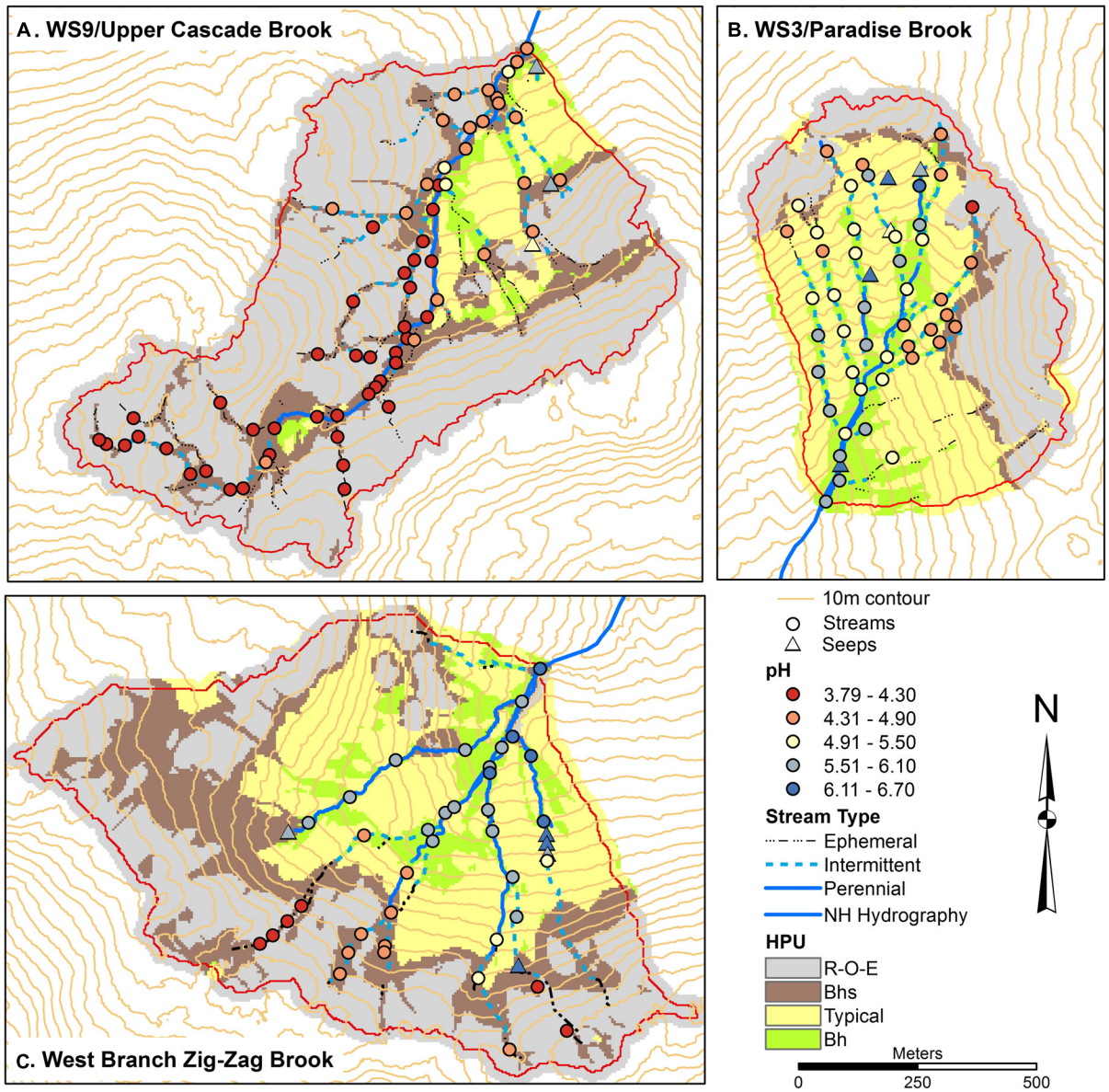


**FIGURE 2 |** Soils maps for W9 **(A)**, W3 **(B)**, and West Branch Zig Zag Brook **(C)** with variation in surface water pH from a synoptic survey conducted July 22–23, 2015. Surface water samples were classified as streams (circles) or seeps (triangles). Soil units include bedrock outcrops, bedrock Histosols, and E podzols (R–O–E), Bhs podzols (Bhs), typical podzols (Typical), and Bh podzols (Bh).

as R–O–E; **Figures 2–7**), whereas ZZ and W3 had 38 and 33%, respectively, of R–O–E soils. These soils are typically saturated to near the surface (i.e., within 10–20 cm of the surface) with every rainfall and snowmelt event, rapidly draining upon the conclusion of those events (**Table 1**). At the other end of the soil depth and groundwater influence spectrum, typical podzols, with little incursion of groundwater in the zone of greatest soil formation (**Table 1**), were most prevalent in W3, contributing 44% whereas they made up 30 and 9% of the ZZ and W9 catchments, respectively (**Figures 2–7**). Bhs podzols, soils of intermediate depth and just downslope of the bedrock controlled portions of the catchments were least common in W3, making up 6% of the catchment, with larger contributions of 17 and 24% in W9 and ZZ, respectively. Bh podzols, the wettest soils mapped in the catchments and generally associated with the near-stream zone in mid to lower portions (**Figures 2–7**) made up 16% of W3 but only 4 and 9% of W9 and ZZ, respectively.

## Groundwater Composition by Soil Type

Groundwater composition was distinct between soil units (**Figure 8**). pH and DOC concentration showed the most regular gradients across the general hillslope sequence. pH was lowest (median 4.0) and DOC was highest (median 2670 μM) in

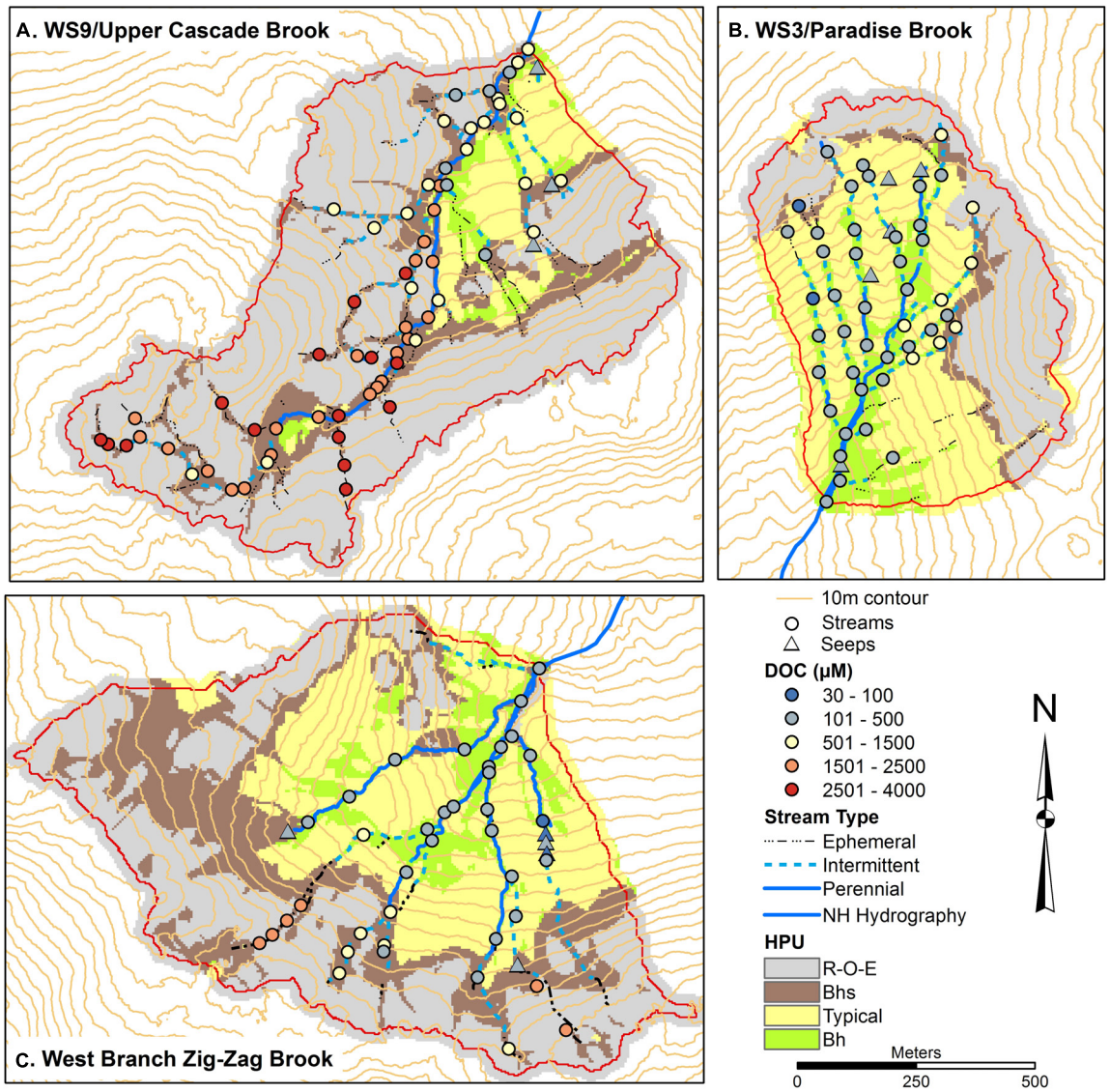


**FIGURE 3 |** Soils maps for W9 **(A)**, W3 **(B)**, and West Branch Zig Zag Brook **(C)** with variation in surface water dissolved organic carbon (DOC) concentrations from a synoptic survey conducted July 22–23, 2015. Surface water samples were classified as streams (circles) or seeps (triangles). Soil units include bedrock outcrops, bedrock Histosols, and E podzols (R–O–E), Bhs podzols (Bhs), typical podzols (Typical), and Bh podzols (Bh).

soils consisting of O horizon directly on shallow bedrock. pH increased to a median of 5.2 in typical podzols while DOC concentrations fell along the same sequence of soils, with a median of 110 µM in typical podzols. Bh podzols had similar pH and DOC to typical podzols.

Al concentrations were highest in E podzols with a median of 30 µM, dropping slightly to 27 µM in Bhs podzols. O podzols and typical podzols had similar median Al concentrations of 10 µM while concentrations in Bh podzols were lower, with a median of 5 µM. Fe concentrations were highest in the O and E units, with median concentrations of 4 and 5 µM. In contrast, most samples from Bhs podzols, typical podzols, and Bh podzols had Fe concentrations below the LOQ of 1.8 µM.

Na showed a low but consistent gradient in groundwater concentrations across the soil sequence, with a low median of 17 µM in O, increasing to 24 µM in E and Bhs podzols, to 36 µM in typical podzols and 38 µM in Bh podzols. Si concentrations in groundwater were low in O horizon on bedrock, with a median of 21 µM while the other soils all had similar Si concentrations, with medians varying between 73 and 92 µM.

## Relationship Between Stream Chemistry and Soil Distribution

The O and E soils generally had the most distinct groundwater chemistry, with low pH, and high DOC, Al, and Fe concentrations. Together with bedrock outcrops, these units

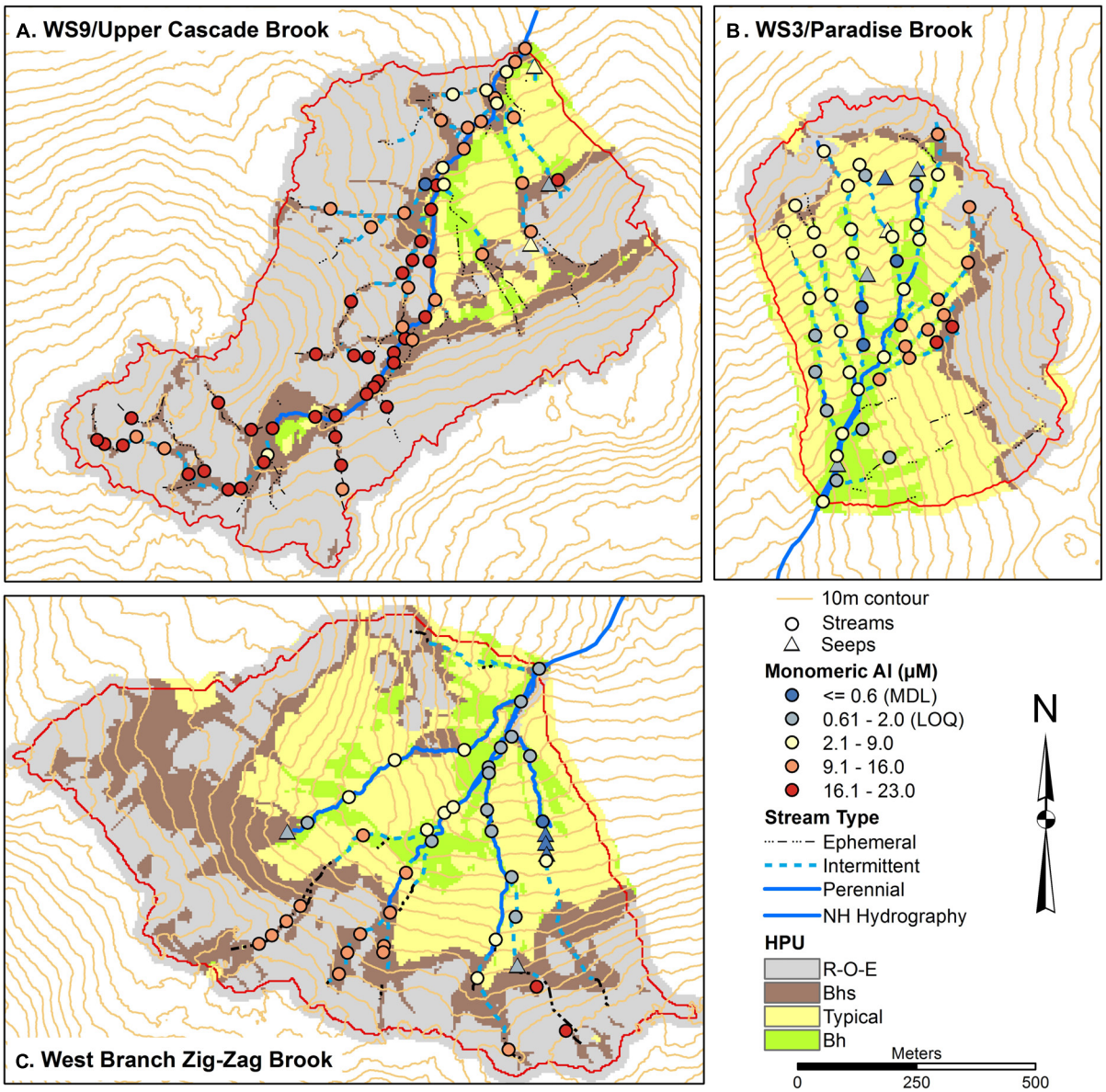


**FIGURE 4 |** Soils maps for W9 **(A)**, W3 **(B)**, and West Branch Zig Zag Brook **(C)** with variation in surface water total monomeric aluminum ($Al_m$) concentrations from a synoptic survey conducted July 22–23, 2015. Surface water samples were classified as streams (circles) or seeps (triangles). Soil units include bedrock outcrops, bedrock Histosols, and E podzols (R–O–E), Bhs podzols (Bhs), typical podzols (Typical), and Bh podzols (Bh).

comprise the bedrock controlled portions of the catchment landscape. In order to evaluate differences in soil influence across sampling sites, the portion of the subcatchment of each stream sampling site underlain by the R–O–E soil complex was calculated and then plotted against the water solute data (**Figure 9**). pH generally increased with decreasing proportion of R–O–E soil units while concentrations of DOC, Al, and Fe were highest when the R–O–E complex made up greater proportions of subcatchments. Subcatchment in R–O–E complex appears to be a threshold with all sites with elevated DOC, AL, and Fe, and the lowest pH sites confined to subcatchments with greater than 50% R–O–E contribution. Na and Si concentrations showed less distinct gradients across this range of subcatchment soil composition. Na concentrations increased slightly with decreasing proportion of R–O–E, with a number of sites in the range of 30–50% R–O–E having the highest concentrations. Si concentrations were highest in a similar range of soil compositions, but showed even less of a consistent gradient across the soil sequence spectrum.

Sampling sites with relatively high pH, low DOC, Al, and Fe that fell off the general relationship with R–O–E tended to be immediately downstream of seeps. W3 fell off of the relationship between Fe and R–O–E seen at W9 and ZZ, with generally low concentrations of Fe in surface water across W3.

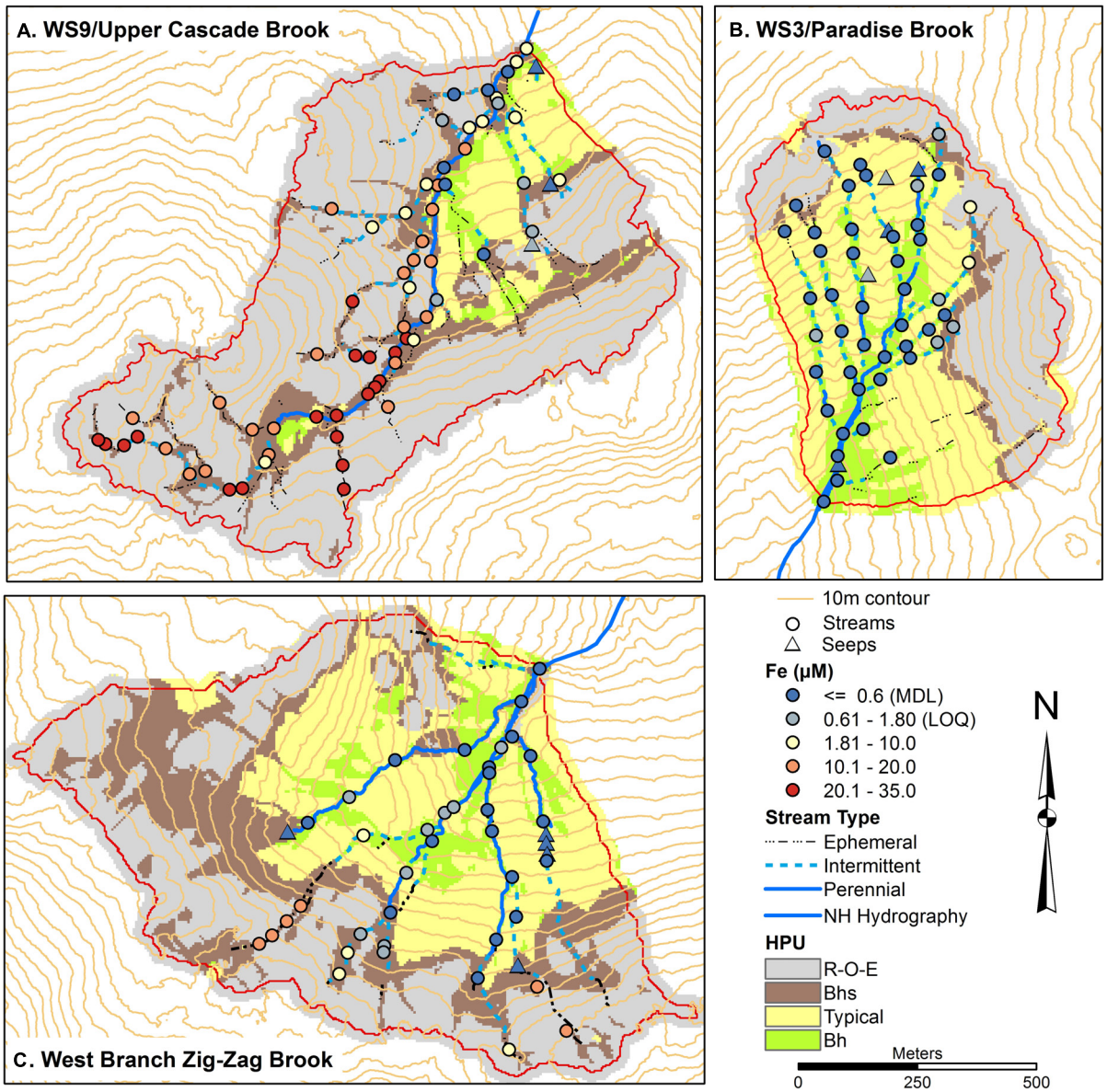


**FIGURE 5 |** Soils maps for W9 **(A)**, W3 **(B)**, and West Branch Zig Zag Brook **(C)** with variation in surface water iron (Fe) concentrations from a synoptic survey conducted July 22–23, 2015. Surface water samples were classified as streams (circles) or seeps (triangles). Soil units include bedrock outcrops, bedrock Histosols, and E podzols (R–O–E), Bhs podzols (Bhs), typical podzols (Typical), and Bh podzols (Bh).

Salt extractable soil pools of Al were very low in O horizon on bedrock and E podzols and highest in the deeper soils with thicker illuvial horizons, downslope, including Bhs, typical, and Bh podzols (**Figure 10**).

# DISCUSSION

## Podzolization Controls on Stream Chemical Gradients

At HBEF, typical of acidic forested landscapes in the Northeastern United States, podzolization is a dominant soil forming process. Organic acids developed through decomposition processes in the forest floor bind with Al and Fe released from primary mineral dissolution to form soluble organometallic complexes, which then leach downward through the soil profile, or downslope via lateral flow of groundwater. Deeper in the soil profile or downslope, in spodic B horizons, these complexes precipitate to form coatings and discrete particles of spodic materials, or SOM stabilized by Al and Fe complexation (e.g., see Bourgault et al., 2015).

Our study shows how headwater streams participate in, and reflect this soil forming process. Upslope portions of the catchments (**Figures 2–7**) are dominated by soils with only, or

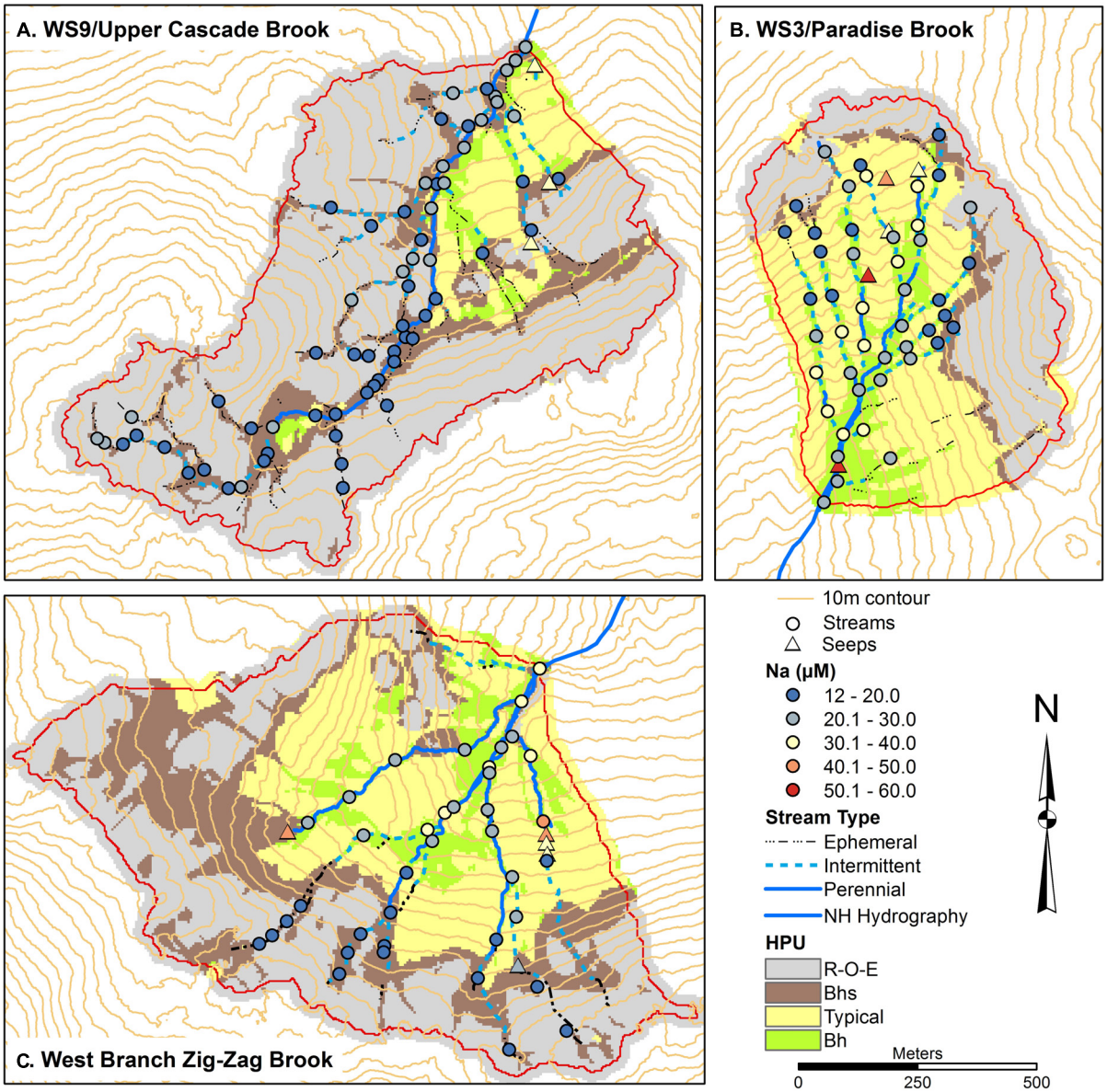


**FIGURE 6 |** Soils maps for W9 **(A)**, W3 **(B)**, and West Branch Zig Zag Brook **(C)** with variation in surface water sodium (Na) concentrations from a synoptic survey conducted July 22–23, 2015. Surface water samples were classified as streams (circles) or seeps (triangles). Soil units include bedrock outcrops, bedrock Histosols, and E podzols (R–O–E), Bhs podzols (Bhs), typical podzols (Typical), and Bh podzols (Bh).

predominately, the horizons that represent the first stage of the podzolization process. These include soils where O horizon sits directly on bedrock and E podzols, where the leached E horizon is the dominant mineral horizon. Complexation of metals with organic matter is followed by transport down through deeper better drained soil profiles, or downslope through shallower soils and soils with frequent groundwater incursions into upper horizons. Many intermittent, or seasonally flowing, stream channels originate and drain this portion of the catchment. Groundwater and streams in this zone reflect this eluvial portion of the podzolization process, with relatively low pH and high concentrations of DOC, Al, and Fe (**Figures 2–8**).

Of our three study catchments, W9 best exemplifies these processes. The R–O–E soil complex makes up 70% of the catchment, extending all the way to the catchment outlet on the west side of the main stream (**Figures 2–7**). Most of the stream sampling sites in W9 have a subcatchment drainage area with >70% in the R–O–E subcatchment, and show low pH and elevated DOC, Al, and Fe (**Figure 9**). For DOC, the highest R–O–E stream sites show concentrations that are at least an order of magnitude higher than the lowest R–O–E sites. These portions of the landscape with R–O–E >70% may be considered to be eluvial landscapes. This fits the concept of Sommer (2006) that landscape

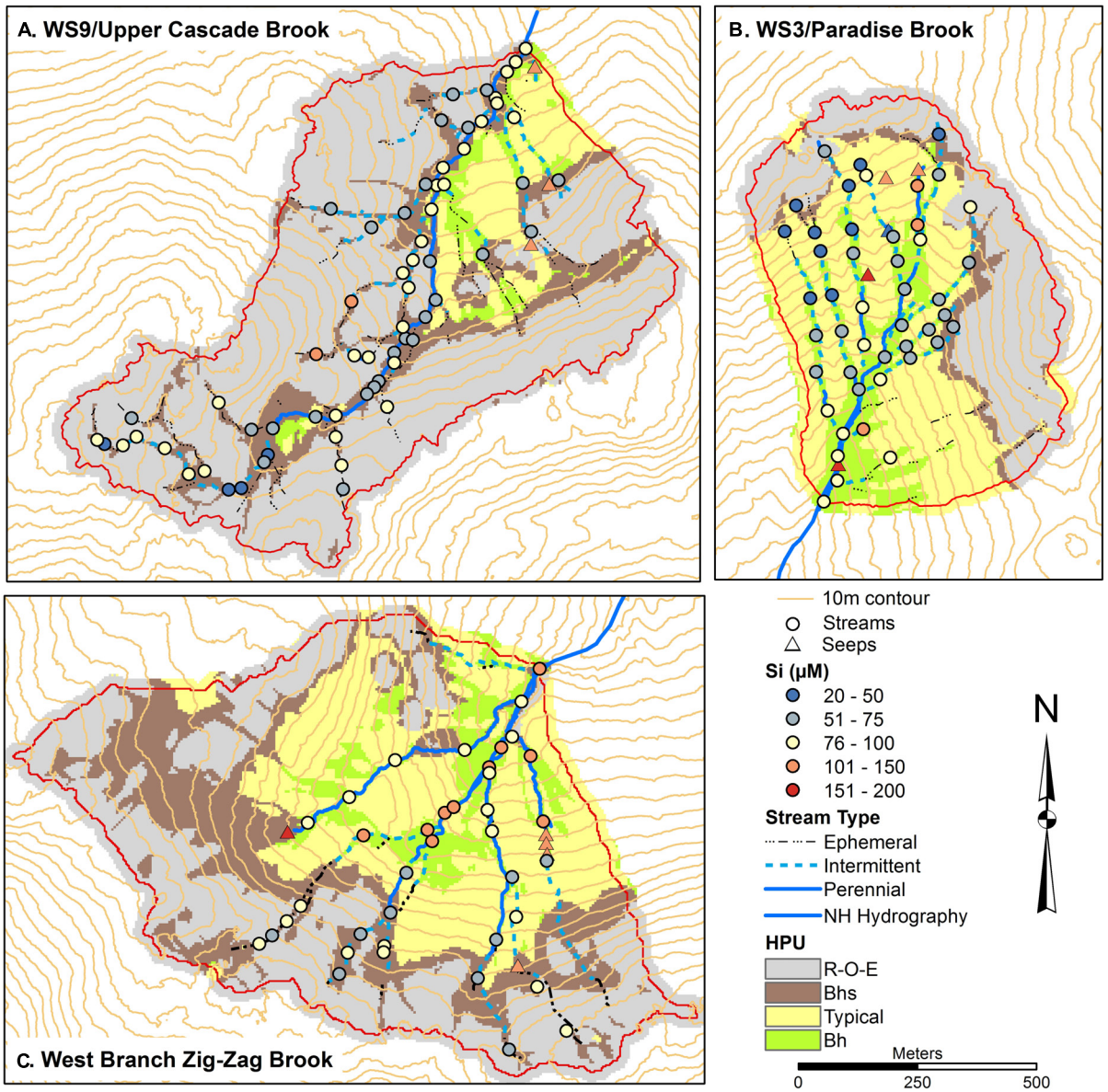


**FIGURE 7 |** Soils maps for W9 **(A)**, W3 **(B)**, and West Branch Zig Zag Brook **(C)** with variation in surface water silicon (Si) concentrations from a synoptic survey conducted July 22–23, 2015. Surface water samples were classified as streams (circles) or seeps (triangles). Soil units include bedrock outcrops, bedrock Histosols, and E podzols (R–O–E), Bhs podzols (Bhs), typical podzols (Typical), and Bh podzols (Bh).

pedology can be used for understanding biogeochemical spatial patterns.

Lower portions of the catchments are dominated by soil units with horizons reflecting the illuvial component of the podzolization process. Typical podzols tend to have a thin Bhs horizon over a thicker Bs horizon. The Bhs horizon with the darkest reddish brown colors generally has the highest illuvial carbon content, reflecting the greatest degree of illuviation. In the Bhs podzol, this darker reddish brown horizon makes up most of the mineral portion of the soil profile, reflecting the greatest degree of illuviation. Bh podzols with a dark but less red Bh horizon are associated with near-stream zones and topographic benches and may reflect a different mode of podzolization based on distinct micromorphology (Bourgault et al., 2015). Stream chemistry at sampling sites with 50% or more the Bhs, typical, and Bh soil units (i.e., 50% or less R–O–E units) tend to have higher pH and lower concentrations of DOC, Al, and Fe. There are several theories that have been proposed to explain illuviation in podzols, which include precipitation of Al and Fe due to decreasing solubility of increasingly metal-rich complexes, microbial degradation of organically bound Al and Fe, co-precipitation between organic-rich soil water and Al from groundwater, and the formation of imogolite-type-materials (Farmer et al., 1983; Lundström et al., 2000).

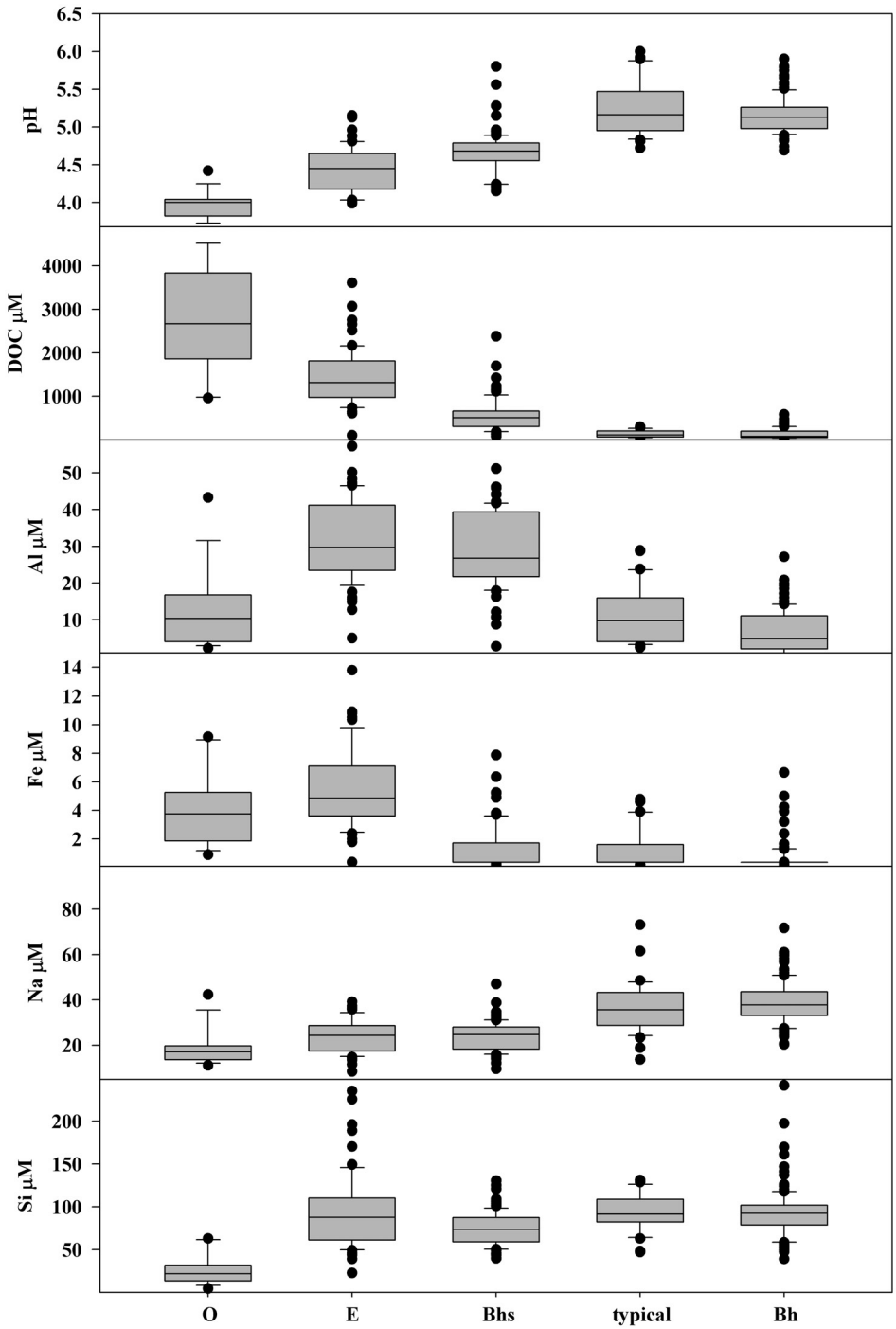


**FIGURE 8 |** Box plots showing the distribution of pH and concentrations of dissolved organic carbon (DOC), total dissolved aluminum Al, iron (Fe), sodium (Na), and silicon (Si) in groundwater samples from shallow wells stratified by soil type. The number of groundwater samples included was O = 16, E = 67, Bhs = 89, typical = 35, Bh = 120.

Where a given sampling site sits relative to this eluvial-illuvial landscape balance may vary with catchment wetness conditions. Gannon et al. (2015) showed how DOC concentrations at the outlet to W3 increased when water table rose in E podzols, and intermittent streams in the bedrock-controlled portion of the drainage network became active. Expansion of the active channel network into the eluvial zone, and the balance of runoff produced from this zone compared to deeper zones in the lower catchment, would influence how far downstream the solute characteristics of the eluvial zone would be detected. The largest

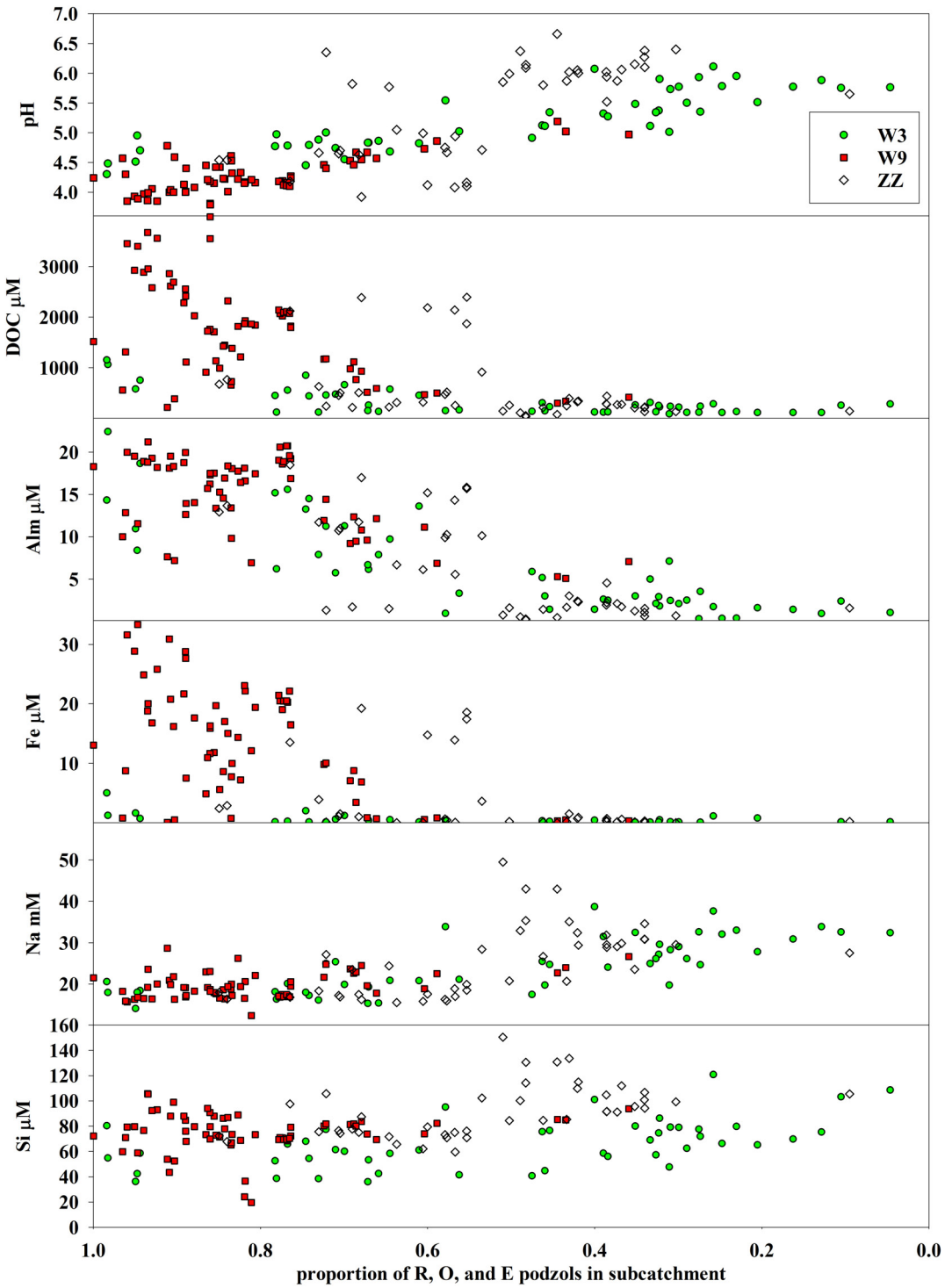


**FIGURE 9 |** Variation in surface water pH and concentrations of dissolved organic carbon (DOC), monomeric aluminum ($Al_m$), iron (Fe), sodium (Na), and silicon (Si) versus proportion of each sampling site's contributing subcatchment in rock outcrops, O-horizon on shallow bedrock, and E-podzols (R–O–E). The proportion of R–O–E soils decreases toward the right, and generally moving downstream along any given tributary.

runoff events, when the entire channel network is active, and when contributions from deeper soils are limited in a relative sense, likely describe conditions when a pulse of water with lower pH and higher concentrations of DOC, Al, and Fe would influence water composition farthest downslope. Such conditions may contribute to the formation of Bh podzols in the near-stream

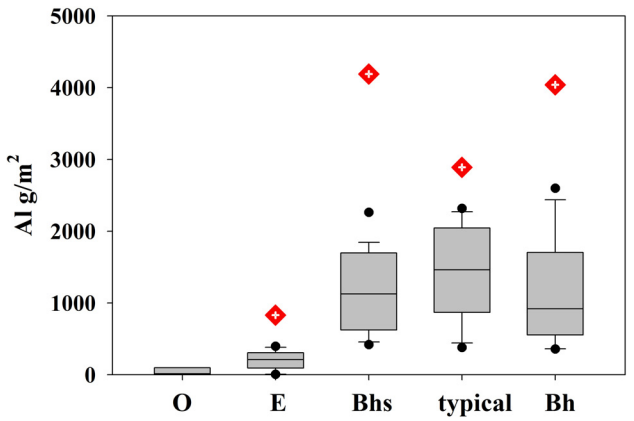


**FIGURE 10 |** Box plots showing the distribution of salt extractable pools of aluminum (Al) stratified by soil type. The number of profiles used for pool size estimates was O = 6, E = 14, Bhs = 19, typical = 11, Bh = 11. For comparison, the mean soil pool of oxalate extractable Al in each soil type (Bourgault, 2014) is also shown.

zone. Similar near-stream soils with illuvial horizons relatively high in Al have been observed elsewhere in similar catchments (Pellerin et al., 2002).

In this landscape with eluvial zones of R–O–E soils upslope, and illuvial zones of typical and Bh podzols downslope, the position of the Bhs podzols in the middle may represent a hinge point where soil and water compositions reflect some characteristics of each zone. Groundwater in Bhs podzols still had elevated DOC concentrations compared to typical and Bh podzols (**Figure 8**) and Al concentrations were nearly as high as they were in E-podzols. Thus, groundwater still partially reflects the mobilization of soluble organometallic complexes of the eluvial zone. On the other hand, storage of organometallic complexes as spodic materials in the solid phase and secondary Al and Fe are as high in this soil unit as they are anywhere along the soil sequence (**Figures 8**, **10**; Bailey et al., 2014; Bourgault et al., 2017), reflecting the strong illuviation in this zone. In some Bhs podzol profiles, organic carbon and secondary Al and Fe concentrations are high and relatively uniform from the top of the mineral soil all the way to the base of the profile at the bedrock interface. In these cases, the soil profile may be approaching a point where the mineral soil has reached its capacity for accumulating spodic material. Similarly, as the portion of a soil profile with high concentrations of spodic materials in the solid phase increases, the efficiency of deposition of further spodic coatings may decrease, leading to more transfer of DOC, Al, and Fe to either lower in the profile or downslope.

## Gradients in Primary Mineral Weathering

As neither Al, Fe, nor Si is contributed to the catchment in soluble form from atmospheric deposition (Likens et al., 1977), appearance of these metals in ionic form in groundwater or streamwater ultimately reflects dissolution from primary minerals. Minor amounts of Na are brought into the catchment dissolved in rain and snow, with a mean concentration of about 5 μM, much less than the median concentration of Na in groundwater, which is 17 μM in organic horizons on bedrock. Thus, the presence of these solutes in groundwater in the shallow soils in the uppermost portions of the catchments is evidence of the action of mineral dissolution, another important soil forming process occurring at the site.

While the concentrations of Al and Fe, metals involved in podzolization, is highest in the groundwater in the eluvial zone, concentrations of Na and Si are more similar across the soils sequence. Si is taken up by plants and sequestered in biogenic phytoliths, which accumulate in soil (Ronchi et al., 2013), a process that may be approximately at steady state in the mature forest of these unmanipulated reference catchments (Conley et al., 2008). In contrast little Na is taken up by plants or stored in secondary soil pools (Bailey S.W. et al., 2003) and may represent the most conservative of the solutes released by primary mineral dissolution. Low gradients in the concentrations of Na and Si in the groundwater (**Figure 8**) and in the streams (**Figures 6**, **7**) suggests that mineral weathering is more or less a contributor to mobile waters throughout the system.

Another piece of evidence of the dominance of primarily mineral dissolution in the eluvial zone of the catchments comes from catchment scale mass balance. Bailey (2019a) found that net export (i.e., streamwater output minus precipitation input) from W9 had a molar ratio of Al:Na of about 1.2–1.4 compared to the ratio in oligoclase, the primary source of both solutes, of 1.5. This is consistent with little net storage of Al in this catchment which is dominated by shallow soils where eluvial processes dominate and where secondary Al pools in the soil are small. In contrast, the net export of Al:Na from W3, where deeper illuvial soils dominate was only 0.2–0.3, suggesting that most Al derived from oligoclase dissolution is stored in secondary soil pools.

## A New Model of Acid Neutralization and Stream Chemistry Evolution

Johnson et al. (1981) proposed a two stage acid neutralization model to explain longitudinal gradients in streamwater pH, and concentrations of Al and base cations, including Na. In their model, hydrogen ion input from mineral acidity delivered from atmospheric deposition was partially replaced by Al derived from soil exchange processes in the headwaters, with further neutralization occurring downstream as the concentrations of base cations rose in response to mineral weathering inputs along longer flowpaths. The spatial patterns in groundwater and stream chemistry observed in our work suggest that mineral weathering is occurring throughout the system, including in shallow mineral soils, and even in soils where O horizon is in direct contact with bedrock. Furthermore, exchangeable metal pools are small in the R–O–E zone, as evidenced by low pools of salt extractable and oxalate extractable Al (**Figure 10**). Most of the cation exchange capacity in these soils is associated with organic matter and most of the pool of exchangeable cations occurs in the B horizon (Johnson et al., 1991; Johnson, 2002), which is more prevalent in the deeper soils further downslope. A final contrast with the Johnson et al. (1981) model is that we find the most acidic waters, including groundwater and streams

draining the R–O–E soils, where DOC concentrations are highest, to have pH values lower than atmospheric inputs, highlighting an organic acidity component to the gradient rather than just mineral acidity from atmospheric inputs that Johnson et al. (1981) focused on.

Therefore, we propose a new conceptual model to explain the dominant longitudinal gradients observed in stream chemistry. Organic acids generated in shallow soils in the upper portions of the catchments serve to drive mineral weathering, even in soils with little or no mineral soil, where weathering is promoted at the bedrock surface frequently flushed by low pH water with high concentrations of metal complexing organic acids. Moving downslope, this organic acidity is partially replaced by Al acidity and partially neutralized by base cations, both derived from mineral dissolution in the eluvial zone. Further downslope, neutralization continues with Al and Fe precipitation with organic ligands in illuvial soil horizons. In catchments where the R–O–E complex dominates, this gradient is truncated with catchment stream exports still low in pH and with high concentrations of DOC, Al, and sometimes Fe. In catchments where a large zone of typical and Bh podzols form in mid to lower sections, a strong gradient in stream chemistry will be expected within the catchment, with export of waters of higher pH and low concentrations of DOC, Al, and Fe.

This conceptual model may be expected to apply to other catchments in upland regions where similar soil forming processes (i.e., podzolization and dissolution of granitic mineral assemblies) predominate. As examples, Bailey et al. (1987) documented a similar longitudinal stream gradient to that seen at W9 at the Cone Pond inlet stream, a site on the White Mountain National Forest away from the Hubbard Brook valley. The Cone Pond catchment is dominated by exposed and shallow bedrock with a high proportion of shallow soils with deep eluvial horizons (Bailey et al., 1996). In contrast (Bailey et al., 1987) showed the highest pH and base cation concentrations at the source of the inlet stream to Black Pond, a catchment where the stream initiation point was in deep soils influenced by a perennial groundwater seep. Development of statistical relationships between soil distribution and stream chemistry (e.g., patterns such as shown in **Figure 9**) may provide a predictive tool that could be applied to other catchments to infer stream chemistry gradients in the absence of stream monitoring data. It may be expected that such a tool may be applicable where soil development processes are similar to those at HBEF, i.e., podzolization and dissolution of a granitic mineral assemblage. Coupled with topographic analysis of LiDAR-based DEMs to predict soil distribution, such tools could provide a powerful reconnaissance method for predicting spatial variations in soils and surface waters.

## CONCLUSION

Three headwater catchments in close proximity to each other, and with many characteristics in common, were found to differ in their longitudinal patterns of stream chemical composition due to differences in the prevalence of functional soil types, which they all had in common, but in much different proportions in each catchment. In this setting, Spodosols are the dominant soil type. However, recently recognized functional types have been distinguished, reflecting the role of groundwater on soil development, resulting in the partitioning of portions of the podzolization process into different zones. Bedrock-controlled landscapes are dominated by bedrock outcrops, thin soils consisting only of organic horizons over shallow bedrock, and E-podzols, mineral soils where organic matter, Al, and Fe are leached from soils developed in thin glacial drift. Deeper soils downslope constitute an illuvial portion of the landscape where organometallic complexes precipitate. Stream chemistry gradients reflect the relative dominance of these two zones in a given catchment. Stream reaches with subcatchments dominated by soils in the predominately eluvial zone have lower pH and higher concentrations of DOC, Al, and Fe, while stream reaches in the illuvial zone have the opposite chemical characteristics.

Past studies have highlighted the role of longer and/or deeper flowpaths in delivering products of mineral dissolution to streams, resulting in higher pH and higher concentrations of base cations. We see some of this influence particularly around groundwater seeps where the transition from eluvial to illuvial dominance may be more abrupt or higher upslope. However, the relatively low gradients in Na and Si in the streams in our study, coupled with high concentrations of Al and Fe in zones where secondary pools of these metals are small suggests the importance of mineral dissolution in bringing all of these metals to the streams right from the headwaters. The role of mineral weathering in shallow soils, or even in exposed bedrock has not been much considered in the past but warrants more study. High concentrations of organic ligands, and frequent flushing of acidic groundwater could counteract the relatively small mineral surface area in bedrock-controlled zone in promoting mineral dissolution.

## AUTHOR CONTRIBUTIONS

SB conceived the study, compiled and processed the data, created the figures, and wrote the first draft of the manuscript. MG led the synoptic sampling campaign. OF conducted the soil modeling and generated subcatchments for the sampling sites. All authors contributed to data interpretation and edited the manuscript.

## FUNDING

Funding for this study was provided by the Northern Research Station, United States Department of Agriculture Forest Service and the National Science Foundation through the Research Experience for Undergraduates Program (DBI/EAR-0754678) and the Hydrological Sciences (EAR-1014507) and Geobiology and Low-Temperature Geochemistry (EAR-1643415/1643327) Programs.

## ACKNOWLEDGMENTS

We thank Jane Hislop and Jeff Merriam, USFS, Durham, NH, United States for water and soil analyses and Rebecca Bourgault, Patricia Brousseau, Margaret Burns, Denise Burchsted, Kyle Corcoran, Dan Demers, Stephanie Duston, J. P. Gannon, Benjamin Geyman, Cody Gillin, Tyler Hampton, Kaitland Harvey, Michaela Kuhn, Brittany LeBeau, Tomoki Oda, Kristen Sapnas, Johali Soleto, Rieko Urakawa, Tammy Wooster, and Margaret Zimmer for fieldwork. Hubbard Brook Experimental Forest is maintained and operated by Northern Research Station, United States Department of Agriculture Forest Service, Newtown Square, PA, United States.

## REFERENCES

Abbott, B. W., Gruau, G., Zarnetske, J. P., Moatar, F., Barbe, L., Thomas, Z., et al. (2018). Unexpected spatial stability of water chemistry in headwater stream networks. *Ecol. Lett.* 21, 296–308. doi: 10.1111/ele.12897

Ågren, A. M., Buffam, I., Cooper, D. M., Tiwari, T., Evans, C. D., and Laudon, H. (2014). Can the heterogeneity in stream dissolved organic carbon be explained by contributing landscape elements? *Biogeosciences* 11, 1199–1213. doi: 10.5194/bg-11-1199-2014

Bailey, A. S., Hornbeck, J. W., Campbell, J. L., and Eagar, C. (2003). *Hydrometeorological Database for Hubbard Brook Experimental Forest: 1955-2000*. Newtown Square, PA: US Department of Agriculture, Forest Service, Northeastern Research Station Available at: http://www.fs.fed.us/ne/newtown_square/publications/technical_reports/pdfs/2003/gtrne305.pdf (accessed June 14, 2013).

Bailey, S. W., Buso, D. C., and Likens, G. E. (2003). Implications of sodium mass balance for interpreting the calcium cycle of a forested ecosystem. *Ecology* 84, 471–484. doi: 10.1890/0012-9658(2003)084[0471:IOSMBF]2.0.CO;2

Bailey, S. W. (2019a). "Tracking the fate of plagioclase weathering products: pedogenic and human influences," in *Biogeochemical Cycles: Ecological Drivers and Environmental Impact. Geophysical Monographs*, eds K. Dontsova, Z. Balogh-Brunstad, and G. Le Roux (Washington, DC: American Geophysical Union).

Bailey, S. W. (2019b). *Hubbard Brook Experimental Forest: Pedon Locations, 1995-Present. Environmental Data Initiative.* Available at: https://doi.org/10.6073/pasta/a7bffc2c0be8052e83b2145993ffa46c (accessed February 22, 2019).

Bailey, S. W., Brousseau, P. A., McGuire, K. J., and Ross, D. S. (2014). Influence of landscape position and transient water table on soil development and carbon distribution in a steep, headwater catchment. *Geoderma* 22, 279–289. doi: 10.1016/j.geoderma.2014.02.017

Bailey, S. W., Hornbeck, J. W., Driscoll, C. T., and Gaudette, H. E. (1996). Calcium inputs and transport in a base-poor forest ecosystem as interpreted by Sr isotopes. *Water Resour. Res.* 32, 707–719. doi: 10.1029/95WR03642

Bailey, S. W., Hornbeck, J. W., Martin, C. W., and Buso, D. C. (1987). Watershed factors affecting stream acidification in the White Mountains of New Hampshire, USA. *Environ. Manage.* 11, 53–60. doi: 10.1007/BF01867179

Bailey, S. W., McGuire, K. J., Ross, D. S., and Green, M. B. (2019). *Hubbard Brook Experimental Forest: Synoptic Surface Water Chemistry, 2015. Environmental Data Initiative.* Available at: https://doi.org/10.6073/pasta/fafd7b2334e34a633577764bc36cbb66 (accessed February 22, 2019).

Barnes, M. C., Todd, A. H., Lilja, R. W., and Barten, P. K. (2009). *Forests, Water and People: Drinking Water Supply and Forest Lands in the Northeast and Midwest United States*. Newtown Square, PA: USDA Forest Service.

Bourgault, R. R. (2014). *Hydropedology of Podzols at Hubbard Brook, New Hampshire.* Ph.D. dissertation, University of Vermont, Burlington, VT, 182.

Bourgault, R. R., Ross, D. S., and Bailey, S. W. (2015). Chemical and morphological distinctions between vertical and lateral podzolization at Hubbard Brook. *Soil Sci. Soc. Am. J.* 79, 428–439. doi: 10.2136/sssaj2014.05.0190

Bourgault, R. R., Ross, D. S., Bailey, S. W., Bullen, T. D., McGuire, K. J., and Gannon, J. P. (2017). Redistribution of soil metals and organic carbon via lateral flowpaths at the catchment scale in a glaciated upland setting. *Geoderma* 307, 238–252. doi: 10.1016/j.geoderma.2017.05.039

Brown, T. C., Hobbins, M. T., and Ramirez, J. A. (2008). Spatial distribution of water supply in the coterminous United States. *JAWRA J. Am. Water Resour. Assoc.* 44, 1474–1487. doi: 10.1111/j.1752-1688.2008.00252.x

Burton, W. C., Walsh, G. J., and Armstrong, T. R. (2000). *Bedrock Geologic Map of the Hubbard Brook Experimental Forest, Grafton County, New Hampshire*. Washington, DC: U.S. Department of the Interior.Conley, D. J., Likens, G. E., Buso, D. C., Saccone, L., Bailey, S. W., and Johnson, C. E. (2008). Deforestation causes increased dissolved silicate losses in the Hubbard Brook Experimental Forest. *Glob. Change Biol.* 14, 2548–2554.

Conrad, O., Bechtel, B., Bock, M., Dietrich, H., Fischer, E., Gerlitz, L., et al. (2015). System for automated geoscientific analyses (SAGA) v. 2.1.4. *Geosci. Model Dev.* 8, 1991–2007. doi: 10.5194/gmd-8-1991-2015

Detty, J. M., and McGuire, K. J. (2010). Topographic controls on shallow groundwater dynamics: implications of hydrologic connectivity between hillslopes and riparian zones in a till mantled catchment. *Hydrol. Process.* 24, 2222–2236. doi: 10.1002/hyp.7656

Farmer, V. C., Skjemstad, J. O., and Thompson, C. H. (1983). Generation of humus B horizons in hydromorphic humus podzols. *Nature* 304, 342–344. doi: 10.1038/304342a0

Federer, C. A., Turcotte, D. E., and Smith, C. T. (1993). The organic fraction-bulk density relationship and the expression of nutrient content in forest soils. *Can. J. For. Res.* 23, 1026–1032. doi: 10.1139/x93-131

Fitzhugh, R. D., Furman, T., Webb, J. R., Cosby, B. J., and Driscoll, C. T. (1999). Longitudinal and seasonal patterns of stream acidity in a headwater catchment on the Appalachian Plateau, West Virginia, U.S.A. *Biogeochemistry* 47, 39–62. doi: 10.1007/BF00993096

Gannon, J. P., Bailey, S. W., and McGuire, K. J. (2014). Organizing groundwater regimes and response thresholds by soils: a framework for understanding runoff generation in a headwater catchment. *Water Resour. Res.* 50, 8403–8419. doi: 10.1002/2014WR015498

Gannon, J. P., Bailey, S. W., McGuire, K. J., and Shanley, J. B. (2015). Flushing of distal hillslopes as an alternative source of stream dissolved organic carbon in a headwater catchment. *Water Resour. Res.* 51, 8114–8128. doi: 10.1002/2015WR016927

Gannon, J. P., McGuire, K. J., Bailey, S. W., Bourgault, R. R., and Ross, D. S. (2017). Lateral water flux in the unsaturated zone: a mechanism for the formation of saptial soil heterogeneity in a headwater catchment. *Hydrol. Process.* 31, 3568–3579. doi: 10.1002/hyp.11279

Gillin, C. P., Bailey, S. W., McGuire, K. J., and Gannon, J. P. (2015). Mapping of hydropedologic spatial patterns in a steep headwater catchment. *Soil Sci. Soc. Am. J.* 79, 440–453. doi: 10.2136/sssaj2014.05.0189

Godsey, S. E., Kirchner, J. W., and Clow, D. W. (2009). Concentration-discharge relationships reflect chemostatic characteristics in US catchments. *Hydrol. Process.* 23, 1844–1864. doi: 10.1002/hyp.7315

Herndon, E. M., Dere, A. L., Sullivan, P. L., Norris, D., Reynolds, B., and Brantley, S. L. (2015a). Biotic controls on solute distribution and transport in headwater catchments. *Hydrol. Earth Syst. Sci.* 12, 213–243. doi: 10.5194/hessd-12-213-2015

Herndon, E. M., Dere, A. L., Sullivan, P. L., Norris, D., Reynolds, B., and Brantley, S. L. (2015b). Landscape heterogeneity drives contrasting concentration-discharge relationships in shale headwater catchments. *Hydrol. Earth Syst. Sci.* 19, 3333–3347. doi: 10.5194/hess-19-3333-2015

Hyman, M. E., Johnson, C. E., Bailey, S. W., Hornbeck, J. W., and April, R. H. (1998). Chemical weathering and cation loss in a base-poor watershed. *Geol. Soc. Am. Bull.* 110, 85–95. doi: 10.1130/0016-7606(1998)110<0085:CWACLI>2.3.CO;2

Johnson, C. E. (2002). Cation exchange properties of acid forest soils of the northeastern USA. *Eur. J. Soil Sci.* 53, 271–282. doi: 10.1046/j.1365-2389.2002.00441.x

Johnson, C. E., Johnson, A. H., and Siccama, T. G. (1991). Whole-tree clear-cutting effects on exchangeable cations and soil acidity. *Soil Sci. Soc. Am. J.* 55, 502–508. doi: 10.2136/sssaj1991.03615995005500020035x

Johnson, N., Driscoll, C. T., Eaton, J. S., Likens, G. E., and McDowell, W. H. (1981). "Acid rain", dissolved aluminum and chemical weathering at the Hubbard Brook Experimental Forest, New Hampshire. *Geochim. Cosmochim. Acta* 45, 1421–1437. doi: 10.1016/0016-7037(81)90276-3

Kim, H., Dietrich, W. E., Thurnhoffer, B. M., Bishop, J. K. B., and Fung, I. Y. (2017). Controls on solute concentration-discharge relationships revealed by simultaneous hydrochemistry observations of hillslope runoff and stream flow: the importance of critical zone structure. *Water Resour. Res.* 53, 1424–1443. doi: 10.1002/2016WR019722

Likens, G. E., Bormann, F. H., Pierce, R. S., Eaton, J. S., and Johnson, N. (1977). *Biogeochemistry of A Forested Ecosystem*. New York, NY: Springer-Verlag. doi: 10.1007/978-1-4615-9993-7

Likens, G. E., and Buso, D. C. (2006). Variation in streamwater chemistry throughout the Hubbard Brook Valley. *Biogeochemistry* 78, 1–30. doi: 10.1007/s10533-005-2024-2

Lundström, U. S., van Breemen, N., and Bain, D. (2000). The podzolization process. A review. *Geoderma* 94, 91–107. doi: 10.1016/S0016-7061(99)00036-1

McGuire, K. J., Torgersen, C. E., Likens, G. E., Buso, D. C., Lowe, W. H., and Bailey, S. W. (2014). Network analysis reveals multiscale controls on streamwater chemistry. *Proc. Natl. Acad. Sci. U.S.A.* 111, 7030–7035. doi: 10.1073/pnas.1404820111

Palmer, S. M., Wellington, B. I., Johnson, C. E., and Driscoll, C. T. (2005). Landscape influences on aluminium and dissolved organic carbon in streams draining the Hubbard Brook valley, New Hampshire, USA. *Hydrol. Process.* 19, 1751–1769. doi: 10.1002/hyp.5660

Pellerin, B. A., Fernandez, I. J., Norton, S. A., and Kahl, J. S. (2002). Soil aluminum distribution in the near-stream zone at the Bear Brook watershed in Maine. *Water. Air Soil Pollut.* 134, 189–204. doi: 10.1023/A:1014115717784

Peralta-Tapia, A., Sponseller, R. A., Ågren, A. M., Tetzlaff, D., Soulsby, C., and Laudon, H. (2015). Scale-dependent groundwater contributions influence patterns of winter baseflow stream chemistry in boreal catchments. *J. Geophys. Res. Biogeosci.* 120, 847–858. doi: 10.1002/2014JG002878

Phillips, R. A., and Stewart, K. M. (1990). Longitudinal and seasonal water chemistry variations in a northern Appalachian stream. *Water Resour. Bull.* 26, 489–498. doi: 10.1111/j.1752-1688.1990.tb01387.x

Ronchi, B., Clymans, W., Barao, A. L. P., Vandevenne, F., Struyf, E., Batelaan, O., et al. (2013). Transport of dissolved Si from soil to river: a conceptual mechanistic model. *Silicon* 5, 115–133. doi: 10.1007/s12633-012-9138-7

Ross, D. S., Bartlett, R. J., Magdoff, F. R., and Walsh, G. J. (1994). Flow path studies in forested watersheds of headwater tributaries of Brush Brook. *Vermont. Water Resour. Res.* 30, 2611–2618. doi: 10.1029/94WR01490

Sauer, D., Sponagel, H., Sommer, M., Giani, L., Jahn, R., and Stahr, K. (2007). Podzol: soil of the year 2007. A review on its genesis, occurrence, and functions. *J. Plant Nutr. Soil Sci.* 170, 581–597. doi: 10.1002/jpln.200700135

Sommer, M. (2006). Influence of soil pattern on matter transport in and from terrestrial biogeosystems—A new concept for landscape pedology. *Geoderma* 133, 107–123. doi: 10.1016/j.geoderma.2006.03.040

Wellington, B. I., and Driscoll, C. T. (2004). The episodic acidification of a stream with elevated concentrations of dissolved organic carbon. *Hydrol. Process.* 18, 2663–2680. doi: 10.1002/hyp.5574

Zimmer, M. A., Bailey, S. W., McGuire, K. J., and Bullen, T. D. (2013). Fine scale variations of surface water chemistry in an ephemeral to perennial drainage network. *Hydrol. Process.* 27, 3438–3451. doi: 10.1002/hyp.9449

**Conflict of Interest Statement:** The authors declare that the research was conducted in the absence of any commercial or financial relationships that could be construed as a potential conflict of interest.

The handling Editor declared a shared affiliation, though no other collaboration, with one of the authors DR at the time of review.

frontiers in Earth Science

ORIGINAL RESEARCH
published: 31 May 2019
doi: 10.3389/feart.2019.00126

# Hysteretic Response of Solutes and Turbidity at the Event Scale Across Forested Tropical Montane Watersheds

*Adam S. Wymore[1]*, Miguel C. Leon[2], James B. Shanley[3] and William H. McDowell[1]*

*[1] Department of Natural Resources and the Environment, University of New Hampshire, Durham, NH, United States, [2] Department of Earth and Environmental Science, University of Pennsylvania, Philadelphia, PA, United States, [3] U.S. Geological Survey, Montpelier, VT, United States*

Concentration-discharge relationships are a key tool for understanding the sources and transport of material from watersheds to fluvial networks. Storm events in particular provide insight into variability in the sources of solutes and sediment within watersheds, and the hydrologic pathways that connect hillslope to stream channel. Here we examine high-frequency sensor-based specific conductance and turbidity data from multiple storm events across two watersheds (Quebrada Sonadora and Rio Icacos) with different lithology in the Luquillo Mountains of Puerto Rico, a forested tropical ecosystem. Our analyses include Hurricane Maria, a category 5 hurricane. To analyze hysteresis, we used a recently developed set of metrics to describe and quantify storm events including the hysteresis index (HI), which describes the directionality of hysteresis loops, and the flushing index (FI), which can be used to infer whether the mobilization of material is source or transport limited. We also examine the role of antecedent discharge to predict hysteretic behavior during storms. Overall, specific conductance and turbidity showed contrasting responses to storms. The hysteretic behavior of specific conductance was similar across sites, displaying clockwise hysteresis and a negative FI indicating proximal sources of solutes and consistent source limitation. In contrast, the directionality of turbidity hysteresis was significantly different between watersheds, although both had strong flushing behavior indicative of transport limitation. Overall, models that included antecedent discharge did not perform any better than models with peak discharge alone, suggesting that the magnitude and trajectory of an individual event was the strongest driver of material flux and hysteretic behavior. Hurricane Maria produced unique hysteresis metrics within both watersheds, indicating a distinctive response to this major hydrological event. The similarity in response of specific conductance to storms suggests that solute sources and pathways are similar in the two watersheds. The divergence in behavior for turbidity suggests that sources and pathways of particulate matter vary between the two watersheds. The use of high-frequency sensor data allows the quantification of storm events while index-based metrics of hysteresis allow for the direct comparison of complex storm events across a heterogeneous landscape and variable flow conditions.

**Keywords: Luquillo, hysteresis, storm events, sensors, specific conductance, turbidity, hurricanes**

OPEN ACCESS

***Edited by:***
*Nicole West,*
*Central Michigan University,*
*United States*

***Reviewed by:***
*Ronny Lauerwald,*
*Free University of Brussels, Belgium*
*Elizabeth Herndon,*
*Kent State University, United States*

****Correspondence:***
*Adam S. Wymore*
*adam.wymore@unh.edu*

***Specialty section:***
*This article was submitted to Biogeoscience, a section of the journal Frontiers in Earth Science*

***Received:*** *01 February 2019*
***Accepted:*** *10 May 2019*
***Published:*** *31 May 2019*

***Citation:***
*Wymore AS, Leon MC, Shanley JB and McDowell WH (2019) Hysteretic Response of Solutes and Turbidity at the Event Scale Across Forested Tropical Montane Watersheds. Front. Earth Sci. 7:126. doi: 10.3389/feart.2019.00126*

## INTRODUCTION

Concentration-discharge (C-Q) relationships provide fundamental insight into the mobilization and export of solutes and sediment from watersheds (Chorover et al., 2017). C-Q relationships offer an integrated signal representing the combined effects of sources, flow paths, biogeochemical cycles, and watershed state-factors such as lithology, soil type, and climate on stream solute and sediment concentrations. Because storm events are responsible for a disproportionate amount of material transfer compared to base flow (Inamdar et al., 2006; Fellman et al., 2009), they are particularly important in estimation of annual fluxes. Developing general models of solute and sediment behavior across a range of flow conditions would thus provide insights into watershed function as well as valuable guidance for sampling regimes that will most efficiently capture the impacts of large events. The study of C-Q relationships from individual events is challenging as individual events can be highly complex. Difficulty in interpreting C-Q patterns from individual storm events results from their spatial and temporal variability, their inherently ephemeral nature, and the challenges associated with traditional sampling approaches (e.g., grab samples) during short-term pulse events.

Recent advancements in the development of *in situ* sensors offer the opportunity to collect temporally high-resolution data that can be used to describe storm events including those in remote locations. High-frequency data are particularly useful for understanding the hysteretic behavior of storm events. Solutes and sediments often display "hysteresis-loops" and the width, magnitude, and direction of these loops provide insight into how reservoirs of solutes and sediments are stored within the hillslope and exported to fluvial networks (Gellis, 2013; Koenig et al., 2017; Vaughan et al., 2017; Olshansky et al., 2018; Rose et al., 2018). Hysteresis occurs when concentrations at a given discharge differ on the rising and falling limbs of the hydrograph. Clockwise hysteresis is interpreted to reflect proximal and rapidly mobilized sources; whereas counterclockwise hysteresis reflects sources that are either proximal to the stream channel with slow travel times or those that are distal to the stream channel. The slope of the line describing C-Q relationships can be positive where the delivery of material is considered transport limited (flushing behavior), negative where the export of material is considered source limited (dilution behavior), or chemostatic where concentrations are independent of discharge (Evans and Davies, 1998; Godsey et al., 2009). Storm events can display complex hysteresis due to variability in the spatial and temporal patterns of precipitation and runoff during a single event (Williams, 1989), which can make comparison among events difficult. Also contributing to this variability and intra-storm complexity is antecedent moisture condition. For example, storms under dry conditions can mobilize solutes rapidly and promote clockwise hysteresis (Ávila et al., 1992; Biron et al., 1999). These events tend to deplete reservoirs of solutes and sediment from both the hillslope and stream channel, causing weaker C-Q relationships during the subsequent storm (McDowell and Asbury, 1994). On the other hand, high antecedent moisture increases connectivity, which expands the contributing area for sediment and solutes to more distal parts of the catchment, promoting counterclockwise hysteresis (Seeger et al., 2004). High-frequency sensor-based data can help provide detailed insights into the complexity of storm events.

Novel quantitative approaches are also providing new ways to describe hysteresis loops. As opposed to simply relying on the slope of the regression line in *log(C)–log(Q)* space, studies are increasingly incorporating an indexed-based approach to quantify event-based hysteretic behavior (Lawler et al., 2006; Lloyd et al., 2016; Zuecco et al., 2016; Vaughan et al., 2017). One of the strengths of an indexed approach is that it can be used to quantify C-Q relationships at multiple time-points during an individual storm event. This allows for a robust quantification of the storm's central tendency (e.g., mean width of hysteresis loop) and variability, while facilitating the comparison of events across space and time. One such approach is the hysteresis index (HI) proposed by Lloyd et al. (2016) and modified by Vaughan et al. (2017). HI uses normalized concentration and discharge values (Lawler et al., 2006; Lloyd et al., 2016) to enumerate differences on the rising and falling limbs of the hydrograph. HI values range between −1 and 1, with negative and positive values representing counterclockwise and clockwise hysteresis, respectively. The magnitude of HI (i.e., width of loop) thus describes the difference in concentration between the rising and falling limb at points of equal discharge. Vaughan et al. (2017) further enhanced these index-based analyses by combining HI with a *"flushing index"* (FI), which compares normalized concentrations at the beginning of the storm and at peak discharge, thereby providing further description of solute and sediment behavior and delivery to the stream channel. Here we use the term "normalized slope" (NS) to describe FI and to avoid confusion with other FI terminology common in the stream biogeochemistry literature (e.g., McKnight et al., 2001) and to better capture the fact that this metric can be used to describe both flushing and diluting behavior. Normalized slope values also range between −1 and 1 with positive values representing a flushing response and negative values representing a dilution response.

In this study we used high-frequency data collected with specific conductance and turbidity sensors to better understand how variation in watershed characteristics across a heterogeneous tropical landscape affects the mobilization of material during storm events. One framework within which to consider spatial variation is the Critical Zone (CZ). The CZ is defined as the layer of the Earth's surface from the lowest extent of freely circulating groundwater to the top of vegetative canopy (National Research Council [NRC], 2001). As such, the CZ incorporates lithology, regolith and soil, all terrestrial biota, and topography, providing a predictive framework for understanding the relationship between watershed structure and function (e.g., Wymore et al., 2017). Watersheds across the Luquillo Mountains, Puerto Rico, provide an ideal laboratory to examine how the structure of the CZ affects the export of material in a tropical landscape as affected by variations in lithology, forest composition, and topography while experiencing a similar climatic regime. It is this CZ template, especially lithology, that influences where material is stored and how flow paths are distributed both laterally and vertically.

We analyzed storm-generated hysteresis loops using the indices described by Lloyd et al. (2016) and Vaughan et al. (2017) in an effort to understand where solutes and sediment are stored within our study watersheds and the role of storms in mobilizing and exporting this material. We analyzed data from 46 unique hydrological events including a major category 5 hurricane.

We hypothesized that each of our study watersheds would have unique hysteretic behavior in response to storms and that these responses would be associated with lithology and would be similar to their long-term C-Q relationships. In the Luquillo Mountains, lithology exerts control on the long-term C-Q relationships of multiple solutes (McDowell and Asbury, 1994; Shanley et al., 2011; Stallard and Murphy, 2012; Gellis, 2013; Wymore et al., 2017) primarily by affecting weathering rates, hydrological flow paths and spatial variation in reservoirs of solutes and sediment (Shanley et al., 2011; Wymore et al., 2017). For example, in the volcaniclastic terrain of the Luquillo Mountains apatite weathering is the primary control on phosphate C-Q behavior, while biotic processes driven by nutrient limitation (Chadwick and Asner, 2016) influence the solute's C-Q behavior in the granitic watershed (Wymore et al., 2017). We also expected that hysteresis metrics (HI and NS) would correlate with the magnitude of the storm (measured as peak Q) and that antecedent discharge would add predictive power to these models (Gellis, 2013). Quantitative and predictive frameworks that describe C-Q relationships across tropical watersheds are important because the tropics are understudied compared to temperate watersheds, despite the fact that they provide a disproportionate contribution to the global flux of solutes and sediment to the oceans (Hilton et al., 2008; Gellis, 2013; Schlesinger and Bernhardt, 2013). Understanding C-Q relationships and the associated drivers provides key information to resource managers who can benefit from predictive frameworks that describe how watersheds respond to disturbance events.

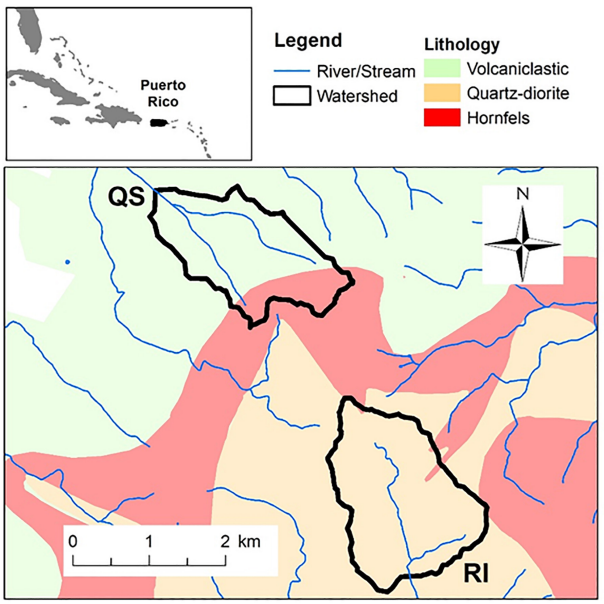


**FIGURE 1 |** Map of the Luquillo Mountains, Puerto Rico, and the drainages of Quebrada Sonadora (QS) and Rio Icacos (RI) outlined in bold. Colors represents differences in lithology.

## MATERIALS AND METHODS

### Site Description

Study watersheds were located in the tropical Luquillo Mountains of northeastern Puerto Rico (**Figure 1**). The Luquillo Mountains are warm and wet, with a mean annual temperature of 20°C and mean annual precipitation varying between 2500 and 4500 mm as a function of elevation (Garcia-Martino et al., 1996; McDowell et al., 2012; Murphy et al., 2017). Our two study watersheds, Quebrada Sonadora (QS) and Rio Icacos (RI), vary in lithology (volcaniclastic rocks at QS and quartz diorite at RI), but have similar vegetation, elevation, and slope. A primary difference besides geology is the considerably higher rainfall and annual runoff at RI (McDowell and Asbury, 1994; **Table 1**).

Hurricane Maria (initially a category 5 hurricane) made landfall in Puerto Rico on September 19$^{th}$, 2017. Hurricane Maria made a direct hit on the southeast corner of the island moving northwest across the island and over the Luquillo Mountains. The peak discharge associated with Hurricane Maria was 5- to 6.5-fold greater than the mean peak discharges of all other storms assessed in this study (**Table 2**). As such, data from Hurricane Maria were treated as an anomaly and not included in calculations of central tendencies or regression analyses (see section "Statistical Analyses"). We do, however, directly compare the hysteretic metrics and behavior of this major Atlantic hurricane to that of the mean storm response experienced by both watersheds (**Table 2**). We do not treat Hurricane Irma, another major Atlantic hurricane which grazed past Puerto Rico 1 week prior to Hurricane Maria, as an anomalous extreme event because the storm's runoff and calculated hysteresis metrics were within the range of the other assessed storm events. Irma's HI and NS values are thus included in calculations of central tendencies.

### *In situ* Sensors

High-frequency specific conductance and turbidity data were collected using *in situ* sensors that were installed in 2014. In these Luquillo streams electrical conductivity is primarily driven by chloride, bicarbonate, magnesium, calcium, and sodium due to weathering and atmospheric inputs of sea salt. (McDowell and Asbury, 1994). Specific conductance was measured with an independent Onset HOBO conductance probe or a Campbell Scientific CS527 conductivity probe connected to a Campbell CR 1000 datalogger. Turbidity was measured with a Turner Designs Cyclops 7 turbidity probe at 850 nm (Turner Designs, Sunnyvale, CA, United States). The Campbell conductance and Turner turbidity probes were controlled and read by a Campbell Scientific CR1000 datalogger and data were transmitted in near real time to a database with CUASHI Observational Data Model (ODM2). Onset HOBO data were manually downloaded from the probe and uploaded to ODM2 on a web interface. QA/QC was performed on the data in ODM2 by staff at the University of

**TABLE 1 |** Watershed characteristics and background hydrologic and stream chemistry metrics for Quebrada Sonadora (QS) and Rio Icacos (RI).

| Site | Area ($km^2$) | Elev (MASL) | Slope (°) | Discharge (mm $h^{-1}$) | Specific conductance ($\mu$S/cm) | TSS (mg/L) | Lithology | Vegetation |
|---|---|---|---|---|---|---|---|---|
| *QS* | 2.62 | 740 | 17.4 | 0.121 | 49.56 | 1.6 | Vc (66.1%)<br>Hf (33.9%) | SP (32%)<br>Co (53%)<br>DP (7%)<br>Tab (8%) |
| *RI* | 3.26 | 686 | 14.6 | 0.306 | 56.93 | 4.09 | QD (99.4%)<br>Hf (0.6%) | SP (20%)<br>Co (78%)<br>DP (2%) |

*Volcaniclastic (Vc); Quartz Diorite (QD); Hornsfels (Hf); Sierra Palm (SP); Colorado (Co); Dwarf Palm (DP); Tabonuco (Tab). Discharge, specific conductance, and turbidity presented as median values.*

**TABLE 2 |** Summary statistics of storm events across Quebrada Sonadora (QS) and Rio Icacos (RI) and during Hurricane Maria.

| | Specific conductance | | | | Turbidity | | | |
|---|---|---|---|---|---|---|---|---|
| Site | # of events | Peak Q (mm $h^{-1}$) | HI | Norm. slope | # of events | Peak Q (mm $h^{-1}$) | HI | Norm. slope |
| *QS* | 8 | 4.97 | **0.373$^{a}$** | **−0.709$^{a}$** | 18 | 6.46 | **0.083$^{a}$** | **0.751$^{a}$** |
| | | | (0.178) | (0.372) | | | (0.138) | (0.286) |
| *Maria* | 1 | 30.62 | 0.233$^{\dagger}$ | −0.092$^{\dagger}$ | 1 | 30.62 | −0.046$^{\dagger}$ | 0.145$^{\dagger}$ |
| | | | (0.152) | (NA) | | | (0.153) | (NA) |
| *RI* | 26 | 8.55 | **0.374$^{a}$** | **−0.809$^{a}$** | 26 | 8.55 | **−0.071$^{b}$** | **0.772$^{a}$** |
| | | | (0.121) | (0.249) | | | (0.150) | (0.215) |
| *Maria* | 1 | 73.18 | 0.372 | −0.082$^{\dagger}$ | 1 | 73.18 | −0.574$^{\dagger}$ | 0.471$^{\dagger}$ |
| | | | (0.271) | (NA) | | | (0.178) | (NA) |

*HI: hysteresis index; Norm Slope: normalized slope describing flushing/diluting behavior of rising limb during storm event. All values are means (± 1SD). Bold-face values are significantly different than zero (one-sample t-test) and different superscript letters represent statistically significant differences between sites (Student's t-test). The symbol (†) denotes significant differences between Hurricane Maria and the mean response of the other storms (one-sample t-test).*

New Hampshire. These measures primarily included eliminating spikes and making linear drift corrections for fouling.

## Runoff and Storm Identification

Instantaneous stream discharge was provided by the USGS National Water Information System (U.S. Geological Survey, 2018) for Rio Icacos (RI: station 50075000) using their 15-min record and a Campbell stage logger at QS. At QS the rating curve was established using historic USGS data. and stage height measured at 15-min intervals. Discharge was measured in cubic feet per second and then converted to runoff. Discharge records, stored in ODM2, were interrogated for high flow events using ODM2 Admin with the Django Object-Relational Mapper (ORM). To identify the start of a storm event, we used a discharge threshold criterion of 3.5 and 6.3 mm $h^{-1}$ at QS and RI, respectively. These threshold criteria represent approximately 30- and 20-fold increases in runoff relative to mean baseflow. The beginning of the storm was then identified as an inflection point that distinguished the start of the event from antecedent conditions. The end of the storm was identified as the point on the falling limb where discharge approached baseflow conditions or when another hydrological event commenced. Using these criteria, we assessed 18 events in QS and 26 storms in RI with peak storm discharge ranging from 3.93 to 21.25 mm $h^{-1}$ in QS and 6.29–27.15 mm $h^{-1}$ in RI. Hurricane Maria had a peak discharge of 30.62 mm $h^{-1}$ in QS and 73.18 mm $h^{-1}$ in RI.

## Hysteresis Indices

Detailed methods describing the calculation of the HI and normalized slope (i.e., flushing index) can be found in Lloyd et al. (2016) and Vaughan et al. (2017) but are also briefly described here.

The HI as proposed by Lloyd et al. (2016) uses normalized concentration and discharge data (Eqs 1A,B):

$$Normalized\ Q_i = \frac{Q_i - Q_{min}}{Q_{max} - Q_{min}} \quad (1A)$$

$$Normalized\ C_i = \frac{C_i - C_{min}}{C_{max} - C_{min}} \quad (1B)$$

where $Q_i$ and $C_i$ are discharge and concentration, respectively, of time interval $i$; $Q_{min}$ and $C_{min}$ are minimum storm values; and $Q_{max}$ and $C_{max}$ are maximum storm values. Normalization of the data is key to facilitate comparison of storm-based metrics across events, as all events are assessed on the same scale (Lloyd et al., 2016). Because real-time measurements do not always occur at 2% intervals of discharge, we used piecewise linear regression to determine normalized solute concentrations ($Ci_{norm}$) at each 2% interval of normalized discharge ($Qi_{norm}$) on both the rising and falling limbs of the storm.

To describe each storm event, HI was calculated at each 2% discharge interval (Vaughan et al., 2017). Values derived from this index range between −1 and 1. Negative values describe counterclockwise hysteresis; positive values describe

clockwise hysteresis. A value of zero indicates no hysteresis (Lloyd et al., 2016).

$$HI = C_{RL} - C_{FL} \quad (2)$$

where $C_{RL}$ and $C_{FL}$ represent normalized concentration values on the rising and falling limbs, respectively. A mean HI and standard deviation for each storm was then calculated for all 50 pairs of values.

We also calculated the NS following Butturini et al. (2008) and Vaughan et al. (2017). This index uses normalized concentration and discharge data at the beginning of the storm and at peak discharge to describe a flushing or dilution effect on the rising limb of the hydrograph (Eq. 3):

$$Normalized\ Slope = C_{Qpeaknorm} - C_{initialnorm} \quad (3)$$

where $C_{Qpeaknorm}$ is the normalized concentration at peak discharge and $C_{initialnorm}$ is the normalized concentration at the beginning of the storm. Normalized slope values also range from −1 to 1. Negative values describe a diluting effect on the rising limb, while positive values indicate a flushing effect (Vaughan et al., 2017).

## Long-Term C-Q Patterns

To compare storm hysteretic behavior to long-term C-Q patterns, we used data collected by the US Geological Survey (USGS) and the Luquillo Long-Term Ecological Research (LTER) and Critical Zone Observatory (CZO) programs. The long-term QS data record incorporates ∼1,500 specific conductance and total suspended sediment (TSS) data points at approximately weekly intervals across 30 years (1983–2013). Discharge data for QS were obtained from the USGS (2018; station 50063440). Long-term RI data include ∼850 specific conductance and 970 TSS samples collected at weekly intervals through much of the same period of record (1983–2014). TSS correlates strongly with turbidity (Gippel, 1995; Lewis, 1996) and thus we used it to compare long-term records with our event-based turbidity data. Both data sets include intensive sampling of individual storms as reported earlier by Stallard and Murphy (2012) and incorporated here into our long-term record. Discharge data for RI were obtained from the USGS (station 50075000). Specific conductance was measured in the field using a handheld probe. TSS was measured by filtering 0.5–2 L of water through pre-combusted Whatman GF/F glass fiber filters and weighed at the International Institute of Tropical Forestry in Rio Piedras, Puerto Rico or at the USGS Caribbean-Florida Water Science Center (Stallard and Murphy, 2012). We used log-log analyses [$log$(C)–$log$(Q)] to determine the long-term C-Q behavior for both specific conductance and TSS within each watershed (e.g., Johnson et al., 1969; Godsey et al., 2009).

## Statistical Analysis

We used a one-sample $t$-test to determine if mean HI and mean NS values for each site were statistically different than zero. In these analyses, zero represents no predictable directionality of the hysteresis loop (HI; clockwise/counterclockwise) and no predictable flushing or dilution behavior (NS). We then used Student's $t$-test to compare HI and NS between sites. We used simple linear regression to determine if there was a relationship between peak storm discharge and peak specific conductance and turbidity, mean HI, and NS. We used multiple linear regression to examine whether adding antecedent discharge explained additional variation in the response variables compared to peak storm Q alone. Accordingly, our multiple regression models examined average Q over the antecedent 6, 12, and 24 h prior to the onset of the storm. We chose these time intervals to be able to compare with results from McDowell and Asbury (1994). We then examined model performance with stepwise backward elimination regression comparing Akaike Information Criterion (AIC). To evaluate the response to Hurricane Maria we used a one-sample $t$-test. In this series of analyses, we set μ to the HI or NS value recorded during the hurricane event and tested whether the mean response of the other storms was significantly different. All analyses were performed in R using the base functions except for the stepwise regression which used the MASS package (Venables and Ripley, 2002).

# RESULTS

## Specific Conductance

Contrary to our hypothesis, the directionality and flushing behavior of specific conductance were highly congruent across our two study watersheds (**Figures 2**, **3** and **Table 2**) with nearly identical mean HI values (0.373–0.374; **Table 2**). In both watersheds, mean HI for specific conductance was positive and significantly different than zero indicating clockwise hysteresis (QS: $p = 0.003$; RI: $p < 0.0001$). Specific conductance normalized slopes were also not significantly different between watersheds ($p = 0.468$; **Table 2**). In both watersheds, NS values were strongly negative and significantly different than zero (QS: $p = 0.0002$; RI: $p < 0.0001$). These results reflect a diluting relationship between discharge and specific conductance during storms and indicate a significant source limitation of the solutes that contribute to specific conductance.

## Turbidity

The response of turbidity to storm events contrasted to the response of specific conductance (**Figures 2**, **3** and **Table 2**). As hypothesized, turbidity HI was significantly different between watersheds ($p < 0.0001$; **Table 2**). In QS, turbidity HI was positive and significantly greater than zero ($p = 0.004$) showing clockwise hysteresis. Turbidity HI in RI was negative and significantly less than zero showing counterclockwise hysteresis ($p < 0.0001$). Both watersheds had turbidity normalized slopes that were positive and significantly greater than zero ($p < 0.0001$ for both), with no statistical difference between watersheds. The positive normalized slopes indicate that the mobilization of sediment in both QS and RI was transport limited.

## Regression Models and Model Performance

The explanatory power of peak and antecedent discharge on hysteresis behavior (i.e., peak specific conductance and turbidity,

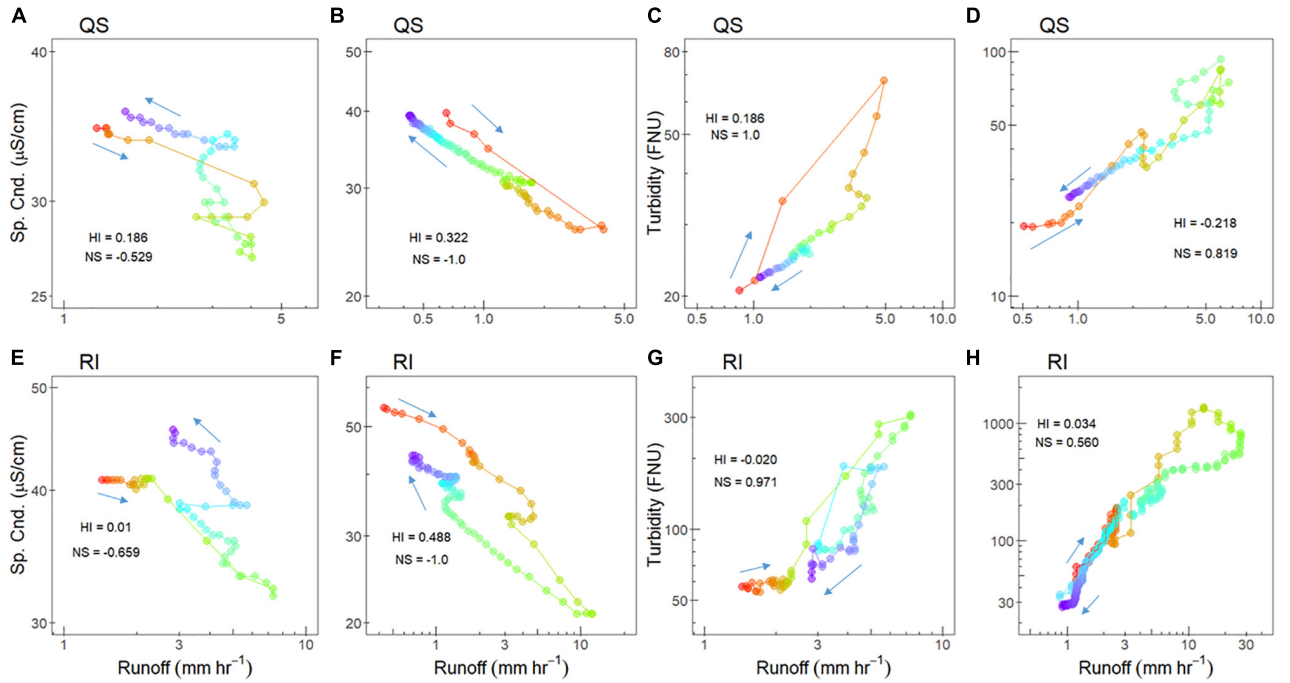


**FIGURE 2 |** Typical specific conductance (Sp. Cnd.) and turbidity responses to increased streamflow during individual storm events. Red/orange colors represent the beginning of the storm and blue/purple colors represent the end of the storm. Arrows also provide beginning and ending points of each event. The top row of **(A–D)** shows the response of specific conductance and turbidity at Quebrada Sonadora (QS) and the bottom row of **(E–H)** shows the response of specific conductance and turbidity at Rio Icacos (RI). Hysteresis index (HI), and normalized slope (NS) values are presented for each storm. Specific conductance generally dilutes in response to increased flow whereas turbidity exhibits flushing behavior. Note that both axes are log-scaled.

mean HI, and NS) was inconsistent across sites, metrics and models (**Table 3**). Evaluation of model performance via AIC indicated, however, that when significant relationships were detected, peak Q alone was consistently the best model to predict minimum and maximum concentrations of specific conductance and turbidity, and metrics of hysteresis. While consideration of antecedent Q added explanatory power to some models, the multi-parameter models performed no better than simple linear regression models of peak Q alone.

As hypothesized, peak discharge correlated significantly with peak turbidity in both watersheds for the individual storms sampled with sensors (**Table 3**). Contrary to our expectations, the relationship between peak turbidity and peak discharge was much stronger in QS ($r^2$ = 0.785) than in RI ($r^2$ = 0.168), even though the larger weekly data set shows that TSS is better predicted by Q in RI than in QS (see section "Long-Term C-Q Patterns"). In contrast, minimum specific conductance was correlated with peak discharge only in RI. The lack of a relationship in QS may be the result of a smaller sample size than in RI.

## Hurricane Maria

Hurricane Maria generated unique hysteretic patterns (**Figure 4** and **Table 2**). In QS, specific conductance HI showed clockwise hysteresis, but average HI was significantly less than the mean of the other analyzed storms ($p$ = 0.046) indicating smaller differences in concentration on the rising and falling limbs of the storm. Normalized slope of specific conductance in QS during Maria was also significantly different from the other storms ($p < 0.001$) and much closer to zero (**Figure 4A**). Patterns of turbidity during Maria in QS also differed significantly from other storms with a slightly negative HI ($p < 0.001$). Although the normalized slope for turbidity in QS during Maria remained positive (**Figure 4B**), there was a significant decrease in the slope ($p < 0.001$) of approximately five-fold.

In RI during Maria, specific conductance HI was positive and nearly identical to the other storms ($p$ = 0.48; **Table 2**), but the normalized slope was significantly less negative than the other storms ($p < 0.001$) and approached zero indicating less pronounced diluting behavior (**Figure 4C**). Turbidity HI was significantly more negative than other storms ($p < 0.001$) in RI demonstrating strong counterclockwise hysteretic behavior. And similar to turbidity in QS, normalized slope in RI during Maria remained positive (**Figure 4D**) but was significantly less (1.64x) than the other storms ($p < 0.001$; **Table 2**).

## Long-Term C-Q Patterns

As hypothesized, storm hysteresis flushing and diluting behavior (i.e., positive and negative FI values, respectively) matched long-term C-Q patterns with respect to source versus transport limitation as the primary control mechanism. In both watersheds, specific conductance demonstrated strong diluting behavior across a range of flow conditions (**Figures 5A,C**) indicating source limitation. Discharge explained 41 and 50% of the variation in specific conductance in QS and RI, respectively. In

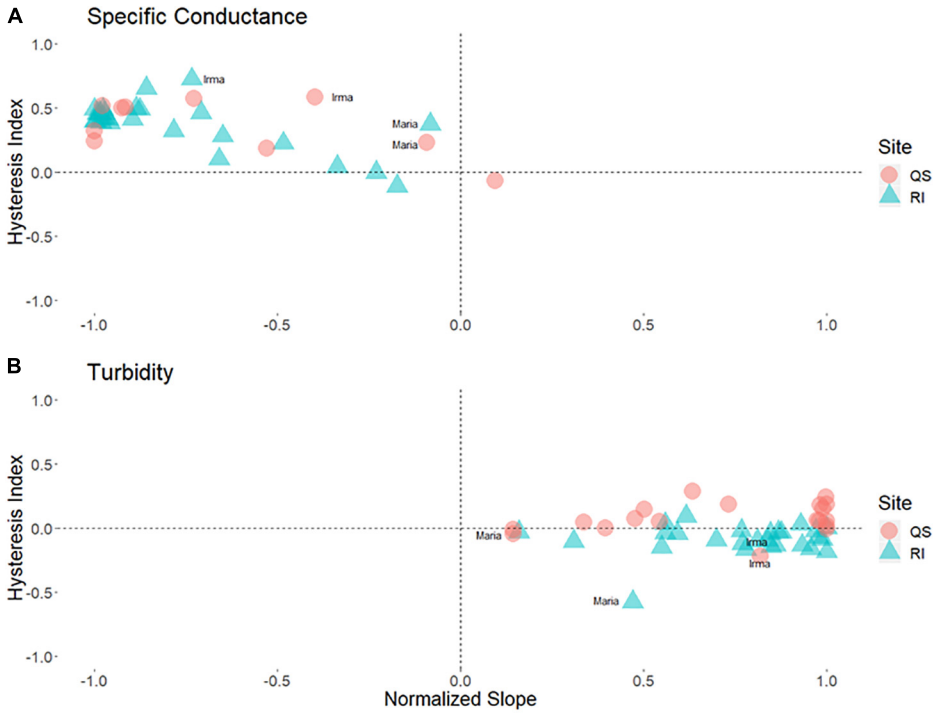


**FIGURE 3 |** Plots of **(A)** specific conductance and **(B)** turbidity storm HI versus storm normalized slope at both Quebrada Sonadora (QS) and Rio Icacos (RI). Upper-left hand quadrants represent a clockwise diluting response; upper right-hand quadrants represent a clockwise flushing response; lower left-hand quadrants represent counterclockwise diluting response; and lower right-hand quadrants represent a counterclockwise flushing response. The responses due to Hurricane Irma and Hurricane Maria are also labeled.

**TABLE 3 |** Simple and multiple linear regression results of storm and hysteresis metrics with peak and antecedent discharge (AQ) averaged over 6, 12, and 24 h at Quebrada Sonadora (QS) and Rio Icacos (RI).

| **Site/model** | | ***Equation parameters (SE)*** | $r^2$ | ***p*** | ***AIC*** |
|---|---|---|---|---|---|
| ***QS: Response variable*** | ***QS: Predictor variables*** | | | | |
| Mean HI specific conductance | Peak Q | 0.002 (0.001) | 0.259 | 0.162 | **−27.04** |
| Mean HI specific conductance | Peak Q + 24 h AQ | −0.011 (0.004) | 0.697 | 0.028 | −25.40 |
| Peak turbidity | Peak Q | 2.18 (0.286) | 0.785 | <0.0001 | **182.91** |
| Peak turbidity | Peak Q + 6 h AQ | −2.12 (3.01) | 0.792 | <0.00001 | 206.90 |
| Peak turbidity | Peak Q + 12 h AQ | 0.444 (3.06) | 0.785 | <0.00001 | 208.09 |
| Peak turbidity | Peak Q + 24 h AQ | 1.21 (2.58) | 0.788 | <0.00001 | 208.71 |
| *RI: Response variable* | *RI: Predictor variables* | | | | |
| Minimum specific conductance | Peak Q | −0.020 (0.007) | 0.232 | 0.013 | **96.94** |
| Minimum specific conductance | Peak Q + 6 h AQ | 0.068 (0.035) | 0.340 | 0.008 | 103.75 |
| Minimum specific conductance | Peak Q + 12 h AQ | 0.093 (0.036) | 0.407 | 0.002 | 103.78 |
| Minimum specific conductance | Peak Q + 24 h AQ | 0.030 (0.029) | 0.267 | 0.028 | 103.71 |
| Norm. slope specific conductance | Peak Q | −0.0004 (0.0003) | 0.067 | 0.201 | **−71.91** |
| Norm. slope specific conductance | Peak Q + 6 h AQ | 0.003 (0.001) | 0.252 | 0.036 | −70.16 |
| Norm. slope specific conductance | Peak Q + 12 h AQ | 0.004 (0.001) | 0.331 | 0.010 | −70.99 |
| Norm. slope specific conductance | Peak Q + 24 h AQ | 0.002 (0.001) | 0.244 | 0.040 | −71.19 |
| Peak turbidity | Peak Q | 1.01 (0.458) | 0.168 | 0.038 | **311.05** |
| Peak turbidity | Peak Q + 6 h AQ | −5.37 (2.01) | 0.358 | 0.006 | 315.64 |
| Peak turbidity | Peak Q + 12 h AQ | −5.72 (2.18) | 0.359 | 0.006 | 315.60 |
| Peak turbidity | Peak Q + 24 h AQ | −2.41 (1.75) | 0.231 | 0.049 | 315.80 |

*Results shown only when a significant relationship ($\alpha$ = 0.05) was detected within a set of analyses. AIC scores determined by stepwise regression with backward elimination. Bold faced AIC values denote best model.*

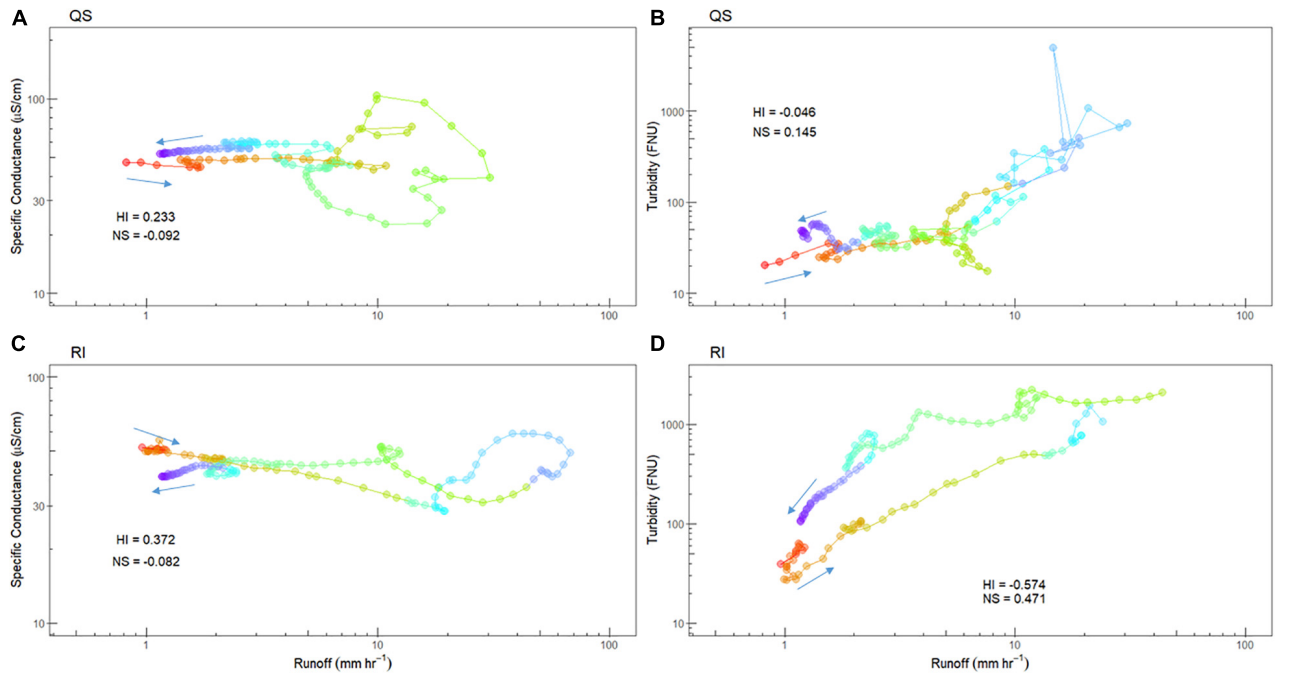


**FIGURE 4 |** The response of specific conductance and turbidity to Hurricane Maria in Quebrada Sonadora (QS: **A,B**) and Rio Icacos (RI: **C,D**). Red/orange colors represent the beginning of the storm and blue/purple colors represent the end of the storm. Arrows also provide beginning and ending points of each event. HI and normalized slope (NS) values are presented for each storm. Note that both axes are log-scaled.

contrast, concentrations of TSS became enriched (flushing) with increases in discharge in both watersheds indicating transport limitation (**Figures 5B,D**). However, the relationship between TSS and discharge was much weaker in QS ($r^2$ = 0.13) compared to RI ($r^2$ = 0.55).

## DISCUSSION

The application of high-frequency sensor data in tandem with indexed-based metrics allowed us to describe and quantify hysteresis and effectively compare storm events. Storm-based C-Q relationships often show complex hysteretic behavior including non-linear and figure-eight patterns where concentrations on the rising and falling limbs intersect multiple times. Index-based approaches such as the HI (Lloyd et al., 2016; Vaughan et al., 2017) can be used to describe an event at multiple time points capturing intra-storm complexities, and objectively integrate the complexity. With the normalization of the data (Lawler et al., 2006; Lloyd et al., 2016), storm events are placed onto a similar scale supporting the direct comparison of the response of solute and sediment across space and time. Storms in the Luquillo Mountains reveal a high degree of complexity making the use of these metrics appropriate for this landscape (e.g., **Figures 2A,D,G**).

Our analysis showed that the mobilization and export of sediments are largely decoupled from that of solutes during storm events (**Figure 3**) and that solutes are generally source limited, while sediment is generally transport limited. Across both study watersheds, specific conductance showed a consistent response to changes in discharge during storm events. The directionality as measured by HI (clockwise) and strong negative normalized slopes of specific conductance were virtually identical in the two sites. These patterns suggest that the primary source of solutes in both watersheds is located near the stream channel and is rapidly mobilized and depleted during storm events due to near-surface flow paths. Higher concentrations on the rising limb likely reflect the storage of solutes in riparian zones and the contribution of marine aerosols transported inland via the predominant east-west storm tracks (McDowell et al., 1990). Contrary to our expectations, we did not see any evidence that the hysteretic responses of specific conductance during storm events is the result of different lithographic templates. While lithology is known to influence flow paths including length, depth, and reaction time (e.g., McDowell et al., 1992), as well as porosity and reactive minerals in the weathering zone, lithology might be responsible for some differences in solute concentration among sites across the Luquillo Mountains (Bluth and Kump, 1994; McDowell and Asbury, 1994; Wymore et al., 2017). Lithology does not, however, appear to play a role in determining hysteretic behavior of those solutes as measured by specific conductance. This finding is consistent with a recent study that did not find a relationship between the structure of the Critical Zone and the C-Q behavior of multiple solutes in streams of the Luquillo Mountains (Wymore et al., 2017).

In contrast to specific conductance, turbidity showed less pronounced patterns of hysteresis with respect to directionality. Although turbidity had a strong flushing response to increases

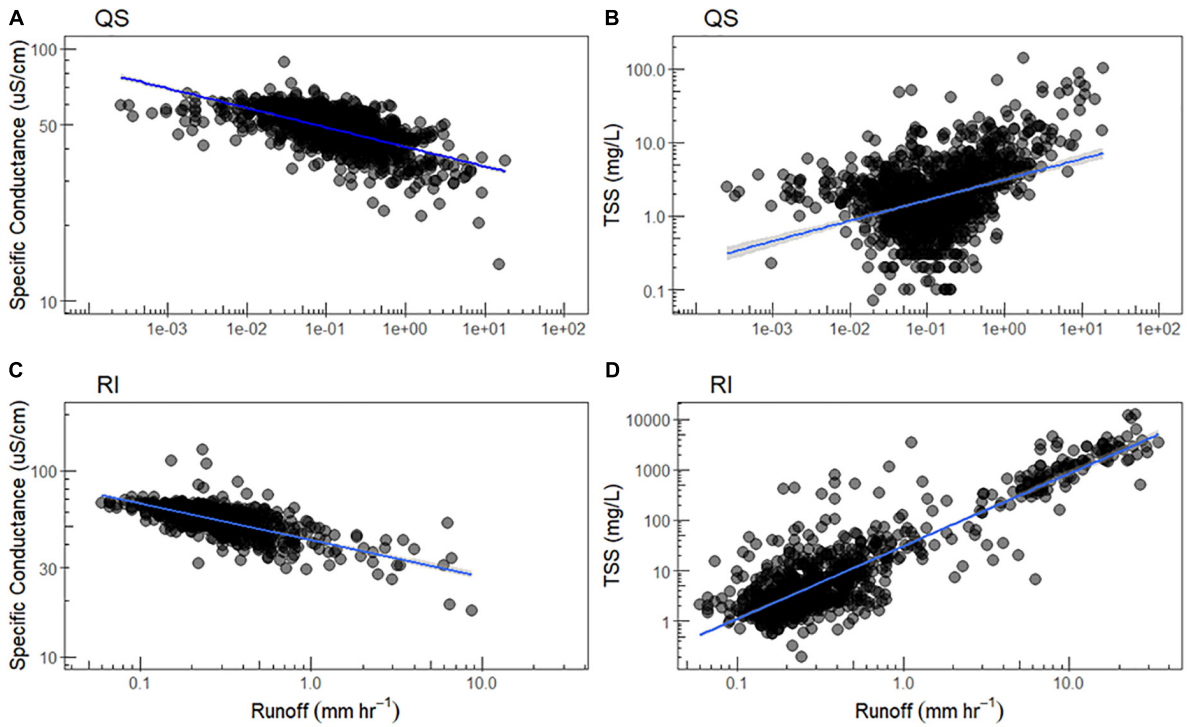


**FIGURE 5 |** Long-term concentration-discharge (C-Q) response of specific conductance and total suspended sediment (TSS) in Quebrada Sonadora (QS: **A,B**) and Rio Icacos (RI: **C,D**). Note that both axes are log-scaled.

in discharge (positive NS values), we computed several near-zero HI values. HI values closer to zero signify minimal hysteresis but may also result from complex concentration dynamics in multi-peaked storms. The lack of differentiation between concentrations on the rising and falling limbs of the storms indicates reservoirs of sediment both proximal and distal to the stream channel. This conclusion contrasts with many reports (Smith and Dragovich, 2009; Aich et al., 2014; Rose et al., 2018) including from the Luquillo Mountains and RI (Gellis, 2013; Clark et al., 2017). In an assessment of sensor-collected turbidity data during rewetting events following a major drought in RI, Clark et al. (2017) reported a clockwise C-Q response for turbidity (**Figure 6**). Our HI analysis on the other hand, indicates that the turbidity C-Q relationship generally lacks directionality across events, including a reanalysis of the data used in Clark et al. (2017; see **Figure 6**). We do not believe this is an artefact of the index-based approach as computed HI values were consistent with the clear hysteresis of specific conductance. The lack of directionality, and supply of seemingly inexhaustible sources of sediment, may be the result of RI's extremely high weathering rates (White et al., 1998). The minimal hysteresis that we have observed challenges the notion that the majority of sediment mobilization occurs within the stream channel (McDowell and Asbury, 1994) and that the increase in energy during the rising limb of the hydrograph is the primary mechanism resulting in hysteresis.

We point to two mechanisms that account for these opposing results and interpretations. First, peak turbidity in RI is not consistently associated with peak flow as visually apparent in **Figures 2H**, **6**, for example, and from the relatively weak correlation coefficient describing the relationship between peak turbidity and peak Q. After peak turbidity is reached, there are distinct periods of dilution behavior as the system continues toward peak flow. We suggest that this offset of peak turbidity coincides with peak storm intensity (Clark et al., 2017) rather than peak stream discharge, and initial flushing behavior is the direct result of sediment mobilization from the hillslope rather than flow in the stream channel. Second, the additional source of sediment that must be activated to maintain concentrations during the falling limb is the result of slopewash (Larsen et al., 1999) and particle movement via subsurface seepage. Recent evidence demonstrates the mobilization of particles can occur within the subsurface (Herndon et al., 2018; Kim et al., 2018), a finding that challenges previously held models that particles in the soil profile are assumed to be difficult to transport. Our field observations show that seepage of groundwater or shallow interflow can occur at many points along the stream banks within the RI watershed. Although we would expect both seepage and particle mobilization within the clay-rich RI soils to occur at very slow rates, it has been documented throughout the Luquillo Mountains that earthworms are an important agent of change within the subsurface responsible for increasing soil porosity (Larsen et al., 2012). Changes within the subsurface due to the burrowing behavior of earthworms provide the needed porosity and macropore space for seepage and saturated overland flow that will introduce novel sources of

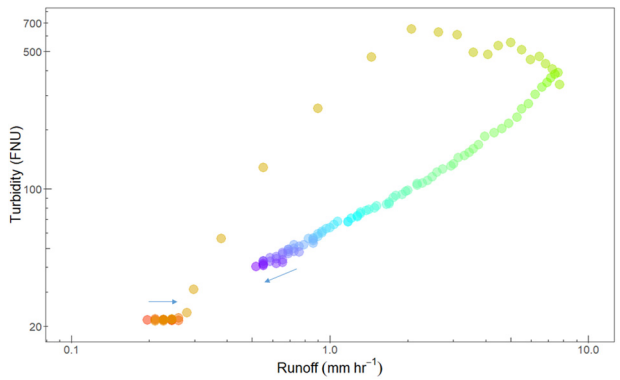


**FIGURE 6 |** The relationship between turbidity and runoff after a major rewetting event in Rio Icacos (September 2015) showing a clockwise hysteresis loop. Red/orange colors represent the beginning of the storm and blue/purple colors represent the end of the storm. Arrows also provide beginning and ending points of the storm event. Note that both axes are log-scaled. Figure redrawn from USGS sensor data available from Clark et al. (2017). When these data are normalized to peak flow the resultant mean HI value for the event is 0.098. HI values closer to zero indicate less pronounced differences in turbidity between the rising and falling limb of the hydrograph. See discussion text for additional insight.

particles. These watershed-scale phenomena, in addition to in-stream processes above the point of sampling, may help to explain the uninterrupted supply of sediment during the recession limb. We conclude that after normalizing the data to peak flow, the processes that mobilize particles during early and late stages of storm events are more evident and their effects result in a lack of strong directionality and hysteresis. This series of observations points to interactions between biological, geological and hydrological mechanisms that can drive watershed exports from the Critical Zone.

We also explored relationships between peak storm discharge and the role of antecedent discharge to influence patterns of hysteresis and found inconsistent patterns between watersheds. Peak turbidity in both QS and RI correlated significantly with peak discharge but this pattern was much stronger in QS than in RI, contrary to expectations derived from the long-term TSS C-Q patterns. These contrasting responses to flow between turbidity and TSS likely reflect both methodological differences and differences in particle size between the two watersheds. TSS is a filtration-based method reflecting only those particles captured typically on a 0.7 μm glass-fiber filter (e.g., Clark et al., 2017). In contrast, optical and sensor-based assessments of turbidity reflect a bulk measurement of all particles and sediment. Volcaniclastic watersheds, such as QS, commonly contain larger particles in the stream bed compared to other lithologies; however, these particles are typically of a more uniform size distribution (Phillips and Jerolmack, 2016). Quartz-diorite and sand-dominated watersheds like RI on the other hand, contain particles of smaller size in the stream bed, yet reflect a more heterogeneous mixture of particle sizes (e.g., Larsen, 1997; Pike et al., 2010). This difference in stream beds is directly related to differences in soil texture between the two lithologies. In the quartz diorite, soils are consistently coarser across the riparian to upland catena than they are in the volcaniclastic lithology, which is exceedingly clay-rich (McDowell et al., 1992) and delivers little sand or gravel to the stream bed compared to the diorite, as reflected in stream bed pebble counts in the two lithologies (Potter et al., 2010). The greater diversity of particle size in the stream bed of RI likely contributes to the high degree of unexplained variation in our analysis. The relative uniformity in particle size in QS is likely why the inclusion of antecedent discharge in our regression models did not add any additional explanatory power to our predictions of hysteresis and peak turbidity. In RI, however, antecedent discharge added explanatory power to our models, suggesting that it may capture the complex manner in which a heterogeneous particle load changes in response to variation in discharge. The negative parameter estimates associated with regression models that include antecedent Q provides some support for a flushing effect of previous storms on bed sediment that can decrease the supply of mobilizable particles ahead of the subsequent storm, a mechanism previously proposed for RI (Gellis, 2013). However, because models that considered antecedent Q did not outperform models of peak Q alone, such results must be interpreted with caution. Although previous Luquillo-based studies also found that antecedent Q provided additional explanatory power in predicting sediment and solute concentrations (McDowell and Asbury, 1994; Gellis, 2013), our analyses suggest that the primary mechanisms controlling the magnitude of material flux and hysteresis metrics are the magnitude and intensity of the individual storm events.

Overall, the response of solute and sediment export to Hurricane Maria differed from the other storms we assessed, including Hurricane Irma. All hysteresis metrics, except RI's specific conductance HI value, were significantly different from the average storm response. Many of Hurricane Maria's metrics also moved closer to zero, suggesting a homogenizing effect of this major hurricane on hysteresis. For example, specific conductance HI in QS decreased approximately 38% indicating less differentiation between concentrations of solutes on the rising and falling limb of the hurricane's hydrograph. Similarly, specific conductance normalized slope in QS went from steeply negative (−0.709) to nearly zero (−0.092) indicating a more chemostatic response during the storm (**Figure 4A**), with a similar pattern observed in RI (**Figure 4C**). These significantly different values in normalized slope values for specific conductance likely reflect the entrainment of sea salt during Hurricane Maria so that the typically observed dilution response was muted. Typically storm events have a strong dilution response in the Luquillo Mountains including for concentrations of sea salt (Shanley et al., 2011). Specific conductance values in QS during Hurricane Maria however, reached as high as 104 μS/cm which is a 2.6x increase above where other more typical storms begin their dilution response. And the intra-storm variability in specific conductance during Hurricane Maria far exceeded other evaluated storms including Hurricane Irma (**Figure 7**). The magnitude of Maria appears to be an exception with respect to delivery of sea salts ultimately resulting in a chemostatic response for specific

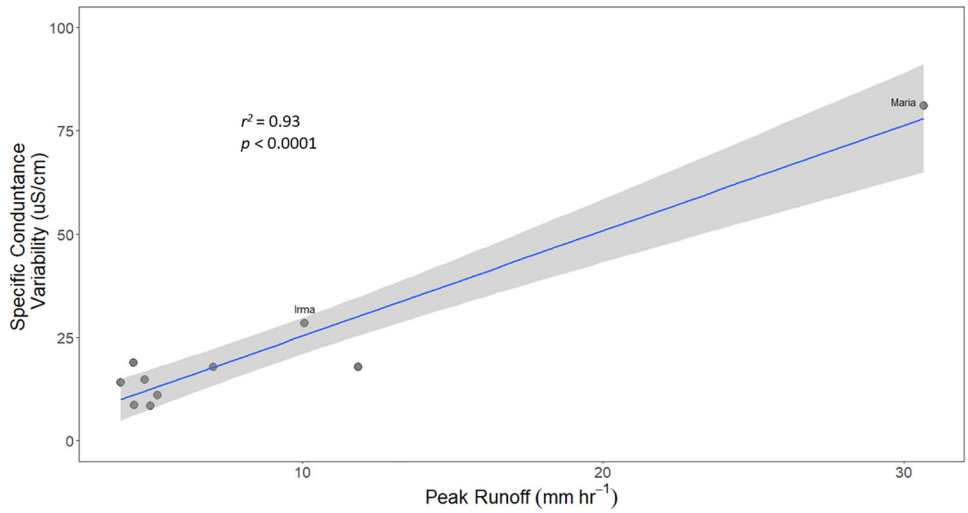


**FIGURE 7 |** Linear regression of intra-storm variability in specific conductance (highest value-lowest value) and peak storm runoff at Quebrada Sonadora (QS). The points associated with Hurricane Irma and Hurricane Maria are labeled.

conductance. RI's mean turbidity HI during the hurricane also became considerably more negative, indicative of strong counterclockwise hysteresis. This unique pattern in RI reflects a significant secondary pulse and mobilization of particles distal to the stream channel that may not occur during storms of smaller magnitude. Possible sources of this large secondary pulse include bank collapse (Simon et al., 2000; Rinaldi et al., 2004), landslides (Larsen and Torres-Sanchez, 1992) and in-channel sand activation, all of which require the additional energy supplied by a storm of such magnitude. Changes in hysteresis due to Hurricane Maria indicate that hurricanes and other large storms may surpass a threshold that activates these unique watershed-scale processes and where the associated flood wave travels faster than the sediment wave (Marcus, 1989; Gellis, 2013), collectively resulting in strong counterclockwise hysteresis.

Few studies have been able to capture within-storm hysteretic dynamics of an extreme event the magnitude of Hurricane Maria. Previous studies have incorporated less frequent ISCO-based sampling (Dhillon and Inamdar, 2013) while others have assessed the falling limb of the hydrograph (Shanley et al., 2011; Rue et al., 2017). To our knowledge, this study represents one of the first to describe and quantify solute and sediment hysteretic behavior during an extreme event using automated high-frequency *in situ* sensors capturing both the rising and falling limbs of the hydrograph. While we might hypothesize an increase in exports resulting from the observed switch from dilution to chemostasis for specific conductance and the effect of landslides (in addition to the overall erosive nature of such events; Larsen and Torres-Sanchez, 1992), measured fluxes due to cyclonic events reveal inconsistent patterns. For example, dissolved organic carbon and particulate organic carbon (POC) from Hurricane Irene accounted for 56 and 19%, respectively, of annual exports from a temperate forested watershed (Dhillon and Inamdar, 2013), whereas in the western and tropical Pacific, cyclones can mobilize 77–92% of the total POC load (Hilton et al., 2008) and deliver approximately 32% of the suspended sediment load (Darby et al., 2016). In contrast, suspended sediment loads due to Hurricane Hugo, which made landfall in Puerto Rico in September 1989, were lower than expected due to debris dams which created local backwater effects, reducing stream velocity and decreasing sediment loads (Gellis, 1993). Hurricane Maria, however, may have surpassed critical thresholds above which exports become highly concentrated.

Previous efforts to understand material export during storms, especially in remote locations, have been hampered due to the difficulties associated with event-based sampling. High-frequency *in situ* sensors provide novel insights into storm-based C-Q dynamics including major hydrological events. Understanding the complexities within and among storms is critical because of the disproportionate effects that storms have on material export (Hilton et al., 2008; Raymond and Saiers, 2010; Inamdar et al., 2017) and the substantial contribution of tropical mountainous landscapes to global exports from land to ocean. Using recently developed index-based approaches, we demonstrate that solutes are generally source limited while sediment is generally transport limited in the Luquillo Mountains. We also provide evidence that turbidity may not have a hysteretic response to changes in flow due to the combined effects of precipitation, seepage and saturation overland flow. Insights from these hysteresis metrics suggest the presence of previously unaccounted for sources of sediment and processes of sediment mobilization that can influence material export from a tropical Critical Zone.

## AUTHOR CONTRIBUTIONS

JS and WM installed and operated the sensors networks. AW and ML designed and performed the analyses. AW, JS, and

WM interpreted results. AW wrote the initial draft. All authors contributed to revisions.

## FUNDING

Funding for this project was provided by the Luquillo Critical Zone Observatory (EAR-0722476 and 1331841), the Luquillo Long-Term Ecological Research program (DEB 0620919, 1239764, and 1546686), the StreamPulse project (EF- 1442444), and a University of New Hampshire CoRE (Collaborative Research Excellence) grant to the Watershed Informatics group. Partial funding was provided by the New Hampshire Agricultural Experiment Station. This is Scientific Contribution Number 2803. This work was supported by the U.S. Department of Agriculture National Institute of Food and Agriculture (McIntire-Stennis) Project (1006760).

## ACKNOWLEDGMENTS

The authors wish to acknowledge the Water Quality Analysis Lab at the University of New Hampshire and field work by Carla Lopez Lloreda. The authors also acknowledge reviews by Jenn Hoyle Fair and two the reviewers. Any use of trade, firm, or product names is for descriptive purposes only and does not imply endorsement by the U.S. Government. Data are available via Hydroshare: https://doi.org/10.4211/hs.f8420c1447fe440eb93e656b2db0b64d. Discharge data are available from the USGS National Water Information System (2018).

## REFERENCES

Aich, V., Zimmermann, A., and Elsenbeer, H. (2014). Quantification and interpretation of suspended-sediment discharge hysteresis patterns: how much data do we need? *Catena* 122, 120–129. doi: 10.1016/j.catena.2014.06.020

Ávila, A., Piñol, J., Rodà, F., and Neal, C. (1992). Storm solute behaviour in a montane Mediterranean forested catchment. *J. Hydrol.* 140, 143–161. doi: 10.1016/0022-1694(92)90238-q

Biron, P. M., Roy, A. G., Courschesne, F., Hendershot, W. H., Côté, B., and Fyles, J. (1999). The effects of antecedent moisture conditions on the relationship of hydrology to hydrochemistry in a small forested watershed. *Hydrol. Process.* 13, 1541–1555. doi: 10.1002/(sici)1099-1085(19990815)13:11<1541::aid-hyp832>3.3.co;2-a

Bluth, G. J. S., and Kump, L. R. (1994). Lithologic and climatologic controls of river chemistry. *Geochim. Cosmochim. Acta* 58, 2341–2359. doi: 10.1016/0016-7037(94)90015-9

Butturini, A., Alvarez, M., Bernal, S., Vazquez, E., and Sabater, F. (2008). Diversity and temporal sequences of forms of DOC and NO3 – discharge responses in an intermittent stream: predictable or random succession? *J. Geophys. Res. Biogeo.* 113:G03016. doi: 10.1029/2008JG000721

Chadwick, K. D., and Asner, G. P. (2016). Tropical soil nutrient distributions determined by biotic and hillslope processes. *Biogeochemistry* 127, 273–289. doi: 10.1007/s10533-015-0179-z

Chorover, J., Derry, L. A., and McDowell, W. H. (2017). Concentration-discharge relations in the critical zone: implications for resolving critical zone structure, function and evolution. *Water Resour. Res.* 53, 8654–8659. doi: 10.1002/2017wr021111

Clark, K. E., Shanley, J. B., Scholl, M. A., Perdrial, N., Perdrial, J. N., Plante, A. F., et al. (2017). Tropical river suspended sediment and solute dynamics in storms during an extreme drought. *Water Resour. Res.* 53, 3695–3712. doi: 10.1002/2016WR019737

Darby, S. E., Hackney, C. R., Leyland, J., Kummu, M., Lauri, H., Parsons, D. R., et al. (2016). Fluvial sediment supply to a mega-delta reduced by shifting tropical-cyclone activity. *Nature* 539, 276–279. doi: 10.1038/nature19809

Dhillon, G. S., and Inamdar, S. (2013). Extreme storms and changes in particulate and dissolved organic carbon in runoff: entering uncharted waters? *Geophys. Res. Lett.* 40, 1322–1327. doi: 10.1002/grl.50306

Evans, C., and Davies, T. D. (1998). Causes of concentration/discharge hysteresis and its potential as a tool for analysis of episode hydrochemistry. *Water Resour. Res.* 34, 129–137. doi: 10.1029/97wr01881

Fellman, J. B., Hood, E., Edwards, R. T., and D'Amore, D. V. (2009). Changes in the concentration, biodegradability, and fluorescent properties of dissolved organic matter during stormflows in coastal temperate watersheds. *J. Geophys. Res. Biogeo.* 114:G01021. doi: 10.1029/2008JG000790

Garcia-Martino, A. R., Warner, G. S., Scatena, F. N., and Civco, D. L. (1996). Rainfall, runoff and elevation relationships in the Luquillo Mountains of Puerto Rico. *Caribb. J. Sci* 32, 413–424.

Gellis, A. C. (1993). The effects of hurricane hugo on suspended-sediment loads, Lago Loiza Basin, Puerto Rico. *Earth Surf. Process. Landforms.* 18, 505–517. doi: 10.1002/esp.3290180604

Gellis, A. C. (2013). Factors influencing storm-generated suspended-sediment concentrations and loads in four basins of contrasting land use, humid-tropical Puerto Rico. *Catena* 104, 39–57. doi: 10.1016/j.catena.2012.10.018

Gippel, C. J. (1995). Potential of turbidity monitoring for measuring the transport of suspended solids in streams. *Hydrol. Process.* 9, 87–97. doi: 10.1002/hyp.3360090108

Godsey, S. E., Kirchner, J. W., and Clow, D. W. (2009). Concentration-discharge relationships reflect chemostatic characteristics of US catchments. *Hydrol. Process.* 23, 1844–1864. doi: 10.1002/hyp.7315

Herndon, E. M., Steinhoefel, G., Dere, A. L. D., and Sullivan, P. L. (2018). Perennial flow through convergent hillslopes explains chemodynamic behavior in a shale headwater catchment. *Chem. Geol.* 493, 413–425. doi: 10.1016/j.chemgeo.2018.06.019

Hilton, R. G., Galy, A., Hovius, N., Chen, M.-C., Horng, M.-J., and Chen, H. (2008). Tropical-cyclone-driven erosion of the terrestrial-biosphere from mountains. *Nat. Geosci.* 1, 759–762. doi: 10.1038/ngeo333

Inamdar, S., Shanely, J. B., and McDowell, W. H. (2017). *Aquatic Ecosystems in a Changing Climate EOS, Transactions of the American Geophysical Union*. Reston: USGS.

Inamdar, S. P., O'Leary, N., Mitchell, M. J., and Riley, J. T. (2006). The impact of storm events on solute exports from a glaciated forested watershed in western New York. USA. *Hydrol. Process.* 20, 3423–3439. doi: 10.1002/hyp.6141

Johnson, N. M., Likens, G. E., Bormann, F. H., Fisher, D. W., and Pierce, R. S. (1969). A working model for the variation in stream water chemistry at the hubbard brook experimental forest, New Hampshire. *Water Resour. Res.* 5, 1353–1363. doi: 10.1029/wr005i006p01353

Kim, H., Gu, X., and Brantley, S. L. (2018). Particle fluxes in groundwater change subsurface share rock chemistry over geologic time. *Earth Planet. Sci. Lett.* 500, 180–191. doi: 10.1016/j.epsl.2018.07.031

Koenig, L. E., Shattuck, M. D., Snyder, L. E., Potter, J. D., and McDowell, W. H. (2017). Deconstructing the effects of flow on DOC, nitrate, and major ion interactions using a high-frequency aquatic sensor network. *Water Resour. Res.* 53, 10655–10673. doi: 10.1002/2017WR020739

Larsen, M. C. (1997). *Tropical Geomorphology and Geomorphicwork–A Study of Geomorphic Processes and Sediment and Water Budgets in Montane Humid-Tropical Forested and Developed Watersheds, Puerto Rico*. Ph.D. Dissertation, University of Colorado, Boulder.

Larsen, M. C., Liu, Z., and Zou, X. (2012). "Effects of earthworms on slopewash, surface runoff, and fine litter transport on a humid tropical forested hillslope, Luquillo Experimental Forest, Puerto Rico," in *Water Quality and Landscape Processes of Four Watersheds in Eastern Puerto Rico: U.S. Geological Survey Professional Paper 1789*, eds S. F. Murphy and R. F. Stallard (Reston, VA: U.S. Geol. Surv.), 179–198. doi: 10.3133/pp1789g

Larsen, M. C., and Torres-Sanchez, A. J. (1992). Landslides triggered by Hurricane Hugo in eastern Puerto Rico, September 1989. *Caribb. J. Sci.* 28, 113–125.

Larsen, M. C., Torres-Sanchez, A. J., and Conception, I. M. (1999). Slopewash, surface runoff and fine-litter transport in forest and landslide scars in humid-tropical steeplands, Luquillo Experimental Forest, Puerto Rico. *Earth Surf. Process. Landforms.* 24, 481–502. doi: 10.1002/(sici)1096-9837(199906)24:6<481::aid-esp967>3.3.co;2-7

Lawler, D. M., Petts, G. E., Foster, I. D. L., and Harper, S. (2006). Turbidity dynamics during spring storm events in an urban headwater river system: the Upper Tame, West Midlands, UK. *Sci. Total Environ.* 360, 109–126. doi: 10.1016/j.scitotenv.2005.08.032

Lewis, J. (1996). Turbidity-controlled suspended sediment sampling for runoff-event load estimation. *Water Resour. Res.* 32, 2299–2310. doi: 10.1029/96WR00991

Lloyd, C. E. M., Freer, J. E., Johnes, P. J., and Collins, A. L. (2016). Testing an improved index for analysing storm discharge–concentration hysteresis. *Hydrol. Earth Sys. Sci.* 20, 625–632. doi: 10.5194/hess-20-625-2016

Marcus, W. A. (1989). Lag-time routing of suspended-sediment concentrations during unsteady flow. *Bull. Geol. Soc. Am.* 101, 644–651. doi: 10.1130/0016-7606(1989)101<0644:ltross>2.3.co;2

McDowell, W. H., and Asbury, C. E. (1994). Export of carbon, nitrogen, and major ions from three tropical montane watersheds. *Limnol. Oceanogr.* 39, 111–125. doi: 10.4319/lo.1994.39.1.0111

McDowell, W. H., Bowden, W. B., and Asbury, C. E. (1992). Riparian nitrogen dynamics in two geomorphologically distinct tropical rain forest watersheds - subsurface solute patterns. *Biogeochemistry* 18, 53–75. doi: 10.1007/bf00002703

McDowell, W. H., Gines-Sanchez, C., Asbury, C. E., and Ramos Perez, C. R. (1990). Influence of sea salt aerosols and long range transport on precipitation chemistry at El Verde. Puerto Rico. *Atmos. Environ.* 24, 2813–2821. doi: 10.1016/0960-1686(90)90168-m

McDowell, W. H., Scatena, F. N., Waide, R. B., Brokaw, N., Camilo, G. R., Covich, A. P., et al. (2012). "Geographic and ecological setting of the Luquillo Mountains," in *A Caribbean Forest Tapestry: The Multidimensional Nature of Disturbance and Response*, eds N. Brokaw, et al. (New York, NY: Oxford Univ. Press), 87–90.

McKnight, D. M., Boyer, E. W., Westerhoff, P. K., Doran, P. T., Kulbe, T., and Anderson, D. T. (2001). Spectrofluorometric characterization of dissolved organic matter for indication of precursor organic material and aromaticity. *Limnol. Oceanogr.* 46, 38–48. doi: 10.4319/lo.2001.46.1.0038

Murphy, S. F., Stallard, R. F., Scholl, M. A., González, G., and Torres-Sánchez, A. J. (2017). Reassessing rainfall in the Luquillo Mountains, Puerto Rico: local and global ecohydrological implications. *PLoS One* 12:e0180987. doi: 10.1371/journal.pone.0180987

National Research Council [NRC] (2001). *Basic Research Opportunities in Earth Science*. Washington, D. C: Natl. Acad. Press.

Olshansky, Y., White, A. M., Moravec, B. G., McIntosh, J., and Chorover, J. (2018). Subsurface pore water contributes to stream concentration-discharge relations across a snowmelt hydrograph. *Front. Earth Sci.* 6:181. doi: 10.3389/feart.2018.00181

Phillips, C. B., and Jerolmack, D. J. (2016). Self-organization of river channels as a critical filter on climate signals. *Science* 352:6286. doi: 10.1126/science.aad3348

Pike, A. S., Scatena, F. N., and Wohl, E. E. (2010). Lithological and fluvial control on the geomorphology of tropical montane stream channels in Puerto Rico. *Earth Surf. Process. Landforms.* 35, 1402–1417. doi: 10.1002/esp.1978

Potter, J. D., McDowell, W. H., Merriam, J. L., Peterson, B. J., and Thomas, S. M. (2010). Denitrification and total nitrate uptake in streams of a tropical landscape. *Ecol. Appl.* 20, 2104–2115. doi: 10.1890/09-1110.1

Raymond, P. A., and Saiers, J. E. (2010). Event controlled DOC export from forested watersheds. *Biogeochemistry* 100, 197–209. doi: 10.1007/s10533-010-9416-7

Rinaldi, M., Casagli, N., Dapporto, S., and Gargini, A. (2004). Monitoring and modeling of pore water pressure changes and riverbank stability during flow events. *Earth Surf. Process. Landforms.* 29, 237–254. doi: 10.1002/esp.1042

Rose, L. A., Karwan, D. L., and Godsey, S. E. (2018). Concentration-discharge relationships describe solute and sediment mobilization, reaction, and transport at event and longer timescales. *Hydrol. Process.* 32, 2829–2844. doi: 10.1002/hyp.13235

Rue, G. P., Rock, N. D., Gabor, R. S., Pitlick, J., Tfaily, M., and McKnight, D. M. (2017). Concentration-discharge relationships during an extreme event: contrasting behavior of solutes and changes to chemical quality of dissolved organic material in the Boulder Creek watershed during the September 2013 flood. *Water. Resour. Res.* 53, 5276–5297. doi: 10.1002/2016wr019708

Schlesinger, W. H., and Bernhardt, E. S. (2013). *Biogeochemistry*, 3rd. Edn. New York, NY: Academic Press, 688.

Seeger, M., Errea, M. P., Beguería, S., Arnáez, J., Martı, C., and Garcıa-Ruiz, J. M. (2004). Catchment soil moisture and rainfall characteristics as determinant factors for discharge/suspended sediment hysteretic loops in a small headwater catchment in the Spanish Pyrenees. *J. Hydrol.* 288, 299–311. doi: 10.1016/j.jhydrol.2003.10.012

Shanley, J. B., McDowell, W. H., and Stallard, R. F. (2011). Long-term patterns and short-term dynamics of stream solutes and suspended sediment in a rapidly weathering tropical watershed. *Water Resour. Res.* 47:W07515. doi: 10.1029/2010WR009788

Simon, A., Curini, A., Darby, S., and Langendoen, E. J. (2000). Bank and near-bank processes in an incised channel. *Geomorphology* 35, 193–217. doi: 10.1016/s0169-555x(00)00036-2

Smith, H. G., and Dragovich, D. (2009). Interpreting sediment delivery processes using suspended sediment-discharge hysteresis patterns from nested upland catchments, south-eastern Australia. *Hydrol. Process.* 23, 2415–2426. doi: 10.1002/hyp.7357

Stallard, R. F., and Murphy, S. F. (2012). "Water quality and mass transport in four watersheds in Puerto Rico," in *Water Quality and Landscape Processes of Four Watersheds in Eastern Puerto Rico: U.S. Geological Survey Professional Paper 1789*, eds S. F. Murphy and R. F. Stallard (Reston, VA: U.S. Geol. Surv.), 113–152. doi: 10.3133/pp1789e

U.S. Geological Survey (2018). *National Water Information System—Web interface*. Reston, VA: U.S. Geol. Surv.

Vaughan, M. C. H., Bowden, W. B., Shanley, J. B., Vermilyea, A., Sleeper, R., Gold, A. J., et al. (2017). High-frequency dissolved organic carbon and nitrate measurements reveal differences in storm hysteresis and loading in relation to land cover and seasonality. *Water Resour. Res.* 53, 5345–5363. doi: 10.1002/2017wr020491

Venables, W. N., and Ripley, B. D. (2002). *Modern Applied Statistics with S-Plus*, 4th Edn. New York, NY: Springer.

White, A. F., Blum, A. E., Schulz, M. S., Vivit, D. V., Stonestrom, D. A., Larsen, M., et al. (1998). Chemical weathering in a tropical watershed, Luquillo Mountains, Puerto Rico: I. long-term versus short-term weathering fluxes. *Geochim. Cosmochim. Acta* 62, 209–226. doi: 10.1016/s0016-7037(97)00335-9

Williams, G. P. (1989). Sediment concentration versus water discharge during single hydrologic events. *J. Hydrol.* 111, 89–106. doi: 10.1016/0022-1694(89)90254-0

Wymore, A. S., Brereton, R. L., Ibarra, D. E., Maher, K., and McDowell, W. H. (2017). Critical zone structure controls concentration-discharge relationships and solute generation in forested tropical montane watersheds. *Water Resour. Res.* 53, 6279–6295. doi: 10.1002/2016WR020016

Zuecco, G., Penna, D., Borga, M., and Meerveld, H. J. (2016). A versatile index to characterize hysteresis between hydrological variables at the runoff event timescale. *Hydrol. Process.* 30, 1449–1466. doi: 10.1002/hyp.10681

**Conflict of Interest Statement:** The authors declare that the research was conducted in the absence of any commercial or financial relationships that could be construed as a potential conflict of interest.

frontiers in Environmental Science

ORIGINAL RESEARCH
published: 07 November 2019
doi: 10.3389/fenvs.2019.00172

# Soil Aggregates as a Source of Dissolved Organic Carbon to Streams: An Experimental Study on the Effect of Solution Chemistry on Water Extractable Carbon

*Malayika M. Cincotta[1], Julia N. Perdrial[1]*, Aaron Shavitz[1], Arianna Libenson[1], Maxwell Landsman-Gerjoi[1], Nicolas Perdrial[1], Jesse Armfield[1], Thomas Adler[1] and James B. Shanley[2]*

[1] Environmental Biogeochemistry Lab, Department of Geology, University of Vermont, Burlington, VT, United States, [2] US Geological Survey, Montpelier, VT, United States

Over the past two decades, headwater streams of the northern hemisphere have shown increased amounts of dissolved organic carbon (DOC), coinciding with decreased acid deposition. The exact nature of the mechanistic link between precipitation composition and stream water DOC is still widely debated in the literature. We hypothesize that soil aggregates are the main source of stream water DOC and that DOC release is greater in organic rich, riparian soils vs. hillslope soils. To test these hypotheses, we collected soils from two main landscape positions (hillslope and riparian zones) from the acid-impacted Sleepers River Research Watershed in northeastern Vermont. We performed aqueous soil extracts with solutions of different ionic strength (IS) and composition to simulate changes in soil solution. We monitored dynamic changes in soil particle size, aggregate architecture and composition, leachate DOC concentrations, dissolved organic matter (DOM) characteristics by fluorescence spectroscopy and trends in bioavailability. In low IS solutions, extractable DOC concentrations were significantly higher, particle size (by laser diffraction) was significantly smaller and organic material was separated from mineral particles in scanning electron microscope observations. Furthermore, higher DOC concentrations were found in $Na^+$ compared to $Ca^{2+}$ solutions of the same IS. These effects are attributed to aggregate dispersion due to expanding diffuse double layers in decreased IS solutions and to decreased bridging by divalent cations. Landscape position impacted quality but not quantity of released DOC. Overall, these results indicate that soil aggregates might be one important link between Critical Zone inputs (i.e., precipitation) and exports in streams.

**Keywords: soil aggregates, dissolved organic carbon, Sleepers River, ionic strength, fluorescence spectroscopy**

OPEN ACCESS

***Edited by:***
*Jiang Helong,*
*Nanjing Institute of Geography and Limnology (CAS), China*

***Reviewed by:***
*Morgan Reed Raven,*
*University of California, Santa Barbara, United States*
*Yihua Cai,*
*Xiamen University, China*

****Correspondence:***
*Julia N. Perdrial*
*Julia.Perdrial@uvm.edu*

***Specialty section:***
*This article was submitted to Biogeochemical Dynamics, a section of the journal Frontiers in Environmental Science*

***Received:*** *25 July 2018*
***Accepted:*** *14 October 2019*
***Published:*** *07 November 2019*

***Citation:***
*Cincotta MM, Perdrial JN, Shavitz A, Libenson A, Landsman-Gerjoi M, Perdrial N, Armfield J, Adler T and Shanley JB (2019) Soil Aggregates as a Source of Dissolved Organic Carbon to Streams: An Experimental Study on the Effect of Solution Chemistry on Water Extractable Carbon. Front. Environ. Sci. 7:172. doi: 10.3389/fenvs.2019.00172*

## INTRODUCTION

Over the last few decades increased levels of dissolved organic carbon (DOC) have been observed in forested streams across the northern hemisphere (Monteith et al., 2007; Porcal et al., 2009) and several processes have been proposed to explain observed patterns. For example, some studies indicate that increases in DOC are consistent with a climate change driver including changing

temperature or hydroclimatic conditions (Freeman et al., 2001; Worrall and Burt, 2007; Eimers et al., 2008; Lepistö et al., 2008). Other suggested drivers include changes in nitrogen deposition (Stuart, 2005) or land management practices (Yallop and Clutterbuck, 2009). Lastly, recovery from acidification is put forth as a general driver for observed changes in stream water DOC (Evans and Monteith, 2001; De Wit et al., 2007; Monteith et al., 2007; Hruška et al., 2009; Kang et al., 2018). The latter is consistent with the observation of a significant reduction in acid anion concentrations (i.e., sulfate) in many catchments that show increases in DOC (Monteith et al., 2007). It is also in agreement with the observations of DOC increases with decrease in ionic strength (IS, Hruška et al., 2009). However, only a few studies have focused on the precise mechanisms of DOC release (Monteith et al., 2007; Haaland et al., 2010), making it difficult to investigate the link between Critical Zone input (i.e., precipitation) and stream water export.

Streams integrate complex and coupled hydrological and biogeochemical processes at hillslopes, riparian areas, in the hyporheic zone, and the stream itself (Lohse et al., 2009). In forested catchments, stream DOC is mostly allochthonous (produced elsewhere) and sourced from organic-rich soils of hillslopes and riparian areas (Boyer et al., 1997; Aitkenhead-Peterson et al., 2003; McDowell et al., 2006) where carbon (C) is typically associated with organo-mineral aggregates (Kaiser and Guggenberger, 2000; Six et al., 2000; Lehmann et al., 2007). These aggregates protect C from microbial attack often by physically shielding it with soil minerals including clays (Mikutta et al., 2006; Angst et al., 2017).

DOC can be stabilized on mineral surfaces via electrostatic interactions but may desorb if solution chemistry changes. For example, the change in type of solute species and concentration in soil solution can cause competition for sorption sites leading to the release or adsorption of certain aggregate constituents (Sokolova and Alekseeva, 2008). Changes in IS and pH fundamentally impact colloidal interactions and aggregation: increased IS such as during acidification, leads to the compression of the charged layer around an ion (i.e., diffuse double layer) so that attractive forces overcome repulsive forces (Derjaguin and Landau, 1941; Verwey, 1947). The higher charge density therefore leads to coagulation and the stabilization of larger colloidal associations and aggregates that can retain organic material (Lagaly, 2006; Monteith et al., 2007; Haaland et al., 2010). Furthermore, increased proton concentration and the presence of divalent cations supply positive charges that can bridge between negatively charged constituents (i.e., clays and organic matter), equally aiding aggregation. The increased anion exchange capacity (due to increased amounts of protons) can furthermore retain negatively charged organic molecules. In acid impacted soils, alteration of soil solution chemistry during recovery (a reduction in IS and an increase of pH) could therefore lead to the dispersion of such colloidal associations and aggregates, desorb organic materials and result in a release of associated DOC.

Many of the catchments showing these increases in stream water DOC amounts are upland headwater catchments with steep topography and variations in soil characteristics along the catena (Wiekenkamp et al., 2016). Typically the accumulation of organic matter and debris is greatest in near stream riparian soils (Holleran et al., 2015; Lybrand and Rasmussen, 2015), likely due to the lateral transfer of materials through the flushing of surface soils (Bourgault et al., 2017; Perdrial et al., 2018). However, when hillslopes are more geomorphically stable they tend to have higher soil organic carbon than the valleys (Johnson et al., 2011), therefore it is necessary to investigate both riparian hotspots as well as hillslope soils.

The objective of this study was to systematically test how changes in IS and composition of soil solution (monovalent vs. divalent cations) impact soil aggregates and DOC release in a combined lab and field study. We hypothesized that, as IS and the concentration of divalent cations decreases (simulating recovery from acid deposition), soil aggregate size is reduced as a result of aggregate breakup, and concentration of DOC in soil solution increases. We further hypothesized that organic-rich soils from riparian toe slope zones release larger amounts of DOC (per mass unit soil) than soils from other hillslope areas. Finally, we hypothesize that DOC released from aggregates is mostly terrestrial (not microbial) and bioavailable because aggregate DOC was shielded from microbial processing.

To test these hypotheses, we collected soils from two main landscape positions (hillslope and riparian zones) from the acid-impacted Sleepers River Research Watershed (SRRW) in northeastern Vermont. Sleepers River is unique from most other watersheds that have been studied in the context of acidification as the bedrock and glacial till contain carbonate minerals that buffer the pH and allow for the study of IS effects. We performed aqueous soil extracts with solutions of different IS and composition to simulate changes in soil solution chemistry. We also monitored dynamic changes in soil particle size, aggregate architecture and composition, leachate DOC concentrations, dissolved organic matter (DOM) characteristics using fluorescence spectroscopy, and bioavailability.

# MATERIALS AND METHODS

## Field Site

SRRW is a USGS site in northeastern Vermont (**Figure 1A**). This site has over 25 years of data on stream water composition and has shown increased DOC stream water effluxes similar to the general trend in many northern hemisphere catchments (e.g., Monteith et al., 2007; Clark et al., 2010; **Supplementary Figure 1**). The headwater catchment W-9 is the focus of this study and covers an area of 40.5 ha with elevation ranging from 524 to 672 m (**Figure 1B**, Shanley et al., 2004). One notable difference between SRRW and other studied northern hemisphere catchments is the bedrock, which contains calcareous granulite and is covered with a layer of calcareous glacial till of varying thickness (1–4 m) (Shanley et al., 2004). Weathering of the glacial till and bedrock results in calcium-bicarbonate water with a well-buffered pH. Groundwater in equilibrium with these carbonates discharges in near stream areas and exhibits high pH and calcium content.

All soils were sampled in the W-9 forest along stream B, a 12.9-ha tributary that has been most intensively studied (**Figure 1C**).

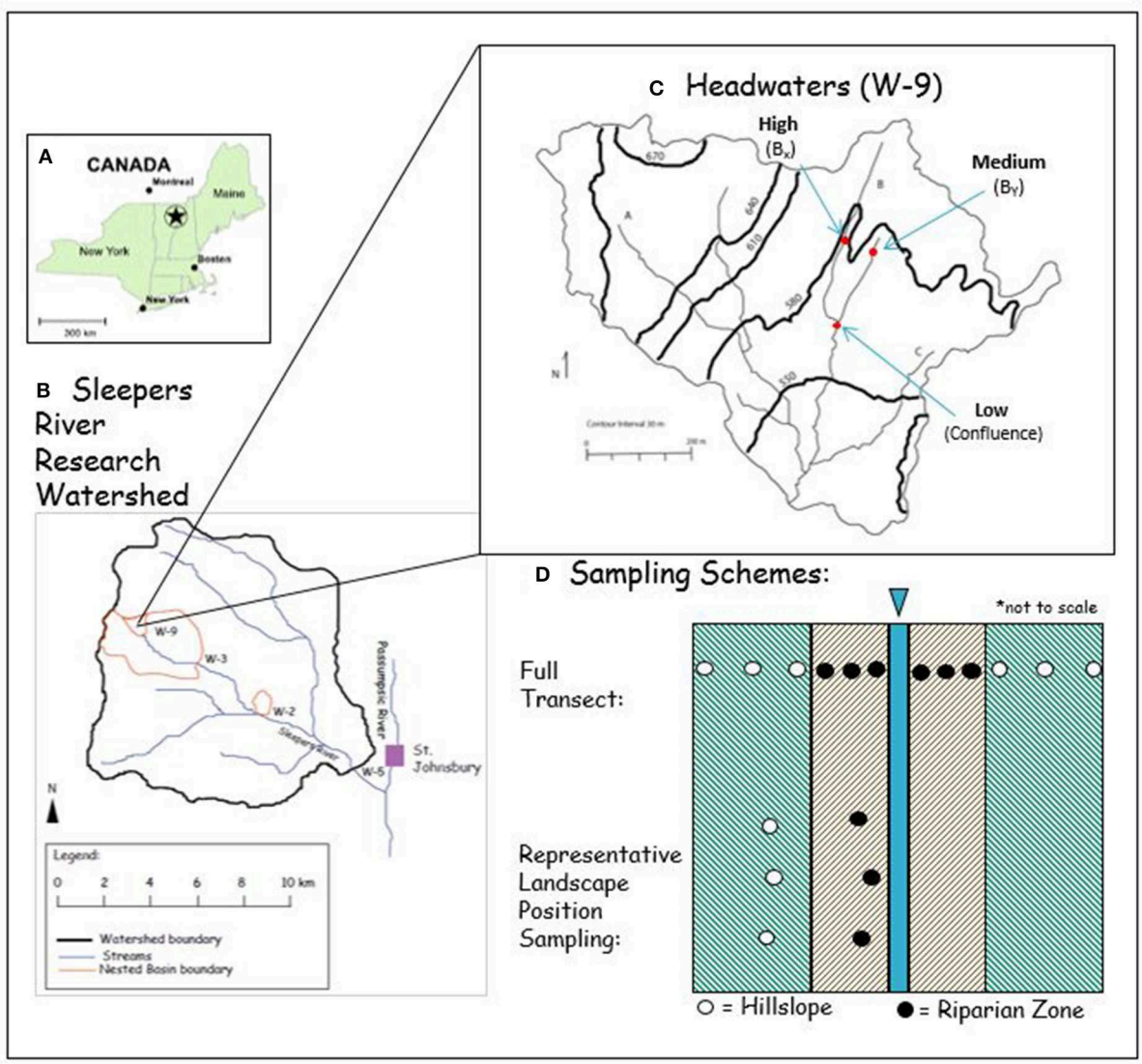


**FIGURE 1 | (A)** The location of the study site in the NE US. **(B)** The Sleepers River Research Watershed is located west of St. Johnsbury, VT (modified after Shanley et al., 2015 with permission from John Wiley and Sons). **(C)** The headwaters (W−9) with stream B is the focus of this study (modified after Kendall et al., 1999 with permission from Elsevier). **(D)** Schematic representation of the sampling design in map view (not to scale) that included samples from full transects from HSs (green shaded area) and RZs (brown shaded areas) to the stream (blue). Representative zone samples included replicated samples for each landscape position (each dot represents 3 samples).

Hillslope soils (Inceptisols and Spodosols) were sampled every 2 m along each of three transects established perpendicular to the channel, spanning from summit, shoulder, backslope and footslope catena positions (hereafter collectively referred to as hillslope = HS soils). Soils from associated toeslope positions (Histosols) in close proximity to the stream were sampled every meter (hereafter referred to as riparian zone = RZ soils), yielding in total ∼10 samples per transect. We chose the 3 transects to include varying degrees of slope gradients including 16% (high), 5% (medium), and 3% (low) (Miller and Schaetzl, 2015; Wysocki and Schoeneberger, 2017). To increase the statistical power of HS and RZ samples, we additionally sampled 3 toeslope (i.e., RZ) and 3 backslope (representing HS) samples of each of the 3 slope gradients for further analysis ($n = 18$).

Soil and aggregate samples were collected from the top 15 cm with a pre-cleaned bucket auger (15 cm in length, 10 cm diameter) after the leaf litter was removed. From a subset of these samples we additionally prepared composite samples for analyses where replication was time- and cost-prohibitive (e.g., Scanning Electron Microscopy (SEM), composite $n = 6$). For composites, we gently combined subsets of each individual, field-moist sample. This type of sampling with bucket-type augers and the preparation of composite samples has been successfully used in previous aggregate studies (Rawlins et al., 2013; Li et al.,

2016). Aggregates are defined as clusters containing mineral particles (e.g., clay minerals and oxides) and organic matter (OM) in various stages of decay, as well as living organisms (Frey, 2005) that cohere more to each other than to their surrounding particles (Nimmo and Perkins, 2002). We therefore do not define aggregates based on size, however, size is an inherent limitation on the methods used. For example, laser diffraction was effectively limited to ca. < 200 μm particles and SEM by the field of view for meaningful analysis (ca. 1,000 μm). We acknowledge that our sampling and processing techniques potentially destroyed macroaggregates, therefore our investigation considered microaggregates (<250 μm) that "survived" field sampling and were relatively stable.

## Elemental Analysis

For elemental analyses, soil samples were air-dried, sieved through a 2-mm mesh, and homogenized using a ball mill. Duplicates of each sample were analyzed for C content using a combustion-based elemental analyzer (CE Instruments NC 2500, Lancashire, UK) in the Geology Stable Isotope Lab at the University of Vermont. Resulting percent C values were compared to standards (B2150 for high organic content sediment standard and B2152 for low organic content soil standard) provided by Elemental Microanalysis Limited.

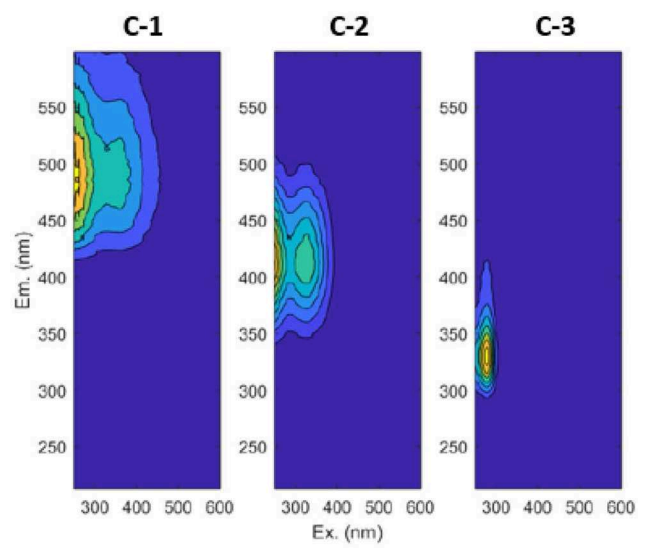


**FIGURE 2 |** Contour plots for the three components validated by PARAFAC. C-1 is terrestrial fulvic-like, C-2 is terrestrial humic-like, and C-3 is microbial protein-like.

**TABLE 1 |** Comparison of our validated PARAFAC components with published models.

| Component | Literature component | Designation |
|---|---|---|
| C1: Terrestrial, fulvic-like (EX: 250–300 nm; EM: 425–575 nm) | (Singh et al., 2013) (FH3) (Fellman et al., 2008) (C3) (Yamashita et al., 2010) (C1) | Fulvic-like Fulvic-like Fulvic-acid like |
| C2: Terrestrial, humic-like (EX: 250–325 nm; EM: 340–500 nm) | (Singh et al., 2013) (FH1) (Fellman et al., 2008) (C1) (Yamashita et al., 2010) (C2) | Humic-like Humic-like Humic-like |
| C3: Microbial, protein-like (EX: 280 nm; EM: 300–420 nm) | (Singh et al., 2013) (FH5) (Fellman et al., 2008) (C8) | Protein-like Tryptophan |

## Scanning Electron Microscopy

To visualize aggregate architecture and determine aggregate composition, we used a *TESCAN VEGA3* Scanning Electron Microscope (SEM) and Oxford Instruments *AZtec* Elemental Mapping software in the Geology Department at Middlebury College in Middlebury, VT. Air-dried samples that were first sieved through a 2-mm mesh to exclude larger particles (i.e., roots and small gravel) were sieved a second time through 250-μm mesh to isolate the aggregate fraction. Replicates of each composite sample were mounted using double-sided C tape on separate metal stubs and sputter-coated with C before analysis. To investigate the effect of simulated soil solution on aggregate size, shape, and composition solution, we added several drops of high IS solution [calcium chloride ($CaCl_2$)] and low IS [Nanopure water (NW)], to one replicate from both locations (HS and RZ) and compared to untreated aggregates. Using a micro-pipette, solutions were carefully dropped directly onto the aggregates and carefully mixed around the aggregates. The solutions were allowed to dry in place to avoid removal of the aggregates, a process completed within 90 min. Because backscattered electron (BSE) SEM mode captures differences in electron density, we used this mode to visualize high electron density mineral grains vs. low electron density organic material. BSE was acquired at 5 keV acceleration voltage and energy-dispersive spectroscopy (EDS) maps were acquired for 5 min with a probe resolution of 15 mm.

## Aqueous Soil Extractions and Analyses

To simulate the higher IS of soil solution during ecosystem acidification and to test the effect of monovalent vs. divalent solutions, we used aqueous soil extracts (ASE) as an analog for soil solution. The high IS solutions consisted of salt solutions

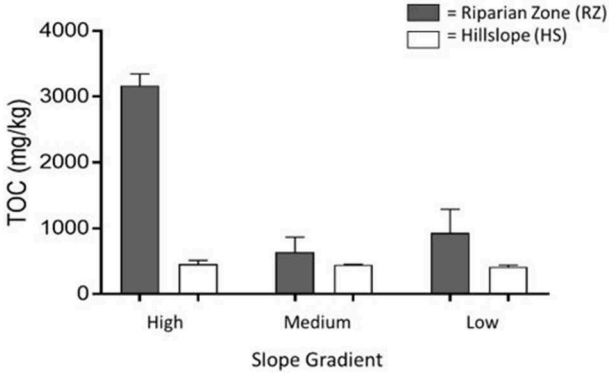


**FIGURE 3 |** Average total organic carbon (TOC) content of composite soils from high, medium, and low hillslopes (HS) as well as riparian zones (RZ) at the base of each slope. The whiskers represent the error between the sample replicates used in this analysis. Samples were collected along stream B in the headwaters (W-9) of Sleepers River Research Watershed.

(0.005M NaCl and 0.005M $CaCl_2$). To simulate the more dilute solution of recovery, we used NW. We also tested pH effects but, presumably because SRRW is well buffered, we saw no effects (**Supplementary Figure 2**). All ASE were prepared from field moist soils (existing water content was accounted for, **Supplementary Materials**, section 2) by mixing soil and aqueous solutions at a 1:5 ratio to simulate concentrated soil solutions. In accordance with a previous study we limited the shaking time on a reciprocal shaker (Eberbach Corporation, Ann Arbor, MI, USA) to 1 h to reduce microbial processing (Perdrial et al., 2012).

To monitor the effect of solution IS and composition on the size of particles and colloids in soil solution (from 0.4 μm to an effective 200 μm), aliquots of ASE were analyzed immediately after shaking or re-suspension (and prior to filtration) using the Micro Volume Module on a *Beckman Coulter* LS230 Laser Particle Analyzer. Although the particle size analyzer is designed to measure particles up to 2000 μm, it was effectively not the case in our measurement as the Micro Volume Module does not allow for good dispersion of heavier particles. Hence, the particle size of an estimated diameter $>$ 200 μm were not properly reflected in our analysis. The amount and type of the DOC in solution was determined after the solids were separated from the colloidal and dissolved matter by centrifugation (30 min, 3000 rpm) and filtration using combusted 0.7 μm glass fiber filters (Whatman Grade GF/F, Buckinghamshire, UK). Filtrates were transferred into combusted amber glass bottles for immediate analyses of C fluorescence characteristics and quantity. We analyzed all ASE samples in duplicate for concentrations of DOC and total dissolved nitrogen (TDN) via combustion using a Total Organic Carbon Analyzer (Shimadzu, Columbia, MD, USA). Results are reported normalized to the exact amount of solution and soil used for each extract (mg/kg) to allow for comparison among samples.

Spectral characteristics of DOM were determined using the Aqualog® Fluorescence and Absorbance Spectrometer (HORIBA, Irvine, CA, USA). The excitation (Ex) wavelength range spanned from 250 to 600 nm and emission (Em) ranged from 212 to 599 nm. All excitation emission matrices (EEMs) were blank-subtracted (NW), corrected for inner filter effects, and Raman normalized. From these data, we computed the following indices: the Fluorescence Index (FI) is calculated as the intensity at Em 470 nm divided by the intensity at Em 520 nm for Ex at 370 nm and can be used to indicate DOM provenance (i.e., terrestrial vs. microbial) and aromaticity (Cory and McKnight, 2005; Wymore et al., 2015). The Humification Index (HIX) is calculated as a ratio of the area under Em 435–480 nm divided by the quantity of the areas under both Em 300–345 nm and Em 435–480 nm, at an Ex of 254 nm and indicated degrees of humification (Zsolnay et al., 1999; Débora et al., 2002).

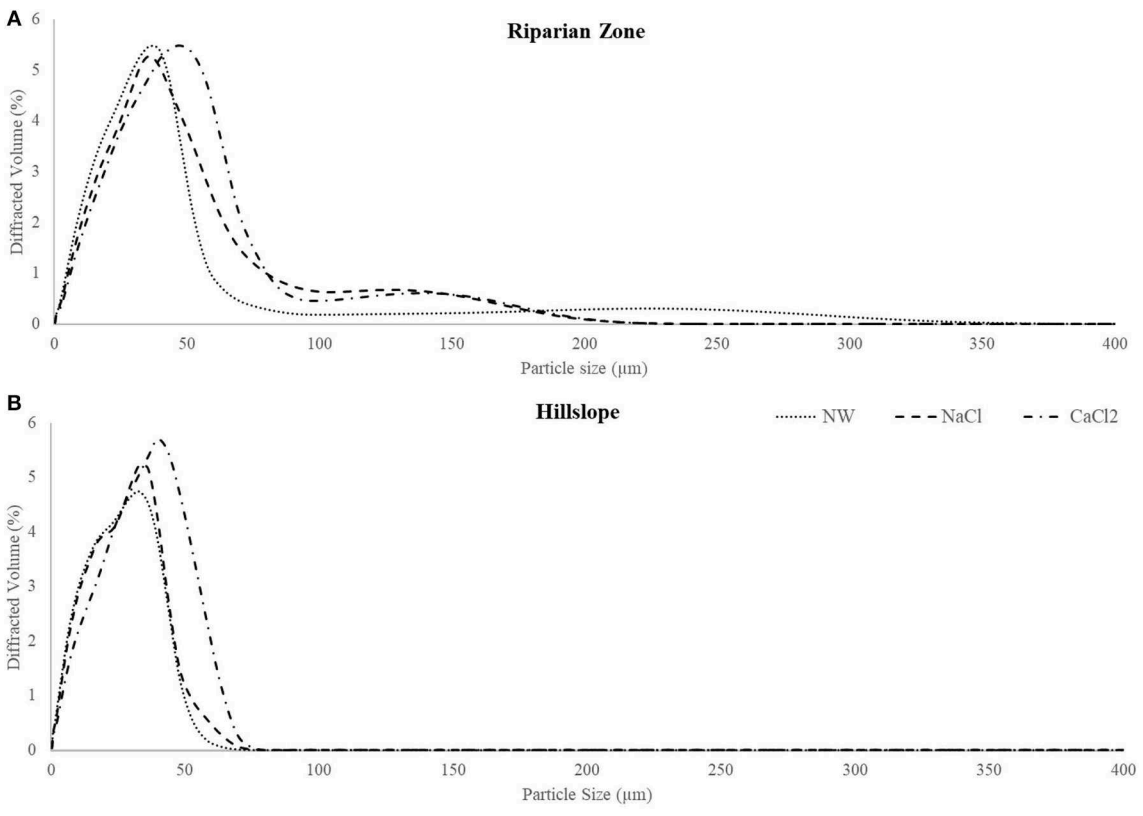


**FIGURE 4 |** Distribution of average particle size by treatment for landscape positions, RZ **(A)** and the HS **(B)**. There is a shift to the left in peaks from higher ionic strength to lower ionic strength solution. NW, Nanopure Water; NaCl, sodium chloride; $CaCl_2$, calcium chloride.

We performed a Parallel Factor Analysis (PARAFAC) using *Matlab R2017b* and the drEEM_4_0_(Ext.) toolbox (Murphy et al., 2013) to validate a 3-component PARAFAC model (**Figure 2**). Our three components are in agreement with components found in most studies (Ishii and Boyer, 2012) and include terrestrial fulvic-like (C-1), terrestrial humic-like (C-2), and microbial protein-like fluorescence (C-3, **Table 1**).

## Bioavailability of Carbon

The bioavailability of dissolved organic C in ASE was assessed using incubation experiments, which measure the decrease in organic C within or the increase in $CO_2$ evaded from a sample over time (McDowell et al., 2006). The results are expressed as % of respired C and give a reliable estimate of how readily C is transformed. An aliquot of each filtered ASE was inoculated using a pipette with 1μL of an unfiltered slurry that contained O-horizon microbes from all 18 soils. This slurry was formed using the unfiltered remnants from each ASE sample and was homogenized prior to the inoculations. The filtered ASE samples as well as laboratory blanks were incubated by shaking for 14 days in the dark in the Environmental Biogeochemistry Laboratory at the University of Vermont. The samples were covered individually with Parafilm (5 holes poked in the cover) and were all tented in foil. Samples were re-analyzed for DOC to determine the fraction of C loss through respiration (evaporation losses were accounted for by tracking sample mass and adding lost solution).

## Statistical Analyses

We used JMP Pro 13.0.0 software by *SAS* for statistical analyses. An Analysis of Variance (ANOVA) and the Tukey's Paired Test were performed to determine significance of variations in DOC amount and DOM composition of ASE by extraction solution composition. The average DOC amounts for each of the representative landscape positions (RZ and HS) were compared using a *T*-test to determine if the means were significantly

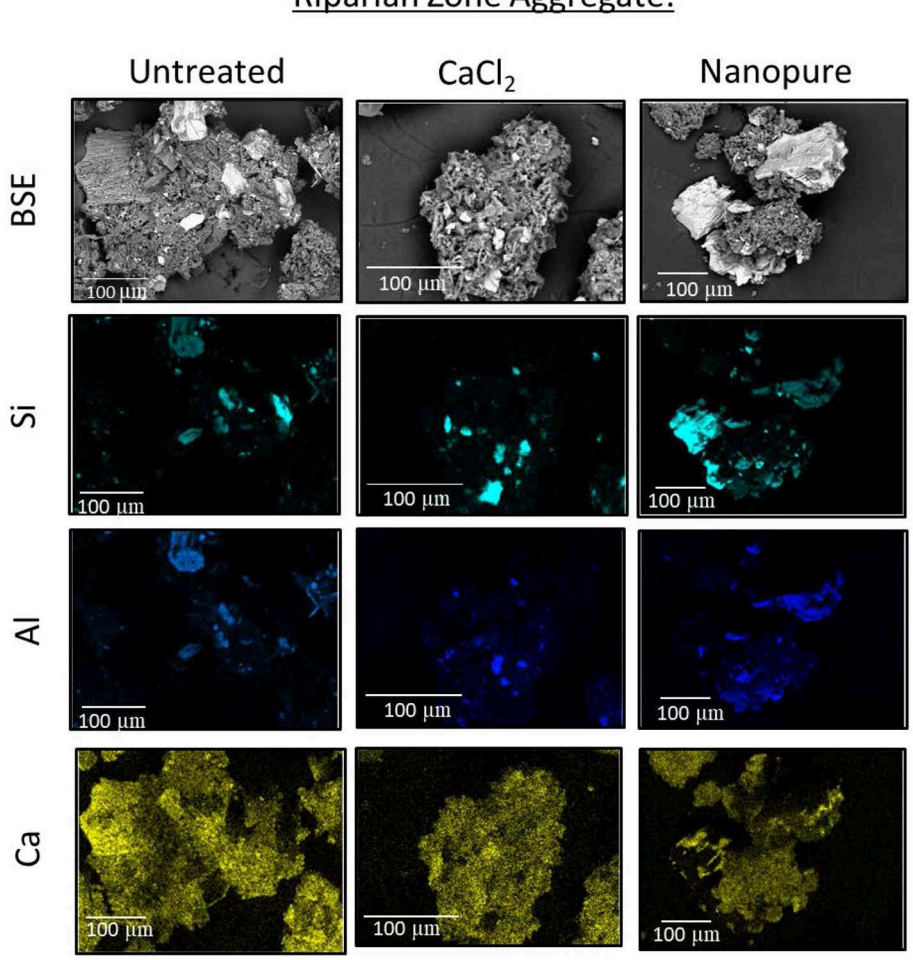


**FIGURE 5 |** Representative riparian zone (RZ) aggregate as a backscatter electron (BSE) image. Maps show the distribution of specific elements in untreated air-dried samples (**left**), treated with high ionic strength $CaCl_2$ solution (**center**), and low ionic strength Nanopure water (**right**).

different. SEM analyses were not used for statistical assessment but provided visualizations of typical aggregates.

# RESULTS

## Effect of Landscape Position on Soil Carbon

The highest C contents were found in the RZ samples of both the transect samples (ranging from 850 to 3,500 mg/kg in RZ and 490–570 mg/kg for HS, **Supplementary Figure 3**) and representative soil samples (**Figure 3**). The RZ adjacent to HS with high slope gradient had the greatest amount of soil C with more than 3,340 mg/kg. The least amount of C was found in HS with low slope gradient (380 mg/kg).

## Particle Size Analysis

Particle size distribution of the soil and extracting solution mixtures prior to filtration varied as a function of position (HS vs. RZ) and solution chemistry (**Figure 4**). Particle size in RZ extracts had a slightly greater range (up to 80 μm, **Figure 4A**), while HS soil extract particle size did not exceed 60 μm (**Figure 4B**). When extracted with higher IS solution, particle size distribution in extracts of soils from both landscape positions shifted toward larger sizes. In contrast, the low IS extracts showed a larger proportion of smaller particles and a smaller proportion of larger particles. Results of typical samples from the RZ and the HS illustrate the distinct change in particle size for each solution (**Supplementary Figure 8**).

## Visualization of Aggregates

SEM analyses of soil aggregates showed that aggregate morphology and size differed with dominant landscape position (RZ vs. HS, typical aggregates are exemplified in **Figures 5**, **6**). Typical RZ aggregates were rounded and contained large amounts of low electron density, organic-rich materials with only small amounts of angular mineral

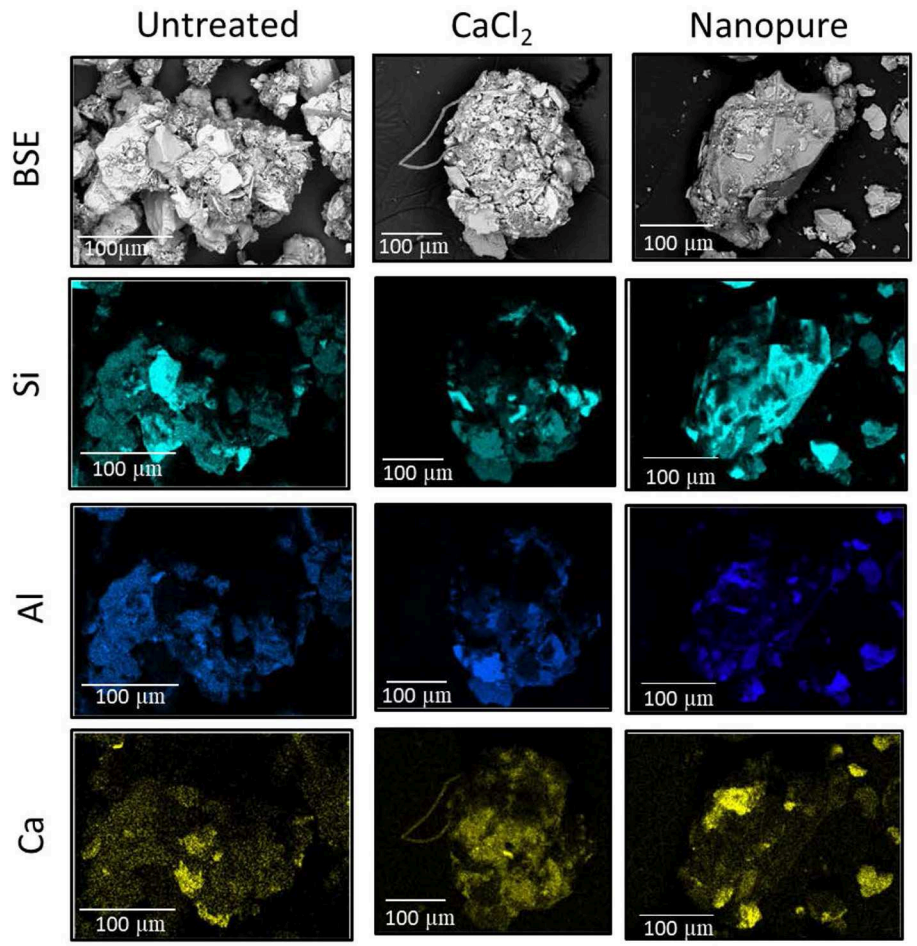


**FIGURE 6 |** Representative hillslope (HS) aggregate as a backscatter electron (BSE) image. Maps show the distribution of specific elements in untreated air-dried samples (**left**), treated with high ionic strength $CaCl_2$ solution (**center**), and low ionic strength Nanopure water (**right**).

fragments (**Figure 5**, top panel). The HS aggregates contained a larger proportion of mineral fragments (visible as high electron density materials) and relatively less organic-rich materials compared to the RZ aggregates (**Figure 6**, top panel). Elemental distribution maps confirmed these mineral fragments to be aluminosilicates and the EDS spectra suggest the presence of chlorite, amphibole, and quartz for RZ minerals (**Figure 7**) and biotite, amphibole, and quartz (**Figure 8**) for HS minerals. In contrast, the organic-rich matrix was devoid of Al and Si but enriched in Ca, specifically for RZ aggregates.

Aggregates from both RZ and HS treated with $CaCl_2$ solution (simulating the high IS of acidic precipitation) showed no change in overall morphology. The main difference was the removal of scattered fragments besides aggregates (**Figures 5**, **6**, center panels). In contrast, when aggregates were treated with NW (simulating the low IS solution during recovery), organic-rich materials were separated from the mineral fragments (**Figures 5**, **6**, right panels). Because the solution was dried in place, however, the organic material was not removed.

## Effect of Extraction Solution on Soils From Different Landscape Positions

DOC content in aqueous soil extracts was strongly impacted by the composition of the extraction solution but did not vary by position (HS vs. RZ, **Figure 9**). Extractions with NW showed the highest DOC (over 55 mg/kg) but also the largest variation ($SD$ = 12.2 mg/kg). The high IS solutions extracted significantly lower DOC concentrations and showed lower variability (averaging 17.7 ± 7.18 mg/kg and 11.6 ± 3.02 mg/kg for NaCl and $CaCl_2$, respectively). The total dissolved nitrogen content leached into the various extraction solutions followed the same pattern as DOC and was not affected by landscape position (**Supplementary Figure 9**).

The value of fluorescence-derived indices (FI and HIX) varied with extraction solution and landscape position, suggesting differences in both precursor material and soil decomposition (**Figure 10**). Highest (most microbial) FI values were observed for $CaCl_2$ extracts (ranging from 1.50 up to 2.04, **Figure 10A**). FI values for NW and NaCl extracts varied but were generally lower (ranging from 1.24 to 1.77 for NW and 1.30 to 1.57 for NaCl; **Figure 10A**). HS soils had higher FI values than RZ soils in all

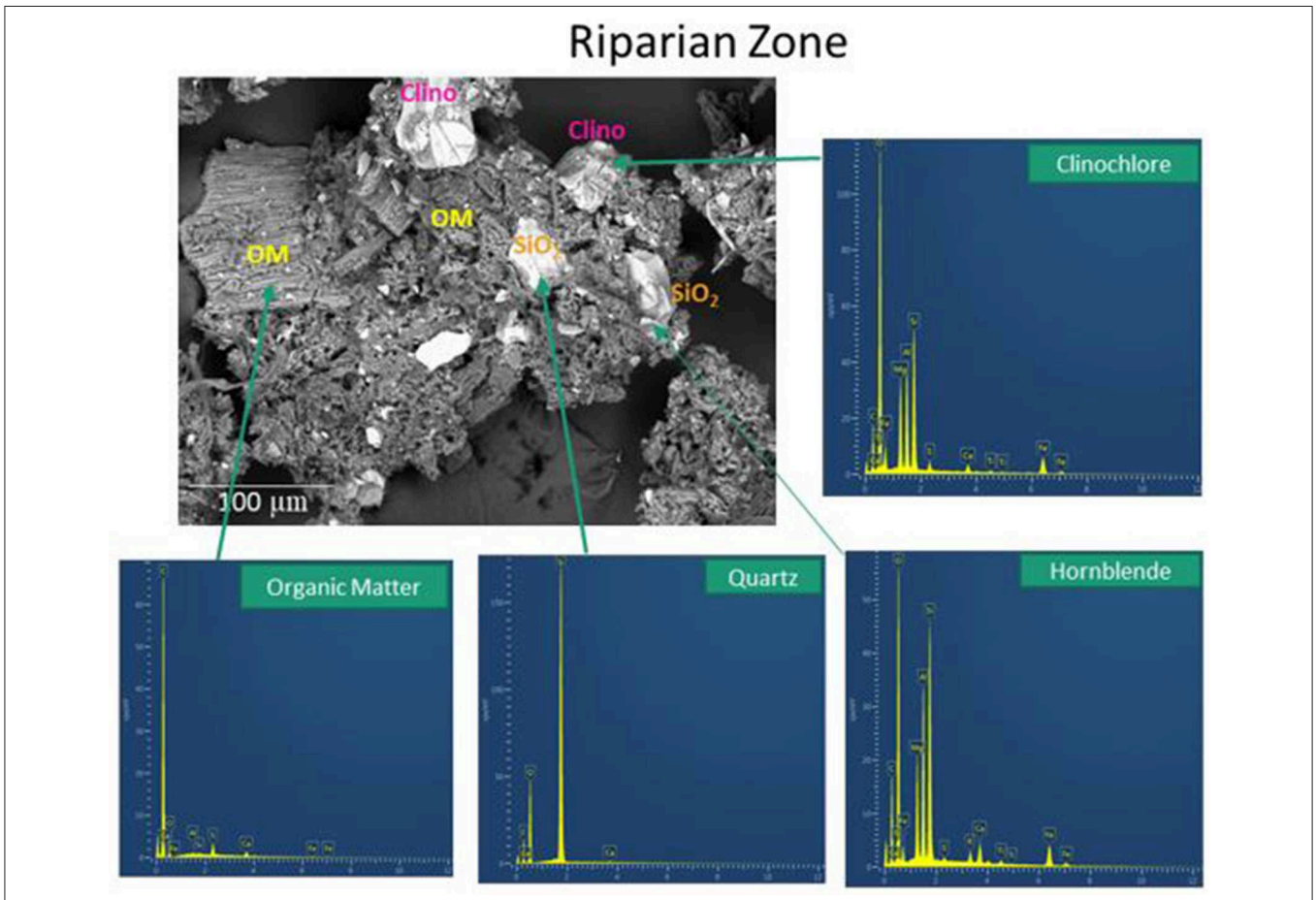


**FIGURE 7 |** Secondary electron scanning electron microscopy (SE SEM) image of soil aggregates present in composite soils from the riparian zone (RZ) of the high transect. OM, organic matter; clino, clinochlore.

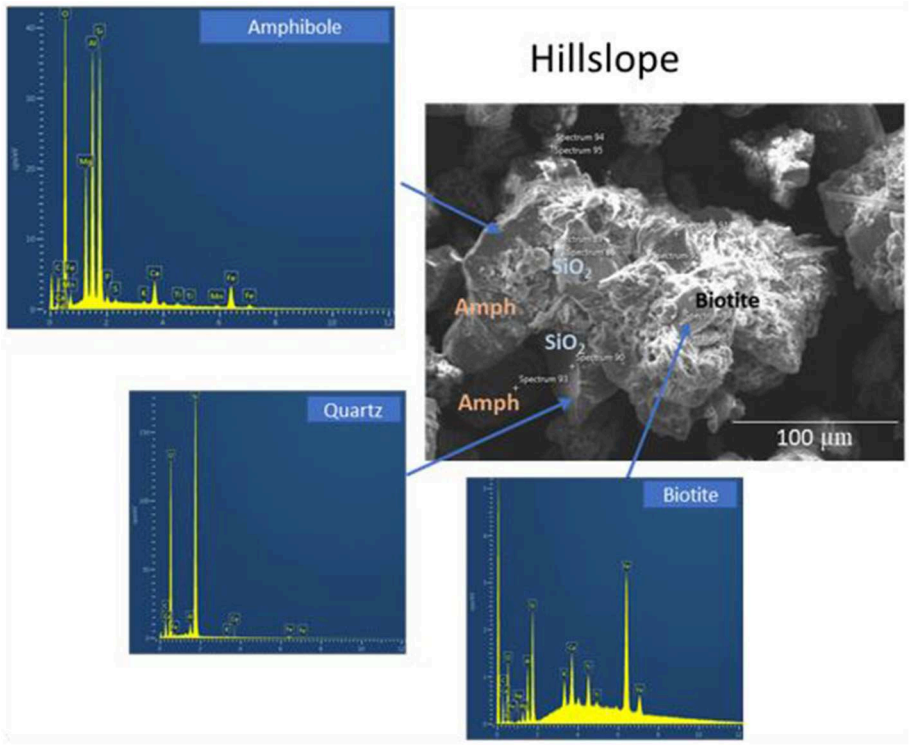


**FIGURE 8 |** Secondary electron scanning microscopy (SE SEM) image of soil aggregates present in composite soils from the hillslope (HS) of the high transect. Amph, Amphibole.

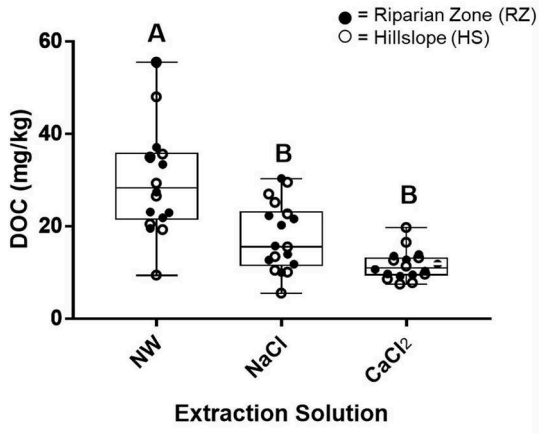


**FIGURE 9 |** Boxplots showing the mean and range of DOC concentrations (mg/kg) determined by treatment with three aqueous soil extraction solutions (NW, Nanopure Water; sodium chloride (NaCl), and calcium chloride ($CaCl_2$). Treatments ($n = 18$) with different letters indicate pairs of means that are significantly different ($p < 0.05$).

extraction solutions (**Figure 10B**). HIX values varied greatly in all extraction solutions but were highest in NW (up to 6.49) while $CaCl_2$ extracts had lowest values (as low as 1.84, **Figure 10C**). Differences in HIX values by extraction solution or landscape position were not significant ($p > 0.05$).

PARAFAC results indicate that the abundance of both the terrestrial, humic-like (C-2) and microbial, protein-like (C-3) components were similar in all three extraction solutions. However, the abundance of the terrestrial, fulvic-like C-1 in the $CaCl_2$ extracted DOM was significantly lower than in other solutions in both landscape positions ($p < 0.05$, **Figure 11**). HS soil extracts generally showed a greater variability in PARAFAC component abundance than RZ extracts. HS soils show a significantly higher abundance of the humic-like C-2 and lower abundance of the protein-like C-3 (both $p < 0.005$ at alpha = 0.05, **Figure 11**).

## Bioavailability of Extracted Carbon

The bioavailability of the extracted organic C in the ASE ranged from minimal to large losses (<1 to almost 60%, **Figure 12**). Generally, extracted DOC in the NaCl treatment decreased very little over the 2-week incubation while decreases in both the $CaCl_2$ and the NW treatments were more pronounced, but differences were not significant ($p > 0.05$).

# DISCUSSION

## Aggregate Dispersion: A Mechanistic Link Between Changes in Solution Composition and DOC Increases?

DOC solubility and mobility is strongly impacted by solution composition, especially by pH, IS, and the presence of polyvalent cations. At the molecular scale, an increase in pH can lead

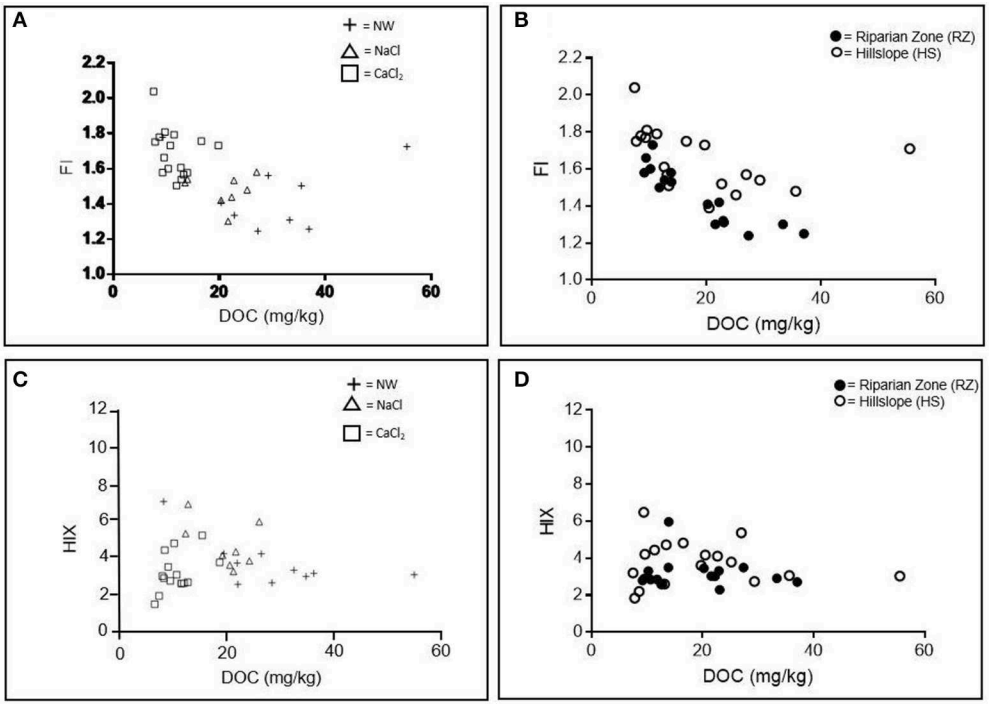


**FIGURE 10 |** Spectral Indices: Fluorescence Index (FI) **(A,B)** and Humification Index (HIX) **(C,D)** by extraction solution (NW, Nanopure water; NaCl, sodium chloride; $CaCl_2$, calcium chloride) and landscape position.

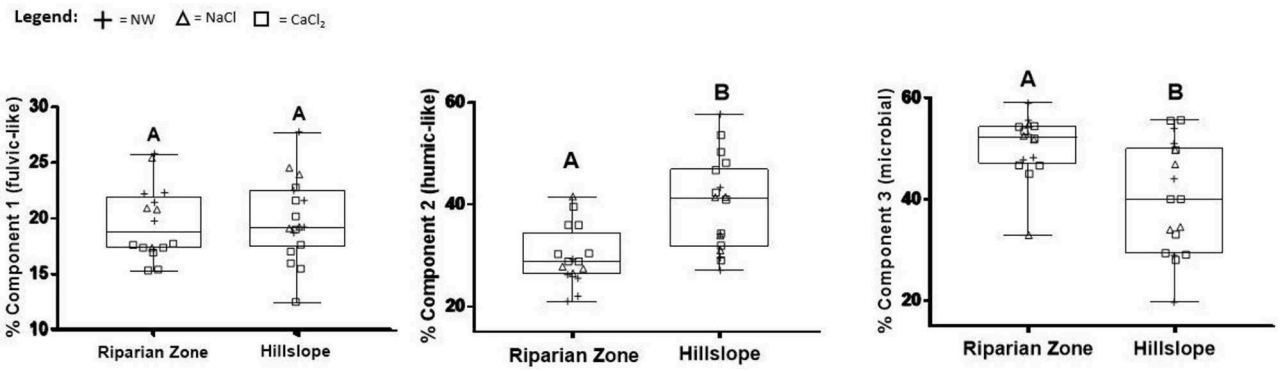


**FIGURE 11 |** The relative abundance of each PARAFAC component by extraction solution (NW, Nanopure water; NaCl, sodium chloride; and $CaCl_2$, calcium chloride) and landscape position. Letters above the boxplots indicate significant differences according to the Tukey Multiple Comparison test at $p < 0.05$.

to the deprotonation of functional groups (exemplified by the carboxyl group in **Figure 13A**) and DOC solubility increases as a result. The formation and shape of colloidal associations (**Figure 13B**) and the stability of aggregates (**Figure 13C**) is also highly controlled by solution chemistry. Colloidal associations, including organic material, deflocculate in low charge density environments (i.e., low IS and high pH, **Figure 13B**) (Stumm and Morgan, 1996; Buffle et al., 1998) contributing to DOC. Aggregate stability decreases in such environments due to expanding of diffuse double layers (again a decreased tendency of flocculation) and a shift from divalent to monovalent cations reduces the propensity for cation bridging (Tisdall and Oades, 1982; Six et al., 2004).

Because surface water DOC is largely sourced from organic soils (Yallop and Clutterbuck, 2009) and because soil C is typically stabilized in aggregates (Six et al., 2000) we hypothesized that particularly the breakup of soil aggregates plays an important role in increasing DOC during recovery from acidification. Based on this hypothesis, we expected to see the highest amounts of DOC (per kg soil) released into low IS solution (NW), followed by NaCl solution and finally the lowest DOC amounts in $CaCl_2$ solution. Indeed, the highest amounts of DOC were leached

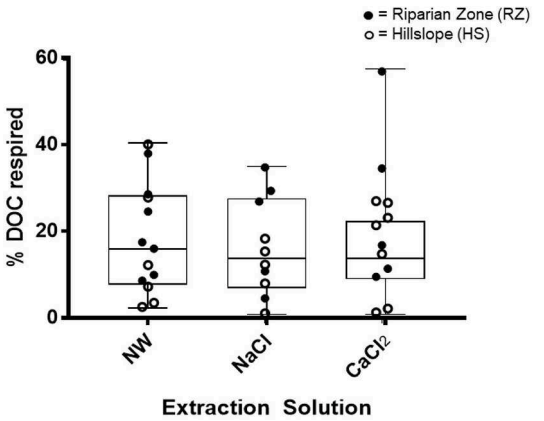


**FIGURE 12 |** The distribution for the bioavailability of carbon by extraction solution (NW, Nanopure Water; NaCl, sodium chloride; and $CaCl_2$, calcium chloride) and representative landscape position reported as % DOC respired (loss). None of the treatments or representative landscape positions were significantly different.

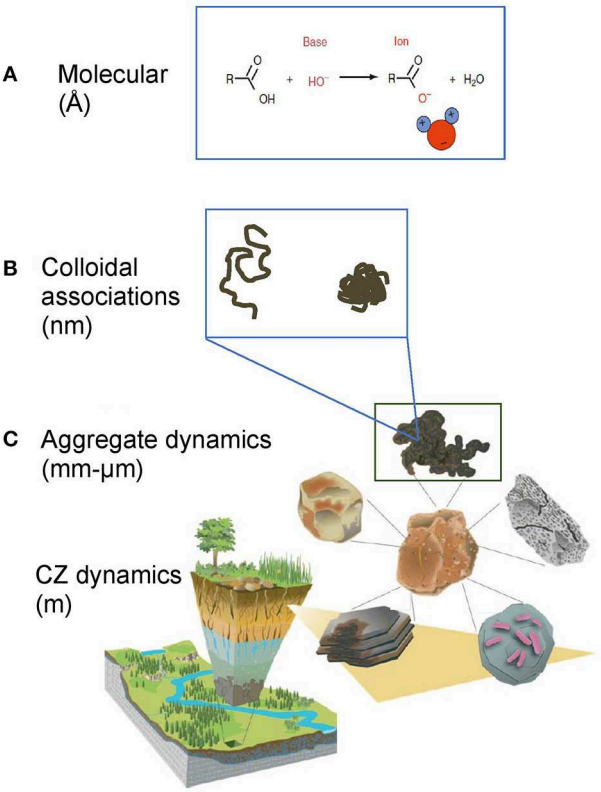


**FIGURE 13 |** Conceptualization of DOC release at varying scales and mechanisms. **(A)** Solution chemistry can change DOM solubility (Å-scale) and **(B)** DOM conformation (nm scale, figure modified after Chorover et al., 2007 with permission from the Mineralogical Society of America and Kleber and Johnson, 2010 with permission from Elsevier). These smaller scale processes would not lead to significant changes in aggregate size. **(C)** Solution composition could lead to aggregate dispersion and release of dissolved organic matter (DOM, mm-μm scale).

into NW and significantly lower amounts were released into the high IS solutions (NaCl and $CaCl_2$, **Figure 9**). This change in DOC amount was accompanied by a systematic shift in particle size distribution where decrease in IS led to losses in the particle size range of 40–100 μm and gains in the smaller size range below 30 μm (**Figure 4**). This could either suggest large aggregates break up to produce smaller aggregates (similar to **Figure 13C**) and/or aggregates of all sizes lose volume by, for example, desorbing colloidal material (e.g., **Figure 13B**).

While the SEM analysis was not performed on a statistically significant number of aggregates, the examples shown here are representative of the general trend we observed, which showed treatment with NW led to a separation of organic materials from larger silicate grains (**Figures 5**, **6**), creating smaller aggregates. We did not remove the treatment solution to limit disturbance of the aggregates, therefore the organic materials were still present as smaller aggregates and it is difficult to tell how much of this organic material dispersed and coagulated again during the drying process. However, it is likely that some of the organics would have passed a 0.7 μm filter (i.e., increasing DOC concentrations in the solution). In contrast, aggregates treated with higher IS $CaCl_2$ solution did not show the separation into organics vs. mineral fragments. These qualitative results support the DOC results that suggest that indeed aggregate dispersion might be more pronounced in low IS solution and could explain the higher amounts of DOC released in these cases.

These results are in agreement with results from a field study of the Pluhuv Bor catchment in the Czech Republic (Hruška et al., 2009) where the concentration of both stream water and soil-water DOC showed large increases between WY1994 and 2007. Of the assessed water quality parameters (pH and IS) under different flow conditions, changes in stream DOC concentration were inversely correlated to changes in IS (Hruška et al., 2009). This pattern was attributed to recovery from acidification but the underlying mechanism was not addressed. However, a study by Haaland et al. (2010) on lakes in Norway suggests decreased ionic strength and the ensuing increased surface charge of organic material could lead to electrostatic repulsion, deflocculation and therefore increased amounts of DOC in surface waters.

Another recent study on water-extractable DOC showed a positive correlation between concentration of monovalent cations in the extraction solution and DOC (Xie et al., 2017). The specific mechanism producing this correlation was not identified; however these results do not necessarily contradict our hypotheses of aggregate dispersion as DOC generator. Soil composition, including mineralogy, strongly affects aggregate composition and as a result, the main mechanism stabilizing aggregates differs; for example, in soils rich in metal oxides such as Oxisols (typical soils for the region of the Xie et al., 2017 study), pH might have a larger effect on aggregate stability than IS.

Because divalent cations are more effective in bridging negative charges (Mikutta et al., 2007; Rowley et al., 2018), potentially promoting aggregation and DOC sequestration, we had also expected lower DOC release for $CaCl_2$ vs. NaCl solutions of the same IS. Particle size analysis showed aggregate size was generally larger in $CaCl_2$ vs. NaCl solution, suggesting that cation bridging might play a role in preserving aggregates. DOC

release into $CaCl_2$ was indeed lower than into NaCl solution, but the effect was not significant (**Figure 9**). However, the trend is in agreement with results from Kerr and Eimers (2012), who conducted a combined laboratory and field study on the effect of monovalent vs. divalent cations on DOC release into soil water. The authors found that DOC release was driven by declines in one or more divalent cation species (not so much by an overall change in IS). The authors explained their results by reduced DOC sorption at low $Ca^{2+}$ concentrations which is most likely the result of cation bridging (Kerr and Eimers, 2012).

Despite the trend of aggregate size reduction with decreasing IS (modulated by the presence of mono vs. divalent cations) our observations show that these aggregates are remarkably stable. For example, the experimental treatment involved 1 h of vigorous shaking with the different extraction solutions, and yet, mean particle size decreased only by 13 to 17% (**Supplementary Table 1**). These results indicate DOC release via this mechanism is likely gradual and limited by overall aggregate stability.

## Landscape Position Modulated the Response to Solution Chemistry

We had hypothesized that soils from low-lying landscape positions contain higher total C than those from the HS locations and therefore would release more DOC. Our results confirm that TOC is consistently higher in RZ soils (**Figure 3**) and SEM analyses show a larger proportion of organic matrix vs. inorganic mineral fragments than HS soil aggregates (**Figures 4**, **5**), which would suggest a greater potential for DOC release. However, RZ soil extracts did not contain significantly higher amounts of DOC or TN (**Figure 9**, **Supplementary Figure 9**), which is remarkable, given that certain locations in the RZ had up to 6 times higher TOC content compared to the HS locations (**Figure 3**). One explanation for the relatively small releases of DOC could be the generally larger aggregate size in riparian soils (**Figures 4**, **6**) resulting in smaller surface areas. This difference in surface area could be significant for DOC desorbing from aggregate surfaces instead of from complete aggregate break up (**Figure 13A**). Another important factor is that RZs at our sites naturally contain large amounts of $Ca^{2+}$ from upwelling ground water (Shanley et al., 2004; Armfield et al., 2019), which could further help to stabilize RZ aggregates through increased sorption capacity or cation bridging (**Figure 5**).

Landscape position strongly impacted fluorescent DOM characteristics. For example, extracts from RZ soils consistently had lower values for FI and the humic-like PARAFAC component C-2, while the protein-like PARAFAC component C-3 was significantly more abundant compared to HS extracts (**Figures 10B,D**, **11**). These results paint a complex picture of the molecular make-up of DOM extracted from RZ soils and likely reflect a mixture of fresh and terrestrial organic matter such as roots and decomposing leaf litter (indicated by low FI) as well as abundant microbial DOM fueled by a wet and nutrient-rich environment (indicated by microbial C-3). In contrast, HS extracts generally had higher values for HIX and the humic – like C-2 (**Figures 10B,D**) and lower values for the microbial C-3, suggesting the presence of typical humified soil DOM with less microbial alteration. However, despite these differences in DOM quality, bioavailability was not significantly different between the different landscape positions (**Figure 12**).

We had also hypothesized that DOC released from aggregates would be mostly terrestrial and bioavailable because it would have been shielded from microbial processing. NW extracts (presumably containing more DOC from aggregates than the other extracts) indeed had the lowest values for FI and the lowest humic-like PARAFAC component C-2 (**Figure 10**). These results are in agreement with the findings of Angst et al. (2017) that most C released into solution was plant-derived (terrestrial). However, our study also showed that DOC in most extracts was only moderately bioavailable and that differences between extraction solutions were not significant (**Figure 12**).

In summary, our experimental results show that changes in solution chemistry, specifically decreases in IS, lead to increased water extractable organic carbon from soils. The breakup of aggregates and colloidal associations due to reduced cation bridging and diffuse double layer effects likely play an important role, and could contribute to recovery induced DOC release to streams if aggregate stability is sensitive to changes in IS.

Such recovery-induced increases in soil and stream DOC have important implications on DOC dynamics and water quality at the watershed-scale. For example, aggregate breakup could release other constituents such as nutrients and metals possibly impacting ecosystem productivity and contaminant movement. However, because aggregate breakup is governed by equilibrium dynamics, aggregate DOC will only be released until a new equilibrium is established (i.e., many decades after recovery begins). In contrast, if watershed DOC release is governed by ongoing drivers with only little potential for recovery (i.e., such as climate and land use change), DOC increase will continue to impact our surface waters for an undetermined amount of time (Freeman et al., 2001; Worrall and Burt, 2007; Eimers et al., 2008; Lepistö et al., 2008; Yallop and Clutterbuck, 2009).

## DATA AVAILABILITY STATEMENT

The stream water dataset analyzed for DOC trends can be found here: doi: 10.5066/P9380HQG and doi: 10.5066/P929KMVK.

## AUTHOR CONTRIBUTIONS

MC was responsible for sample collection, preparation, analyses, production of all figures and tables, as well as primary authorship. JP as MS thesis advisor aided in interpretation, authorship, field work, lab work, lab training, and allowed lab use. AS assisted with field work, lab work, and aided in interpretations. AL, ML-G, and TA assisted with field sampling and lab work. NP contributed through interpretations, authorship, and lab training. JA assisted with field sampling, lab work, and interpretations through research published in this issue. JS introduced authors to watershed, aided in interpretations, and provided pre-research consulting.

## FUNDING

This research was supported by the National Science Foundation, grant no. EAR-1724171, the College of Arts and Sciences at the University of Vermont and by the Vermont Space Grant Consortium/NASA EPSCoR Graduate Student Fellowship award.

## ACKNOWLEDGMENTS

The authors would like to thank Andrea Lini and Gaby Mora-Klepeis in the Department of Geology at the University of Vermont for their help and support. We also thank our colleagues at Middlebury College: Dave West for allowing the use of the SEM and Jody Smith for her time and assistance with using the SEM and its software. USGS participation was supported by the Land Change Science Program. Any use of trade, firm, or product names is for descriptive purposes only and does not imply endorsement by the US Government.

## SUPPLEMENTARY MATERIAL

The Supplementary Material for this article can be found online at: https://www.frontiersin.org/articles/10.3389/fenvs.2019.00172/full#supplementary-material

## REFERENCES

Aitkenhead-Peterson, J. A., McDowell, W. H., Neff, J. C., Stuart, E. G. F., and Robert, L. S. (2003). "Sources, production, and regulation of allochthonous dissolved organic matter inputs to surface waters," in *Aquatic Ecosystems,* eds S. E. G. Findlay and R. L. Sinsabaugh (Burlington, NJ: Academic Press), 25–70. doi: 10.1016/B978-012256371-3/50003-2

Angst, G., Mueller, K. E., Kögel-Knabner, I., Freeman, K. H., and Mueller, C. W. (2017). Aggregation controls the stability of lignin and lipids in clay-sized particulate and mineral associated organic matter. *Biogeochemistry* 132, 307–324. doi: 10.1007/s10533-017-0304-2

Armfield, J. R., Perdrial, J. N., Gagnon, A., Ehrenkranz, J., Perdrial, N., Cincotta, M., et al. (2019). Does stream water composition at sleepers river in vermont reflect dynamic changes in soils during recovery from acidification? *Front. Earth Sci.* 6:246. doi: 10.3389/feart.2018.00246

Bourgault, R. R., Ross, D. S., Bailey, S. W., Bullen, T. D., McGuire, K. J., and Gannon, J. P. (2017). Redistribution of soil metals and organic carbon via lateral flowpaths at the catchment scale in a glaciated upland setting. *Geoderma* 307, 238–252. doi: 10.1016/j.geoderma.2017.05.039

Boyer, E. W., Hornberger, G. M., Bencala, K. E., and McKnight, D. M. (1997). Response characteristics of DOC flushing in an alpine catchment. *Hydrol. Process.* 11, 1635–1647. doi: 10.1002/(SICI)1099-1085(19971015)11:12<1635::AID-HYP494>3.0.CO;2-H

Buffle, J., Wilkinson, K. J., Stoll, S., Filella, M., and Zhang, J. (1998). A generalized description of aquatic colloidal interactions: the three-colloidal component approach. *Environ. Sci. Technol.* 32, 2887–2899. doi: 10.1021/es980217h

Chorover, J., Kretzschmar, R., Garcia-Pichel, F., and Sparks, D. L. (2007). Soil biogeochemical processes within the Critical Zone. *Elements* 3, 321–326. doi: 10.2113/gselements.3.5.321

Clark, J. M., Bottrell, S. H., Evans, C. D., Monteith, D. T., Bartlett, R., Rose, R., et al. (2010). The importance of the relationship between scale and process in understanding long-term DOC dynamics. *Sci. Total. Environ.* 408, 2768–2775. doi: 10.1016/j.scitotenv.2010.02.046

Cory, R. M., and McKnight, D. M. (2005). Fluorescence spectroscopy reveals ubiquitous presence of oxidized and reduced quinones in dissolved organic matter. *Environ. Sci. Technol.* 39, 8142–8149. doi: 10.1021/es0506962

De Wit, H. A., Mulder, J., Hindar, A., and Hole, L. (2007). Long-term increase in dissolved organic carbon in streamwaters in norway is response to reduced acid deposition. *Environ. Sci. Technol.* 41, 7706–7713. doi: 10.1021/es070557f

Débora, M. B. P. M., Ladislau, M. N., Cimélio, B., João, M., and Vanderlei, S. B. (2002). Humification degree of soil humic acids determined by fluorescence spectroscopy. *Soil Sci.* 167, 739–739. doi: 10.1097/00010694-200211000-00004

Derjaguin, B., and Landau, L. (1941). Theory of the stability of strongly charged lyophobic sols and of the adhesion of strongly charged particles in solutions of electrolytes. *Acta Physicochim. URSS* 14, 633–662.

Eimers, M. C., Watmough, S. A., Buttle, J. M., and Dillon, P. J. (2008). Examination of the potential relationship between droughts, sulphate and dissolved organic carbon at a wetland-draining stream. *Glob. Chang. Biol.* 14, 938–948. doi: 10.1111/j.1365-2486.2007.01530.x

Evans, C. D., and Monteith, D. T. (2001). Chemical trends at lakes and streams in the UK acid waters monitoring network, 1988-2000: evidence for recent recovery at a national scale. *Hydrol. Earth Syst. Sci.* 5, 351–366. doi: 10.5194/hess-5-351-2001

Fellman, J. B., D'Amore, D. V., Hood, E., and Boone, R. D. (2008). Fluorescence characteristics and biodegradability of dissolved organic matter in forest and wetland soils from coastal temperate watersheds in southeast Alaska. *Biogeochemistry* 88, 169–184. doi: 10.1007/s10533-008-9203-x

Freeman, C., Evans, C. D., Monteith, D. T., Reynolds, B., and Fenner, N. (2001). Export of organic carbon from peat soils. *Nature* 412, 785–785. doi: 10.1038/35090628

Frey, S. D. (2005). Microbial aspects. *Aggregation* 1, 22–28. doi: 10.1016/B0-12-348530-4/00130-2

Haaland, S., Hongve, D., Laudon, H., Riise, G., and Vogt, R. D. (2010). Quantifying the drivers of the increasing colored organic matter in boreal surface waters. *Environ. Sci. Technol.* 44, 2975–2980. doi: 10.1021/es903179j

Holleran, M., Levi, M., and Rasmussen, C. (2015). Quantifying soil and critical zone variability in a forested catchment through digital soil mapping. *Soil* 1, 47–64. doi: 10.5194/soil-1-47-2015

Hruška, J., Krám, P., McDowell, W. H., and Oulehle, F. (2009). Increased dissolved organic carbon (DOC) in central European streams is driven by reductions in ionic strength rather than climate change or decreasing acidity. *Environ. Sci. Technol.* 43, 4320–4326. doi: 10.1021/es803645w

Ishii, S. K. L., and Boyer, T. H. (2012). Behavior of reoccurring PARAFAC components in fluorescent dissolved organic matter in natural and engineered systems: a critical review. *Environ. Sci. Technol.* 46, 2006–2017. doi: 10.1021/es2043504

Johnson, K. D., Scatena, F. N., and Silver, W. L. (2011). Atypical soil carbon distribution across a tropical steepland forest catena. *Catena* 87, 391–397. doi: 10.1016/j.catena.2011.07.008

Kaiser, K., and Guggenberger, G. (2000). The role of DOM sorption to mineral surfaces in the preservation of organic matter in soils. *Org. Geochem.* 31, 711–725. doi: 10.1016/S0146-6380(00)00046-2

Kang, H., Kwon, M. J., Kim, S., Lee, S., Jones, T. G., Johncock, A. C., et al. (2018). Biologically driven DOC release from peatlands during recovery from acidification. *Nat. Commun.* 9:3807. doi: 10.1038/s41467-018-06259-1

Kendall, K. A., Shanley, J. B., and McDonnell, J. J. (1999). A hydrometric and geochemical approach to test the transmissivity feedback hypothesis during snowmelt. *J. Hydrol.* 219, 188–205. doi: 10.1016/S0022-1694(99)00059-1

Kerr, J. G., and Eimers, M. C. (2012). Decreasing soil water $Ca2^{+}$ reduces DOC adsorption in mineral soils: implications for long-term DOC trends in an upland forested catchment in southern Ontario, Canada. *Sci. Total. Environ.* 427–428, 298–307. doi: 10.1016/j.scitotenv.2012.04.016

Kleber, M., and Johnson, M. G. (2010). "Chapter 3 - Advances in understanding the molecular structure of soil organic matter: implications for interactions in

the environment," in *Advances in Agronomy,* ed L. S. Donald (Academic Press), 77–142.

Lagaly, G. (2006). "Colloid clay science," in *Developments in Clay Sciences,* eds F. Bergaya, B. K. G. Teng, and G. Lagaly (Kiel: Elsevier), 141–245. doi: 10.1016/S1572-4352(05)01005-6

Lehmann, J., Kinyangi, J., and Solomon, D. (2007). Organic matter stabilization in soil microaggregates: implications from spatial heterogeneity of organic carbon contents and carbon forms. *Biogeochemistry* 85, 45–57. doi: 10.1007/s10533-007-9105-3

Lepistö, A., Kortelainen, P., and Mattsson, T. (2008). Increased organic C and N leaching in a northern boreal river basin in Finland. *Glob. Biogeochem. Cycles* 22, 1–10. doi: 10.1029/2007GB003175

Li, L., Vogel, J., He, Z., Zou, X., Ruan, H., Huang, W., et al. (2016). Association of soil aggregation with the distribution and quality of organic carbon in soil along an elevation gradient on Wuyi Mountain in China. *PLoS ONE* 11:e0150898. doi: 10.1371/journal.pone.0150898

Lohse, K., Brooks, P. D., McIntosh, J., Meixner, T., and Huxman, T. E. (2009). Interactions between biogeochemistry and hydrologic systems. *Annu. Rev. Environ. Resour.* 34, 65–96. doi: 10.1146/annurev.environ.33.031207.111141

Lybrand, R. A., and Rasmussen, C. (2015). Quantifying climate and landscape position controls on soil development in semiarid ecosystems. *Soil Sci. Soc. Am. J.* 79, 104–116. doi: 10.2136/sssaj2014.06.0242

McDowell, W. H., Zsolnay, A., Aitkenhead-Peterson, J. A., Gregorich, E. G., Jones, D. L., Jödemann, D., et al. (2006). A comparison of methods to determine the biodegradable dissolved organic carbon from different terrestrial sources. *Soil Biol. Biochem.* 38, 1933–1942. doi: 10.1016/j.soilbio.2005.12.018

Mikutta, R., Kleber, M., Torn, M. S., and Jahn, R. (2006). Stabilization of soil organic matter: association with minerals or chemical recalcitrance? *Biogeochemistry* 77, 25–56. doi: 10.1007/s10533-005-0712-6

Mikutta, R., Mikutta, C., Kalbitz, K., Scheel, T., Kaiser, K., and Jahn, R. (2007). Biodegradation of forest floor organic matter bound to minerals via different binding mechanisms. *Geochim. Cosmochim. Acta* 71, 2569–2590. doi: 10.1016/j.gca.2007.03.002

Miller, B. A., and Schaetzl, R. J. (2015). Digital classification of hillslope position. *Soil Sci. Soc. Am. J.* 79, 132–145. doi: 10.2136/sssaj2014.07.0287

Monteith, D. T., Stoddard, J. L., Evans, C. D., de Wit, H. A., Forsius, M., Hogasen, T., et al. (2007). Dissolved organic carbon trends resulting from changes in atmospheric deposition chemistry. *Nature* 450, 537–540. doi: 10.1038/nature06316

Murphy, K. R., Stedmon, C. A., Graeber, D., and Bro, R. (2013). Fluorescence spectroscopy and multi-way techniques. PARAFAC. *Anal. Methods* 5, 6557–6566. doi: 10.1039/c3ay41160e

Nimmo, J. R., and Perkins, K. S. (2002)."Aggregate stability and size distribution," in *Methods of Soil Analysis*, eds J. H. Dane, and G. C. Topp (Madison, WI: Soil Science Society of America), 317–328.

Perdrial, J., Brooks, P. D., Swetnam, T., Lohse, K. A., Rasmussen, C., Litvak, M., et al. (2018). A net ecosystem carbon budget for snow dominated forested headwater catchments: linking water and carbon fluxes to critical zone carbon storage. *Biogeochemistry* 138, 225–243. doi: 10.1007/s10533-018-0440-3

Perdrial, J. N., Perdrial, N., Harpold, A., Gao, X., LaSharr, K. M., and Chorover, J. (2012). Impacts of sampling dissolved organic matter with passive capillary wicks versus aqueous soil extraction. *Soil Sci. Soc. Am. J.* 76, 2019–2030. doi: 10.2136/sssaj2012.0061

Porcal, P., Koprivnjak, J. F., Molot, L. A., and Dillon, P. J. (2009). Humic substances-part 7: the biogeochemistry of dissolved organic carbon and its interactions with climate change. *Environ. Sci. Pollut. Res. Int.* 16, 714–726. doi: 10.1007/s11356-009-0176-7

Rawlins, B. G., Wragg, J., and Lark, R. M. (2013). Application of a novel method for soil aggregate stability measurement by laser granulometry with sonication. *Eur. J. Soil Sci.* 64, 92–103. doi: 10.1111/ejss.12017

Rowley, M. C., Grand, S., and Verrecchia, É. P. (2018). Calcium-mediated stabilisation of soil organic carbon. *Biogeochemistry* 137, 27–49. doi: 10.1007/s10533-017-0410-1

Shanley, J. B., Kram, P., Hruska, J., and Bullen, T. D. (2004). A biogeochemical comparison of two well-buffered catchments with contrasting histories of acid deposition. *Water Air Soil Pollut.* 4, 325–342. doi: 10.1023/B:WAFO.0000028363.48348.a4

Shanley, J. B., Sebestyen, S. D., McDonnell, J. J., McGlynn, B. L., and Dunne, T. (2015). Water's Way at Sleepers River watershed - revisiting flow generation in a post-glacial landscape, Vermont USA. *Hydrol. Proc.* 29, 3447–3459. doi: 10.1002/hyp.10377

Singh, S., Inamdar, S., and Scott, D. (2013). Comparison of two PARAFAC models of dissolved organic matter fluorescence for a mid-atlantic forested watershed in the USA. *J. Ecosyst.* 2013, 1–16. doi: 10.1155/2013/532424

Six, J., Bossuyt, H., Degryze, S., and Denef, K. (2004). A history of research on the link between (micro)aggregates, soil biota, and soil organic matter dynamics. *Soil Tillage Res.* 79, 7–31. doi: 10.1016/j.still.2004.03.008

Six, J., Elliott, E. T., and Paustian, K. (2000). Soil macroaggregate turnover and microaggregate formation: a mechanism for C sequestration under no-tillage agriculture. *Soil Biol. Biochem.* 32, 2099–2103. doi: 10.1016/S0038-0717(00)00179-6

Sokolova, T. A., and Alekseeva, S. A. (2008). Adsorption of sulfate ions by soils (a review). *Eur. Soil Sci.* 41, 140–148. doi: 10.1134/S106422930802004X

Stuart, E. G. F. (2005). Increased carbon transport in the hudson river: unexpected consequence of nitrogen deposition? *Front. Ecol. Environ.* 3, 133–137. doi: 10.1890/1540-9295(2005)003[0133:ICTITH]2.0.CO

Stumm, W., and Morgan, J. J. (1996). *Aquatic Chemistry*. New York, NY: John Wiley & Sons, Inc. 1022.

Tisdall, J., and Oades, M. (1982). Organic matter and water-stable aggregates in soils. *J. Soil Sci.* 33, 141–163. doi: 10.1111/j.1365-2389.1982.tb01755.x

Verwey, E. J. W. (1947). Theory of the stability of lyophobic colloids. *J. Phys. Colloid Chem.* 51, 631–636. doi: 10.1021/j150453a001

Wiekenkamp, I., Huisman, J. A., Bogena, H. R., Lin, H. S., and Vereecken, H. (2016). Spatial and temporal occurrence of preferential flow in a forested headwater catchment. *J. Hydrol.* 534, 139–149. doi: 10.1016/j.jhydrol.2015.12.050

Worrall, F., and Burt, T. P. (2007). Trends in DOC concentration in Great Britain. *J. Hydrol.* 346, 81–92. doi: 10.1016/j.jhydrol.2007.08.021

Wymore, A. S., Compson, Z. G., McDowell, W. H., Potter, J. D., Hungate, B. A., Whitham, T. G., et al. (2015). Leaf-litter leachate is distinct in optical properties and bioavailability to stream heterotrophs. *Freshw. Sci.* 34, 857–866. doi: 10.1086/682000

Wysocki, D. A., and Schoeneberger, P. J. (2017). "Soils in geomorphic research," in *International Encyclopedia of Geography: People, the Earth, Environment and Technology*, eds D. Richardson, N. Castree, M. F. Goodchild, A. Kobayashi, W. Liu, and R. A. Marston (Hoboken, NJ: John Wiley & Sons, Ltd.), 1–19. doi: 10.1002/9781118786352.wbieg1008

Xie, W., Zhang, S., Ruan, L., Yang, M., Shi, W., Zhang, H., et al. (2017). Evaluating soil dissolved organic matter extraction using three-dimensional excitation emission matrix fluorescence spectroscopy. *Pedosphere*. 27, 968–973. doi: 10.1016/S1002-0160(17)60466-1

Yallop, A. R., and Clutterbuck, B. (2009). Land management as a factor controlling dissolved organic carbon release from upland peat soils 1: spatial variation in DOC productivity. *Sci. Total Environ.* 407, 3803–3813. doi: 10.1016/j.scitotenv.2009.03.012

Yamashita, Y., Maie, N., Briceño, H., and Jaffé R. (2010). Optical characterization of dissolved organic matter in tropical rivers of the Guayana Shield, Venezuela. *J. Geophys. Res.* 115, 1–15. doi: 10.1029/2009JG000987

Zsolnay, A., Baigar, E., Jimenez, M., Steinweg, B., and Saccomandi, F. (1999). Differentiating with fluorescence spectroscopy the sources of dissolved organic matter in soils subjected to drying. *Chemosphere* 38, 45–50. doi: 10.1016/S0045-6535(98)00166-0

**Conflict of Interest:** The authors declare that the research was conducted in the absence of any commercial or financial relationships that could be construed as a potential conflict of interest.

# Advantages of publishing in Frontiers

**OPEN ACCESS**
Articles are free to read for greatest visibility and readership

**FAST PUBLICATION**
Around 90 days from submission to decision

**HIGH QUALITY PEER-REVIEW**
Rigorous, collaborative, and constructive peer-review

**TRANSPARENT PEER-REVIEW**
Editors and reviewers acknowledged by name on published articles

**Frontiers**
Avenue du Tribunal-Fédéral 34
1005 Lausanne | Switzerland

**Visit us:** www.frontiersin.org
**Contact us:** info@frontiersin.org | +41 21 510 17 00

**REPRODUCIBILITY OF RESEARCH**
Support open data and methods to enhance research reproducibility

**DIGITAL PUBLISHING**
Articles designed for optimal readership across devices

**FOLLOW US**
@frontiersin

**IMPACT METRICS**
Advanced article metrics track visibility across digital media

**EXTENSIVE PROMOTION**
Marketing and promotion of impactful research

**LOOP RESEARCH NETWORK**
Our network increases your article's readership